Role of Rhizaria in biogeochemical cycles of the epi- and mesopelagic oceans

Manon Laget

Thèse de Doctorat

Mention Sciences agronomiques et écologiques
Spécialité Sciences de la Mer – Biologie et écologie

présentée à *l'Ecole Doctorale en Sciences Technologie et Santé (ED 585)*

de l'Université du Littoral et de la Côte d'Opale

par

Manon Laget

pour obtenir le grade de Docteur de l'Université du Littoral et de la Côte d'Opale

Rôle des Rhizaria dans les cycles biogéochimiques de l'océan épi- et mésopélagique

Role of Rhizaria in biogeochemical cycles of the epi- and mesopelagic oceans

Soutenue le 4 décembre 2023, après avis des rapporteurs, devant le jury d'examen :

Pr. Lars Stemmann, Professeur à Sorbonne Université	Rapporteur
Dr. Mike Stukel, Professeur associé à Florida State University	Rapporteur
Dr. Grégory Beaugrand, Directeur de recherche CNRS	Examinateur/Président
Dr. Brivaëla Moriceau, Directrice de recherche CNRS	Examinatrice
Dr. Morten Iversen, Professeur associé à MARUM	Examinateur
Dr. Colleen Durkin, Research Faculty à MBARI	Examinatrice
Pr. Urania Christaki, Professeure à l'ULCO	Directrice de thèse
Dr. Tristan Biard, Maître de Conférences à l'ULCO	Co-encadrant

Chaque génération, sans doute, se croit vouée à refaire le monde. La mienne sait pourtant qu'elle ne le refera pas. Mais sa tâche est peut-être plus grande. Elle consiste à empêcher que le monde se défasse.

Albert Camus, *Discours de Suède*, 1957

Acknowledgements

First of all, I acknowledge the French 'Agence Nationale de la Recherche' and the Université du Littoral Côte d'Opale for funding this work.

I would like to thank the members of my jury, **Lars Stemmann**, **Mike Stukel**, **Grégory Beaugrand**, **Brivaëla Moriceau**, **Morten Iversen**, and **Colleen Durkin** for agreeing to read and evaluate this 3-year project.

Je remercie mes encadrants, **Tristan Biard** et **Urania Christaki**, pour ces trois années de thèse et pour votre confiance. Merci Tristan de m'avoir acceptée pour ce sujet ambitieux, de m'avoir introduite au monde de l'imagerie in situ et des Rhizaires, et de m'avoir donné l'opportunité de participer à des missions et des conférences qui m'ont permis de rencontrer des chercheurs et chercheuses de tout bord. Ευχαριστώ Urania d'avoir encadré cette thèse, pour ton soutien et particulièrement pour m'avoir offert ma première expérience d'enseignement.

Je remercie les trois membres de mon comité de thèse, **Lionel Guidi**, **Frédéric Le Moigne**, et **Brivaëla Moriceau** pour avoir suivi mon travail et m'avoir apporté leurs conseils au fil de ces trois années.

Mes prochains remerciements vont à l'ensemble des personnes avec qui j'ai pu travailler au cours de ces trois années. A Villefranche, je remercie **Marc Picheral** et **Camille Catalano** avec qui j'ai eu la chance de collaborer. Merci pour votre gentillesse et pour tout ce que j'ai pu apprendre à vos côtés sur l'UVP. Ça a été un vrai plaisir de travailler avec vous. Merci à tous deux et à **Amanda Elineau** pour votre aide et votre réactivité face aux problèmes rencontrés au cours des missions auxquelles j'ai participé. Je remercie **John Dolan** pour nous avoir fourni des échantillons de filets provenant de Villefranche. Un grand merci à **Jean-Olivier Irisson** pour tous ses bons conseils sur les stats. Merci également à **Matthieu Bressac** et **Louis Petiteau** pour avoir permis les déploiements de notre piège à DYFAMED. A Brest, ¡Muchas gracias! à **Natalia Llopis-Monferrer** pour sa bonne humeur et pour avoir accepté d'isoler plein de Rhizaires avec moi lors de la campagne P2107. Je remercie aussi **Aude Leynaert** et **Jean-François Maguer** pour les analyses élémentaires silice et carbone. A Lille, je remercie **Enrico Calzavarini** pour avoir échangé avec nous au sujet de l'hydrodynamisme dans les pièges à sédiments. From the United States, I would like to thank **Mark Ohman** and **Mike Landry** for having me on their respective cruises, and the crew and science party of the R/V *Revelle* who made sampling possible. I will always be grateful to Mark for his efforts to make it possible for us to come to the U.S.

during the covid period! I also thank **Mike Stukel** and his team for agreeing to deploy our traps.

Au labo, je remercie **Lucie Courcot**, **Alice Delegrange** et **Séverine Alvain** pour m'avoir initiée à la médiation scientifique et m'avoir permis de participer aux Fêtes de la Science. Je remercie les stagiaires que j'ai eu le plaisir d'encadrer, pour leur intérêt et leur motivation. Bien sûr, je remercie mes amies d'aventure **Marine Casetta**, ma coloc de l'été à la villa-MREN, et **Ioli Skouroliakou**, spécialiste à la fois de la *spanakópita* et du welsh boulonnais. Votre soutien aura été des plus importants au cours de cette aventure nordique.

Un merci tout particulier à mes proches qui se reconnaîtront.

Contents

Abbreviation list

ANOVA Analysis of variance.

BCP Biological Carbon Pump.

BRT Boosted Regression Trees.

CCE California Current Ecosystem.

CTD Conductivity, Temperature, Depth.

DOC Dissolved Organic Carbon.

ESD Equivalent Spherical Diameter.

NASS Normalized Abundance Size Spectra.

PCA Principal Component Analysis.

POC Particulate Organic Carbon.

UVP Underwater Vision Profiler.

CHAPTER 1

General introduction

"There are other ways of saying it, but really the most urgent question for biological oceanography is whether the marine biosphere will mitigate or reinforce the increase of anthropogenic greenhouse gases in the atmosphere."

A. R. Longhurst, *Role of the marine biosphere in the global carbon cycle*

Contents

1.1 Overview: biogeochemical cycles in the pelagic ocean

1.1.1 The pelagic ocean structure and its key biogeochemical processes

Since the pioneering nineteenth-century oceanographic expeditions, our exponential knowledge of the global ocean has highlighted its crucial influence on Earth's climate system and oxygen production required for living organisms. Particularly, it has absorbed 90% of the heat gained by the Earth since 1970 (Cheng et al., 2017), as well as a significant part of carbon dioxide (CO_2) released by human activities (Friedlingstein et al., 2022). Its most voluminous part, the pelagic domain, is defined as the worldwide water column beyond the continental shelf or neritic zone (Fig. 1.1), with the exception of the water near the ocean floor (demersal zone) and the seafloor itself. Strong gradients of light, temperature, density and hydrostatic pressure govern this environment. In its three-dimensional structure, global ocean dynamics is influenced by winds, the Coriolis force, and variations in temperature and salinity of water masses, operating across different scales to distribute heat and nutrients (Ganachaud and Wunsch, 2000). Unlike terrestrial ecosystems, pelagic ecosystems are shaped by constantly turbulent and advective waters.

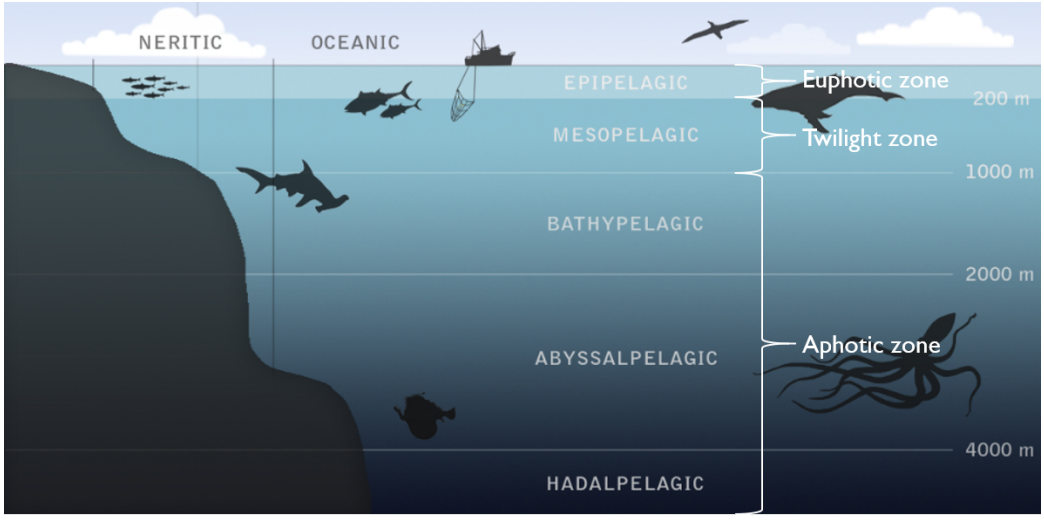

Figure 1.1: Vertical and zonation of the ocean, modified from Davies et al. (2012).

Consequently, pelagic ecosystems are home to organisms that drift with currents on the horizontal plane, known as plankton, as opposed to nekton which are

capable to swim against currents. Plankton encompass organisms from all three domains of life (Bacteria, Archaea, and Eukaryota) along with viruses. They vary greatly in size, ranging over more than six orders of magnitude (Sieburth, 1979; Fig. 1.2), and occupy diverse ecological niches. Indeed, plankton are found at all depths and span various feeding modes: they can be autotrophic (i.e., they produce organic matter from simple chemical compounds), heterotrophic (i.e., they feed on existing organic matter), or mixotrophic (i.e., they can use both pathways). Planktonic organisms are major contributors to the biological production and export of particulate organic carbon (POC) from the surface to the intermediate and deep ocean, a process called the biological carbon pump (BCP; Fig. 1.3).

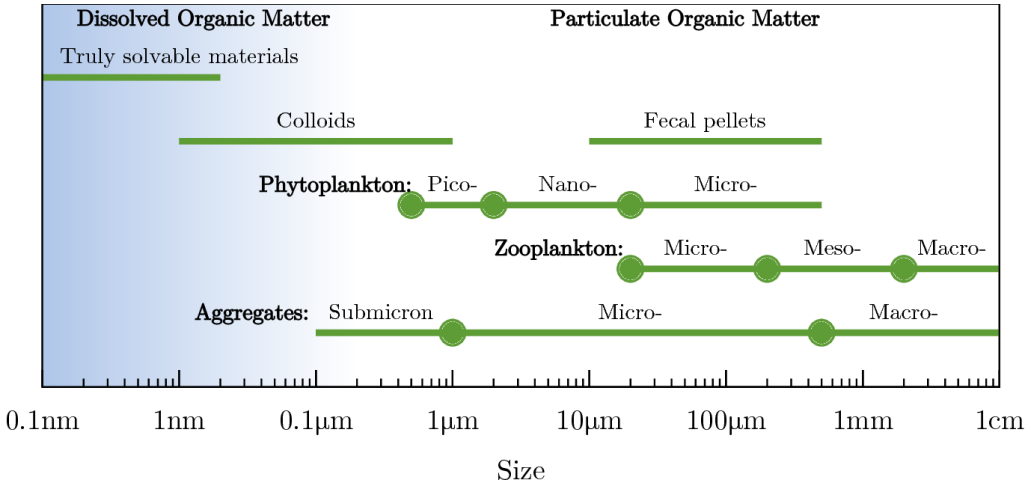

Figure 1.2: Size range of marine particles and plankton, from Monroy et al. (2017).

Indeed, photoautotrophic phytoplankton take up CO_2 and available nutrients to produce organic matter in the epipelagic layer (Fig. 1.1, 1.3). Its lower boundary, generally found between 100 and 250 m (Fig. 1.1), is defined as the depth at which 99% of daytime sunlight is absorbed. Phytoplankton encompass tiny prokaryotic and eukaryotic single-cell organisms and contribute to half of Earth's biomass production (Field et al., 1998). Primary production varies considerably across time and space with marked differences between oceanic regions. Central, mid-latitude oceanic gyres are vast areas of quasi-permanent low productivity (also referred to as oligotrophic environment or oceanic deserts). In contrast, high latitude waters are characterized by high seasonal productivity, especially during spring phytoplankton bloom (Fig. 1.4). In equatorial and coastal (eastern Pacific and Atlantic) waters, wind-driven upwelling areas convey deep nutrient-rich waters into warm surface waters, offering areas of high productivity which support some of the most diverse oceanic ecosystems (Kaempf and Chapman, 2016; Fig. 1.4).

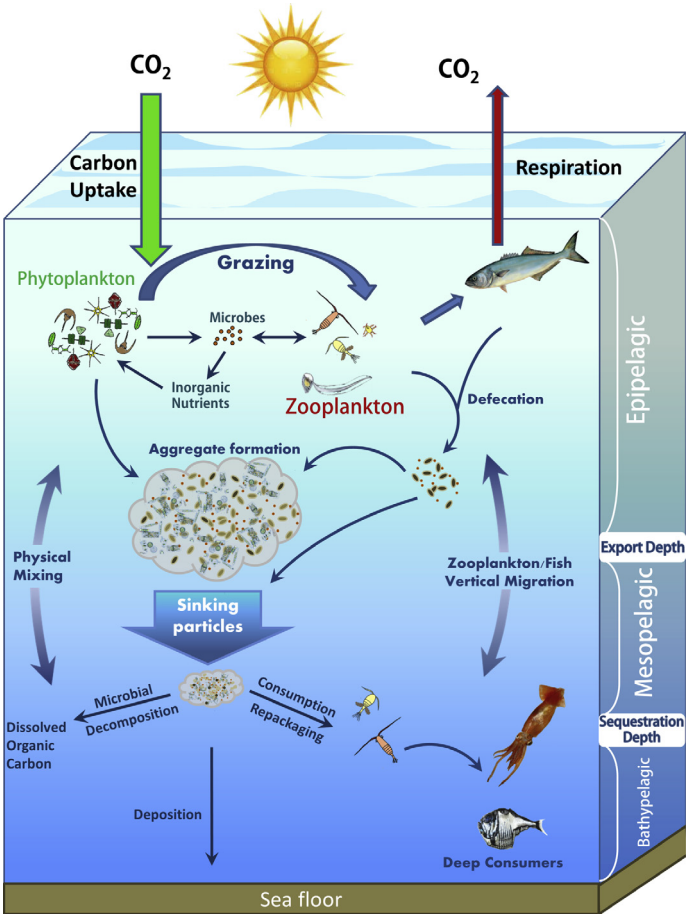

Figure 1.3: Schematic view of the biological carbon pump, from Turner (2015).

Just below the epipelagic layer, the mesopelagic layer starts when light is insufficient for photosynthesis and ends at 1,000 m (Fig. 1.1). The dim light that reaches this layer enables some visual predators to effectively capture prey; this is why this layer is commonly referred to as the "twilight zone" (e.g., Buesseler et al., 2007). Other organisms have developed special adaptations to these light conditions through bioluminescence, a widespread phenomenon in this layer (Martini and Haddock, 2017). The mesopelagic zone is connected (and connects deeper layers) to the surface ocean by hosting diel vertical migrations of zooplankton and micronekton, considered the most important animal migration on the planet (Hays, 2003). Although photosynthesis does not occur in the mesopelagic zone, this layer is paradoxically characterized by high inorganic nutrient concentrations, transferred to the surface ocean by water mass movements (Robinson et al., 2010). Indeed, the upper boundary of the mesopelagic layer often coincides with the thermocline, a transition zone between temperate surface waters and colder,

deeper water masses. As a result, warmer and less dense waters are found at the surface and are mixed by the action of winds. This mixed layer deepens during winter and is enriched with nutrients from deeper waters, creating a favorable environment for surface organisms. Therefore, the mesopelagic layer is a key interface within the entire pelagic environment. Yet, studying this stratum is challenged by inherent sampling limitations (difficult access, mechanical disruptions and decompression of organisms). Its ecology remains much less understood compared to that of the surface ocean, and recent calls have highlighted the urgency to explore and study this layer (Martin et al., 2020).

Deeper than the mesopelagic zone, the aphotic (i.e., no sunlight is coming through) zone includes the bathypelagic, the abyssalpelagic and the hadalpelagic layers (Fig. 1.1). Physical gradients are less marked and conditions are more homogeneous. Thus, this thesis will focus on the epi- and mesopelagic layers.

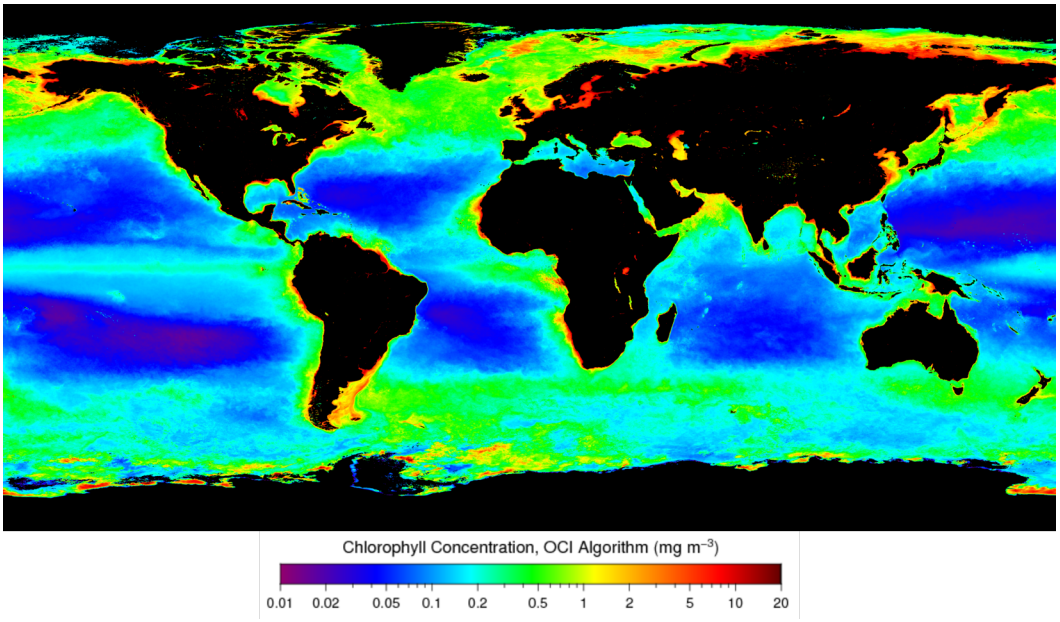

Figure 1.4: Annual chlorophyll *a* concentration, a proxy of ocean productivity, for the year 2020. Data come from the NASA satellite Aqua-MODIS.

The epi- and mesopelagic oceans host a rich abundance of life. Zooplankton, including protist (i.e., unicellular eukaryotes) and metazoan (multicellular organisms) taxa, link primary producers to higher trophic levels. Phytoplanktonic material can also be transformed into dissolved organic carbon (DOC; Fig. 1.2) and assimilated by heterotrophic bacteria. These bacteria are then eaten by heterotrophic protists, which are grazed by metazoan zooplankton. This microbial

loop has a major role in transferring organic matter to higher trophic levels (Azam, 1998). Both pathways result in the formation of detrital material, crucial in the functioning of the pelagic ecosystem. Phytoplankton cells in the surface layer can form sinking aggregates, termed marine snow given their snow-like appearance (Fig. 1.3). Similarly, fecal pellets and carcasses of larger organisms contribute to this snow of detrital material toward the deep ocean (Silver and Gowing, 1991; Wilson et al., 2013; Fig. 1.3).

As it distributes biologically available carbon along the water column from the surface to the interior of the ocean, the BCP is a key component of marine food webs. It results from a set of mechanisms, including gravitational settling of particles, physical mixing, subduction-driven lateral transport and active transport by vertically-migrating zooplankton and fishes (Boyd et al., 2019; Stukel et al., 2023). However, most of the POC produced in the euphotic layer is recycled back to CO_2 there. Only a fraction is exported to the mesopelagic realm (Fig. 1.5a), and this export is estimated to range between 5 and 12 Pg C y^{-1} globally (e.g., Henson et al., 2011; Nowicki et al., 2022; Clements et al., 2023). As the main food source for mesopelagic biota, organic matter undergoes various processes of consumption, repackaging and microbial decomposition (Fig. 1.3). Remineralization processes will eventually break down organic matter into DOC (Fig. 1.2) or respired back into CO_2. As a consequence, gravitational POC flux declines exponentially with depth and is commonly modeled by a power law (Martin et al., 1987; Fig. 1.5b) or by an exponential law (Lutz et al., 2002). The fraction of exported organic carbon that escapes remineralization and reaches at least 1,000 m is referred to as the transfer efficiency (Francois et al., 2002). The depth at which organic carbon is remineralized back to CO_2 eventually determines the time needed for its return to the surface ocean, thereby impacting atmospheric CO_2 concentration (Kwon et al., 2009).

Ultimately, only 1-3% of the surface primary production reaches depths below 1,000 m (Lampitt et al., 2010), at which it is said to be sequestered until the thermohaline circulation brings it back to the upper ocean (Fig. 1.3; Passow and Carlson, 2012). Sequestration varies spatially because of ocean circulation patterns (DeVries et al., 2012). The sequestration timescale (i.e, the time until carbon is returned as CO_2 to the atmosphere) depends on the depth at which particles are injected as well as their circulation through the ocean before they are remineralized to CO_2 (Boyd et al., 2019). Among the previously mentioned components of the BCP, the gravitational pump exports most particles out of the

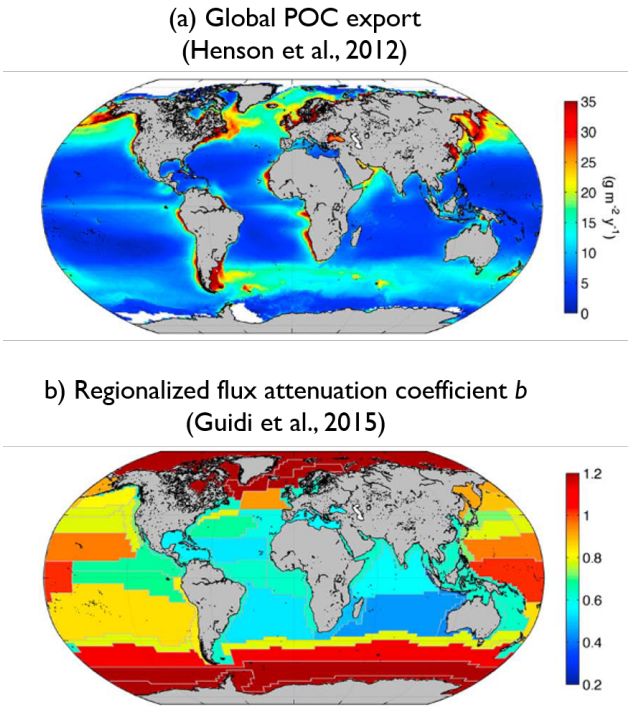

Figure 1.5: (**a**) Particulate organic carbon export from the euphotic zone at an arbitrary depth of 100 m, modified from Henson et al. (2012). (**b**) Regionalized estimates of the power law exponent b (Martin et al., 1987), also known as the attenuation coefficient, modified from Guidi et al. (2015). Values of the dimensionless coefficient b mostly range from 0.2 to 1.2. High values imply high flux attenuation and thus high remineralization.

surface ocean and is associated to longer sequestration timescale (Stukel et al., 2017; Boyd et al., 2019; Stukel et al., 2023). The following of the thesis will focus on this component and its mechanisms.

1.1.2 The gravitational pump

At global scale, export and transfer efficiencies due to gravitational sinking display strong variations over a range of oceanic provinces (Buesseler et al., 2007; Henson et al., 2012; Guidi et al., 2015; Cavan et al., 2019; Fig. 1.5). They are linked to surface phytoplankton (Francois et al., 2002; Guidi et al., 2009), zooplankton (Steinberg et al., 2008b; Henson et al., 2019), and microbial (Le Moigne et al., 2016) communities. Indeed, their combined action determines the amount and properties of sinking material and the proportion of marine snow aggregates versus fecal pellets (Buesseler et al., 2007). Deeper, mesopelagic communities also play a critical role in the fate of sinking material. Zooplankton and bacteria contribute to flux attenuation by fragmenting, consuming, and respiring organic

material. Total mesopelagic carbon demand have been estimated to exceed the loss of sinking POC flux by up to 10 times (Steinberg et al., 2008b), highlighting the need to accurately quantify all sources of demand and flux for accurate carbon budget assessments. Zooplankton can repackage sinking particles into fast-sinking fecal pellets, enhancing transport of organic carbon to depths (Burd et al., 2010). These activities are influenced by local temperature, oxygen and resource availability conditions (López-Urrutia et al., 2006; Iversen and Ploug, 2013; Marsay et al., 2015; Laufkötter et al., 2017; Cram et al., 2018). Still, the role of mesopelagic organisms is yet poorly understood and this layer is often under-parameterized in biogeochemical models (e.g., Aumont et al., 2015), despite its high heterogeneity (Robinson et al., 2010; Cavan et al., 2019). Understanding biological activities occurring in this layer is of paramount importance for our knowledge of the BCP and its responses to future changes. Zooming in to a smaller scale, the magnitude of the gravitational pump ultimately depends on the ability of particles to reach great depth before their carbon is respired. Therefore, it also depends on particles' individual properties as well as ecological processes they are exposed to (De La Rocha and Passow, 2007).

Sinking particles are diverse, including single or aggregated planktonic organisms, fecal pellets, organic debris, or a mixture of those (Alldredge and Silver, 1988). Given their distinct origin and age, they are composed of various organic molecules, such as lipids or carbohydrates, whose concentrations vary (Kharbush et al., 2020). There is a lability gradient from surface to depth, with highly labile POC close to the surface, where it forms, and more refractory material in deeper layers (Kharbush et al., 2020). As a consequence, organic particles are remineralized at slower rates the deeper they are found (Ducklow et al., 2001; Herndl and Reinthaler, 2013). Further modifying their composition during their sinking, bacteria colonize particles and release polymeric compounds, which increase particle stability and specific density (Alldredge et al., 1990; Stoderegger and Herndl, 1999).

Particle composition, which determines the specific density of particles relative to the surrounding water, directly impacts their sinking speed. This latter parameter has a key role in controlling flux attenuation (De La Rocha and Passow, 2007; Fig. 1.6). Indeed, the faster a particle sinks, the less remineralization it will undergo before reaching the deep ocean. Besides composition, the speed of a particle depends on its individual properties, such as size, shape and porosity (McNown and Malaika, 1950; Engel et al., 2009; Iversen and Ploug, 2010), in

addition to ambient water viscosity (Bach et al., 2012; Taucher et al., 2014). Given the intricacy of these factors, assessing their effect is challenging. Hence, the sinking velocity of particles is often modeled from size only (e.g., Guidi et al., 2008; Iversen and Ploug, 2010; Ramondenc et al., 2016; Guidi et al., 2016; Fender et al., 2019). Slow-sinking particles are typically assumed to be either small or large with low density. Marine particles sink at a speed up to more than 2,000 m d^{-1} (Turner, 2002; Turner, 2015), with fecal pellets usually sinking faster than other aggregates (Turner, 2002). Over their course to the deep ocean, particles undergo aggregation and disaggregation processes, altering their speed (Burd and Jackson, 2009). Reworking by heterotrophs induces a change in fecal pellets types (Urrere and Knauer, 1981) and possibly the loss of slowest sinking particles. Consequently, the sinking speed of the population of particles has been observed to increase with depth (Berelson, 2001).

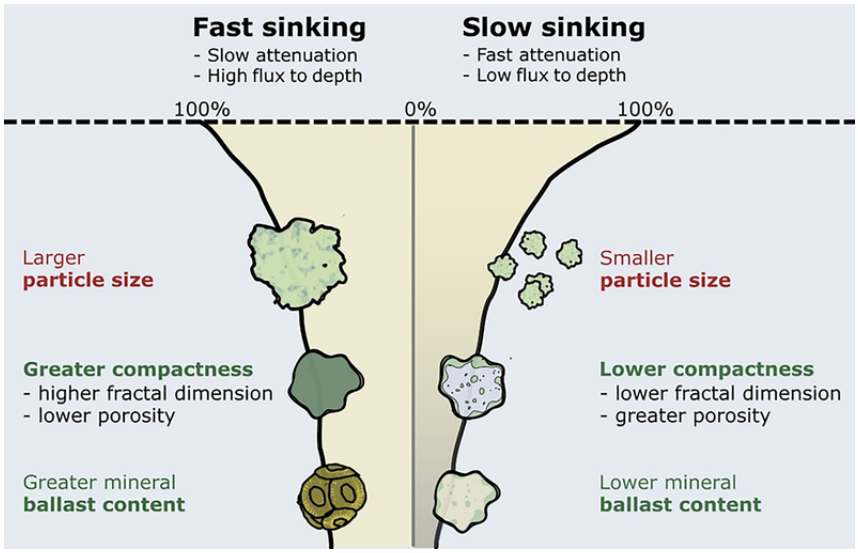

Figure 1.6: Factors playing a role in particle sinking speeds. As described in Stokes' law (Stokes, 1851), these factors are related to size (red) or density (green). Fast-sinking particles lead to a slower flux attenuation (left curve) and slow-sinking particles are associated to fast attenuation (right curve). Modified from Williams and Giering (2022).

If particles are commonly assumed to sink to the deep ocean, a substantial pool of carbon-rich suspended (i.e., neutrally buoyant) particles exists at all depths. Their concentration can be two orders of magnitude higher than that of sinking particles (Baltar et al., 2010). They constitute major substrates for heterotrophs and are linked to deep metabolic activity (Baltar et al., 2009; Duret et al., 2019; Baumas et al., 2021). Their concentration is constant in the deep ocean (Herndl and Reinthaler, 2013). While a part comes from the surface ocean and becomes

buoyant by entering dense water, another part is possibly produced at depth (Herndl and Reinthaler, 2013).

Aside from their organic elements, particles can host mineral molecules, mostly lithogenic silica, biogenic silica (biogenic Si or opal, of formula SiO_2) and biogenic carbonates. These minerals can play a role in two ways. By protecting aggregates, they could slow down remineralization processes (Hedges et al., 2001). Then, the high density of minerals increases the excess density of the particle with respect to the ambient seawater, and thus its sinking velocity (Armstrong et al., 2001; Klaas and Archer, 2002 Francois et al., 2002). The latter is known as the "ballast hypothesis". However, the integration of minerals also has an influence on size and porosity of the particle. Thus, the relationship between mineral ballasting and POC fluxes is not straightforward. It was hypothesized that POC fluxes control mineral fluxes instead, by scavenging and sticking together mineral particles (Passow, 2004; Passow and De La Rocha, 2006).

In particular, the BCP is tightly coupled with the silica pump. Indeed, silica accumulates in marine sediments (Tréguer et al., 2021) and is a vital element for several pelagic taxa: diatoms, radiolarians, phaeodarians and silicoflagellates all require dissolved silica (dissolved Si) to precipitate biogenic Si and build silica shells or skeletons. Diatoms are the main primary producers of organic matter (Field et al., 1998), and a decrease of dissolved Si in the epipelagic layer could lead to a fall in their biomass (Martin-Jézéquel et al., 2000). Diatom-dominated ecosystems are associated to high transfer efficiency through to mesopelagic zone (Buesseler et al., 2007), though the relationship with export can be more complex (Lam and Bishop, 2007). In the mesopelagic layer, diatoms are absent but several heterotrophic groups take part in controlling dissolved Si distribution, such as radiolarians and phaeodarians, contributing to silica circulation (Biard et al., 2018; Llopis-Monferrer et al., 2020). However, in regions dominated by biogenic Si, the transfer efficiency of organic carbon to the deep ocean is lower than in regions dominated by calcium carbonate minerals, likely because the exported organic matter during bloom events is more labile and packaged into looser aggregates, thus being more effectively remineralized during its transit through intermediate depths (Francois et al., 2002).

To summarize, gravitational export and flux attenuation are driven by the nature of sinking material, with zooplankton playing a central role in determining its ability to reach the deep ocean (Steinberg and Landry, 2017). While studies of the role of zooplankton in the BCP is often focusing on crustaceans, recent

studies showed that protists, occupying diverse functions in pelagic foodwebs, play an important role in the cycling of elements.

1.1.3 The role of heterotrophic and mixotrophic protists

The kingdom Protista (from the Greek *proto*, "first") was introduced in 1866 by the German biologist Ernest Haeckel to include organisms that did not belong neither to Animalia nor to Plantae (Haeckel, 1866). This term, which no longer holds taxonomic significance, is still frequently used to refer to unicellular eukaryotes, which constitute the majority of the Eukaryota domain (Keeling and Burki, 2019). In addition to phototrophy, protists feature a wide range of feeding modes, among which mixotrophy and heterotrophy (Worden et al., 2015). In the well-lit epipelagic layer, a significant proportion of protists are mixotrophic (Flynn et al., 2013), i.e., the cell is capable to engage both phototrophy and heterotrophy. These protists initiate a shortened pathway from nutrient regeneration to primary production, impacting foodweb dynamics and the functioning of the BCP (Mitra et al., 2014). Heterotrophy is also a common mode of nutrition in marine protists. Although the specific mechanisms of protist heterotrophy are not fully resolved yet, protists can feed extensively on phytoplankton cells and detrital aggregates and they can be associated to both sinking and suspended material (Duret et al., 2020). As a result, they contribute to flux attenuation (Worden et al., 2015). Still, the magnitude of their impact is not fully understood, particularly in the twilight zone. Furthermore, several protist taxa can prey upon and be preyed upon metazoan larger than themselves, such as copepods, leading to longer food chains and therefore more carbon losses (Worden et al., 2015, and references therein).

Heterotrophic and mixotrophic protists make up most of the microzooplankton size class (>200 μm) (Paffenhöfer, 1998). The mesozooplankton size class (200 μm - 2 mm) consists mainly of metazoans, but also includes large protists, such as Rhizaria (Steinberg and Landry, 2017, and references therein). Protist assemblages differ between the epipelagic and the mesopelagic layers, but mesopelagic protist communities remain poorly known (Edgcomb, 2016).

Among these diverse protist taxa are found planktonic Rhizaria, ubiquitous protists which encompass both heterotrophy and mixotrophy. They span a size range from a few tens of μm to several mm and display a great ecological diversity, inhabiting both the epipelagic and the mesopelagic layers. A handful studies showed their contribution to both elemental flux (carbon and silica; e.g., Biard

et al., 2018; Ikenoue et al., 2019) and flux attenuation (Stukel et al., 2019). In the next section, we will review the knowledge about their biology and ecology and then dig further into their role in pelagic biogeochemistry.

In summary

- A fundamental question in oceanography is to determine the origin and fate of sinking flux, as it has significant implications for atmospheric CO_2 concentrations.
- By producing and mediating organic matter and minerals, pelagic organisms influence the composition of sinking particles and their sinking velocity, ultimately playing a key role in the BCP.
- Among the diversity of pelagic organisms, this thesis focuses on Rhizaria, a group of heterotrophic and mixotrophic protists which has been overlooked until recently.

1.2 Planktonic Rhizaria in pelagic ecosystems

1.2.1 Classification, biology and ecology of planktonic Rhizaria

Like for animals and plants, protist classification has historically relied on morphological criteria, but detailed relationships were difficult to establish (Keeling and Burki, 2019). Recent advances in molecular phylogeny have drawn attention to the great diversity of unicellular eukaryotes. The SAR assemblage is composed of the supergroups Stramenopila, Alveolata and Rhizaria (Fig. 1.7), embodying half of eukaryotic diversity (Burki et al., 2007; Keeling and Burki, 2019). Stramenopila and Alveolata include respectively diatoms and dinoflagellates, two major planktonic lineages in modern oceans. On the other hand, Rhizaria are less well-known than their sister clades, partly due to the impossibility to culture most of them. The name Rhizaria refers to their root-like pseudopodia or axopodia, which characterize the majority of organisms belonging to this group (Cavalier-Smith, 2002; Nikolaev et al., 2004). This thesis focuses on two planktonic rhizarian taxa, most of which producing silica skeletons: Radiolaria and Phaeodaria.

Radiolaria are included in the superphylum Retaria together with Foraminifera (Moreira et al., 2007). These two ancient protistan lineages produce mineral

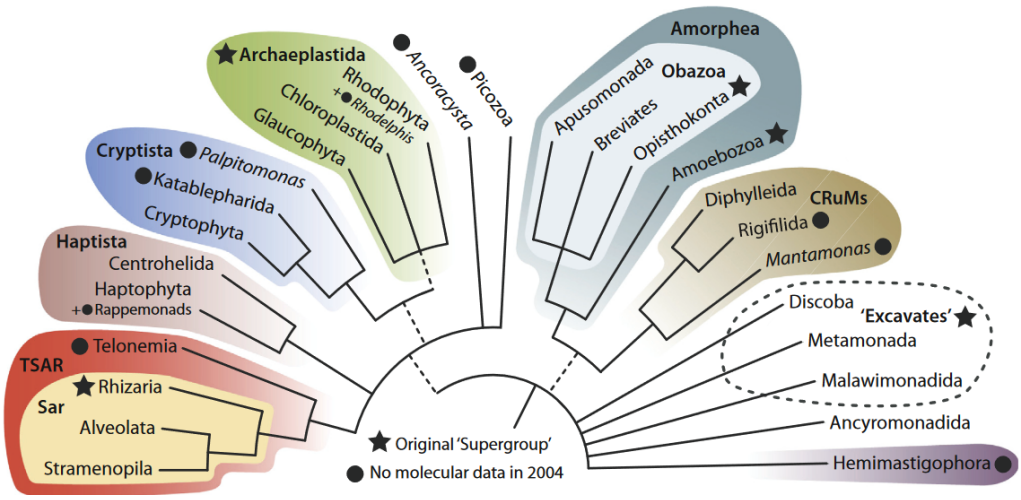

Figure 1.7: Most recent schematic tree of Eukaryota based on a consensus of recent phylogenomic studies, from Burki et al. (2020).

skeletons which have accumulated on the seafloor through time and have helped to determine past environmental conditions (De Wever et al., 2002). Originally classified as Radiolaria based on their morphological characteristics (e.g., Haeckel, 1887), Phaeodaria are now included in the phylum Cercozoa (Nikolaev et al., 2004; Polet, 2004; Sierra et al., 2013) thanks to the use of molecular phylogeny. Cercozoa is a highly diversified and ubiquitous phylum, bringing together a majority of free heterotrophic protists (Bass and Cavalier-Smith, 2004; Howe et al., 2011).

Radiolaria include six orders: Acantharia, Taxopodia, and the four orders Nassellaria, Spumellaria, Collodaria and Orodaria forming the class Polycystinea (Adl et al., 2018; Nakamura et al., 2021; Biard, 2022a; Fig. 1.8). The cytological structure consists of a double-layered cytoplasm which has extensions called pseudopodia. The inner part of the cytoplasm contains the nucleus and cellular organelles. The capsular wall separates it from its outer part which comprises food vacuoles and algal symbionts. Pseudopodia are cytoplasmic strands extending outside of the ectoplasm, whose contraction and elongation serve for buoyancy control and capture of preys (Suzuki and Aita, 2011; Suzuki and Not, 2015). Almost every species of Radiolaria has a mineral structure, made of strontium sulfate ($SrSO_4$) for Acantharia and biogenic Si for all other orders, although some Collodaria are naked (reviewed in Biard, 2022a). The structure and appearance of this skeleton vary greatly among orders (Fig. 1.8).

Phaeodaria, on the other hand, possess a central capsule, a spherical cytoplasmic body which is enclosed in a double-walled membrane separating it from the

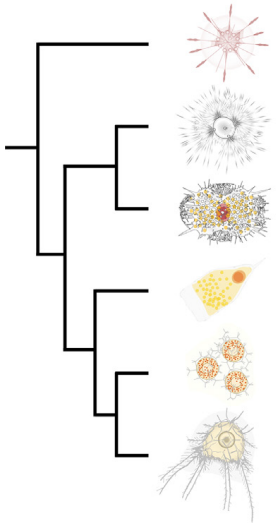

order	body size (µm)	skeleton type	main skeletal component	colony formation	symbiotic algae
Acantharia	50–1,000	shell	$SrSO_4$	-	+
Taxopodia	200–800	oar-like spines	$SiO_2\,n\,H_2O$	-	-
Spumellaria	50–2,000	shell	$SiO_2\,n\,H_2O$	-	+
Nassellaria	50–300	shell	$SiO_2\,n\,H_2O$	-	+
Collodaria	100–1.5 m*	dispersed shell/spicules or naked	$SiO_2\,n\,H_2O$	+	+
Orodaria ordo. nov.	1,000–7,000	shell	$SiO_2\,n\,H_2O$	-	-

Figure 1.8: General characteristics of current radiolarian orders, with the topology based on based on Nakamura et al. (2020). * indicates the length or diameter of a colony. +: reported in some species. -: not reported. Modified from Nakamura et al. (2021).

extracapsular zone. This membrane is perforated to allow communication between these two parts. Through these pores, cytoplasmic strands named axopods and filopods project into the environment (Cachon and Cachon, 1973; Anderson, 1983). At the oral pole lays a dark phaeodium, an assemblage of food and waste vacuoles which does not exist in Radiolaria. Once their food is captured using filopods and axopods, it can be digested outside the central capsule or inside after ingestion (Gowing, 1986; Gowing, 1989; Cachon et al., 1990; Takahashi and Anderson, 2000). In most Phaeodaria, these organic parts are supported by their internal silica skeleton of porous nature (Takahashi and Hurd, 2007; Nakamura et al., 2018a). Its overall appearance differ greatly from one group to another (Takahashi and Hurd, 2007) (Fig. 1.9).

Although the composition of Radiolaria and Phaeodaria skeletons is similar (Nakamura et al., 2018a), their structure differs greatly (Fig. 1.10). Compared to that of Nassellaria and Spumellaria, the skeleton of Phaeodaria easily dissolves in seawater, because of its porous nature, and does not preserve in sediments (Erez et al., 1982; Takahashi and Hurd, 2007). Radiolaria and Phaeodaria display a great morphological diversity and occupy a large size spectrum spanning over three orders of magnitude (Fig. 1.8, 1.9). In Radiolaria, smallest Nassellaria species only reach a few tens of μm, whereas Orodaria specimens of more than 6 mm were collected in the North Pacific (Nakamura et al., 2021). In Phaeodaria, cell diameter

(a)

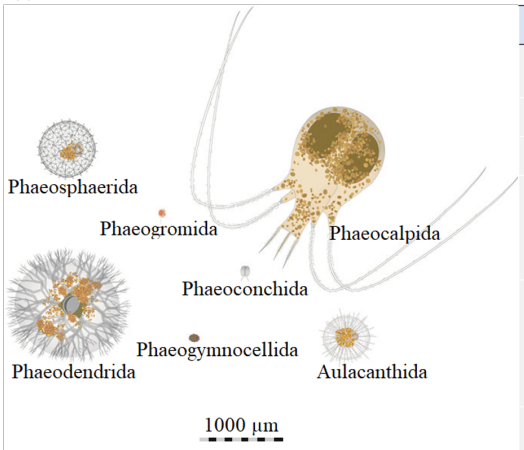

(b)

Order	Scleracoma type	Surface of test
Phaeocystida (Aulacanthida)	spherical veil	---
Phaeogymnocellida	---	---
Phaeosphaerida	lattice-shell	---
Phaeocalpida	spherical test with tubular spines	trizonal meshwork
	test with long oral feet	smooth
Phaeogromida	cape-shaped or ovate test usually with spines	smooth or with regularly arranged pores
	campanulate test with oral arches	dimpled or alveolated
Phaeoconchida	test composed of two valves	large-pored
Phaeodendrida	inner shell and styles	---

Figure 1.9: General characteristics of current phaeodarian orders. (**a**) Cell size of phaeodarian orders, modified from Nakamura and Suzuki (2015); (**b**) Skeletal characteristics of current phaeodarian orders, based on the information from Nakamura et al. (2015).

ranges from about 100 μm to several mm (Nakamura and Suzuki, 2015). Present in most of the world open ocean during their entire life cycle, they occupy various ecological niches depending on their trophic mode and their vertical habitat.

Radiolaria can harbor algal symbionts from eukaryotic and prokaryotic lineages (Ogane et al., 2010; Decelle et al., 2012; Biard et al., 2015). They can thus be mixotrophic, enabling them to thrive in the epipelagic layer of oligotrophic environments (Suzuki and Not, 2015; Biard and Ohman, 2020; Fig. 1.11). They can also capture prey larger than them through adhesion on their pseudopodia (Suzuki and Not, 2015). Regarding their predators, specimens have been found in the gut of crustaceans and fishes mainly, but observations are scarce (Biard, 2022a, and references therein).

Contrary to Radiolaria, no photosymbiont has yet been seen in Phaeodaria (Takahashi and Anderson, 2000; Nakamura and Suzuki, 2015). They are thus strictly heterotrophic. Being non-motile, small species have been observed to consume nearby suspended particles, but they mostly feed on sinking marine snow and fecal pellets, plus their associated organisms (Gowing, 1986; Gowing, 1989; Gonzalez, 1992). Phaeodaria are omnivorous and generalist feeders: in their phaeodium and mini-pellets have been found organisms as diverse as viral particles, bacteria, phytoplankton cells, microheterotrophs or fragments of metazoans (Gowing, 1986; Gowing, 1989; Gowing and Bentham, 1994; Nakamura et al., 2013). This flux-feeding behavior can in part explain the high occurrence of phaeodarian

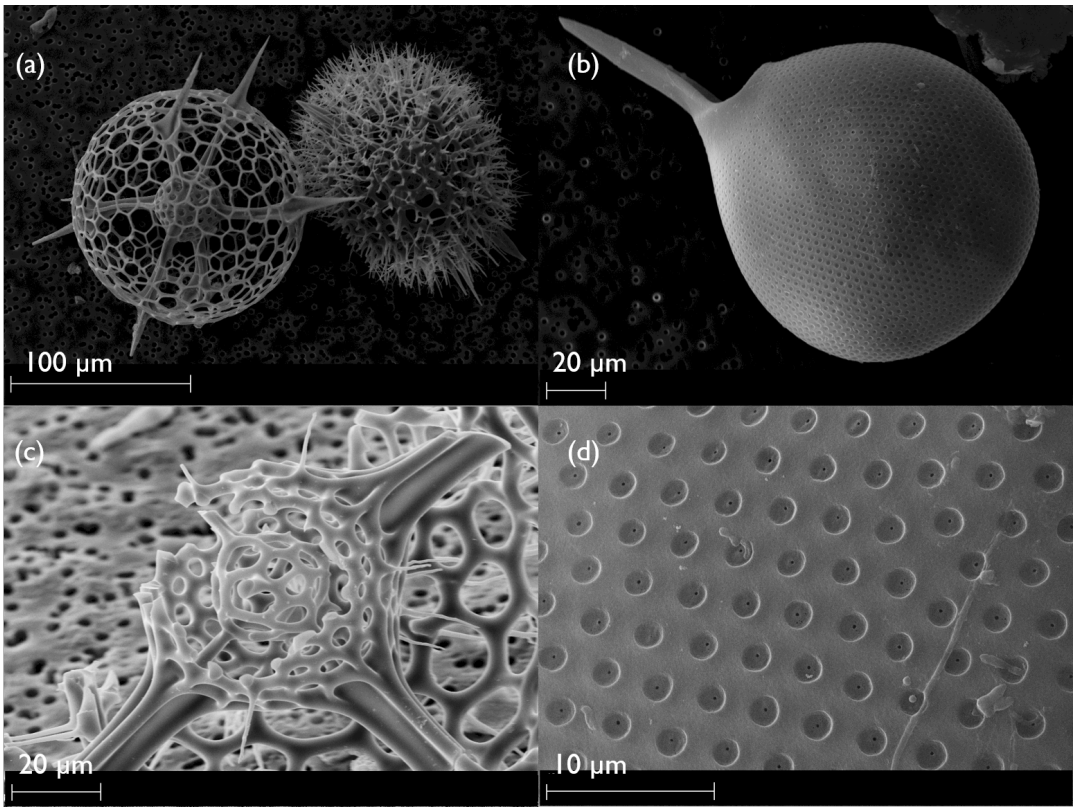

Figure 1.10: Scanning electron microscope photos of Rhizaria skeletons. (**a**) Skeleton of two Spumelleria (Radiolaria). (**b**) Skeleton of Phaeogromida (Phaeodaria). (**c**) Broken skeleton of Spumellaria, allowing to see central structures. (**d**) Pores covering the surface of the Phaeogromida skeleton shown in (**b**). Photos: Dr. Lucie Courcot, Laboratoire d'Océanologie et de Géosciences.

species in the subsurface waters (Nakamura et al., 2013; Biard and Ohman, 2020) where they can obtain their food sinking from the euphotic layer. Phaeodaria also dwell in the deep ocean. They were observed to more than 8,000 m in the Kuril-Kamtchatka trench (Reshetnyak, 1966) and many species inhabit the meso- and bathypelagic domains (e.g., Nakamura et al., 2013). They are as well found in surface and subsurface waters, at high latitudes (e.g., Gonzalez, 1992; Gowing and Garrison, 1992), but also in warmer areas such as the Mediterranean Sea (Cachon-Enjumet, 1961) and the California Current (Biard and Ohman, 2020).

Seasonal fluctuations in Rhizaria assemblages, due to changes in ocean circulation, were reported in the epipelagic layer, but not in the mesopelagic layer (Casey, 1966; Biard and Ohman, 2020). Likewise, small-scale wind-driven disturbances can mix communities through the water-column and lead to occasionally high densities in frontal regions (Faillettaz et al., 2016; Biard and Ohman, 2020).

To summarize, food and dissolved silica availability, together with tempera-

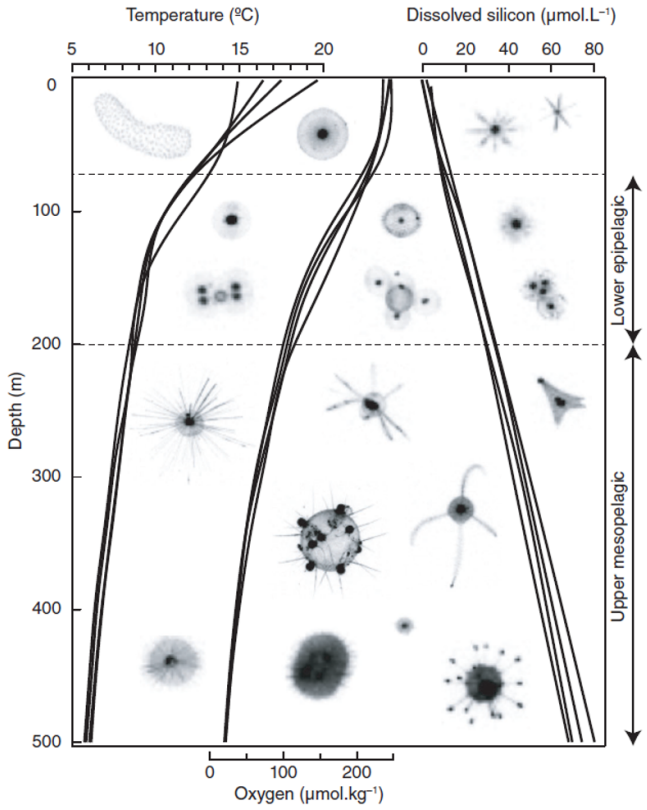

Figure 1.11: Vertical distribution in the California Current Ecosystem of large (>600 μm) rhizarian morphological categories resolved with in situ imaging, from Biard and Ohman (2020). In the upper epipelagic, i.e., above 100 m depth, are found colonial Collodaria, solitary Collodaria and Acantharia, all symbiont-bearing groups belonging to Radiolaria. Phaeodarian families Castanellidae, Aulosphaeridae and Coelodendridae are found in the lower epipelagic. In the upper mesopelagic mostly dwell the phaeodarian Medusettidae, Coelodendridae, Tuscaroridae and Aulacanthidae.

ture and water column stratification, are the main factors known to affect the distribution of planktonic Rhizaria (Nakamura et al., 2013; Dolan et al., 2017; Stukel et al., 2018; Biard and Ohman, 2020). Their morphological, trophic and habitat diversity leads to various pathways through which they contribute to element cycling. Nevertheless, although planktonic Rhizaria are common residents of the pelagic realm, many gaps remain regarding their role in biogeochemical cycles.

1.2.2 Role in biogeochemical cycles

Abundance and biomass

The fragile skeleton of many Rhizaria quickly dissolve in sediment traps (Beers and Stewart, 1970) or can break upon collection with plankton nets. Hence, they have long been undersampled and their abundance and biomass overlooked. Recently, automated in situ imaging methods have, through their non-destructive nature, highlighted the abundance of these fragile taxa, locally (Dennett et al., 2002) and on a global scale (Stemmann et al., 2008; Biard et al., 2016).

Solitary Collodaria could be the third most important mesozooplanktonic group in terms of global carbon biomass between 0 and 200 m (Drago et al., 2022). This group contributes most to the carbon biomass of Rhizaria between 0-100 m (Biard et al., 2016) and are largely present at low and mid-latitudes (Fig. 1.12). Large Acantharia show high biomass in the epipelagic layer, which declines in the mesopelagic (Michaels, 1988; Drago et al., 2022). They are mostly present in intertropical areas (Bottazzi and Andreoli, 1982), although high biomass was observed in higher latitudes such as the Gulf of Alaska and the Southern Ocean (Drago et al., 2022). This pattern is easily explained by their mixotrophic behavior. Overall, the contribution of Collodaria and Acantharia to primary production is estimated to 0.18% of total primary production in oligotrophic waters (Biard et al., 2016). By being directly available to large consumers, this primary production could shortcut trophic levels of marine food webs (Anderson, 1983; Biard et al., 2016).

The contribution of Phaeodaria to zooplankton carbon biomass mostly occurs in coastal areas and is low in oligotrophic gyres (Drago et al., 2022). It has been shown that they can represent a significant carbon stock in the mesopelagic layer in the North Pacific (Ikenoue et al., 2019) and in the Sea of Japan (Nakamura et al., 2013). In general, abundances of Rhizaria increase at mid and low latitudes and decrease towards the poles (Biard et al., 2016). This pattern contrasts with the global copepod-driven pattern of abundance, possibly because of differences in life strategy (Brandão et al., 2021). Particularly, their high abundance in oligotrophic areas, which are likely to expand with ocean warming (Polovina et al., 2008), supports the need to have an accurate estimation of their biomass.

Still, given the lack of an accurate conversion factor, biomass estimates are highly variable. Biard et al. (2016) estimated the global standing stocks of largest Rhizaria (>600 μm) in the top 200 m to be of 0.089 Pg C. This was estimated to

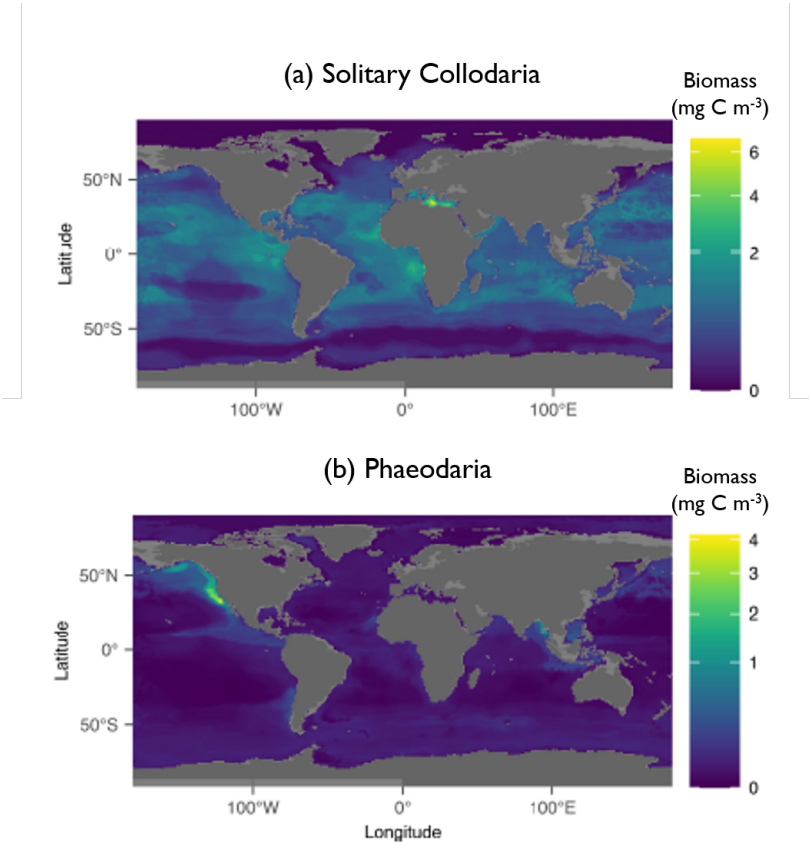

Figure 1.12: Global distribution of carbon biomass in the epipelagic layer (0-200 m) (in mg C m^{-3}) for (**a**) solitary Collodaria; (**b**) Phaeodaria. Modified from Drago et al. (2022).

represent 5.2% of the whole oceanic biotic carbon reservoir. However, the overall biomass of the Phaeodaria family Aulosphaeridae in the California Current was revised downward. They could contribute up to at most 10% of the total mesozooplankton biomass, although their contribution to mesozooplankton abundance is higher (Stukel et al., 2018). Regarding their silica biomass, siliceous rhizarian skeletons are on average a hundred times more silicified than diatom frustules of comparable size. This makes them the most silicified pelagic organisms (Takahashi, 1982; Biard et al., 2018; Llopis-Monferrer et al., 2020), enhancing their role in vertical fluxes.

A contrasting contribution to vertical fluxes

Rhizaria are believed to occasionally be major exporters of POC and biogenic Si. Their occurrence in sediment traps has shown that they contribute substantially to vertical fluxes of matter (e.g., Takahashi and Honjo, 1981; Takahashi et al., 1983;

Gowing, 1993; Ikenoue et al., 2015). They can be associated to high carbon flux events (Lampitt et al., 2009), promoting fast-sinking particle aggregation (Riley et al., 2012). In the North Pacific Ocean, >1-mm Phaeodaria can account for 10% of total POC from the sinking particles population (Ikenoue et al., 2019). In the California Current, Aulosphaeridae and Castanellidae, two Phaeodaria families, contribute on average to 10% of silica export from the euphotic zone, a number that increases towards oligotrophic environments and mesopelagic depths (Biard et al., 2018).

This contribution of siliceous Radiolaria and Phaeodaria to vertical fluxes can be attributed to the density of their silica skeleton, acting as a ballast and increasing their speed through the water column, but whose effect is not accurately quantified yet. Still, because of skeletal differences (Nakamura et al., 2018a), the sinking behavior differs between the two groups. Indeed, preservation is a function of skeleton thickness rather than its size (Hurd and Takahashi, 1983), and Phaeodaria have a more porous skeleton (Nakamura et al., 2018a). Polycystinea generally reach the seabottom, but their dissolution level depends on the residence time. Conversely, phaeodarian species with a heavy skeleton quickly sink to the seabottom, where they dissolve in a few months, whereas small species are unlikely to reach it (Erez et al., 1982; Takahashi and Honjo, 1983; Hurd and Takahashi, 1983).

As for other particles, the sinking velocity of Rhizaria is influenced by their mass, size, density, and the presence of ornaments such as spines (Takahashi and Honjo, 1983). Rhizaria can act as nucleation points (Riley et al., 2012; Fig. 1.13) and package fast-sinking particles which can serve as major carriers of elements (Ikenoue et al., 2019). Indeed, Phaeodaria are known to aggregate various cells and detritus around them (Gowing, 1989; Stemmann and Boss, 2012; Ikenoue et al., 2019) and Radiolaria can adhere particles to their pseudopodia. However, the sinking speed of these particles, the amount of material they carry, and therefore the extent of their contribution to vertical fluxes are poorly understood yet.

Recent metagenomic studies have also highlighted the correlation of Acantharia and Collodaria with carbon export at 150 m in tropical and subtropical waters (Guidi et al., 2016) and the prevalence of Radiolaria in organic matter sinking out of the epipelagic layer in the California Current (Gutierrez-Rodriguez et al., 2018). In the Southern Ocean, sequences of siliceous Radiolaria were mostly enriched in suspended particles, whereas Phaeodaria sequences were enriched in sinking particles (Duret et al., 2020), suggesting a diverging role in mitigating

organic matter. Furthermore, Phaeodaria eliminate waste through the production of mini-pellets (Gowing and Silver, 1985) with sizes ranging from 3-50 μm, but whose abundance have been observed to be four to five orders of magnitude greater than krill fecal pellets in the Weddell Sea (Gonzalez, 1992). These pellets can contribute to a large proportion of sinking flux mediated by small particles (Durkin et al., 2021).

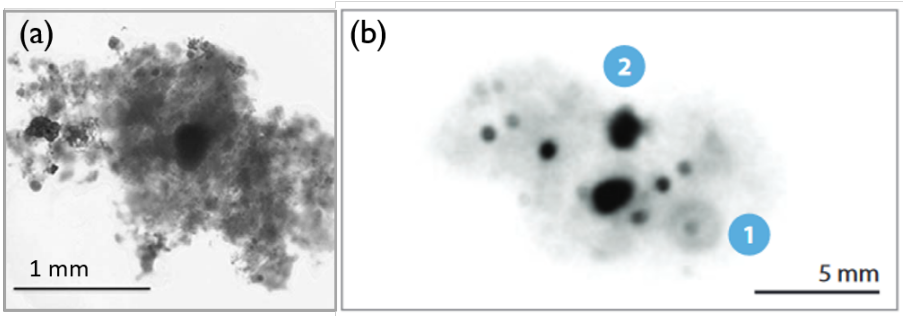

Figure 1.13: Examples of Rhizaria aggregates. (**a**) Protist-complex aggregate from the North Atlantic, modified from Riley et al. (2012). (**b**) Rhizaria aggregate recorded in situ, 1: Rhizaria organism, 2: Particles embedded in the matrix, modified from Stemmann and Boss (2012).

This contribution to carbon export is partly counterbalanced by the trophic ecology of several taxa. Phaeodaria are known to be flux-feeders (Gowing, 1986; Gowing, 1989), they are thus likely to play a role in carbon flux attenuation by feeding on rapidly sinking particles. In the California Current, members of the family Aulosphaeridae can contribute up to 10% of total flux attenuation at the base of the euphotic zone where they reach their maximum abundance (Stukel et al., 2019). However, an accurate measurement of the carbon content of various taxa would help to refine estimates of their carbon demand and thus their contribution to flux attenuation. In addition, only one study has tackled this question, and their influence on carbon flux at larger scale is unknown.

Knowledge about the contribution of Rhizaria to element fluxes and about their role in the BCP and the silicon cycle is scarce. To fill existing gaps, several complementary tools can be used for both biomass and flux assessments.

In summary

- Rhizaria are widespread, ubiquitous planktonic protists which can build silica skeletons.
- Recent studies showed their ability to carry carbon and silica to the deep ocean, yet heterotrophic taxa can contribute to flux attenuation.
- Such studies are scarce and the lack of adequate carbon-to-volume conversion factors prevent accurate estimates of both carbon flux and demand.

1.3 Studying the role of plankton in biogeochemical cycles

1.3.1 Plankton sampling

Plankton nets

Living Rhizaria can be collected with plankton nets. These instruments are made of a nylon mesh net of various mesh size, attached to a cod end to collect the sample, and to a towing line. They allow for accurate taxonomic identifications, chemical or biochemical measurements, in addition to plankton counting. However, large rhizarian specimens are less effectively collected than small ones, because they are too fragile and are often fragmented or broken by nets. Therefore, their abundance has often been underestimated with this tool.

In situ imaging

While they enable to collect specimens, plankton nets are not suited for accurate estimations of the abundance of large Rhizaria. Moreover, it is not always possible to get the accurate sampling depth range, as nets are often towed over tens or hundreds of meters. Addressing these issues, in situ imaging methods encompass many instruments developed recently (Lombard et al., 2019; Fig. 1.14) which are non-destructive and allow to know the sampling depth. Among these instruments, the Underwater Vision Profiler consists of a camera connected to a red-emitting light unit. This light unit illuminates a water volume imaged by the camera to record particles and organisms. It includes several generations of intercalibrated

instruments which have been deployed almost all over the world ocean (Gorsky et al., 2000; Stemmann et al., 2008; Picheral et al., 2010; Picheral et al., 2022). The versions 5 (Picheral et al., 2010; Fig. 1.15a) and 6 (Picheral et al., 2022; Fig. 1.15b) record the size of particles >100 μm and vignettes (i.e., thumbnails) of particles and organisms whose size is >600 μm (Fig. 1.14). Upon recovery, particle data and vignettes can be imported to the EcoPart and EcoTaxa applications (Picheral et al., 2017). In EcoTaxa, vignettes can be classified both manually and by using machine learning algorithms (Irisson et al., 2022). These instruments can sample at 6,000 m depth and be integrated on a CTD (Conductivity, Temperature, Depth) rosette for vertical profiles of abundance. In addition, the UVP6 can be mounted and deployed on moorings, autonomous underwater vehicles or gliders. Data from UVP have been used to study plankton ecology (e.g., Biard et al., 2016; Biard and Ohman, 2020) and ocean biogeochemistry (e.g., Guidi et al., 2008; Ramondenc et al., 2016).

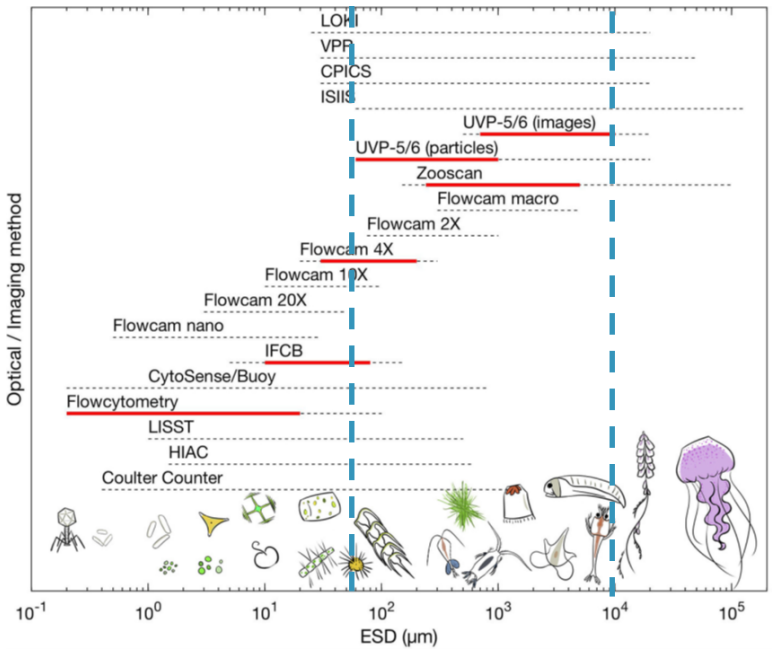

Figure 1.14: Size range (in equivalent spherical diameter; ESD) sampled by available optical and imaging methods. Total operational size range is represented by dashed lines. Red lines show the size range that provides efficient quantitative information. Blue dashed lines delineate the size range covered by the Underwater Vision Profiler, for both versions 5 and 6. Modified from Lombard et al. (2019).

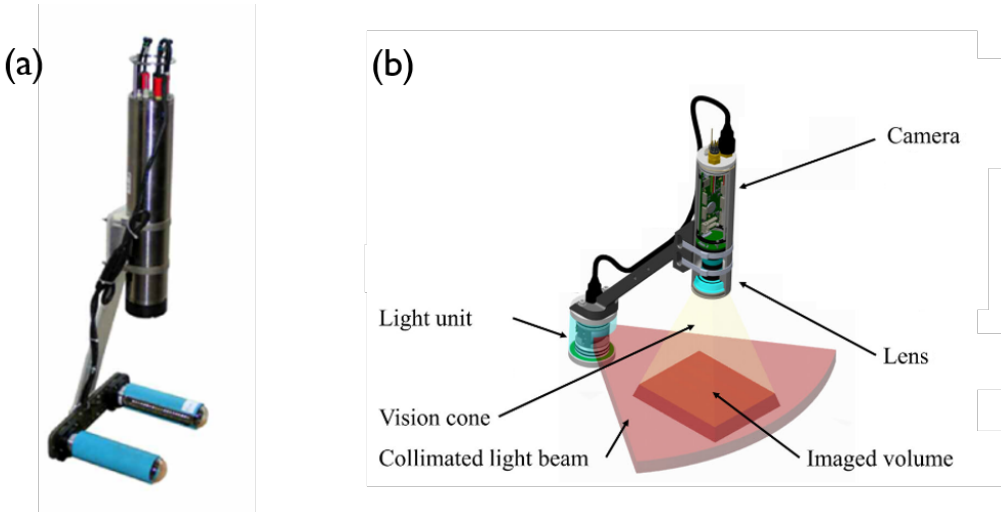

Figure 1.15: UVP cameras. (**a**) UVP5, from Picheral et al. (2010); (**b**) UVP6, modified from Picheral et al. (2022).

1.3.2 Estimating biogeochemical parameters

Concentration and carbon mass

As we saw previously, the concentration of fragile rhizarian taxa can be resolved with in situ imaging tools. These tools size imaged organisms and enable to use simple carbon-to-volume content conversion factors to obtain their carbon mass. However, obtaining accurate conversion factors requires the collection of living organisms using plankton nets and accurate measurements of their carbon content, which are yet scarce (Biard et al., 2018; Llopis-Monferrer et al., 2020; Mansour et al., 2021).

Carbon demand

Zooplankton carbon demand depends on their metabolism and carbon content. Stukel et al. (2019) established a relationship to estimate the carbon demand (CD, in μg C cell^{-1} d^{-1}) of Aulosphaeridae (Phaeodaria):

$$CD = CV \times \frac{\pi \times ESD^3}{6 \times GGE \times \tau}$$

with CV a carbon-to-volume conversation factor in μg C mm^{-3}, ESD the equivalent spherical diameter of the cell in mm and GGE the growth gross efficiency. However, accurate estimate of carbon content and turnover times are needed.

Elemental flux

Elemental flux (in g m^{-2} d^{-1}) can be expressed as the product of the concentration of a pool of particles or organisms, of their elemental mass and of their sinking velocity. Thus, assessing the contribution of planktonic organisms to vertical fluxes rely on accurate estimations these parameters.

Sinking velocity of marine particles

Small planktonic organisms do not interact with seawater in the same way as larger organisms. The dimensionless Reynolds number (Reynolds, 1883) determines the relative importance of inertial forces (such as currents and winds) and viscous forces (related to friction) acting on an organism or a particle moving through a fluid. This number decreases with the density of the fluid and the size and velocity of the particle, as well as with the increase of the dynamic viscosity of the fluid. When it is less than 1, viscous forces are dominant, conversely when it is greater than 1 inertial forces dominate. Thus, it allows to characterize the fluid regime: at low values of Re, the flow is laminar. When Re increases, instabilities appear, followed by turbulence (i.e., chaotic fluctuations). This transition occurs when Re is of the order of 1,000. The estimated Reynolds number for marine organisms increases with their size and spans more than 10 orders of magnitude, from 10^{-5} for bacteria to 10^{8} for largest mammals (Okubo, 1987). Stokes' law (Stokes, 1851) predicts the terminal sinking velocity of a spherical particle in a fluid at low values of Re ($Re < 0.5$) as a function of its diameter D, its density and that of the surrounding fluid:

$$U_{th} = \frac{1}{18}\frac{g(\rho_p - \rho_f)D^2}{\mu_f}$$

with U_{th} the sinking velocity of the particle in m s^{-1}, g the acceleration due to gravity (9.81 m s^{-2}), and ρ_p and ρ_f the density of the particle and of the fluid in kg m^{-3}.

Stokes' law is commonly used to represent the sedimentation rate of particles in biogeochemical models (Omand et al., 2020). However, this law was first formulated for slowly settling spheres at low Re. Sinking velocities of marine particles, usually non-spherical, porous, and for which $Re > 0.5$, often exhibit a significant deviation from Stokes' law (McDonnell and Buesseler, 2010). This is especially true for radiolarian- and phaeodarian-mediated particles, whose

skeleton exhibits various structures such as spines, known to increase the drag of particles. Thus, experimentally measured sinking velocities deviate from Stokes' law for numerous taxa (Takahashi et al., 1983).

A handful studies focused on measuring sinking velocities of marine particles and organisms ex situ (e.g., Ploug et al., 2010). Laboratory experiments allow to gather a pool of homogeneous particles and therefore and ability to measure their characteristics (Fig. 1.16; Williams and Giering, 2022). However, this less realistic pool of particles is likely to not reflect the pool encountered in the water column. On the other hand, in situ measurements provide measurements on the actual particle population, but they often fail at capturing detailed particle characteristics (Fig. 1.16).

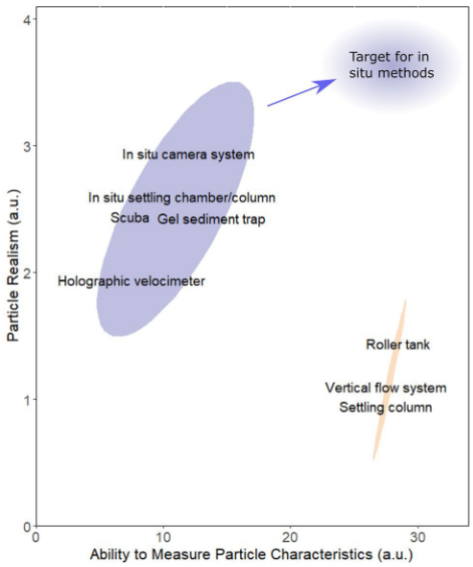

Figure 1.16: Relative strengths of in situ (blue) and ex situ (orange) sinking velocity measurement methods, regarding their ability to measure particle characteristics and realism. Figure is from Williams and Giering (2022).

Limitations of sinking velocity measurement methods hinder our understanding of particle sinking behavior, and especially of the link with particle characteristics. In situ imaging, and especially the UVP, already assembled a worldwide dataset of abundance of marine particles and organisms and their associated morphological data. However, these morphological data, giving information about particle characteristics, have seldom been taken into account in flux estimates.

In summary...

- While plankton nets enable specimen collection, in situ imaging is a powerful tool to estimate rhizarian abundance and obtain measurements such as organisms' size.
- An adequate carbon-to-volume conversion factor is crucial to estimate carbon demand and flux.
- Another key parameter is the sinking speed of particles, whose estimation from particle size or by ex situ methods is often biased.

1.4 Hypotheses and thesis objectives

As previously mentioned, planktonic Rhizaria cover a broad size spectrum and have an extended range of vertical habitat. Both have consequences for their trophic ecology and ability to sink to the deep ocean. By hypothesizing that their contribution to biogeochemical cycles depends on these two aspects, we define the thesis objectives as follows:

1. To measure the elemental content and production of a broad variety of Rhizaria at cellular scale;
2. To reassess the global carbon biomass and the carbon demand of Rhizaria, and to estimate their global biogenic Si biomass and production rates;
3. To develop a methodology to measure the sinking speeds of marine particles from in situ imaging data, and to investigate links between particle sinking speeds, morphological properties, and environmental conditions.

1.5 Work structure and datasets

Chapter 2 addresses the individual carbon and nitrogen content and biogenic silica production rates of various Rhizaria taxa, using both literature values and providing original measurements. The purpose is to investigate the relationship between these values and organisms' size. In **chapter 3**, I use a global UVP5 dataset, which includes 4,252 vertical profiles deployed during oceanographic cruises spanning from 2008 to 2021, covering the world ocean. Particle data of part

of this dataset were recently published (Kiko et al., 2022). While previous work has addressed the global distribution (Drago et al., 2022) and the community structure (Panaïotis et al., 2023) of zooplankton, here, I solely focus on Rhizaria data. In total, this dataset encompasses 167,551 Rhizaria images ranging from 0.6 to 20 mm. These images were all classified and validated by Tristan Biard into 18 taxa, following the classification outlined in Biard and Ohman (2020). Using boosted regression trees, I then use the relationship developed in the previous chapter to re-estimate their global carbon biomass, but also their global biogenic Si biomass using the equation established by Llopis-Monferrer et al. (2020). To assess their role in biogeochemical processes, I apply the formula 1.3.2 (Stukel et al., 2019) to estimate the global carbon demand of large, flux-feeder Phaeodaria. Lastly, I use literature biogenic Si production rates to estimate the global production rates of large Phaeodaria. **Chapter 4** is less Rhizaria-oriented. While the initial purpose was to measure the sinking speed of Rhizaria-mediated particles, it involves a new methodological development using the UVP6. Therefore, an assessment of the sinking speeds of all marine particles, regardless their origin, is first attempted. This has led to the collection during lagrangian cycles of small-scale datasets in the California Current, the Indian Ocean, the Mediterranean Sea, and the Atlantic Ocean, targeting specific water masses, although not all results could be shown in this thesis and will be presented in the future.

CHAPTER 2

Cell composition and uptake rates of Rhizaria

"[...], organisms must adjust their structure and function to compensate for the geometric, physical, and biological consequences of being different sizes. The principles of mathematics and physics are universal, but their biological consequences depend on the size of the organism."

J. H. Brown et al. *Scaling in Biology: Patterns and Processes, Causes and Consequences*

Contents

2.1 Elemental content allometries and silicon uptake rates of planktonic Rhizaria: Insights into their ecology and role in biogeochemical cycles

Laget, M., N. Llopis-Monferrer, J.-F. Maguer, A. Leynaert, and T. Biard.
This work has been published in *Limnology and Oceanography* (Laget et al., 2023).

2.1.1 Abstract

The last two decades have shown the importance of Rhizaria in the biogeochemical cycles of carbon and silicon in modern oceans. This eukaryotic supergroup, which includes Radiolaria and Phaeodaria, represents an important part of zooplanktonic carbon biomass and contributes to carbon and silica export. Still, accurate estimations of their carbon biomass are hindered by poor knowledge of their elemental composition, contrasting with well-established allometric carbon-to-volume relationships for smaller protists such as phytoplankton. Here, we directly measured carbon, nitrogen, and biogenic silica content as well as silicon uptake rates of planktonic Rhizaria. We highlight that size can be used as a predictor of elemental content for a broad variety of planktonic Rhizaria ranging from 200 μm to several mm, whereas size is weakly correlated with silicon uptake rates. Our results indicate that the scaling exponent of the carbon-to-volume allometry is significantly lower than those for smaller protists, underlining the low carbon strategy of these organisms. Still, we show that carbon and nitrogen densities span over four orders of magnitude, possibly accounting for the differences in depth ranges, nutritional modes and colonial or solitary forms. We estimate Rhizaria sinking speeds by combining carbon, nitrogen, and silica content data and show that great variability exists among the different taxa. Besides giving a better understanding of rhizarian ecology and biogeochemistry, these analyses, at the individual scale, are a first step to subsequent biomass and flux estimations at larger scales.

2.1.2 Introduction

Marine plankton are a major reservoir of organic carbon (C) and nitrogen (N) and the main driver of the biological carbon pump, one of the mechanisms

by which atmospheric CO_2 is transported to the deep ocean (Ducklow et al., 2001). In addition, many planktonic taxa require silicic acid to precipitate into biogenic silica (biogenic Si) to form skeletons, a process that has likely been responsible for a decline in silicic acid concentration in the oceans through geologic times (Siever et al., 1991). Therefore, knowledge of small-scale planktonic physiological processes is crucial for understanding the functioning of global oceanic biogeochemistry. Besides giving insights into organisms' physiology, quantifying the elemental composition and uptake rates of planktonic individuals is a key step to subsequently estimate stocks and fluxes at the population level. Allometric relationships scale traits of organisms with morphological criteria such as size over many orders of magnitude and are used for almost all forms of life (Brown et al., 2002). Accordingly, they enable elemental composition-to-volume relationships to provide trends that can be utilized in models. Indeed, size is a common trait in plankton community models (Finkel et al., 2010; Andersen et al., 2015) as well as in size-based ecosystem models (Blanchard et al., 2017), stressing the strength of this approach to provide model parameters. Allometric relationships linking individual C and N contents to cell volume relationships have been developed for diatoms and various protists; however, they are likely to overestimate elemental content of large protists such as Rhizaria (Menden-Deuer and Lessard, 2000).

Planktonic representatives of Rhizaria are unicellular protists, with cell sizes ranging from a few tens of micrometers to several millimeters (Biard, 2022b). Among them, Retaria includes Foraminifera and Radiolaria (Sierra et al., 2013). Foraminifera build calcium carbonate skeletons, whereas among Radiolaria, the skeleton is made of strontium sulfate for the order Acantharia and biogenic Si for the orders Nassellaria, Spumellaria, Collodaria, and Orodaria (Nakamura and Suzuki, 2015; Suzuki and Not, 2015; Biard, 2022a). Phaeodaria, whose skeletons are made of biogenic Si, have long been considered radiolarians, but are now classified as Cercozoa, a sister group to Retaria (Sierra et al., 2013). Most rhizarians live as solitary cells, but some (e.g., collodarian families Collosphaeridae and Sphaerozoidae and the phaeodarian families Tuscaroridae and Medusettidae) are able to form large colonies (Nakamura and Suzuki, 2015; Suzuki and Not, 2015).

Despite their close morphologies, Phaeodaria and siliceous Radiolaria differ in their skeletal structure (Nakamura et al., 2018a). Phaeodaria have porous skeletons that easily dissolve in seawater, whereas Radiolaria possess thick, dense skeletons that can preserve well in sediments and are commonly used in paleoclimate studies

(De Wever et al., 2002). Even though diatoms account for the largest part of the biomass and production of biogenic Si (Tréguer et al., 2021, siliceous Rhizaria (i.e., siliceous Radiolaria and Phaeodaria) are the most silicified pelagic organisms known to date, considering the amount of silica per unit volume (Biard et al., 2018; Llopis-Monferrer et al., 2020). Partially because of these high biogenic Si densities, their skeleton is expected to act as ballast upon their death. Ultimately, skeletal remains increase fluxes of organic C and biogenic Si to the deep ocean, which will be integrated in seafloor sediments if not dissolved or remineralized on the way.

Siliceous Rhizaria inhabit the open ocean worldwide from the surface to the bathypelagic realm (Nakamura and Suzuki, 2015; Suzuki and Not, 2015; Biard, 2022a). Their distribution is taxon dependent and influenced mostly by temperature, dissolved Si concentration and the amount of food available (Boltovskoy and Correa, 2016; Biard and Ohman, 2020). Although they all are heterotrophic, epipelagic radiolarian populations include many mixotrophic species, harboring a large diversity of algal symbionts (Decelle et al., 2015). On the other hand, deep-living populations are strictly heterotrophic, some also feed on sinking marine snow (Gowing, 1986). For example, the phaeodarian family Aulosphaeridae can intercept on average 10% of total sinking flux at the depth of their maximum abundance, therefore reducing the efficiency of the biological carbon pump (Stukel et al., 2018). Despite their widespread occurrence in pelagic ecosystems, sampling and culturing them are challenging, hampering our knowledge of their biology and ecology. Still, over the last decade, non-destructive in situ imaging methods and environmental metagenomics have expanded understanding of their role at the community level. At a global scale, they represent a large part of mesozooplankton biomass (Biard et al., 2016) and could account for 2% to 19% of world biogenic Si production in the epipelagic layer (Llopis-Monferrer et al., 2020). Yet, substantial production by Rhizaria occurs below 200 m depth, where diatoms are absent. Furthermore, Rhizaria communities can contribute to a large component of vertical C export (Lampitt et al., 2009; Guidi et al., 2016; Gutierrez-Rodriguez et al., 2018). Large Phaeodaria (>1 mm) are responsible for up to 10% of the total organic C flux in the North Pacific by contributing to the enlargement and aggregation of sinking particles in the mesopelagic zone (Ikenoue et al., 2019).

Nevertheless, gaps remain in our knowledge of their organic C and N composition. Previous global C biomass assessments for large Rhizaria (Biard et al., 2016) relied upon a C-to-volume conversion factor of 80 μg C mm^3 measured on a

variety of zooplanktonic organisms (Beers and Stewart, 1970). In contrast, Stukel et al. (2018) demonstrated that flux feeders Aulosphaeridae (Phaeodaria) could meet their C demand only if their C density was one order of magnitude lower (1.1 μg C mm^3, corresponding to 4.8 μg C cell^{-1} for a 2-mm cell). This revised estimate was further supported by an average C content of 13 μg C cell^{-1} measured on >1 mm Phaeodaria found in sediment traps (Ikenoue et al., 2019). In comparison, the equation provided by Menden-Deuer and Lessard (2000) gives a value of 234 μg C cell^{-1} for a 2-mm cell. Such high variability in conversion factors and its impact on biomass assessment emphasizes the need for accurate quantification of elemental content. To date, only three studies have provided C and N data from direct measurements, as well as estimates of C : N ratios (Michaels et al., 1995; Llopis-Monferrer et al., 2020; Mansour et al., 2021), but they focused solely on a few limited taxa. A robust tool that could be used in biogeochemical or size-based models is still lacking.

On the other hand, cell biogenic Si content correlates with cell volume over the entire size spectrum, including many taxa (Biard et al., 2018; Llopis-Monferrer et al., 2020; Llopis Monferrer et al., 2021). The silica-to-carbon ratio (Si : C) is lower than for diatoms, without significant regional variation, but it has only been investigated for the smallest taxa (Llopis Monferrer et al., 2021). Also, little is known about silicon uptake rates of siliceous Rhizaria (i.e., the rates at which they take up silicic acid to build their biogenic Si skeleton). In addition to knowing their silica biomass, such values are essential to understanding how they use silica from their environment at the physiological scale, opening the door to subsequent estimates of their turnover times, as well as to refining their role in the Si cycle. Likely because they are highly silicified cells, their Si uptake rate displays greater values than that of diatoms (Llopis Monferrer et al., 2021). Current data are too scarce to investigate a potential link with cell size or dissolved silica (dissolved Si) concentration in the ocean.

Here, using original and literature data, we investigate how size relates to elemental content for a broad variety of solitary and colonial Rhizaria. We also further examine the Si : C ratio and Si uptake rates. Finally, we discuss biogeochemical and ecological implications of these results.

2.1.3 Material and methods

Sampling

We collected 2036 Rhizaria specimens either in the coastal or oligotrophic waters of the California Current Ecosystem (CCE) during the P2107 process cruise (July–August 2021, as part of the CCE-LTER program) onboard R/V *Roger Revelle* (Fig. 2.1a). We used various net tows to gather individuals from different depth intervals from the surface to as deep as 800 m (Supporting Information Table S2.1). In addition, we collected 55 individuals from the family Aulacanthidae (Phaeodaria) in the bay of Villefranche-sur-Mer (Mediterranean Sea, France; 43.69°N, 7.31°E; Fig. 2.1b) in 2019. Immediately after sampling, we isolated Rhizaria specimens under a stereomicroscope and rinsed them with filtered surface seawater. We then sorted individuals at the order, family or genus level based on the classifications from Nakamura et al. (2015) for Phaeodaria and from Suzuki and Not (2015) for Radiolaria (Fig. 2.2). Large Nassellaria (Radiolaria) found in the California Current were identified as *Phlebarachnium* sp. according to Strelkov and Reshetnyak (1959).

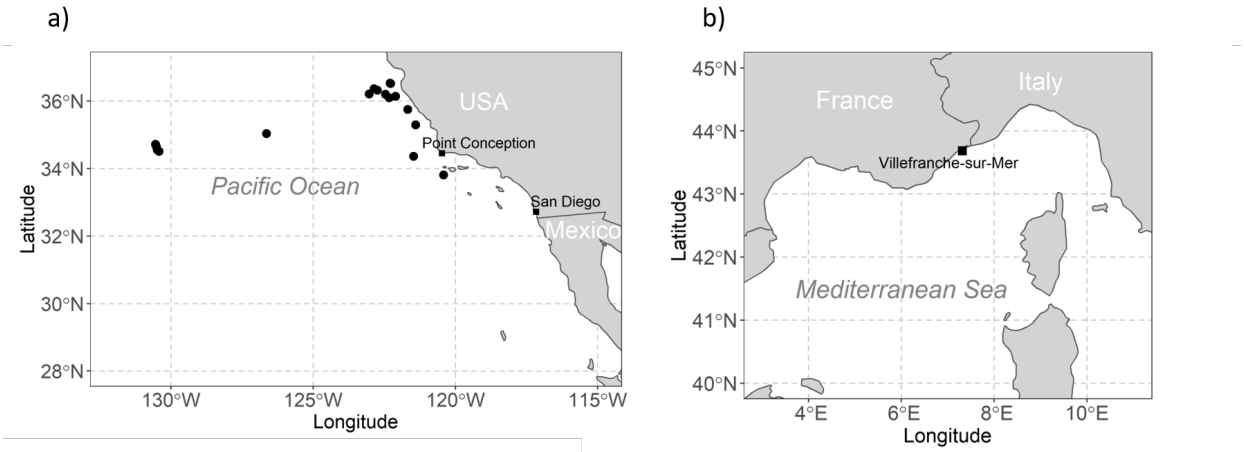

Figure 2.1: Sampling locations for this study. (**a**) Sampling stations during the P2107 process cruise and, (**b**) location of Villefranche-sur-Mer, France.

Organic C and N content

To obtain sufficient organic C and N matter for analysis, we deposited from 1 to 40 cells onto 25 mm GF/F filters that had been precombusted at 450°C for 4 h. Filters were placed in glass vials, previously washed for 24 h with HCl, rinsed with MilliQ water and combusted at 450 °C for 4 h. The vials containing the dry filters were stored at –20°C and dried at 55°C overnight before analysis. Blank

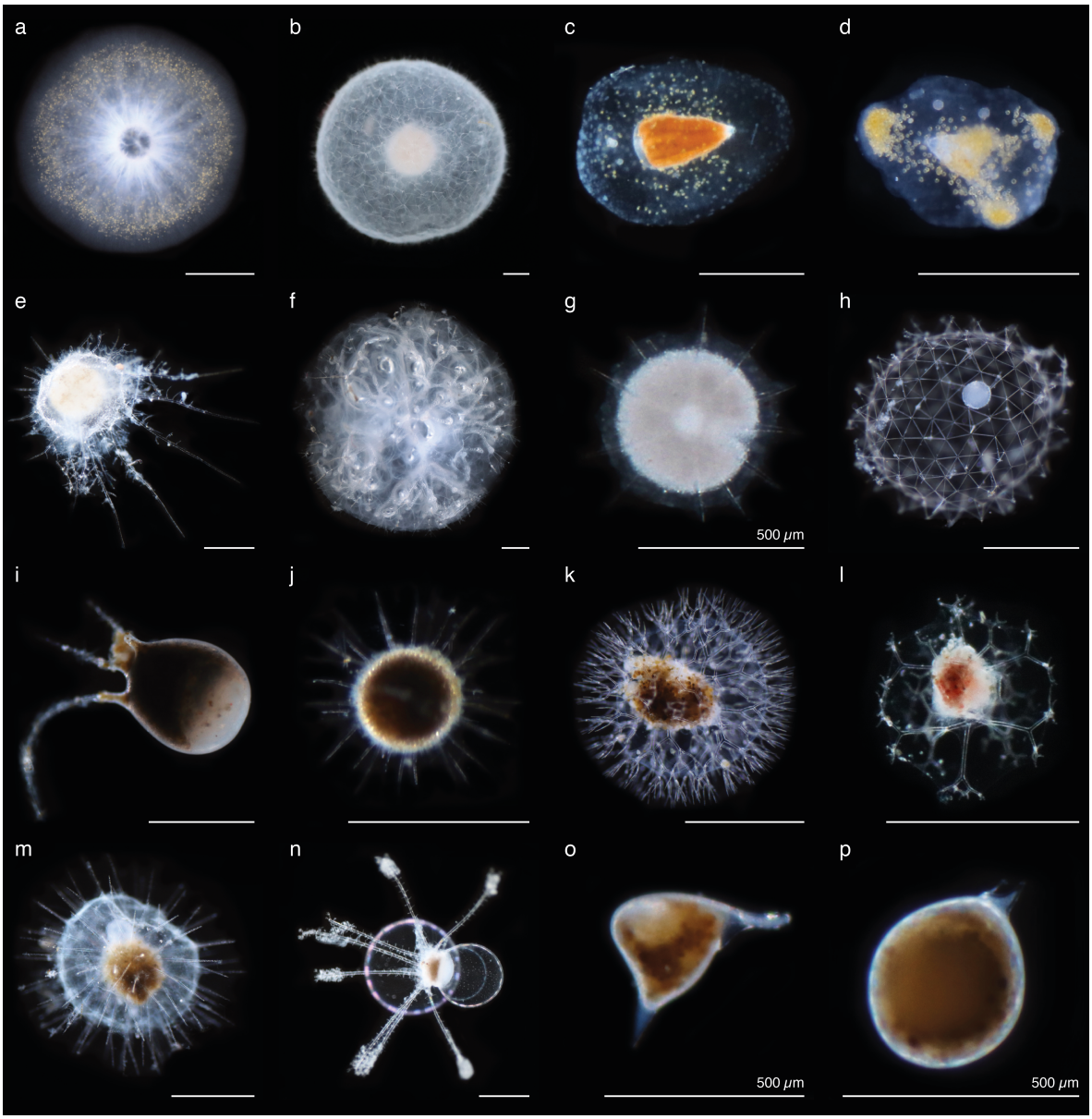

Figure 2.2: Representatives of the sampled Rhizaria, observed under a stereomicroscope. (**a**–**g**) Radiolaria, (**h**–**p**) Phaeodaria. (**a**) *Thalassicolla* sp. (Collodaria), (**b**) *Thalassosphaera* sp. (Collodaria), (**c**,**d**) *Phlebarachnium* sp. (Nassellaria), (**e**) *Oroscena* sp. (Orodaria), (**f**) *Cytocladus* sp. (Orodaria), (**g**) Spumellaria, (**h**) Aulosphaeridae, (**i**) Tuscaroridae, (**j**) Castanellidae, (**k**–**l**) Coelodendridae, (**m**) Aulacanthidae, (**n**) Medusettidae, (**o**–**p**) *Protocystis* sp. (Challengeridae). All scale bars are 1 mm, unless otherwise indicated.

filters were prepared in the same way (i.e., combusted the same day and stored in the same conditions). C and N contents were quantified with a mass spectrometer (Delta plus, Thermo Fisher Scientific) coupled with a C/N analyzer (Flash EA, Thermo Fisher Scientific) via a Type III interface. Data were normalized to cell counts to obtain mean individual values (Q_C in μg C cell^{-1} or Q_N μg N cell^{-1}).

Biogenic Si content

The biogenic Si content of isolated Rhizaria was quantified according to Llopis-Monferrer et al. (2020). Briefly, we added 0.2 mL of 2.5 N hydrofluoric acid (HF) to the polymethylpentene tubes containing the filters with isolated specimens. The biogenic Si contained in the filters was then digested for 48 h at room temperature with HF acid to allow digestion of the robust Rhizaria skeletons. We then added 9.8 mL of saturated boric acid (H_3BO_3) solution to eliminate interference from HF in the subsequent colorimetric analysis for Si. Analyses were performed on a Technicon Auto-Analyzer II by colorimetric quantification of the orthosilicic acid (Aminot and Kérouel, 2007). The standards used for calibration were prepared with the same matrix as for the samples (HF/H_3BO_3). As C and N data, biogenic Si concentrations were normalized to cell counts to obtain individual biogenic Si content (Q_{bSi} in μg bSi cell^{-1}).

Si uptake rates (ρ_{Si})

For these measurements, we used the radioisotope of Si (^{32}Si) following protocols previously described (Tréguer et al., 1991; Leynaert et al., 1996; Llopis-Monferrer et al., 2020). Briefly, samples containing from 1 to 30 individuals were spiked with a ^{32}Si silicic acid solution and incubated on deck for 24 h in a flowing-seawater incubator to maintain constant water temperature. After incubation, isotope samples were filtered by gentle (<150 mmHg) vacuum filtration onto 47 mm diameter, 0.6 μm pore-size polycarbonate membrane filters (Nuclepore), rinsed twice with filtered seawater to wash away nonparticulate ^{32}Si and dried at room temperature for 48 h. The activity of ^{32}Si in the samples was determined using the Cerenkov counting method (Leynaert, 1993) on a scintillation counter (Tri-Carb 4910TR, Perkin Elmer) 3 months after the samples were filtered. Counts yielding less than three times the background (23 CPM) were discarded. Results were normalized to cell counts to obtain individual uptake rates (ρ_{Si} in nmol Si cell^{-1} d^{-1}). Samples were then analyzed for biogenic Si content as previously described. The specific uptake rate (V_{Si} in d^{-1}) was calculated by normalizing the Si uptake rate to the biogenic Si concentration. Subsequently, we deduced the turnover time t as ($\frac{ln2}{V_{\mathrm{Si}}}$) (in d).

Volume estimations

During the isolation process, photographs of each specimen were taken (Canon Eos 77D camera) to relate elemental data to various morphological criteria. From the pictures, we measured the length of major and minor axes using ImageJ software (Abràmoff et al., 2004). Volumes (V) were estimated by approximating the shape and size of each taxon using simple geometric shapes that allowed calculation of the associated volume (Mansour et al., 2021; Supporting Information Table S2.2; Fig. S2.1). Finally, the equivalent spherical diameter (ESD) was determined from the volume (Supporting Information Eq. 2.1.7). All images used for measurements are available at https://doi.org/10.17882/89409.

Statistical analyses

We combined C and N content data measured for this study with literature data (Mansour et al., 2021). All data analyses were conducted using R software (R Core Team, 2020).

To test the relationship between individual elemental content and volume, we assumed that it was adequately described by a power law:

$$Q_i = a \times V^b \tag{2.1}$$

where Q_i is the individual C or N content in μg C cell^{-1} or μg N cell^{-1}, V is the individual volume in mm^3, a is the normalization constant, and b is the scaling exponent of the power law. We used $\log_{10}$-transformed elemental content and volume data, as this is the most appropriate method to assess allometric-scaling relationships (Kerkhoff and Enquist, 2009). This led to the transformed equation:

$$\log_{10} Q_i = \log_{10} a + b \log_{10} V \tag{2.2}$$

For these linear regression analyses, we choose Model I (ordinary least squares regression) instead of Model II, as Model I is largely recommended for application in allometry (Kilmer and Rodríguez, 2017) and because measurement error of the independent variable, the individual volume, is considered to be low. Moreover, our purpose was to provide a predictive relationship. The linear models were validated by leave-one-out cross-validation using the R package `caret` (Kuhn et al., 2020) and by analysis of normality and homoscedasticity of residuals. We compared the regression slope of the C-to-volume relationship with those found

previously for diatoms and various protists (Menden-Deuer and Lessard, 2000) with Student's t tests. Difference in the regression slopes between Radiolaria and Phaeodaria was tested using ANOVA. We then calculated the C and N density in μg C mm^{-3} and μg N mm^{-3}, respectively, and tested for differences in mean values between taxa with ANOVA. We evaluated the correlation between Q_{C} and Q_{N} using a Kendall's τ correlation test.

To determine the Si : C ratio (mol : mol), we compiled our Q_{bSi} data with literature data (Biard et al., 2018; Llopis-Monferrer et al., 2020; Supporting Information Table S2.3) and when available, we calculated the ratio using the median values of C (in nmol C cell^{-1}) and biogenic Si content (in nmol Si cell^{-1}) for each taxon and geographic area. Excess densities were computed from C, N, and biogenic Si content according to Baines et al. (2010) and Stukel et al. (2018) (see details in Supporting Information Text S1). We then estimated the theoretical sinking U_{th} speed from Stokes' law.

Correlations between Si uptake rates ρ_{Si} and specific uptake rates V_{Si}, on the one hand, and cell volume and averaged daily silicic acid concentrations, on the other hand, were tested with a Kendall's τ correlation test. Dissolved Si concentrations were measured on water samples collected with Niskin bottles.

All the data and code used for these statistical analyses are available on GitHub (https://github.com/MnnLgt/Elemental_composition_Rhizaria).

2.1.4 Results

C and N contents and molar C : N ratio

We measured Q_{C} for 153 samples of pooled Rhizaria, corresponding to 1555 specimens from 8 families of Phaeodaria and 536 specimens belonging to the radiolarian orders Collodaria (Fig. 2.2a,b), Nassellaria (Fig. 2.2c,d), Orodaria (Fig. 2.2e,f), and Spumellaria (Fig. 2.2g). Q_{N} was quantified for 136 of the samples, corresponding to 2002 specimens covering the same taxonomic groups (Table 2.1). Overall, ESD covered almost three orders of magnitude (Table 2.1), ranging from 220 $\pm$ 60 μm for Spumellaria to 9.7 mm for *Cytocladus* sp. (Fig. 2.2f). We found the highest average Q_{C} and Q_{N} per taxon for solitary Collodaria (65.1 $\pm$ 32.8 μg C cell^{-1} and 15.4 $\pm$ 10.4 μg N cell^{-1}). The largest values, 717 μg C cell^{-1} and 76.8 μg N cell^{-1}, were measured for the only specimen of *Cytocladus* sp. (order Orodaria), which was large (diameter = 9.7 mm). The lowest Q_{C} and Q_{N} were observed for the phaeodarian genus *Protocystis* sp. (0.71 $\pm$ 0.37 μg C cell^{-1} and 0.12 $\pm$ 0.08 μg

N cell^{-1}) (Table 2.1). The average C : N ratio was 7.8 $\pm$ 2.1, reaching its highest value for the nassellarian *Phlebarachnium* sp. (11.3 $\pm$ 2.8) and its lowest for solitary collodarians (5.7 $\pm$ 1.4) (Table 2.1).

Along with 103 samples available from the literature (Mansour et al., 2021; Table 2.1), we tested for the relationship between elemental composition and cell size using ordinary least-square regressions of $\log_{10}$-transformed C or N content on $\log_{10}$-transformed cell volume for a total of 256 samples for C and 235 for N. For both elements, we found a significant relationship (R^2 = 0.76, p-value < 0.0001, RMSE = 0.40 for C; R^2 = 0.78, p-value < 0.0001, RMSE = 0.41 for N), described by the equations:

$$\log_{10} Q_{\mathrm{C}} = [0.455 \pm 0.016] \times \log_{10} V + [0.958 \pm 0.025] \tag{2.3}$$

$$\log_{10} Q_{\mathrm{N}} = [0.477 \pm 0.017] \times \log_{10} V + [0.157 \pm 0.026] \tag{2.4}$$

where V is the volume in mm^3, Q_{C} is the individual C content in μg C cell^{-1}, and Q_{N} is the individual N content in μg N cell^{-1}. In both cases, residuals were normally distributed and showed homoscedasticity (Supporting Information Figs. S2.2, S2.3). These equations can be transformed into:

$$Q_{\mathrm{C}} = 10^{[0.958 \pm 0.025]} \times V^{[0.455 \pm 0.016]} \tag{2.5}$$

$$Q_{\mathrm{N}} = 10^{[0.157 \pm 0.026]} \times V^{[0.477 \pm 0.017]} \tag{2.6}$$

Volume explained 76% and 78% of the total variance of Q_{C} and Q_{N}. For both relationships, the phaeodarian families Castanellidae and Tuscaroridae and the radiolarian order Orodaria were almost always found above the regression lines, whereas the phaeodarian family Aulosphaeridae was systematically below (Fig. 2.3).

Considering the whole dataset, the regression slopes of the individual element content-to-volume relationship were 0.455 and 0.477 for C and N, respectively (Eqs. 2.3, 2.4), but there was a significant difference in the slopes between Radiolaria and Phaeodaria (ANOVA: p-value = 0.006 for C, p-value < 0.0001 for N), with the highest slopes for Radiolaria (Supporting Information Table S2.4). This difference could be due in part to a potential effect of the uneven distribution of data from both groups along the size axis (Supporting Information Figs. S2.4, S2.5).

Table 2.1: Summary of carbon and nitrogen content (denoted Q_C and Q_N, respectively) data used for this analysis, compiled from Mansour et al. (2021) and this study. Elemental content and density are expressed as mean ± standard error.

				Carbon			Nitrogen				
Group	Order	Taxon	ESD* (μm)	n_C**	Q_C (μg C cell^{-1})	Density (μg C mm^{-3})	n_N**	Q_N (μg N cell^{-1})	Density (μg N mm^{-3})	C:N (mol:mol)	Reference
Phaeodaria	Aulacanthida	Aulacanthidae	909 ± 671	34[596]	5.8 ± 10.0	11.2 ± 8.8	23[540]	1.2 ± 2.0	1.4 ± 0.6	7.0 ± 0.6	This study
		Aulacanthidae	733 ± 124	17[302]	3.1 ± 1.6	18.0 ± 15.3	17[302]	0.3 ± 0.2	1.8 ± 1.6	12.4 ± 2.3	Mansour et al., 2021
	Phaeocalpida	Castanellidae	632 ± 89	35[567]	7.4 ± 2.6	52.9 ± 13.1	34[566]	1.1 ± 0.4	8.0 ± 2.1	7.7 ± 0.7	This study
	Phaeodendrida	Tuscaroridae	1210 ± 93	7[10]	45.3 ± 23.1	48.9 ± 25.1	7[10]	7.5 ± 4.0	8.0 ± 3.9	7.1 ± 0.5	This study
		Coelodendridae	1609 ± 695	13[45]	12.5 ± 10.1	4.9 ± 2.1	9[26]	2.6 ± 1.3	0.8 ± 0.3	7.8 ± 0.8	This study
		Challengeria sp.	184 ± 73	2[48]	1.2 ± 1.4	241.2 ± 108.8	2[48]	0.1 ± 0.1	14.6 ± 1.7	19.0 ± 6.6	Mansour et al., 2021
		Medusettidae	1893 ± 456	3[4]	23.8 ± 12.5	7.4 ± 4.1	3[4]	4.1 ± 1.8	1.3 ± 0.7	6.7 ± 0.6	This study
		Protocystis sp.	318 ± 53	11[213]	0.7 ± 0.4	39.7 ± 13.0	10[200]	0.1 ± 0.1	6.1 ± 2.7	7.9 ± 2.0	This study
		Protocystis sp.	97 ± 8	12[414]	0.7 ± 0.5	2224.4 ± 1283.2	12[414]	0.1 ± 0.0	259.3 ± 131.4	10.0 ± 2.1	Mansour et al., 2021
	Phaeosphaerida	Aulosphaeridae	1959 ± 206	10[120]	2.3 ± 0.7	0.6 ± 0.2	10[120]	0.4 ± 0.1	0.1 ± 0.0	6.5 ± 0.8	This study
Radiolaria	Acantharia	Various		18[540]	0.2 ± 0.2						Mansour et al., 2021
	Collodaria	Collosphaeridae (colonial)	94 ± 29	8[15033]	80.7 ± 41.2	0.6 ± 0.4	6[14589]	17.0 ± 4.5	0.1 ± 0.1	7.4 ± 2.0	Mansour et al., 2021
		Solitary spp.	286 ± 404	2[32]	21.6 ± 0.0	155.1 ± 47.7	2[32]	3.7 ± 0.0	26.8 ± 8.2	6.8 ± 0.0	Mansour et al., 2021
		Solitary spp.	3425 ± 558	13[33]	65.1 ± 32.8	3.1 ± 1.9	13[33]	15.4 ± 10.4	0.7 ± 0.5	5.7 ± 1.4	This study
		Sphaerozoidae (colonial)	116 ± 25	54[41111]	99.8 ± 87.5	1.9 ± 1.7	52[39511]	13.7 ± 8.2	0.4 ± 0.4	7.6 ± 3.1	Mansour et al., 2021
	Nassellaria	Various	83 ± 6	6[241]	0.5 ± 0.2	1472.1 ± 729.7	6[241]	0.1 ± 0.0	171.3 ± 85.3	10.3 ± 1.7	Mansour et al., 2021
		Phlebarachnium sp.	1175 ± 289	19[468]	6.4 ± 1.6	8.9 ± 5.1	19[468]	0.7 ± 0.3	0.9 ± 0.3	11.3 ± 2.8	This study
	Orodaria	*Cytocladus* sp.	9719	1[1]	717.6	1.5	1[1]	76.8	0.2	10.9	This study
		Oroscena sp.	1492 ± 571	5[8]	44.3 ± 34.0	25.0 ± 14.1	5[8]	7.2 ± 5.3	4.1 ± 2.4	7.2 ± 0.8	This study
	Spumellaria	Various	157 ± 38	2[74]	0.8 ± 0.3	328.1 ± 126.9	2[74]	0.1 ± 0.0	45.6 ± 32.5	9.7 ± 3.7	Mansour et al., 2021
		Various	220 ± 60	2[26]	1.5 ± 0.6	279.7 ± 104.8	2[26]	0.3 ± 0.1	45.1 ± 14.4	7.2 ± 0.4	This study

* Equivalent Spherical Diameter.
** Number of samples analyzed, along with the total number of cells (in brackets).

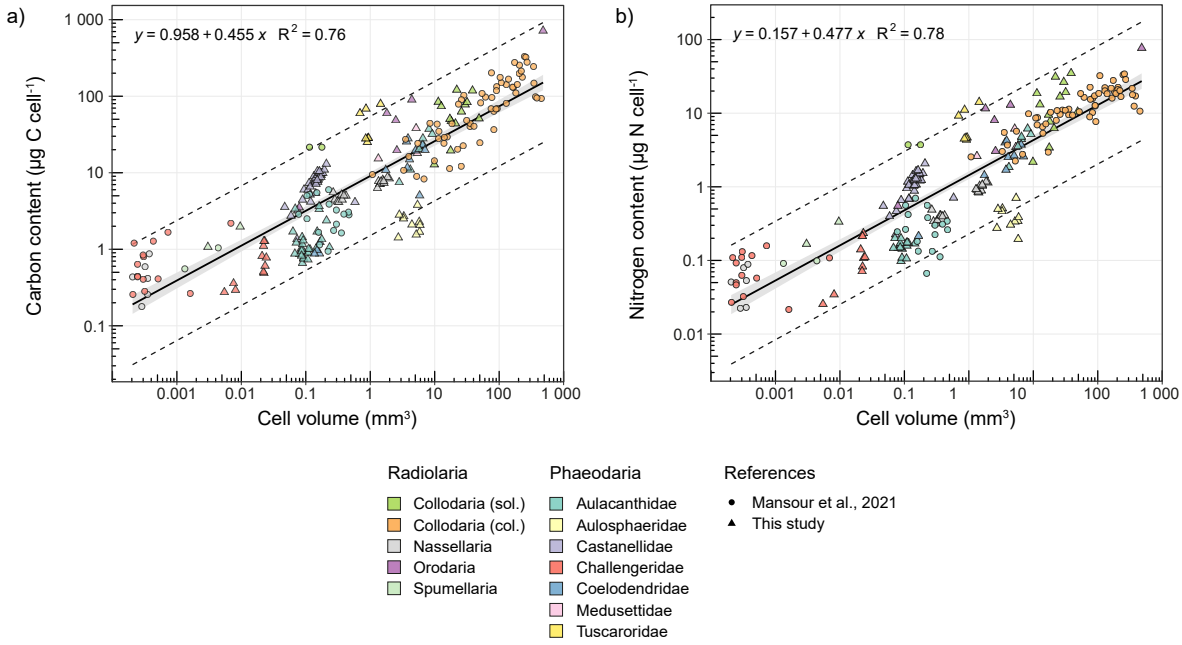

Figure 2.3: General allometry for elemental composition of planktonic Rhizaria. (**a**) Carbon (μg C cell^{-1}) to volume (mm^3) and (**b**) nitrogen (μg N cell^{-1}) to volume (mm^3). Collodaria include solitary (sol.) and colonial (col.) specimens. Black solid lines represent the Model 1 least-squares regressions of $\log_{10}$-transformed data. Gray ribbons represent the 95% confidence level intervals and black dashed lines show the 95% prediction intervals. Data are compiled from Mansour et al. (2021) and this study.

We compared the regression slope of the C-to-volume relationship (0.455; Eq. 2.3) with those obtained by Menden-Deuer and Lessard (2000). Ours differed significantly from the slopes obtained for diatoms (slope = 0.811; t-test: p-value < 0.0001) and other various protists (slope = 0.939; t-test: p-value < 0.0001).

C and N densities ranged over four orders of magnitude (Fig. 2.4) and mean values showed significant differences among taxa (ANOVA: p-value < 0.0001 for both C and N). The phaeodarian family Aulosphaeridae displayed the lowest average C density (0.56 ± 0.23 μg C mm^{-3}) and the collodarian family Collosphaeridae the lowest average N density (0.08 ± 0.06 μg N mm^{-3}). *Protocystis* sp. collected in the Southern Ocean and Nassellaria collected in the Mediterranean Sea reached the highest mean densities for both C and N (>1000 μg C mm^{-3} and >100 μg N mm^{-3}). In contrast, *Protocystis* sp. and the nassellarian *Phlebarachnium* sp. found in the CCE had much lower mean C (39.3 ± 12.5 and 8.9 ± 5.1 μg C mm^{-3}) and N (6.1 ± 2.7 and 0.9 ± 0.3 μg N mm^{-3}) densities (Table 2.1).

A Kendall's rank correlation τ test showed a strong significant correlation between Q_C and Q_N (τ = 0.91, p-value < 0.0001). Molar C : N ratios differed

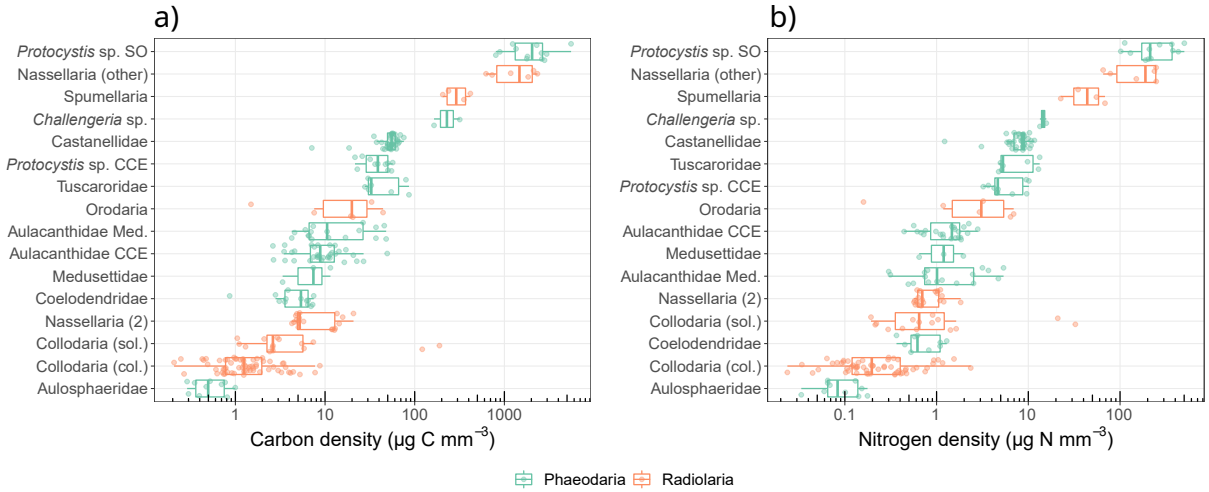

Figure 2.4: Elemental densities for planktonic Rhizaria. (**a**) Carbon densities and (**b**) nitrogen densities. Nassellaria (2) refers to *Phlebarachnium* sp. Collodaria include solitary (sol.) and colonial (col.) specimens. The central value indicates the median. The lower and upper limits of the box correspond to the 25th and 75th percentiles. The lower whisker extends from the 25th percentile to the smallest value at most 1.5 × IQR (inter-quartile range) of the 25th percentile and the upper whisker extends from the 75th percentile to the largest value no further than 1.5 × IQR from the 75th percentile. Data are compiled from Mansour et al. (2021) and this study.

significantly among groups (ANOVA: p-value < 0.0001), even though they differed greatly within each group (Fig. 2.5; Supporting Information Fig. S2.6).

Biogenic Si content, molar Si : C ratios, and excess densities

We measured the Q_{bSi} for 68 samples, representing 802 individuals from 4 radiolarian taxa and 7 phaeodarian taxa. We converted these data into μg Si cell^{-1} considering a molecular weight of 67 g mol^{-1} for hydrated amorphous silica (Mortlock and Froelich, 1989) to include them in the regression equation linking Q_{bSi} (in μg Si cell^{-1}) to V (in μm^3) provided by Llopis-Monferrer et al. (2020). Our Q_{bSi} results ranged from 0.29 ± 0.16 μg Si cell^{-1} for *Phlebarachnium* sp. to 136 μg Si cell^{-1} for a solitary collodarian. By fitting a new model combining literature and new data, we observed that the new slope (0.55) did not show a significant difference from the previous one (0.52) (t-test: p-value = 0.83) (Supporting Information Fig. S2.7).

Using our data and literature data (Biard et al., 2018; Llopis-Monferrer et al., 2020), we could determine the molar Si : C ratio for seven phaeodarian families and the radiolarian orders Spumellaria and Orodaria (Fig. 2.6; Supporting Information Table S2.5). We did not consider Collodaria, as most specimens used for C analyses

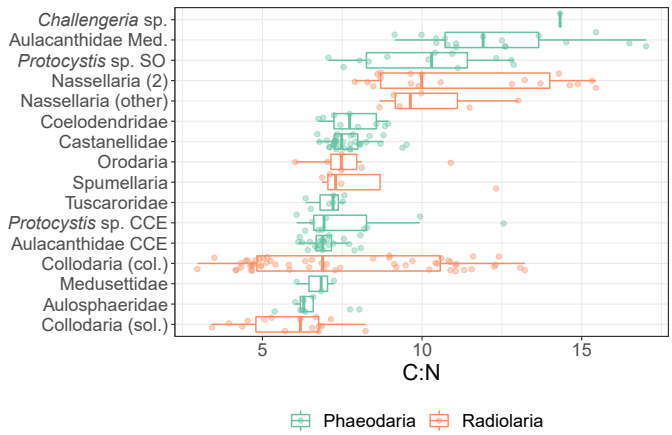

Figure 2.5: C : N ratios (mol : mol) for planktonic Rhizaria. Nassellaria (2) refers to *Phlebarachnium* sp. Collodaria include solitary (sol.) and colonial (col.) specimens. The central value indicates the median. The lower and upper limits of the box correspond to the 25th and 75th percentiles. The lower whisker extends from the 25th percentile to the smallest value at most 1.5 × IQR (inter-quartile range) of the 25th percentile and the upper whisker extends from the 75th percentile to the largest value no further than 1.5 × IQR from the 75th percentile. Data are compiled from Mansour et al. (2021) and this study.

were not skeleton-bearing taxa. Aulosphaeridae reached the highest value (0.71) and the nassellarian *Phlebarachnium* sp. the lowest (0.01). Among phaeodarians, Coelodendridae displayed the lowest ratio (0.04) while Aulacanthidae showed a marked difference between specimens from the California Current (0.31) and the Mediterranean Sea (0.12).

Estimated excess densities ranged from 0.7 μg mm^{-3} for Coelodendridae to 545 μg mm^{-3} for Spumellaria (Table 2.2). Except for the latter and the phaeodarian Castanellidae, Tuscaroridae, and *Protocystis* sp., all excess densities were below 10 μg mm^{-3}. The lowest theoretical sinking speed was observed for the nassellarian *Phlebarachnium* sp. (20–43 m d^{-1}) and the highest for Tuscaroridae (883–2044 m d^{-1}).

Si uptake rates

We measured Si uptake rates ρ_{Si} for 26 samples corresponding to 347 cells belonging to 4 phaeodarian and 3 radiolarian taxa. Values ranged from 0.07 nmol Si cell^{-1} d^{-1} for our only sample of *Protocystis* sp. to 4.31 nmol Si cell^{-1} d^{-1} for our only sample of *Thalassosphaera* sp. (solitary Collodaria) (Supporting Information

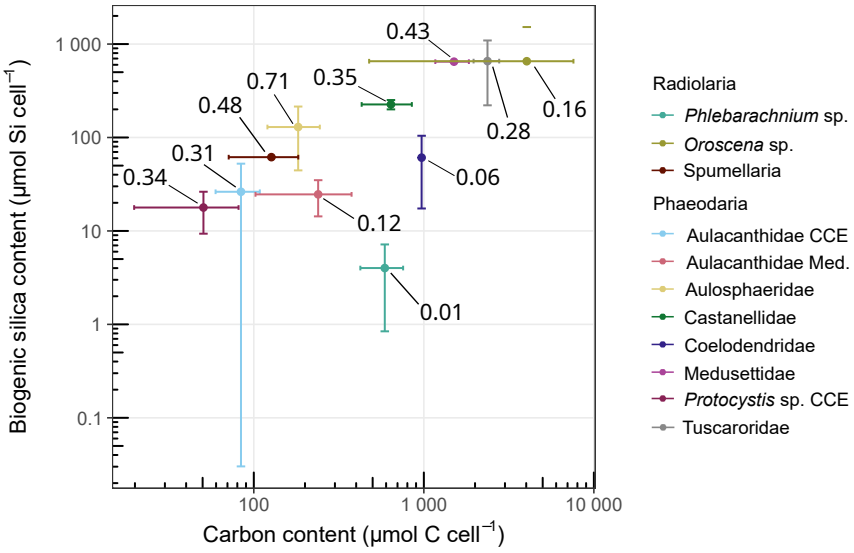

Figure 2.6: General biogenic silica-to-carbon relationships for planktonic Rhizaria. Values are expressed as median biogenic silica (μmol Si cell^{-1}) and carbon (μmol C cell^{-1}) contents. Error bars show the median $\pm$ median absolute deviation of each distribution. Data are compiled from Biard et al. (2018), Llopis-Monferrer et al. (2020), Mansour et al. (2021), and this study.

Table S2.6). The specific uptake rate V_{Si} spanned three orders of magnitude, with a minimal value for Orodaria and Castanellidae (0.0007 d^{-1}) and a maximal value for the nassellarian *Phlebarachnium* sp. (0.06 $\pm$ 0.03 d^{-1}) (Table 2.3). This corresponds to a turnover time ranging from 10 to 1061 d (Table 2.3). Average daily silicic acid concentration (Supporting Information Table S2.7) showed no correlation with ρ_{Si} (Kendall's τ = -0.04, p-value = 0.79) and a weak correlation with V_{Si} (Kendall's τ = -0.55, p-value = 0.0001). When merged with 31 data points available from literature, cell volume showed a very weak positive correlation with ρ_{Si} (τ = 0.24, p-value = 0.008) and a weak negative correlation with V_{Si} (τ = -0.50, p-value < 0.0001).

Table 2.2: Excess densities and theoretical sinking speeds computed from Stokes' law for planktonic Rhizaria.

Group	Type	Area	ESD (μm)	Excess density (μg mm^{-3})	Theoretical sinking speed (m d^{-1})
Phaeodaria	Aulacanthidae	CCE	593	8.7 [4.0-42.7]	143 [66-707]
	Aulacanthidae	Med	679	5.6 [3.8-6.9]	121 [83-149]
	Aulosphaeridae	CCE	2076	1.0 [0.7-1.8]	199 [142-355]
	Castanellidae	CCE	648	57.0 [40.8-60.6]	1127 [806-1199]
	Coelodendridae	CCE	1930	0.7 [0.4-3.2]	115 [67-567]
	Medusettidae	CCE	2142	4.5 [4.5-4.6]	975 [973-986]
	Protocystis sp.	CCE	349	28.7 [25.5-54.2]	164 [146-311]
	Tuscaroridae	CCE	1177	27.8 [13.5-31.3]	1817 [883-2044]
Radiolaria	*Phlebarachnium* sp.	CCE	881	0.9 [0.6-1.2]	33 [20-43]
	Oroscena sp.	CCE	1682	9.8 [5.3-14.0]	1298 [709-1864]
	Spumellaria	CCE	197	545 [543-546]	1001 [999-1004]

Med, Mediterranean Sea.
Data used are compiled from Biard et al. (2018), Llopis-Monferrer et al. (2020), Mansour et al. (2021) and this study. ESD is the median ESD. Excess densities were calculated with the medians of carbon content, silica content and volume data. Between brackets are the excess densities calculated with the 1st and 3rd quantiles of carbon content and silica content, and associated sinking speeds.

Table 2.3: Silicic acid uptake rates ρ_{Si}, specific silicic acid uptake rates V_{Si} and turnover times t for planktonic Rhizaria and diatoms.

Group	Type	Area	n	ρ_{Si}* (nmol Si cell^{-1} d^{-1})	V_{Si}* (d^{-1})	t (d)	Reference
Phaeodaria	Aulacanthidae	CCE	4	0.46 ± 0.70	0.008 ± 0.008	87	This study
	Aulacanthidae	Med			0.061 ± 0.089	11	Llopis-Monferrer et al. (2020)
	Aulosphaeridae	CCE	6	0.62 ± 0.54	0.006 ± 0.007	116	This study
	Castanellidae	CCE	3	0.17 ± 0.11	0.0007 ± 0.0005	990	This study
	Protocystis sp.	CCE	1	0.07	0.002	347	This study
	Protocystis sp.	Med			0.167 ± 0.148	4	Llopis-Monferrer et al. (2020)
Radiolaria	Collodaria	CCE	1	4.31	0.002	347	This study
	Collodaria	Med			0.422 ± 0.312	2	Llopis-Monferrer et al. (2020)
	Phlebarachnium sp.	CCE	10	0.31 ± 0.25	0.065 ± 0.035	11	This study
	Nassellaria	Med			0.086 ± 0.021	8	Llopis-Monferrer et al. (2020)
	Oroscena sp.	CCE	1	0.81	0.0007	990	This study
	Spumellaria	Med			0.372 ± 0.348	2	Llopis-Monferrer et al. (2020)
Diatoms		Various			0.06 - 1.80	0.4 - 11.6	See references in Llopis-Monferrer et al. (2020)

Med, Mediterranean Sea.
*ρ_{Si} and V_{Si} are denoted ρ_P and V_P in Llopis-Monferrer et al. (2020). Except for diatoms, ρ_{Si} and V_{Si} are expressed as mean ± standard error. t is determined from mean V_{Si}. See Supporting Information Table S2.6 for details of biogenic silica content Si uptake rates.

2.1.5 Discussion

Elemental composition and stoichiometry of planktonic Rhizaria

In this study, we successfully measured C and N contents for 2091 rhizarian specimens covering 12 taxa. By combining these data with literature data, we found that over a size range extending three orders of magnitude (100 μm to 10 mm), the Q_C and Q_N values for Rhizaria can be reliably predicted from cell volume (Fig. 2.3). We report here a C : V scaling exponent for Rhizaria (0.455) which is significantly lower than those found for diatoms (0.811) and other protists (0.939) (Menden-Deuer and Lessard, 2000), supporting the conclusion that the equations for diatoms are not suited for these giant protists. From our results, the scaling exponents for the two rhizarian lineages Radiolaria and Phaeodaria differ significantly, being higher for Radiolaria; however, since we could not rule out the possibility of a bias due to differences in samples sizes, we recommend the use of the general relationship. Individual volume did not fully explain the variations in elemental composition (R^2 = 0.76 and 0.78 for the Q_C : V and Q_N : V relationships), with the remaining unexplained variability potentially linked to taxa-specific differences or physiological state of specimens. However, our purpose here was to determine general trends to provide a basis for comparison, even if specific taxa may deviate from them.

These differences between taxa were also reflected in elemental densities, which varied over four orders of magnitude (Table 2.1). The lowest mean C density (0.56 ± 0.23 μg C mm^{-3}) observed for the phaeodarian family Aulosphaeridae is one order of magnitude lower than the conversion factor (80 μg C mm^{-3}) used for the global assessment of Rhizaria biomass (Biard et al., 2016). However, it corroborates the density value of 1.1 μg C mm^{-3} based on the assessment of their C demand (Stukel et al., 2018). For a 2-mm cell, our allometry gives a C content of 17.4 μg C cell^{-1} while our mean Q_C for Aulosphaeridae is 2.3 μg C cell^{-1}. The value of 4.8 μg C cell^{-1} calculated by Stukel et al. (2018) falls within this range. This low value can be explained by the ratio of the central mass diameter, which consists of the central capsule and the phaeodium and is likely to contain most of the organic matter of the cell, to the skeleton diameter. In comparison, the family Aulacanthidae, known to co-occur with Aulosphaeridae in the California Current (Biard and Ohman, 2020) and for which the combination of the central capsule and phaeodium occupies about half of the skeleton, has a mean C density of 11.2 ± 8.8 μg C mm^{-3}, a value one to two orders of magnitude higher than

for Aulosphaeridae. The other phaeodarian families containing large species (i.e., Castanellidae and Tuscaroridae), for which organic matter almost entirely fills the skeleton, have a mean C density of 52.9 ± 13.1 and 48.9 ± 25.1 μg C mm^{-3}. For these taxa, our observations are consistent with values measured on a bulk > 1-mm Phaeodaria population dominated by the same taxa in the North Pacific Ocean, but for which the taxon-specific Q_C values are not known (7.225 μg C cell^{-1}; Ikenoue et al., 2019). In contrast, the smallest phaeodarian group of our study, *Protocystis* sp. collected in the Southern Ocean (mean ESD = 97 μm), reaches the highest C and N densities (>1000 μg C mm^{-3}, >100 μg N mm^{-3}), probably because the organic matter occupies the entire cell. Among Radiolaria, Nassellaria other than Phlebarachnium sp. are the most C and N dense (>1000 μg C mm^{-3}, >100 μg N mm^{-3}), which could also be explained by organic matter entirely filling the skeleton. Foraminifera, the sister clade of Radiolaria among Retaria that builds $CaCO_3$ skeletons, have a mean C density of 89 μg C mm^{-3} (Michaels et al., 1995) which is a higher value than those reported for colonial and solitary Collodaria as well as Orodaria and photosymbiotic Nassellaria, but one to two orders of magnitude lower than C densities of Spumellaria and other Nassellaria.

For all taxa, the high variability in intragroup elemental densities is also reflected in regional differences. For example, the observed difference between *Protocystis* sp. collected in the CCE and those collected in the Southern Ocean, of one order of magnitude for both C and N, suggests that polar species are denser than their relatives living in warmer waters. Intragroup variability was previously observed for solitary Collodaria (9–280 μg C mm^{-3}; Michaels et al., 1995) and is most likely explained by environmental or cellular conditions. Indeed, it has been shown that life history or nutritional status, such as the composition of the phaeodium that is used to store food in Phaeodaria (Gowing, 1986), could influence the Q_C and Q_N values as well as the C : N ratios (Sterner and Elser, 2017).

Our results showed that Q_C and Q_N values were strongly correlated, but their ratio did not seem to be linked with size. Mean C : N ratios (mol : mol) are within the range of values reported for Radiolaria (Michaels et al., 1995) and showed significant variations among taxa. Overall, the mean C : N ratio (7.8 ± 2.1) is higher than the Redfield ratio of 6.6 (Redfield, 1934), as well as C : N ratios for smaller protists (3.46.5; Menden-Deuer and Lessard, 2000) and the mean ratio for all zooplankton (4.9; Kiørboe, 2013). Elemental stoichiometry of phytoplankton is

known to depend on environmental conditions such as N availability (Finkel et al., 2009). We can hypothesize that such effects could impact nutrient assimilation and thus growth rates for Rhizaria as well, but knowledge about physiological processes of Rhizaria is lacking.

Our values of Q_{bSi} fit well with the established allometric relationship (Biard et al., 2018; Llopis-Monferrer et al., 2020), underlining the robustness of this tool. Except for the photosymbiotic nassellarian *Phlebarachnium* sp. and the phaeodarian families Coelodendridae and Aulacanthidae from the Mediterranean Sea, all molar Si : C ratios were higher than those reported for diatoms (0.13 ± 0.04; Brzezinski, 1985). This result is expected since we showed that Rhizaria have overall a low Q_{C} value and they are known to be the most highly silicified pelagic organisms per unit volume (Llopis-Monferrer et al., 2020). The high variations in molar Si : C ratios among taxa highlight the morphological as well as ecological diversity of these organisms. These ratios are likely to also be influenced by abiotic factors (e.g., temperature or nutrient availability), as stated by Brzezinski (1985) for diatoms, or biotic factors such as exposure to predation (Pondaven et al., 2007). Our data are based on individuals coming from different depths and different environmental conditions; thus, we still need to better constrain such factors in order to account for intragroup variability.

From individual to global biomass and flux estimations

Accurate global biomass estimations are needed to better constrain ecological as well as biogeochemical roles of marine organisms. Today, in situ imaging allows quantification and distinction at low taxonomic level of large Rhizaria as well as measurement of their biovolume (Nakamura et al., 2017; Biard and Ohman, 2020). Following our measurements of elemental composition on individual Rhizaria, it is very likely that previous global C biomass assessments based on in situ imaging (Biard et al., 2016; Drago et al., 2022) need to be revised. Indeed, all giant Phaeodaria (> 600 μm) sampled by this method have a C density much lower (ranging from 0.6 ± 0.2 μg C mm^{-3} for Aulosphaeridae to 52.9 ± 13.1 μg C mm^{-3} for Castanellidae; Table 2.1) than the conversion factor used previously (80 μg C mm^{-3}). Nevertheless, it is important to note that small Rhizaria (< 600 μm), currently not reliably sampled by in situ imaging, are mostly much more C-dense, but their regional and global biomass and contribution to fluxes remain poorly constrained. For example, Radiolaria Polycystinea (including Nassellaria, Spumellaria, and Collodaria) are abundant in the first 100 m of the global tropical

and subtropical ocean (Boltovskoy, 2017) and, to our knowledge, their biomass has never been accurately assessed.

When computing biomass over a large spatial scale, choosing whether to use taxon-specific conversion factors or allometric relationships is not trivial. Errors in biomass estimations at the individual scale will propagate and be responsible for under or over estimations at the global scale. Using allometry can introduce variability especially for taxa deviating from the regression line; however, identification to the genus, species, or family level is not always possible as it relies on skeletal details that are generally not visible with in situ imaging instruments. Allometry thus provides a way to infer the biomass of a related organism. Moreover, allometric relationships are a straightforward way to compute the bulk biomass of a population. In the future, the availability of taxon-specific conversion factors as well as allometric relationships for C, N, and biogenic Si will allow us to refine regional or global mass estimations with greater accuracy.

From biomass estimations, the next step is to assess the magnitude of export to the deep ocean. In addition to their mass, fluxes of particles are mainly determined by their sinking speed and their abundance. Although the last parameter is not in the scope of this study, constraining the elemental composition of an organism allows an initial estimate of its excess density with respect to the surrounding water (Baines et al., 2010) and thus its theoretical sinking speed determined from Stokes' law. Our computed excess densities for the Aulosphaeridae, Coelodendridae, and *Phlebarachnium* sp. are consistent with a previous estimated value for Aulosphaeridae (0.72 μg C mm^{-3}; Stukel et al., 2018). Still, the other taxa displayed an excess density 1–3 orders of magnitude higher (Table 2.2). This variability between taxa is reflected in their estimated theoretical sinking speeds, which span three orders of magnitude. These results are expected, as the silica skeleton, which is the main ballast of the cell, shows large structural variations among taxa. Phaeodaria have a porous skeleton, whereas Radiolaria have a dense skeleton (Nakamura et al., 2018a). This could explain why Spumellaria (Radiolaria) have a theoretical sinking speed one order of magnitude higher than specimens of *Protocystis* sp. (Phaeodaria), of comparable size. It would take 5 d for one spumellarian cell to sink from the upper mesopelagic to more than 5000 m depth, whereas it would take about 16 d for *Protocystis* sp. The same order of magnitude difference is observed between the radiolarian *Oroscena* sp. and the phaeodarian families Coelodendridae and Aulosphaeridae. However, the phaeodarian families Castanellidae, Tuscaroridae and Medusettidae, known to be more silica-dense

(Biard et al., 2018), have a theoretical sinking speed ranging from ~800 to ~2000 m d^{-1}. Together with the radiolarian Spumellaria and *Oroscena* sp., their very high sinking speeds, coupled with their high elemental content, indicate that these taxa could be efficient exporters of organic matter and biogenic Si to the deep ocean upon their death. Even though Phaeodaria show higher dissolution rates than Radiolaria (Erez et al., 1982), they would quickly transit to great depths where loss caused by dissolution is lower than in surface waters because of colder temperatures and higher nutrient concentrations. Furthermore, their heavy skeleton likely prevents the organic matter of the cell from being remineralized along the way. In contrast, the other phaeodarian taxa and the nassellarian *Phlebarachnium* sp. have a much lower theoretical sinking speed. Therefore, because of their fragile nature, the delicate skeletons of Aulosphaeridae, Aulacanthidae, and Coelodendridae probably entirely dissolve on descent and never reach the seafloor. We can thus hypothesize that not all Rhizaria contribute equally to vertical export. Further investigation combining abundance data and dissolution rates should bring to light the relative contribution of each. Overall, the sinking rates we have calculated for Spumellaria, Castanellidae, and *Protocystis* sp. are one order of magnitude higher than those measured experimentally by Takahashi and Honjo, 1983). Nevertheless, the values that they calculated from Stokes' law conformed to ours. For most taxa, they noted that the ratios of measured sinking speeds to theoretical sinking speeds were below 1, with great variations among taxa. Therefore, it is likely that our data are maximal values. Indeed, Stokes' law assumes that particles are perfect spheres and the morphology of planktonic Rhizaria can deviate significantly from this shape. The presence of skeletal ornamentation such as spicules or spines increases the drag of the cell, slowing it down. Moreover, Stokes' law predicts that the sinking speed of a sphere is proportional to the square of its radius, but it has been shown for diatoms that this exponent in fact varies between 1 and 2 (Miklasz and Denny, 2010).

Si uptake rates and turnover times

Si uptake rate ρ_{Si} was only weakly positively correlated with size and not with silicic acid concentration. Specific Si uptake rate V_{Si} showed a weak but significant negative correlation with size, a pattern consistent with observed allometric scaling of nutrient uptake for phytoplankton (Edwards et al., 2012). Still, the weakness of the correlation indicates that other parameters may influence uptake rates. The significant, but also weak, correlation with silicic acid concentrations

suggests that environmental conditions influence V_{Si}. However, care should be taken as dissolved Si concentrations were daily averages over large depth ranges. Our measured specific uptake rates V_{Si} were low (0.0007–0.06 d^{-1}) compared to those measured on small Rhizaria (Llopis-Monferrer et al., 2020) and diatoms (summarized in Claquin et al., 2006). It seems paradoxical that these silica-rich organisms take up dissolved Si at such a slow rate. Nonetheless, many Rhizaria live below the epipelagic layer, where diatoms are absent and where competition for silicic acid is expected to be limited. This may explain why *Phlebarachnium* sp., which competes with diatoms in the surface layer, have the highest V_{Si}. To date, very little is known about Si uptake dynamics of rhizarians, nor about cell lifespan. Laboratory studies on a few radiolarian species have shown no evidence of enhanced skeletal growth with higher silicate concentrations (Sugiyama and Anderson, 1997). It is possible that there are phases in the life cycle where the consumption of Si is more important than at other times. Our measurements are first estimates that will be refined once we succeed in cultivating these cells over a longer period of time, with cells that reproduce. Until now, we have only kept them alive for 1–2 weeks and reproduction has never been observed.

Rhizaria are known to have SIT-L Si transporters (Marron et al., 2016), but the number of uptake sites as well as their affinity with dissolved Si are unknown. There is evidence that uptake affinity in phytoplankton does not scale linearly with cell size (Lindemann et al., 2016). Thus, it is not because Rhizaria are larger that their affinity with dissolved Si is higher. In addition, the number of nutrient uptake sites and their specific affinity are expected to decrease with cell size (Fiksen et al., 2013). If this is also true for Si, it could partially account for the negative correlation between cellular volume and specific uptake rate. This could also help explain why larger individuals take up Si at a slower rate comparatively to their size. Further investigation of uptake processes at the cellular level as well as uptake kinetics, either through modeling or experimental observations, should shed light on the observed values. Such refinements should ultimately enhance understanding of their consequences at a population scale.

From our data, estimated turnover times t extended between 10 and > 1000 d. These values are higher than for phytoplanktonic organisms, which usually range from a few hours to a few days (Flynn et al., 2018). This result is to be expected since these organisms are much larger and are thus expected to have a slower growth rate. Skeletal composition should follow the same pattern, so the organism can keep its equilibrium Si : C ratio. Many of our observed values are nevertheless

much higher than expected. For a protist, a turnover time longer than 100 d seems unrealistic. Net sampling could have damaged some cells, although we took care during the sampling process. Moreover, some of the organisms were sampled in the mesopelagic layer, which could have altered their physiological state during recovery. However, collection depth ranges using net tows were too broad to investigate a potential effect of sampling depth (Supporting Information Table S2.8). Our results also question the way we calculated turnover rates, which assumes constant growth and binary fission. However, production of swarmers has been observed in both Phaeodaria and Radiolaria (Nakamura and Suzuki, 2015; Yuasa and Takahashi, 2016). In fact, V_{Si} might not be constant over time: swarmers or juvenile cells could silicify at high rates when producing the skeleton, but then silicification could be reduced at a minimal rate once the skeleton is formed. On the other hand, if the Si transporters in planktonic Rhizaria take up a constant amount of dissolved Si per unit of time, regardless of the life stage of the individual, this would then imply that V_{Si} decreases as the cell grows. Therefore, differences with literature data (Llopis-Monferrer et al., 2020) may be the result of differences in cell growth stage, as well as environmental differences. The evolution of V_{Si} with time has not yet been investigated. Doing so would require culturing Rhizaria, which has barely been successful so far, with a few in vivo experiments maintaining Radiolaria for up to 23 d (Anderson et al., 1989). Overall, these results highlight the strategy of low mass, low growth rate of these organisms. Further analysis of their Si and C uptake rates will provide insight into the life cycle of these organisms, as well as about their ecology.

Insights into the ecology of planktonic Rhizaria

By scaling elemental composition to individual size over several orders of magnitude, empirical allometric relationships provide clues to underlying processes that govern the ecology of planktonic Rhizaria. The scaling exponents of the C to V and N to V relationships are much lower than one, meaning that elemental content does not increase in proportion to cell volume. Moreover, the C-to-volume exponent is significantly lower than for smaller protists, implying a low C strategy for this planktonic group, as previously suggested (Menden-Deuer and Lessard, 2000; Stukel et al., 2018). This difference could be explained by several factors. Rhizaria can be either heterotrophic or mixotrophic and many taxa feed on sinking marine snow or are diffusion feeders (Gowing, 1986). Their large size, from 100 μm to several mm, is responsible for an increased gap between

nutrient delivery, depending on the cross-section area of the organism (Jackson, 1993), and food demand, related to its volume. However, since most of the organic matter is located within the central part of the cell, increasing the radius allows a wider intercepting cross-section and a higher potential clearance rate for these non-swimming organisms, whereas this enlarged body is compensated by a low C density. In addition, it has been suggested that cells with little organic matter are less attractive and more difficult for predators to grasp (Kiørboe, 2013), in addition to their large size making them less accessible to small grazers. Only a few predators have been reported for Radiolaria (summarized in Biard, 2022a) and even less for Phaeodaria, which are usually larger organisms than Radiolaria. As proposed by Stukel et al. (2018), another advantage of this low C strategy is the maintenance of neutral buoyancy. This would allow them to stay at their optimal depth range, which can be restricted for some Phaeodaria because of abiotic factors as well as the presence of food (Biard and Ohman, 2020). Low C density could counteract the presence of a silica skeleton, which increases the overall density of the cell. This could be an explanation of the high molar Si : C ratios, in comparison with diatoms, that we observed for most taxa. Therefore, in addition to the presence of spicules and other skeletal elements, as well as the porous skeleton in Phaeodaria, a lower organic matter density diminishes the sinking speed, while the inflated volume increases the drag of the organism.

Even though the C-to-volume regression equation provides a general trend, it does not fully explain the variations among data, drawing attention to taxon-specific characteristics (Fig. 2.3). This result contrasts with the lower scatter of C content data along the regression line for diatoms and other protists (Menden-Deuer and Lessard, 2000). These differences are not surprising, since the taxa considered in the present study encompass various depth ranges, from the surface to the mesopelagic (Biard and Ohman, 2020), two nutrition modes (mixotrophy and strict heterotrophy) and colonial and solitary individuals. Thus, several taxa are systematically lower or higher than the regression line (e.g., Aulosphaeridae, Castanellidae), accounting for their taxon-specific particularities. Notably, several points belonging to the family Aulosphaeridae are outside the 95% prediction interval. These results are also reflected in the C and N densities spanning four orders of magnitude. Symbiont-bearing taxa (Collodaria, *Phlebarachnium* sp.) are among the least C and N dense. In particular, the photosymbiotic nassellarian *Phlebarachnium* sp. showed C and N densities two orders of magnitude lower than other Nassellaria. One hypothesis is that these taxa need to maintain neutral

buoyancy to stay in surface waters and allow their symbionts to photosynthesize, which could also be facilitated by the presence of the gelatinous matrix along the presence of large lipid vacuoles in Collodaria (Anderson, 1983). Conversely, deep living populations must generally adapt to a food-depleted environment, as well as colder temperature, which could lead to lower metabolic rates. Therefore, we can hypothesize that not only size, but also morphology and trophic strategy have consequences for cell composition and stoichiometry, and that the relative effect of each variable needs to be further examined.

2.1.6 Conclusion

From direct measurements of C and N content and literature data, we provided allometric relationships linking C and N composition to size for a broad variety of Rhizaria ranging from 100 μm to several mm in size, completing the allometric relationship relating biogenic Si content to volume. These simple equations that focus on size rather than species identity are powerful tools to be implemented in models. The combination of the three allometries is of key interest to improve estimates of rhizarian biomass, which have been poorly constrained in the past because of the lack of reliable conversion factors. In contrast, we have measured Si uptake rates and found that they are weakly correlated with size, likely because of the influence of other physiological processes and environmental variables that need to be further explored. From elemental data, we estimated the sinking speed of Rhizaria and showed that they can be fast exporters of organic matter and biogenic Si to the bottom of the ocean. Overall, our study highlights the low-C and slow-growth strategy of these large protists. These results will improve future assessments of the biomass of planktonic Rhizaria as well as refinement of understanding of their physiology and ecology.

Supporting information

See section 2.1.7 of this chapter.

Author Contribution Statement

T.B. and M.L. designed the study. M.L. and N.L.M. performed the sampling and filtrations. N.L.M. took the photographs and performed the incubations. J.F.M. was responsible for carbon and nitrogen content analysis. A.L. and N.L.M. were

responsible for silica content and uptake rate analysis. M.L. performed image analysis, processed the data and wrote the manuscript. All authors edited the manuscript.

Data availability statement

Data and scripts used for analyses are available in the GitHub repository https://github.com/MnnLgt/Elemental_composition_Rhizaria. All images used for morphometric measurements were deposited in the SEANOE database at https://doi.org/10.17882/89409.

Acknowledgments

The authors thank the captain, crew and science team of the R. V. *Roger Revelle* during the CCE-LTER P2107 cruise. The authors particularly thank M. Décima, S. Matthews and G. Cawley for their help in sampling. The authors are grateful to the CCE-LTER (National Science Foundation grants OCE-1637632 and OCE-1614359) program and its lead PI M. Ohman without whom this research would not have been possible. This work was supported by the "Agence Nationale de la Recherche" projects RhiCycle (ANR-19-CE01-0006) and ISblue (ANR-17-EURE-0015).

2.1.7 Supporting Information

Sampling details

Table S2.1: Sampling nets used during the CCE-LTER P2107 cruise.

Date	Latitude	Longitude	Gear	Depth range (m)
14/07/2021	33.8064	-120.4189	MOCNESS	400-600
17/07/2021	36.2005	-123.036	DeepNet	700-1000
17/07/2021	36.5122	-122.273	DeepNet	300-500
18/07/2021	36.5196	-122.2968	MOCNESS	400-600
21/07/2021	35.7467	-121.6759	RingNet	0-400
23/07/2021	36.1346	-122.102	BongoNet	0-500
24/07/2021	36.1927	-122.4567	RingNet	0-500
27/07/2021	36.0881	-122.3225	MOCNESS	300-600
28/07/2021	36.316	-122.7499	MOCNESS	350-450

Image analysis

Table S2.2: Assigned shapes for rhizarian taxa.

Group	Taxon	Shape
Radiolaria	Spumellaria	cylinder
	Phlebarachnium sp.	prolate ellipsoid
	Oroscena sp.	prolate ellipsoid
	Cytocladus sp.	sphere
	solitary Collodaria	sphere
Phaeodaria	Aulacanthidae	sphere
	Aulosphaeridae	sphere
	Castanellidae	sphere
	Tuscaroridae	prolate ellipsoid
	Coelodendridae	sphere
	Medusettidae	sphere or sum of spheres for colonies
	Protocystis sp. (type 1)	prolate ellipsoid
	Protocystis sp. (type 2)	sphere

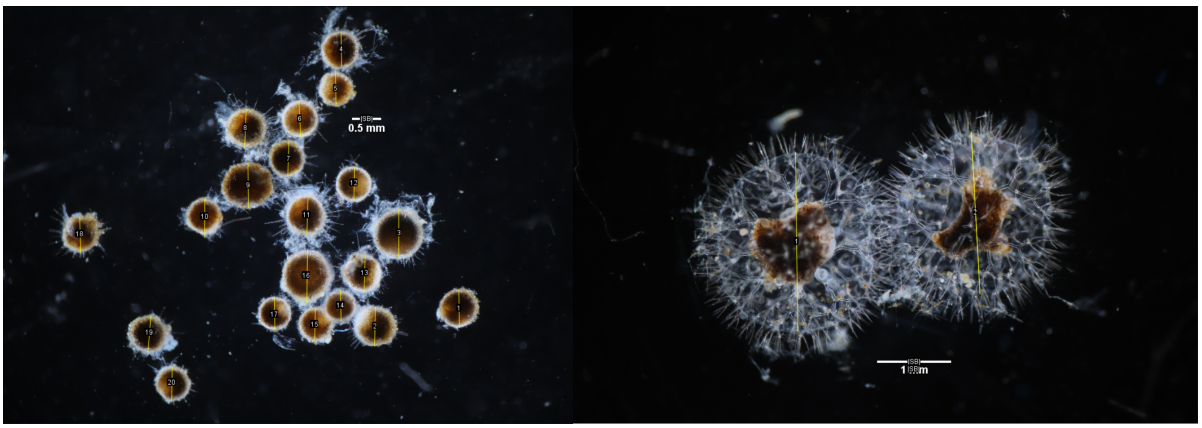

(a) Sample of Castanellidae (b) Sample of Coelodendridae

Figure S2.1: Light microscopy photographs of Rhizaria specimens to describe the methodology for cell measurements

For non spherical objects, the Equivalent Spherical Diameter (ESD) was computed from the volume V as:

$$ESD = \left(\frac{3}{4} \times \frac{V}{\pi}\right)^{\frac{1}{3}} \times 2$$

Silica data from literature

Table S2.3: Biogenic silica content data available from literature

Type	Mean cell vol. (mm)	nmol Si $cell^{-1}$	μg Si $cell^{-1}$	Area*	Reference
Aulacanthidae CCE	0.1	12.46	0.83	CCE	Biard et al., 2018
Aulacanthidae CCE	0.13	13.85	0.93	CCE	Biard et al., 2018
Aulacanthidae CCE	0.08	7.48	0.5	CCE	Biard et al., 2018
Aulacanthidae CCE	0.07	7.21	0.48	CCE	Biard et al., 2018
Aulacanthidae CCE	0.14	52.5	3.52	CCE	Biard et al., 2018
Aulacanthidae CCE	0.1	11.67	0.78	CCE	Biard et al., 2018
Aulacanthidae CCE	0.07	6.01	0.4	CCE	Biard et al., 2018
Aulacanthidae CCE	0.15	12.06	0.81	CCE	Biard et al., 2018
Aulacanthidae CCE	0.14	11.19	0.75	CCE	Biard et al., 2018
Aulacanthidae CCE	0.11	7.76	0.52	CCE	Biard et al., 2018
Aulacanthidae CCE	0.11	24.76	1.66	CCE	Biard et al., 2018
Aulacanthidae CCE	0.21	22.62	1.52	CCE	Biard et al., 2018
Theoperidae	0.2	8.61	0.58	CCE	Biard et al., 2018
Theoperidae	0.14	5.47	0.37	CCE	Biard et al., 2018
Castanellidae	0.17	242.62	16.26	CCE	Biard et al., 2018
Castanellidae	0.16	225.83	15.13	CCE	Biard et al., 2018
Castanellidae	0.17	219.21	14.69	CCE	Biard et al., 2018
Castanellidae	0.16	248.29	16.64	CCE	Biard et al., 2018
Castanellidae	0.14	234.75	15.73	CCE	Biard et al., 2018
Aulosphaeridae	7.27	235.87	15.8	CCE	Biard et al., 2018
Aulosphaeridae	7.36	278.41	18.65	CCE	Biard et al., 2018
Aulosphaeridae	5.39	158.75	10.64	CCE	Biard et al., 2018
Aulosphaeridae	6.25	215.92	14.47	CCE	Biard et al., 2018
Aulosphaeridae	5.59	160.8	10.77	CCE	Biard et al., 2018
Aulosphaeridae	10.74	127.6	8.55	CCE	Biard et al., 2018
Aulosphaeridae	6.7	247.16	16.56	CCE	Biard et al., 2018
Aulosphaeridae	8.2	286.7	19.21	CCE	Biard et al., 2018
Aulosphaeridae	2.25	93.74	6.28	CCE	Biard et al., 2018
Aulosphaeridae	5.62	220.31	14.76	CCE	Biard et al., 2018
Aulosphaeridae	7.83	98.34	6.59	CCE	Biard et al., 2018
Aulosphaeridae	1.45	55.1	3.69	CCE	Biard et al., 2018
Medusettidae	26.45	648.02	43.42	CCE	Biard et al., 2018
Aulosphaeridae	5.54	107.27	7.19	CCE	Biard et al., 2018
Coelodendridae	5.6	265.72	17.8	CCE	Biard et al., 2018
Aulosphaeridae	5.7	109.09	7.31	CCE	Biard et al., 2018
Aulosphaeridae	4.86	109.09	7.31	CCE	Biard et al., 2018
Aulosphaeridae	1.53	75.69	5.07	CCE	Biard et al., 2018
Aulosphaeridae	1.56	67.61	4.53	CCE	Biard et al., 2018
Aulosphaeridae	4.02	77.85	5.22	CCE	Biard et al., 2018

Aulosphaeridae	5.4	115.49	7.74	CCE	Biard et al., 2018
Aulosphaeridae	9.67	326.86	21.9	CCE	Biard et al., 2018
Aulosphaeridae	6.72	265.72	17.8	CCE	Biard et al., 2018
Aulosphaeridae	1.41	81.18	5.44	CCE	Biard et al., 2018
Aulosphaeridae	1.61	130.5	8.74	CCE	Biard et al., 2018
Aulosphaeridae	2.42	91.59	6.14	CCE	Biard et al., 2018
Aulosphaeridae	0.94	68.57	4.59	CCE	Biard et al., 2018
Aulosphaeridae	5.45	257.99	17.29	CCE	Biard et al., 2018
Aulacanthidae CCE	0.24	39.95	2.68	CCE	Biard et al., 2018
Aulacanthidae CCE	0.3	65.52	4.39	CCE	Biard et al., 2018
Aulacanthidae CCE	0.11	52.53	3.52	CCE	Biard et al., 2018
Aulacanthidae CCE	0.13	41.05	2.75	CCE	Biard et al., 2018
Aulacanthidae CCE	0.13	41.75	2.8	CCE	Biard et al., 2018
Aulacanthidae CCE	0.14	27.73	1.86	CCE	Biard et al., 2018
Aulacanthidae CCE	0.09	52.37	3.51	CCE	Biard et al., 2018
Coelodendridae	0.21	39.95	2.68	CCE	Biard et al., 2018
Coelodendridae	0.15	39.13	2.62	CCE	Biard et al., 2018
Coelodendridae	0.15	31.6	2.12	CCE	Biard et al., 2018
Coelodendridae	0.15	31.48	2.11	CCE	Biard et al., 2018
Coelodendridae	0.18	54.64	3.66	CCE	Biard et al., 2018
Castanellidae	0.05	190.2	12.74	CCE	Biard et al., 2018
Aulosphaeridae	1.74	354.3	23.74	CCE	Biard et al., 2018
Castanellidae	0.1	243.3	16.3	CCE	Biard et al., 2018
Castanellidae	0.07	175.6	11.77	CCE	Biard et al., 2018
Aulosphaeridae	0.72	137.3	9.2	CCE	Biard et al., 2018
Castanellidae	0.05	173.6	11.63	CCE	Biard et al., 2018
Collodaria	0.0042	1.65	0.11	Med	Llopis-Monferrer et al., 2020
Collodaria	0.0023	1.04	0.07	Med	Llopis-Monferrer et al., 2020
Collodaria	0.0006	0.37	0.02	Med	Llopis-Monferrer et al., 2020
Collodaria	0.0024	0.81	0.05	Med	Llopis-Monferrer et al., 2020
Collodaria	0.0012	0.96	0.06	Med	Llopis-Monferrer et al., 2020
Collodaria	0.0013	2.63	0.18	Med	Llopis-Monferrer et al., 2020
Nassellaria	0.0003	2.15	0.14	Med	Llopis-Monferrer et al., 2020
Nassellaria	0.0003	3.23	0.22	Med	Llopis-Monferrer et al., 2020
Nassellaria	0.0003	1.08	0.07	Med	Llopis-Monferrer et al., 2020
Spumellaria	0.0031	12.64	0.85	Med	Llopis-Monferrer et al., 2020
Spumellaria	0.0037	9.27	0.62	Med	Llopis-Monferrer et al., 2020
Spumellaria	0.0006	0.81	0.05	Med	Llopis-Monferrer et al., 2020
Spumellaria	0.0004	1.62	0.11	Med	Llopis-Monferrer et al., 2020
Aulacanthidae Med.	0.2730	42.97	2.88	Med	Llopis-Monferrer et al., 2020
Aulacanthidae Med.	0.3830	23.33	1.56	Med	Llopis-Monferrer et al., 2020
Aulacanthidae Med.	0.1453	24.62	1.65	Med	Llopis-Monferrer et al., 2020
Aulacanthidae Med.	0.4943	35.51	2.38	Med	Llopis-Monferrer et al., 2020

Aulacanthidae Med.	0.3103	16.62	1.11	Med	Llopis-Monferrer et al., 2020
Aulacanthidae Med.	0.5738	29.93	2.01	Med	Llopis-Monferrer et al., 2020
Aulacanthidae Med.	0.4928	16.59	1.11	Med	Llopis-Monferrer et al., 2020
Aulacanthidae Med.	0.4604	16.83	1.13	Med	Llopis-Monferrer et al., 2020
Aulacanthidae Med.	0.1724	59.63	3.99	Med	Llopis-Monferrer et al., 2020
Aulacanthidae Med.	0.1724	16.33	1.09	Med	Llopis-Monferrer et al., 2020
Aulacanthidae Med.	0.1724	22.29	1.49	Med	Llopis-Monferrer et al., 2020
Aulacanthidae Med.	0.1724	9.39	0.63	Med	Llopis-Monferrer et al., 2020
Aulacanthidae Med.	0.4100	25.22	1.69	Med	Llopis-Monferrer et al., 2020
Aulacanthidae Med.	0.3115	24.64	1.65	Med	Llopis-Monferrer et al., 2020
Aulacanthidae Med.	0.3115	21.68	1.45	Med	Llopis-Monferrer et al., 2020
Aulacanthidae Med.	0.3115	31.58	2.12	Med	Llopis-Monferrer et al., 2020
Aulacanthidae Med.	0.3115	26.45	1.77	Med	Llopis-Monferrer et al., 2020
Protocystis Med.	0.0072	9.04	0.61	Med	Llopis-Monferrer et al., 2020
Protocystis Med.	0.0007	1.59	0.11	Med	Llopis-Monferrer et al., 2020
Protocystis Med.	0.0002	2.03	0.14	Med	Llopis-Monferrer et al., 2020
Protocystis Med.	0.0005	1.06	0.07	Med	Llopis-Monferrer et al., 2020
Protocystis Med.	0.0005	1.73	0.12	Med	Llopis-Monferrer et al., 2020

* CCE stands for California Current Ecosystem and Med for Mediterranean Sea.

Excess densities and sinking speeds

The excess density (μg mm^{-3}) of an organism is given by:

$$\sigma_{cell} = \rho_{cell} - \rho_{sw} \tag{2.7}$$

with ρ_{cell} the density of the cell and ρ_{sw} the density of seawater. For these calculations, we assumed that density of seawater was 1027.5 kg m^{-3} in the Mediterranean Sea (salinity = 37, temperature = 15°C) and 1025.2 kg m^{-3} in the California Current (salinity = 34, temperature = 15°C).

According to Baines et al. (2010) and Stukel et al. (2018), we computed the cell densities as follows:

$$\rho_{cell} = \frac{M_{cell}}{V_{cell}} \tag{2.8}$$

V_{cell} the cellular volume (mm^3) was expressed as:

$$V_{cell} = V_{skel} + V_{om} + V_w \tag{2.9}$$

V_{cell} was directly measured on photos. V_{skel} and V_{om} were deduced from the

elemental mass and the assumed excess densities of 2.15 g ml^{-1} for biogenic silica and 1.05 g ml^{-1} for organic matter, i.e.:

$$V_{skel} = \frac{Q_{bSi}}{2.15 \times 10^{-3}} \tag{2.10}$$

$$V_{om} = \frac{Q_C + Q_N}{1.05 \times 10^{-3}} \tag{2.11}$$

with Q_{bSi}, Q_C and Q_N the bSi, C and N contents in μg cell^{-1}, respectively.

M_{cell} the cellular mass (μg) was expressed as:

$$M_{cell} = M_{skel} + M_{om} + M_w \tag{2.12}$$

with $M_{skel} = Q_{bSi}$, $M_{om} = Q_C + Q_N$ and $M_w = \rho_{sw} \times V_w$.

The theoretical sinking speeds U_{th} (in m s^{-1}) were computed from Stokes' Law (Stokes, 1851) as:

$$U_{th} = \frac{1}{18} \frac{g(\rho_{cell} - \rho_{sw}) ESD^2}{\mu_{sw}} \tag{2.13}$$

with g = 9.81 m s^2 the gravitational acceleration and μ_{sw} = 0.001 Pa s the assumed dynamic viscosity of the fluid.

Elemental content-to-volume relationships: residual analysis

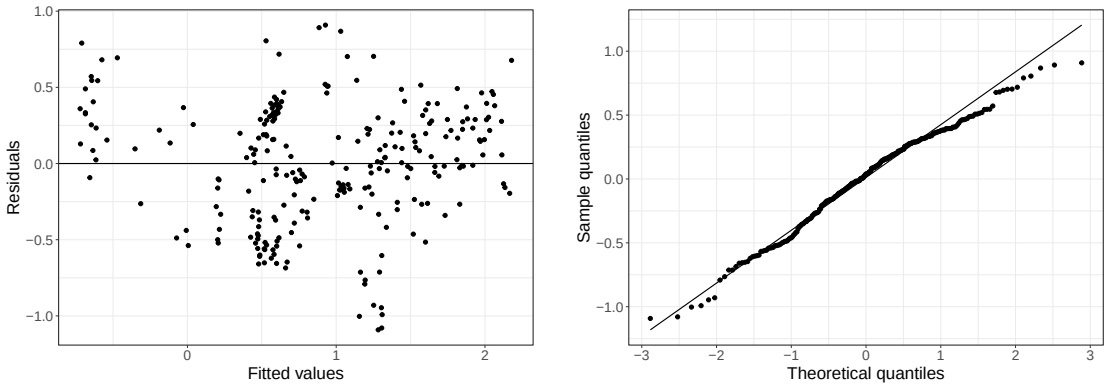

(a) Residuals as a function of fitted values

(b) Quantile-quantile plot

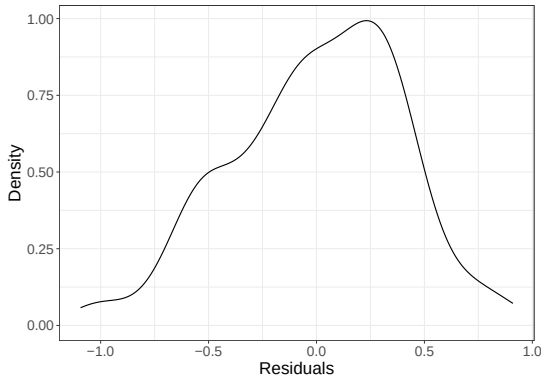

(c) Density plot of the residuals

Figure S2.2: Residual analysis for the model 1 least-squares regression of $\log_{10}$–transformed Q_{C} (μg C cell^{-1}) to V (mm^3) for Rhizaria specimens including solitary cells and colonies.

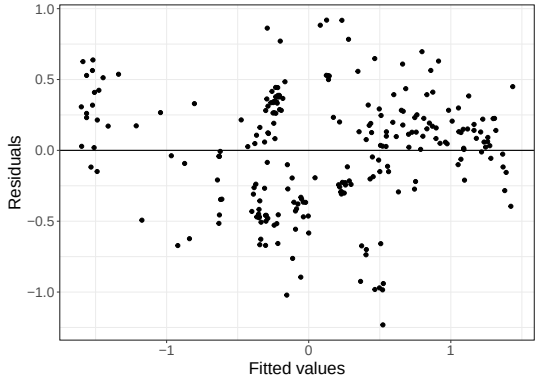

(a) Residuals as a function of fitted values

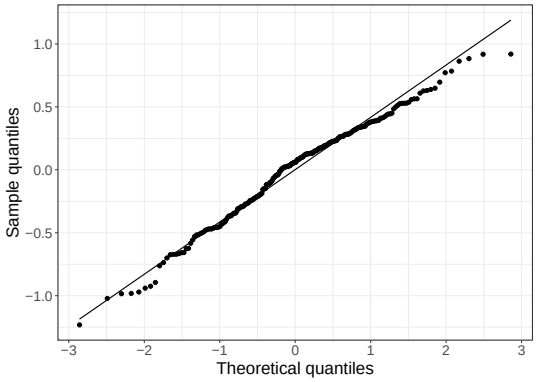

(b) Quantile-quantile plot

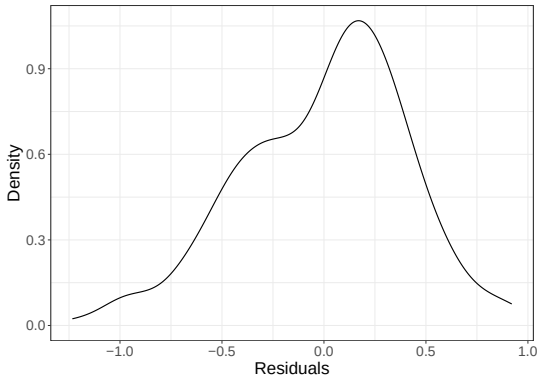

(c) Density plot of the residuals

Figure S2.3: Residual analysis for the model 1 least-squares regression of $\log_{10}$–transformed Q_{N} (μg N cell^{-1}) to V for Rhizaria specimens including solitary cells and colonies.

Comparison of models for Phaeodaria and Radiolaria

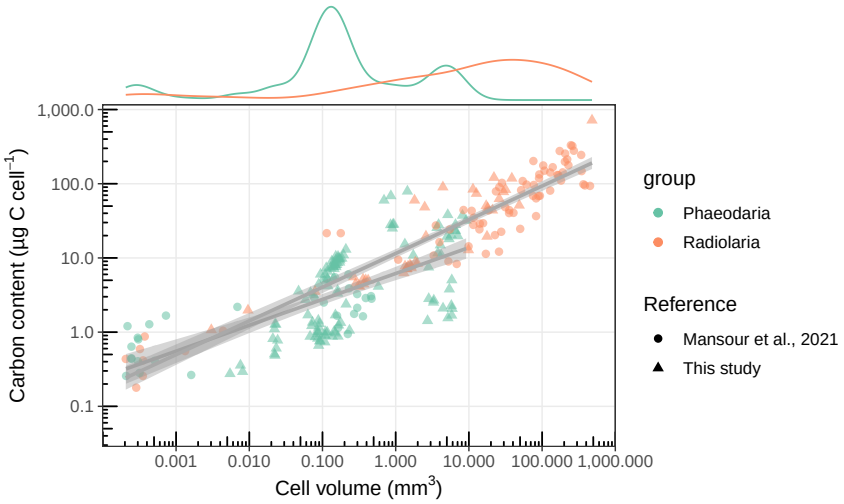

Figure S2.4: Model 1 least-squares regression of $\log_{10}$–transformed Q_{C} (μg C cell^{-1}) to V (mm^3) for Radiolaria and Phaeodaria considered separately. Grey area represents the 95% confidence level intervals for predictions. Above density plots show the repartition of data per group. Data are compiled from Mansour et al. (2021) and this study.

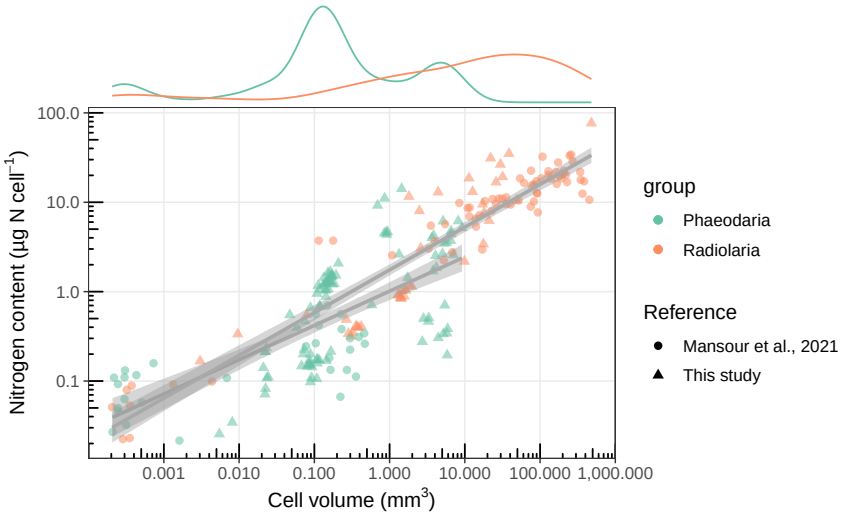

Figure S2.5: Model 1 least-squares regression of $\log_{10}$–transformed Q_{N} (μg N cell^{-1}) to V (mm^3) for Radiolaria and Phaeodaria considered separately. Grey area represents the 95% confidence level intervals for predictions. Above density plots show the repartition of data per group. Data are compiled from Mansour et al. (2021) and this study.

Table S2.4: Equations from models 1 ordinary least-squares regression of $\log_{10}$-transformed Q_C or Q_N (μg C cell^{-1} or μg N cell^{-1}) to V (mm^3) for Radiolaria and Phaeodaria considered separately. Data are compiled from Mansour et al. (2021) and this study.

Group	Equation	R^2
Radiolaria C	$\log_{10} Q_C = [1.06 \pm 0.03] + [0.45 \pm 0.02] \times \log_{10} V$	0.866
Phaeodaria C	$\log_{10} Q_C = [0.79 \pm 0.05] + [0.35 \pm 0.03] \times \log_{10} V$	0.435
Radiolaria N	$\log_{10} Q_N = [0.24 \pm 0.03] + [0.48 \pm 0.02] \times \log_{10} V$	0.869
Phaeodaria N	$\log_{10} Q_N = [0.01 \pm 0.05] + [0.38 \pm 0.04] \times \log_{10} V$	0.482

Molar C:N ratios

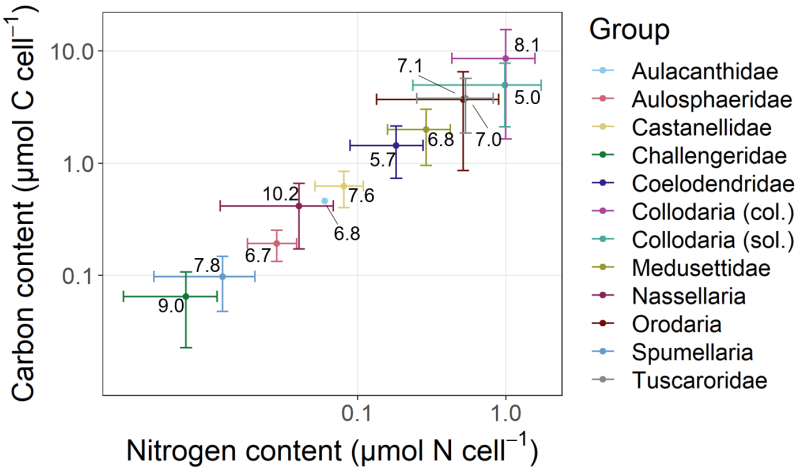

Figure S2.6: Mean carbon content (μmol C cell^{-1}) as a function of mean nitrogen content (μmol N cell^{-1}) for various Rhizaria taxa. Values are for each group the molar ratio of the mean carbon content to the mean nitrogen content. Error bars show mean $\pm$ standard error. Data are compiled from Mansour et al. (2021) and this study.

Biogenic silica content to volume allometry

The previous allometry was given by (Llopis-Monferrer et al., 2020):

$$\log_{10}(Q_{bSi}) = -4.05 + 0.52 \times \log_{10}(V)$$

with Q_{bSi} in μg Si cell^{-1} and V in μm^3.

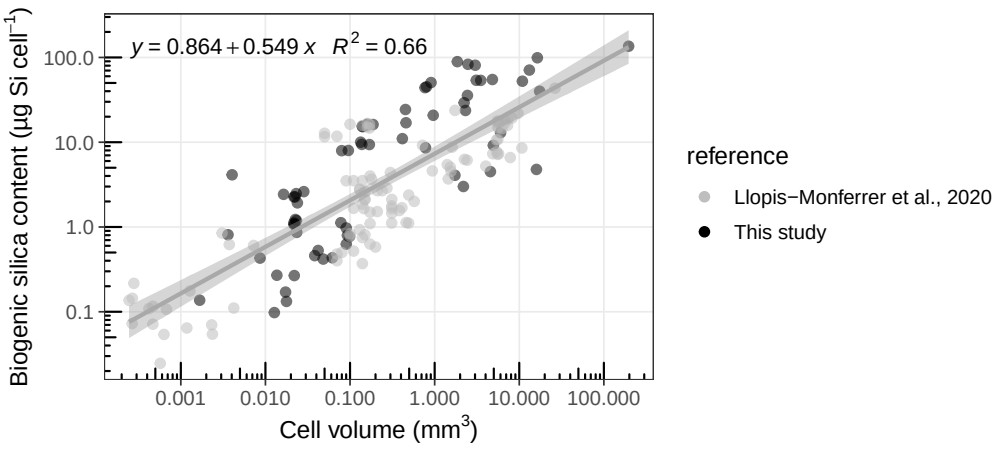

Figure S2.7: New model 1 least-squares regression of $\log_{10}$–transformed silica content (μg Si cell^{-1}) to cell volume (μm^3) for siliceous Rhizaria. Data are compiled from Llopis-Monferrer et al. (2020) and this study.

Table S2.5: Summary of carbon and biogenic silica contents. Si:C ratio are calculated as the ratio of the median silica content to the median carbon content. Data are compiled from Biard et al. (2018), Llopis-Monferrer et al. (2020), Mansour et al. (2021) and this study.

Group	Taxon	Area*	n_C	Median nmol C cell^{-1}	Range nmol C cell^{-1}	n_{bSi}	Median nmol Si cell^{-1}	Range nmol Si cell^{-1}	Si:C
Phaeodaria	Aulacanthidae	CCE	24	84	54–3114	32	26	6–1479	0.31
	Aulacanthidae	Med	27	208	78–500	17	24	9–59	0.12
	Aulosphaeridae	CCE	10	182	118–316	34	129	44–595	0.71
	Castanellidae	CCE	35	640	112–1086	19	225	118–248	0.35
	Coelodendridae	CCE	13	970	73–2337	10	60	31–819	0.06
	Medusettidae	CCE	3	1504	1277–3179	1	648	648–648	0.43
	Challegenridae (*Protocystis* sp.)	CCE	11	50	22–106	13	17	6–39	0.34
	Tuscaroridae	CCE	7	2367	2093–6596	7	656	164–1331	0.28
Radiolaria	Nassellaria (*Phlebarachnium* sp.)	CCE	19	589	343–730	10	4	1–7	0.01
	Orodaria (*Oroscena* sp.)	CCE	5	4029	292–7507	2	654	71–1238	0.16
	Spumellaria	CCE	2	126	89–164	1	61	61–61	0.48

* CCE stands for California Current Ecosystem and Med for Mediterranean Sea.

Silicon uptake rates ρ_{Si}

Table S2.6: Summary data of biogenic Si contents (Q_{bSi}), Si uptake rates (ρ_{Si}) and Si specific uptake rates (V_{Si}) from this study.

Group	Taxon	*n*	ESD[1,2] (μm)	Q_{bSi} [1] (nmol Si cell^{-1})	ρ_{Si} [1] (nmol Si cell^{-1} d^{-1})	V_{Si} [1] (d^{-1})
Phaeodaria	Aulacanthidae	4	832 ± 558	142.52 ± 259.73	0.46 ± 0.70	0.0077 ± 0.0079
	Aulosphaeridae	6	1948 ± 736	193.37 ± 204.47	0.62 ± 0.54	0.0056 ± 0.0074
	Castanellidae	3	655 ± 43	232.95 ± 7.33	0.17 ± 0.11	0.0007 ± 0.0005
	Challegenridae (*Protocystis* sp.)	1	353	36.95	0.07	0.0020
Radiolaria	Collodaria	1	7209	2024.30	4.31	0.0021
	Nassellaria (*Phlebarachnium* sp.)	10	346 ± 99	4.35 ± 2.35	0.31 ± 0.25	0.0647 ± 0.0350
	Orodaria (*Oroscena* sp.)	1	1678	1238.69	0.81	0.0007

[1] Values are expressed as mean ± standard error. [2] Equivalent Spherical Diameter.

Table S2.7: Daily averaged silicic acid concentration measured from sample collected with Niskin bottles.

Date (GMT)	Silicic acid conc. (μmol L^{-1})	Minimum depth (m)	Maximum depth (m)
18/07/2021	14.96400	5.495	80.958
24/07/2021	20.88050	3.738	522.860
25/07/2021	20.13625	4.832	519.776
29/07/2021	21.78250	5.015	518.891
30/07/2021	17.63312	4.737	519.135
03/08/2021	12.05937	4.721	522.432
04/08/2021	11.84625	5.311	519.642
06/08/2021	12.29625	5.488	520.188
10/08/2021	17.55813	5.392	204.520

Table S2.8: Detailed data and metadata of biogenic Si contents (Q_{bSi}), Si uptake rates (ρ_{Si}) and Si specific uptake rates (V_{Si}) from this study.

Latitude	Longitude	Gear	Date	Depth range (m)	Taxon	n[1]	ESD[2] (μm)	Volume (μm^3)	ρ_{Si} (nmol Si cell^{-1} d^{-1})	Q_{bSi} (nmol Si cell^{-1})	V_{Si} (d^{-1})
		DeepNet	18/07/2021	1000 - 50	Aulosphaeridae	2	1606	2187105107	0.92	0.045	0.0205
36.3241	-122.7686	RingNet	24/07/2021	500 - 0	Aulacanthidae	14	561	98737338	0.22	0.012	0.0192
36.3241	-122.7686	RingNet	24/07/2021	500 - 0	Aulacanthidae	1	1671	2443025342	1.50	0.532	0.0028
36.3241	-122.7686	RingNet	24/07/2021	500 - 0	Castanellidae	4	643	141379762	0.30	0.228	0.0013
36.3241	-122.7686	RingNet	24/07/2021	500 - 0	Aulosphaeridae	4	1121	780518746	0.58	0.128	0.0045
36.3241	-122.7686	RingNet	24/07/2021	500 - 0	Aulosphaeridae	1	3215	17399004222	1.54	0.596	0.0026
36.1676	-122.4665	Mocness	25/07/2021	600 - 400	*Protocystis* sp.	5	353	23088581	0.07	0.037	0.0020
36.6044	-123.4352	Bongo	29/07/2021	300 - 0	Aulacanthidae	15	554	93152137	0.07	0.012	0.0063
36.6044	-123.4352	Bongo	29/07/2021	300 - 0	Aulacanthidae	18	546	90229089	0.04	0.015	0.0025
36.6044	-123.4352	Bongo	29/07/2021	300 - 0	Aulosphaeridae	3	1490	1737189540	0.23	0.061	0.0038
36.6044	-123.4352	Bongo	29/07/2021	300 - 0	Castanellidae	5	620	139534319	0.12	0.230	0.0005
36.6044	-123.4352	Bongo	29/07/2021	300 - 0	Orodaria	1	1678	2474195264	0.81	1.239	0.0007
36.705	-123.0394	RingNet	30/07/2021	300 - 0	Aulosphaeridae	13	2014	4939335975	0.10	0.137	0.0007
36.705	-123.0394	RingNet	30/07/2021	300 - 0	Castanellidae	9	704	187127543	0.10	0.241	0.0004
34.7136	-130.5414	RingNet	03/08/2021	50 - 0	Nassellaria	25	144	1669750	0.24	0.002	0.1185
34.7136	-130.5414	RingNet	03/08/2021	50 - 0	Nassellaria	25	293	13655738	0.25	0.004	0.0613
34.7136	-130.5414	RingNet	03/08/2021	300 - 0	Nassellaria	25	428	42002596	0.46	0.008	0.0580
34.7136	-130.5414	RingNet	03/08/2021	300 - 0	Nassellaria	25	412	38251196	0.51	0.007	0.0744
34.6385	-130.5178	RingNet	04/08/2021	50 - 0	Nassellaria	25	282	12748444	0.07	0.001	0.0505
34.6385	-130.5178	RingNet	04/08/2021	50 - 0	Nassellaria	30	316	17736047	0.06	0.002	0.0297
34.6385	-130.5178	RingNet	04/08/2021	300 - 0	Nassellaria	25	446	48186747	0.63	0.006	0.1004
34.6385	-130.5178	RingNet	04/08/2021	300 - 0	Nassellaria	25	484	61693415	0.70	0.006	0.1075
34.5029	-130.4235	RingNet	06/08/2021	300 - 0	Nassellaria	20	344	21931830	0.10	0.004	0.0256
34.5029	-130.4235	RingNet	06/08/2021	300 - 0	Nassellaria	20	317	17296937	0.05	0.003	0.0212
35.2885	-121.3928	SalpNet	10/08/2021	350 - 0	Collodaria	1	7209	1.96166E+11	4.31	2.024	0.0021
35.2885	-121.3928	SalpNet	10/08/2021	350 - 0	Aulosphaeridae	6	2248	6015315528	0.32	0.193	0.0017

[1] Number of specimens per sample. [2] Equivalent Spherical Diameter.

CHAPTER 3

Planktonic Rhizaria in global biogeochemical cycles

"When asked “why study plankton?” We might invoke carbon flux, climate change, etc. If the answer seems inadequate to explain a devotion to plankton, do not hesitate to say that the organisms of the plankton are gorgeous, “art forms of the drifting world”. It is not difficult to provide evidence."

J. R. Dolan, *Beauty of the plankton: from the first issue of Haeckel's* Art Forms of Nature

Contents

3.1 A global census of the significance of giant mesopelagic protists to the biogeochemical cycles of carbon and silicon

Laget, M., L. Drago, T. Panaïotis, R. Kiko, L. Stemmann, A. Rogge, N. Llopis-Monferrer, A. Leynaert, J.-O. Irisson, and T. Biard

3.1.1 Abstract

In the world ocean, constant downward export of material from the surface to depths shapes element cycling. Below the epipelagic layer, the mesopelagic layer is a transition zone whose biota affects the fate of exported material – whether organic or mineral – and its long-term storage in the deep ocean. Quantifying the role of mesopelagic organisms is therefore crucial to understand biogeochemical cycles. Thriving in both layers, Rhizaria are biomineralizing protists, mixotrophs or flux-feeders, often reaching gigantic sizes. Recently, in situ imaging showed their contribution to the ocean carbon stock, but left their contribution to element cycling unquantified. Here, we compile a dataset of >4,000 Underwater Vision Profiler 5 profiles, incorporating appr. 168,000 Rhizaria images from all oceanic regions, and apply machine learning models to predict their global organic carbon and biogenic silica (biogenic Si) biomasses in the uppermost 1,000 m. We reveal that these giant protists, dominated by flux-feeding Phaeodaria, represent carbon and bSi biomasses more than twice as important in the mesopelagic than in the epipelagic layer. Globally, we estimate the carbon demand of mesopelagic Phaeodaria to be 0.46 Pg C y^{-1}, representing 3.8 to 9.2% of gravitational carbon export. Furthermore, we find that these silicifying protists co-dominate the silicon cycle, along with diatoms and sponges, by constituting a unique source of biogenic Si production and stock in the mesopelagic layer, where no other silicifiers are present. Our study is the first global census that highlights the importance of these elusive organisms for ocean biogeochemistry.

3.1.2 Main

Life in the surface ocean produces biogenic material that is constantly exported to depth, fueling deep-sea ecosystems with numerous nutrients and minerals. In

particular, exported particulate organic carbon (POC) is the basis of the biological carbon pump (BCP), a key process in regulating atmospheric CO_2 levels (Kwon et al., 2009). This export results from various pathways, including transport by gravitational settling of particles, vertically migrant organisms and lateral transport (Boyd et al., 2019). Just below the epipelagic layer, the mesopelagic layer, whose upper limit is defined as the depth horizon where light becomes insufficient for photosynthesis, receives a rain of organic material punctuated by episodic inputs from the surface ocean (Robinson et al., 2010). This mesopelagic realm is a vast transition zone where ecological interactions determine the fate and amount of material that will ultimately reach the deep ocean. Because of inherent sampling constraints, our knowledge of stocks and processes is scarcer in the deep than in the upper ocean, leaving severe uncertainties in the response of the BCP to global changes (Henson et al., 2022). Settling particles are sources of food for heterotrophic organisms, ranging from bacteria to metazoans with diverse feeding modes, all inhabiting the peculiar mesopelagic environment. Overall, these organisms will respire roughly 90% of POC exported from surface waters through consumption and degradation before it reaches 1,000 m (Robinson et al., 2010). Therefore, conducting a census of the mesopelagic biota and quantifying its contribution to biogeochemical cycling in regard to its trophic role is essential to understand the fate of sinking material and the magnitude of ocean carbon sequestration (Robinson et al., 2010; Martin et al., 2020). Most previous studies on mesopelagic biota focused on metazoan taxa such as copepods, euphausiids or fishes, which are more easily accessible using nets or active acoustics (Irigoien et al., 2014: Steinberg et al., 2008b). In contrast, the role and contribution of fragile unicellular zooplankton such as Rhizaria, known to be abundant in this layer (Nakamura and Suzuki, 2015; Suzuki and Not, 2015; Stemmann et al., 2008), have been overlooked.

Rhizaria are a 515-Ma ancient eukaryotic lineage (Suzuki and Oba, 2015), among which planktonic taxa have evolved to populate modern oceans from the surface to the abyss (Nakamura and Suzuki, 2015; Suzuki and Not, 2015; Biard and Ohman, 2020) and from equatorial to polar waters (Nakamura and Suzuki, 2015; Suzuki and Not, 2015; Stemmann et al., 2008). These ubiquitous protists cover a wide size range spanning from a few μm to several mm, with some of them being able to form colonies of up to one meter (Biard, 2022b). Because they are at the upper end of the protist size spectrum, they are often referred to as giant protists. In the current classification, planktonic Rhizaria include Phaeodaria,

Radiolaria and Foraminifera (Biard, 2022b). Phaeodaria and Radiolaria (including the polycystine orders Spumellaria, Nassellaria, Orodaria and Collodaria) mostly biomineralize siliceous skeletons, although many Collodaria are naked (Nakamura and Suzuki, 2015; Suzuki and Not, 2015). Additionally, these organisms possess various trophic modes while inhabiting different ecological niches. Many Radiolaria and Foraminifera are mixotrophs, harboring photosynthetic algal endosymbionts which sustain energetic requirements of the host cell (Decelle et al., 2015). These mixotrophic Rhizaria thus contribute to atmospheric CO_2 uptake and can thrive in the surface layer of oligotrophic oceans, where organic food resources are scarce (Suzuki and Not, 2015). Phaeodaria, on the other hand, are strictly heterotrophic and mostly found below the epipelagic, where they passively feed upon sinking aggregates (Gowing, 1986; Gowing, 1989). Despite such opposed trophic modes, all large planktonic Rhizaria adapted their lifestyle to food-depleted environments through a low cellular carbon density, particularly compared to other non-autotrophic protists (Laget et al., 2023). Contrastingly, siliceous Rhizaria are the most silicified pelagic organisms known to date (Biard et al., 2018). As they are abundant from the epipelagic down to the bathypelagic ocean, they contribute to silicon uptake where no other planktonic organism takes up dissolved silica (dissolved Si) (Llopis-Monferrer et al., 2020). Moreover, their silicate skeletons act as ballasting minerals and increase the settling velocity of incorporated and attached POC towards the deep ocean. However, because traditional sampling techniques damage their most fragile representatives, especially larger ones, Rhizaria have often been neglected in biogeochemical studies (Biard et al., 2016). Still, during the last decade, considerable progress in quantifying the abundance of these fragile zooplanktonic organisms could be achieved thanks to the fast development of in situ imaging tools. This revealed their substantial contribution to elemental stocks (Biard et al., 2016; Drago et al., 2022) and fluxes (Biard et al., 2018) as well as their role as gatekeepers of the BCP (Stukel et al., 2018; Stukel et al., 2019). Nevertheless, an assessment of both their carbon and silica biomasses using accurate size-to-volume allometric relationships, as well as their carbon demand and biogenic silica (biogenic Si) production, has never been conducted globally. This leaves the full extent of their contribution and importance in biogeochemical cycles unclear and unquantified.

Sampling planktonic Rhizaria and modeling their distribution

Here we present a global dataset with unprecedented information regarding Rhizaria distribution and abundance collected in situ throughout all oceans between 2008 and 2021. The dataset consists of 4,252 vertical profiles acquired with the Underwater Vision Profiler 5 (UVP5; Picheral et al., 2010) down to 1,000 m depth (Fig. 3.1, Supplementary Table S3.1). The UVP5 records an image of each encountered organism larger than 0.6 mm, enabling size measurement and identification at coarse taxonomic level. With Equivalent Spherical Diameters (ESD) ranging from 0.6 mm to 20 mm (therefore excluding smaller Rhizaria; Fig. Ext. 3.1), the 167,551 validated Rhizaria images cover 18 taxonomic categories (Biard and Ohman, 2020) included in Acantharia, Collodaria, Foraminifera, Phaeodaria and other Rhizaria (Fig. 3.2, Table Ext. 3.1). We apply the most recent allometric volume-to-element content relationships (Llopis-Monferrer et al., 2020; Laget et al., 2023) to obtain carbon content of all Rhizaria groups, as well as the silica content for Phaeodaria only (as UVP5 images do not allow distinguishing silicified collodarians from naked ones). Besides their contribution to element stocks, we further investigate their role in biogeochemical processes by estimating Phaeodaria carbon demand (Stukel et al., 2018) and biogenic Si production (Llopis-Monferrer et al., 2020). Associating each of the 167,551 Rhizaria images with a set of environmental values, we quantify these processes on a global 1° × 1° grid by using boosted regression trees (see Methods section 3.1.3).

Global distribution of planktonic Rhizaria from the epipelagic to the mesopelagic

Our models predict the global carbon biomass of large Rhizaria (>0.6 mm) within the upper 1,000 m to be 0.012 Pg C (Table Ext. 3.2) and 0.007 Pg C within the top 500 m, obtained by integrating biomass within the epipelagic layer and the top 300 m of the mesopelagic layer. This is about one to two orders of magnitude lower than prior estimates (0.204 Pg C and 0.061 Pg C in the top 500 m; Biard et al., 2016; Drago et al., 2022). In contrast to these studies, our estimates rely on dedicated volume-to-elemental content allometric relationships established from carbon and volume measurements on living specimens (Laget et al., 2023), which showed lower carbon densities of large Rhizaria and the inadequacy of previous conversion factors. Based on total mesozooplankton biomass estimates (Drago et al., 2022), we now assess the contribution of large Rhizaria to total mesozooplankton biomass in the top 500 m to be 1.7%. Although we revise downward their contribution to

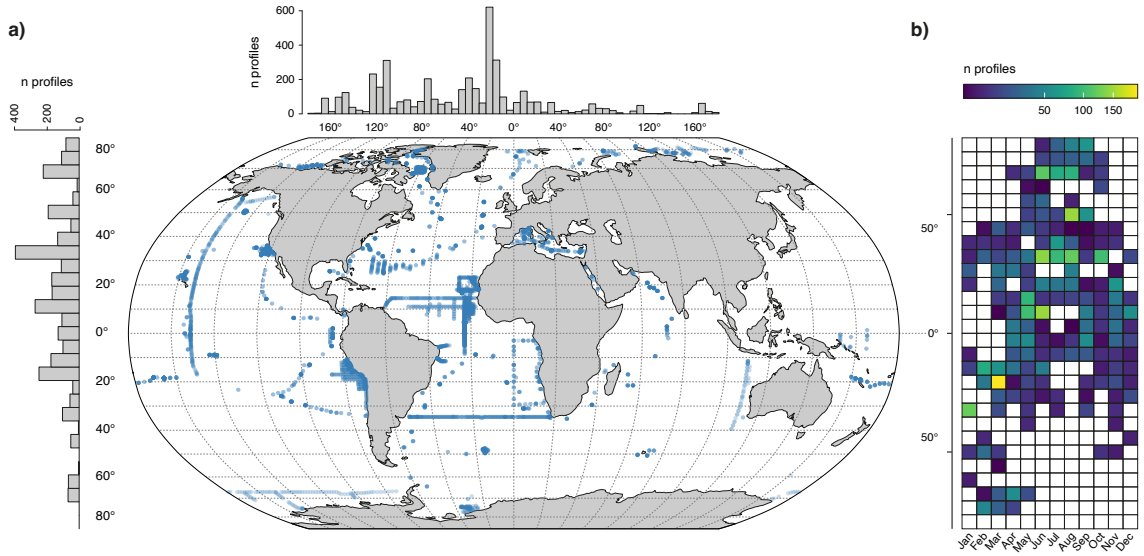

Figure 3.1: Spatial and temporal coverage of the 4,252 vertical in situ profiles. (**a**) Geographic location of Underwater Vision Profiler 5 profiles used in this study. Left and top histograms show the latitudinal and longitudinal distribution of profiles along 3° bins. (**b**) Seasonal distribution of sampling points according to latitude. Squares are colored proportionally to the sampling effort. Details about sampling are summarized in Supplementary Table S3.1.

biomass, the statement that these low carbon density organisms could contribute globally to 31% of mesozooplankton abundance (Biard et al., 2016) still holds true. Moreover, given their gigantic sizes (for protists), their contribution to zooplankton biovolume is substantial (Biard et al., 2016; Biard and Ohman, 2020), acknowledging their importance in pelagic food webs.

All taxa considered, large Rhizaria are distributed worldwide in both the epipelagic and the mesopelagic layers (Fig. 3.3a, 3.3b, 3.3c). In particular, by extending our spatial coverage polewards, we now reveal the prevalence of these organisms at high latitudes, where their biomass was previously shown to be lower (Stemmann et al., 2008; Biard et al., 2016; Brandão et al., 2021). Most importantly, the worldwide carbon concentration of large Rhizaria is of the same order of magnitude between the epipelagic and the mesopelagic layer (Fig 3.3a, 3.3b), highlighting their important role also in the global deep ocean. Integrated biomass values are similar between layers around 20° N and S, but get consistently higher in the mesopelagic near the equator and above 30° N and S (Fig. 3.3c). The two peaks at 50°N and 60° S follow recent biomass pattern delineations in subpolar regions and around the equator (Brandão et al., 2021; Drago et al., 2022), likely due to the presence of fronts at these high latitudes. Nonetheless, these

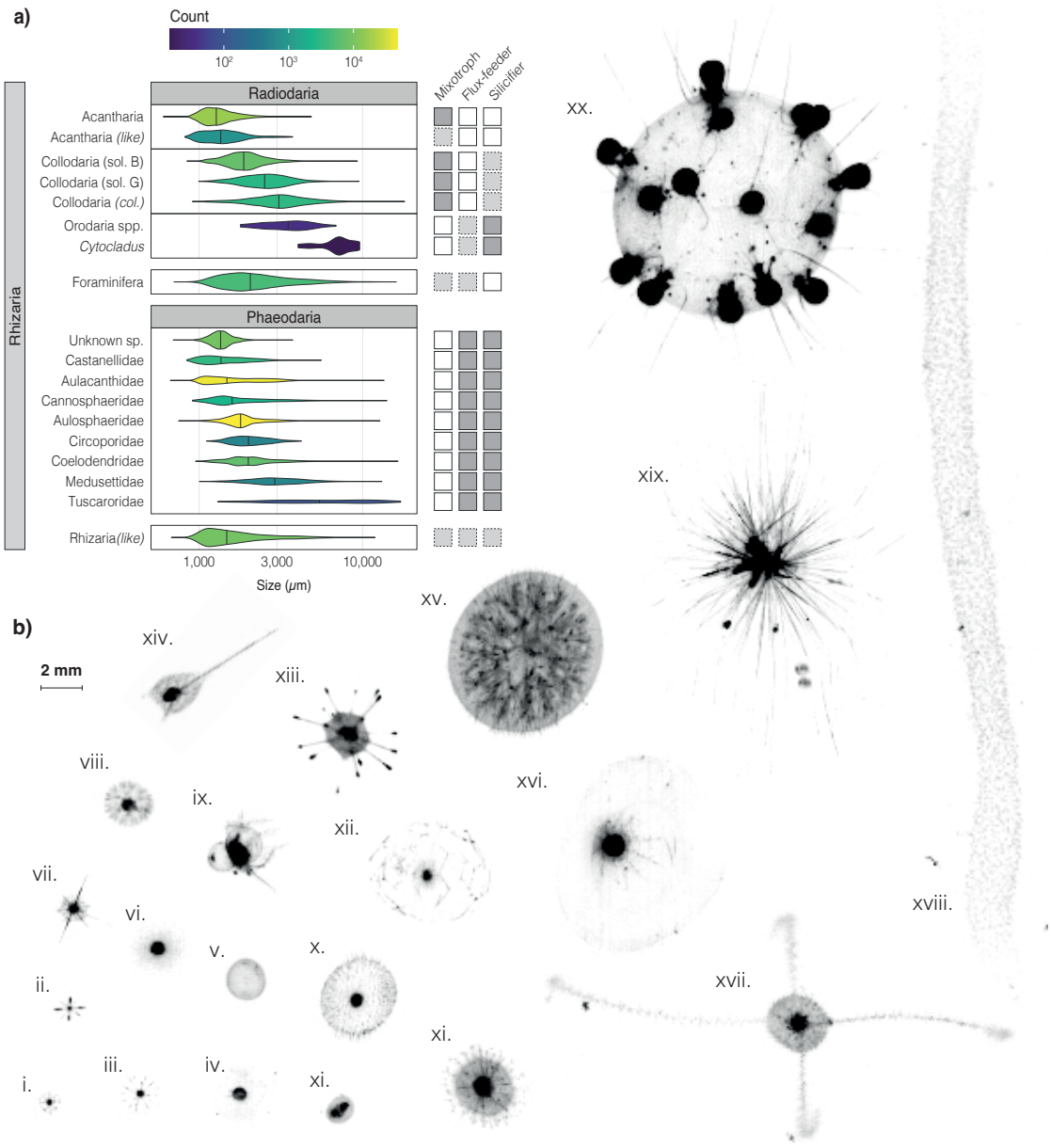

Figure 3.2: Overview of sampled rhizarian specimens. (**a**) Equivalent spherical diameter distribution, counts and characteristics of each taxon considered. Characteristic mixotrophic, flux feeding and silicifying lifestyles are indicated on the right hand side (dark gray indicates a proven attribute, light gray an evident attribute for at least parts of the species within this taxon, and white its proven absence). (**b**) Examples for analyzed Rhizaria taxa (all images are on the same scale): i. Rhizaria (like), ii. Acantharia, iii. Acantharia (like), iv. Castanellidae, v. Collodaria (sol. G, solitary globule), vi. Collodaria (sol.B, solitary black), vii. Acantharia, viii. Coelodendridae, ix. Medusettidae, x. Aulosphaeridae, xi. Aulacanthidae, xii. Cannosphaeridae, xiii. Circoporidae, xiv. Coelodendridae, xv. *Cytocladus* spp., xvi. Orodaria, xvii. Coelodendridae, xvii. Collodaria (col., colonial), xix. Foraminifera, and xx. Tuscaroridae.

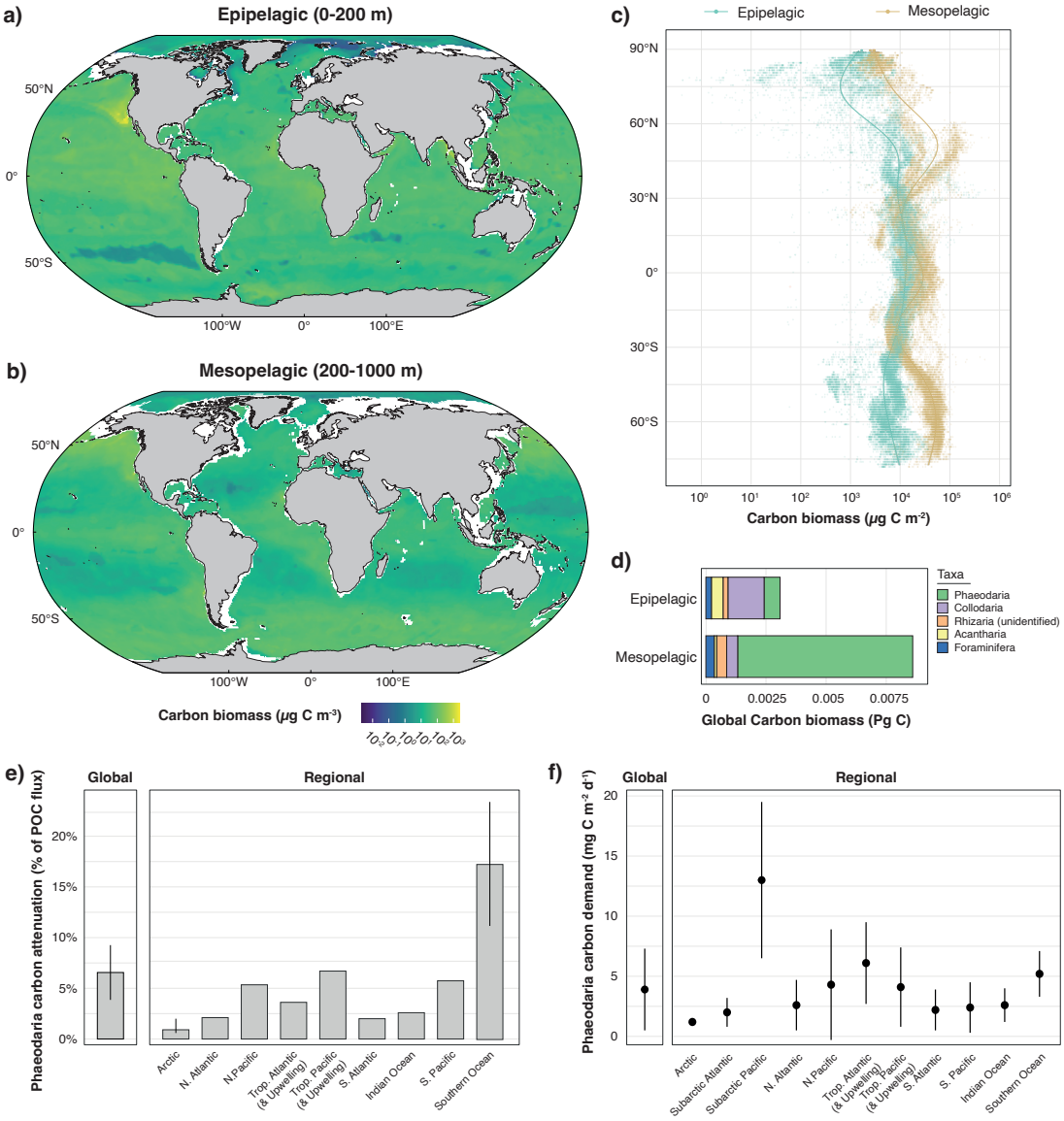

Figure 3.3: Predicted global organic carbon biomass in planktonic Rhizaria, their impact on carbon flux attenuation and their carbon demand. (**a**) and (**b**) Maps of the predicted average 1° × 1° carbon concentration in the epipelagic (0-200 m; **a**) and mesopelagic layer (200-1,000 m; **b**). (**c**) Integrated carbon biomass as a function of latitude for both layers. Regression curves were derived using Generalized Additive Models. Note the logarithmic scaling for carbon biomass. (**d**) Total carbon biomass for Rhizaria groups in both layers. Only groups whose model's R^2 calculated by random cross-validation is >0.05 are shown (see also Table Ext. 3.2). (**e**) Global and regional contribution of large mesopelagic Phaeodaria to gravitational carbon flux attenuation, based on their annual carbon demand and the respective carbon export (i.e., transport out of the euphotic zone) as reported elsewhere (Laws et al., 2000; Dunne et al., 2007; Nowicki et al., 2022). Error bars show the range of estimated values. (**f**) Global and regional integrated daily carbon demand of large mesopelagic Phaeodaria. Dots show mean values, bars show mean ± standard deviation as presented in Table Ext. 3.4.

global patterns hide taxon-driven differences.

Contrasting spatial patterns between mixotrophic and heterotrophic Rhizaria

Given their different trophic modes and life styles, we observe distinct patterns between mixotrophic and heterotrophic Rhizaria groups (Fig. 3.3d, Fig. Ext. 3.2). Globally, Collodaria, Acantharia, and, to a lower extent, Foraminifera, make up most of the Rhizaria biomass in the epipelagic layer of inter-tropical regions (45°N-S), particularly within subtropical oligotrophic gyres (Fig. Ext. 3.3). This pattern is expected given the mixotrophic nature of these radiolarian orders (Decelle et al., 2015; Biard et al., 2016; Biard, 2022a). Through nutrient retention, mixotrophs can enhance primary production (Decelle et al., 2015), besides shortcutting energy pathways to higher trophic levels (Decelle et al., 2015; Biard et al., 2016). As these environments are expected to expand as a consequence of global changes (Polovina et al., 2008), the importance of these protists in ecosystem functioning is likely to increase in warmer and more oligotrophic oceans. More investigations about their role in CO_2 uptake and carbon export is yet needed to provide more detailed predictions about their role in future oceans.

In contrast to mixotrophic taxa, Phaeodaria dominate Rhizaria biomasses in the mesopelagic layer (Fig. 3.3d, Fig. Ext. 3.2). Unlike Radiolaria which prey upon various organisms ranging from bacteria to small Metazoa (Biard, 2022a), these non-motile organisms are floating in particle-rich zones, where they intercept aggregates by extending cytoplasmic strands (i.e, pseudopodia; Nakamura and Suzuki, 2015). Often thought to be restricted to deep waters (Nakamura and Suzuki, 2015), our observations reveal important epipelagic biomasses of Phaeodaria in several high latitude areas, which is in agreement with previous observations in the Southern Ocean (Morley and Stepien, 1984; Gonzalez, 1992; Llopis Monferrer et al., 2021), in particular the Weddell Sea (Gonzalez, 1992), the North Pacific (Steinberg et al., 2008a; Biard et al., 2016), but also the Sea of Japan (Nakamura et al., 2013). Globally, their total carbon biomass is 10-fold higher in the mesopelagic than in the epipelagic zone (Fig 3.3d, Table Ext. 3.2), with an overall contribution of 81% to total Rhizaria biomass. In particular, we show the prevalence of Phaeodaria in deep waters and in cold high latitude areas can be explained by their adaptation to cold water environments due to their gigantic size and low cellular carbon density. Despite their important abundance and biovolume (Biard et al., 2016) in many regions and depths, a result of their low carbon density is that their average contribution to total mesozooplankton carbon biomass is low (0.9% in

the top 500 m). However, it is also highly variable in different ocean regions: their proportion on the total C biomass ranges from 2.7–13.7% between 150 and 1,000 m in the North Pacific (Steinberg et al., 2008a) up to 22.3% between 250 and 3,000 m in the Sea of Japan (Nakamura et al., 2013). This is consistent with observed patterns in detritivore organisms which dominate zooplankton abundance while contributing less to biomass in the mesopelagic zone (Steinberg et al., 2008a). Despite their low cellular carbon content (Laget et al., 2023), large Phaeodaria can aggregate and carry detrital particles, which increases the amount of POC per organism as well as its settling velocity substantially while sinking out of the mesopelagic layer upon death (Ikenoue et al., 2019). Since these abundant mesopelagic organisms are flux-feeders (Gowing, 1986; Gowing, 1989), we further investigate their metabolic requirements and potential impact on carbon fluxes in the mesopelagic layer.

Contribution of mesopelagic Phaeodaria to global carbon-flux attenuation

Globally, we estimate an annual carbon demand of 0.46 Pg C y^{-1} by mesopelagic Phaeodaria alone (Table Ext. 3.3). Scaled to recent global gravitational POC export estimates, ranging from 5 to 12 Pg C y^{-1} (see Nowicki et al., 2022, and references therein), they would intercept between 3.8 and 9.2% of the gravitational POC flux exported out of the euphotic zone (Fig 3.3e). By modulating their turnover times over the full span of observed values (Stukel et al., 2018; see Methods section 3.1.3), the global flux attenuation by Phaeodaria could range from 2.8-6.7% to 8.9-21.4%. Such attenuation, driven by simple unicellular organisms, has never been taken into account in previous assessments of carbon flux attenuation, which was thought to be restricted to copepods, small protists, bacteria and fishes (Steinberg et al., 2008b; Robinson et al., 2010; Irigoien et al., 2014). Integrating this number into the global carbon budget is therefore necessary to refine biogeochemical models and to improve predictions of the future ocean state.

Maximum potential Phaeodaria-driven attenuation is found in the Southern Ocean, where it ranges between 11.2 and 23.4% of the gravitational POC export (0.62-1.3 Pg C y^{-1}; Laws et al., 2000; Dunne et al., 2007). In contrast, it approximates 3.8 to 6.7% in equatorial and upwelling areas (Dunne et al., 2007; Nowicki et al., 2022; Fig. 3.3e), where large Phaeodaria are also abundant. These observations align with previous findings showing more important zooplankton carbon demands in high latitudes and productive areas (Steinberg et al., 2008b). Their daily integrated carbon demand averages 3.9 ± 3.4 mg C m^{-2} d^{-1} worldwide

(Fig. 3.3f, Table Ext. 3.4), with highest values in the subarctic Pacific (13.0 ± 6.5 mg C m^{-2} d^{-1}; Fig. 3.3f, Table Ext. 3.4). In subtropical gyres, where they are least abundant, they could account for 18.9% of the total zooplankton carbon demand (3.4 ± 3.1 mg C m^{-2} d^{-1} from 17.9 mg C m^{-2} d^{-1} reported for the North Pacific Subtropical Gyre; Hannides et al., 2015). Contrastingly, in the subarctic Pacific where their demand is maximum, their contribution to total zooplankton demand (133.1 mg C m^{-2} d^{-1}; Steinberg et al., 2008b) drops to 9.7%, as metazoan zooplankton may outcompete them for food.

As Phaeodaria are known to consume sinking particles, rather than suspended ones (Gowing, 1986; Gowing, 1989), they can exert a substantial influence on rapidly sinking particles, which are expected to be preferentially transferred to the deep ocean due to their high sinking speed. In the California Current, the Phaeodaria family Aulosphaeridae alone can be responsible for on average 10% of total flux attenuation at their depth of maximum abundance (Stukel et al., 2019), located in the upper mesopelagic zone where food is the most abundant. Still, as substantial amounts of Phaeodaria feed in the lower epipelagic, above 200 m (Stukel et al., 2019; Biard and Ohman, 2020; Fig. Ext. 3.4), our estimates are likely conservative as we only estimated Phaeodaria carbon demand between 200 and 1,000 m. Ingested material is used for Phaeodaria growth but is ultimately processed into mini-pellets, ejected in the water column and thought to play an important role in carbon export (Gowing and Silver, 1985). Indeed, mini-pellet abundance can be almost 5 orders of magnitude higher than that of krill fecal pellets in the Weddell Sea (Gonzalez, 1992). Therefore, the nature of the exported material - either fecal pellets or aggregated bodies (Stemmann and Boss, 2012; Ikenoue et al., 2019) - and the associated differences in sinking velocities and carbon contents as well as the resulting effects on global export must be further explored. As Phaeodaria aggregates can be observed with in situ imaging (Stemmann and Boss, 2012), this tool can be used to estimate phaeoarian-mediated fluxes. Their silicified skeleton is likely increasing sinking velocities of dead individuals and aggregates into which such are incorporated; thus, we further investigated the role of Phaeodaria in the silicon cycle and potential impacts for the carbon cycle.

Global biogenic silica stocks and production mediated by Phaeodaria

Globally, our models predict that Phaeodaria account for 4.25 Tg of biogenic Si standing stocks in the upper 1,000 m of the oceans, among which 0.34 Tg

are in the epipelagic and 3.91 Tg in the mesopelagic layer (Fig. 3.4, Table Ext. 3.3). The mean integrated value for the epipelagic layer is 1.1 ± 3.3 mg Si m^{-2} (range 0-204.4 mg Si m^{-2}; Fig. 3.4c), which is in the range of values measured on small Rhizaria not within the size spectrum of the UVP5 (Llopis-Monferrer et al., 2020). The whole population of Rhizaria would thereby account for 7 to 18% of the total integrated biogenic Si pool in the epipelagic layer (Tréguer and De La Rocha, 2013) while most of the remaining stock is being attributed to diatoms (Tréguer et al., 2021). In the mesopelagic layer, the mean integrated value is 11.6 ± 12.1 mg Si m^{-2} (range 0-378.3 mg Si m^{-2}; Fig. 3.4c) and would account for approximately 0-15% of the total biogenic Si integrated pool, based on average estimates from the other studies (Leynaert et al., 2001; Krause et al., 2009). We further quantify the role of Phaeodaria in the silicon cycle by estimating total biogenic Si production (or silicon uptake). Average global annual biogenic Si production by Phaodaria is 0.70 Tg Si y^{-1} (range 0.22 - 2.33) in the epipelagic and 3.95 Tg Si y^{-1} (range 1.25 - 13.1) in the mesopelagic zone (Table Ext. 3.3) while daily integrated production rates averaged 0.005 ± 0.016 mg Si m^{-2} d^{-1} in the epipelagic and 0.030 ± 0.031 in the mesopelagic layer. In the Southern Ocean, the mean production rate within the top 200 meters (0.006 ± 0.004 m^{-2} d^{-1}) is about three orders of magnitude lower compared to previous estimates that included small Rhizaria only (Llopis Monferrer et al., 2021). Although biomasses and production rates in the epipelagic layer are seemingly low compared to diatoms (Tréguer et al., 2021), the overwhelming majority of Phaeodaria is located in the mesopelagic zone (Fig. 3.4). Our results provide the first positive biogenic Si production rates within this layer, as previous attempts to quantify mesopelagic biogenic Si production (Tréguer et al., 2021) did not use sufficient sample volumes to capture Phaeodaria specimens. While this production was suspected (Biard et al., 2018), most recent estimates (Tréguer et al., 2021) only focused on diatom- and sponge-mediated bulk biogenic Si production in the sunlit epipelagic and benthic environments, leaving a gap regarding the deep ocean. Therefore, the role of Phaeodaria in mediating silica through production, export and dissolution is unique and has never been quantified nor considered to this extent previously (Tréguer et al., 2021), leaving the fate of deeply produced biogenic Si unknown.

Due to the porous nature of Phaeodaria skeletons (Nakamura and Suzuki, 2015), the skeleton of epipelagic populations dissolves in the upper part of the ocean (Erez et al., 1982). As a result, dissolved Si is spread throughout the water column, with the potential to resurface through physical mixing, and export to

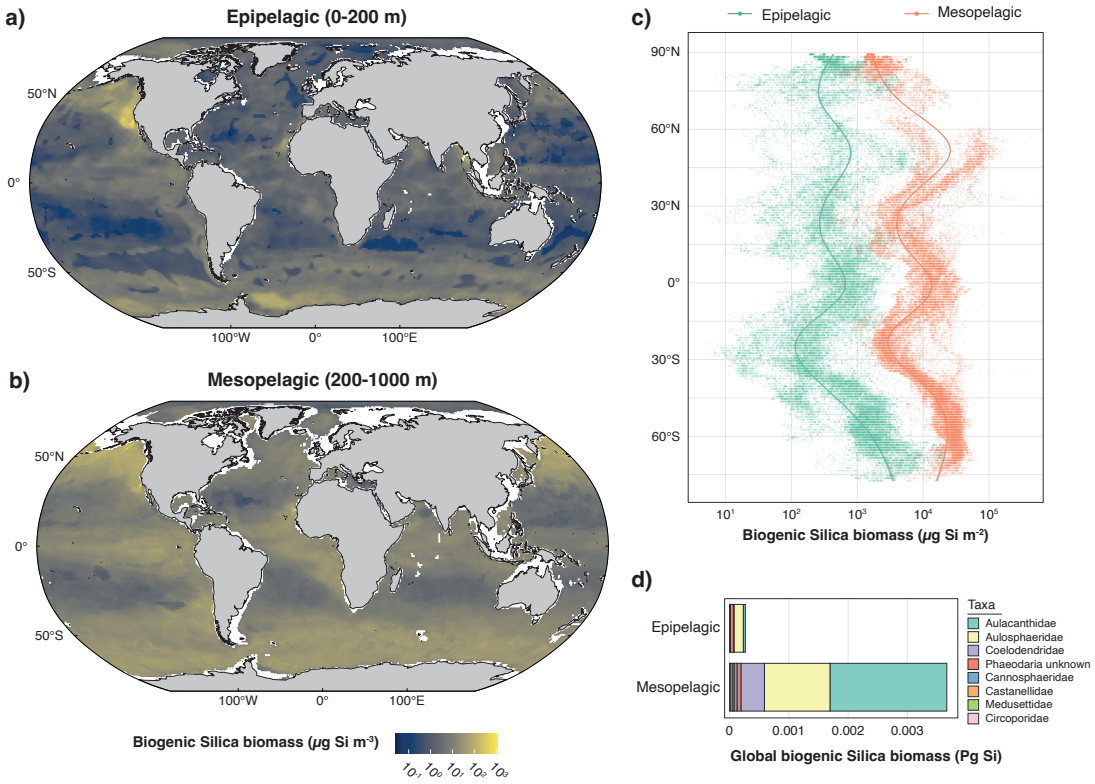

Figure 3.4: Predicted biogenic silica (biogenic Si) biomass of planktonic Rhizaria. (**a**) and (**b**) Maps of the predicted average 1° × 1° biogenic Si concentration in the epipelagic (0-200 m; **a**) and mesopelagic layer (200-1,000 m; **b**). (**c**) Integrated biogenic Si biomass as a function of latitude for both layers. Regression curves were derived using Generalized Additive Models. Note the logarithmic scaling for biogenic Si biomass. (**d**) Total biogenic Si biomass for Phaeodaria families in both layers. Only groups whose model's R^2 calculated by random cross-validation is >0.05 are shown.

the deep ocean is minimal. In contrast, as mesopelagic Phaeodaria biogenic Si production occurs at depths, we can expect that their carcasses reach great depths before undergoing total dissolution, exporting and spreading biogenic Si more efficiently to the deep ocean. Furthermore, as Phaeodaria accumulate siliceous material within their phaeodium, with quantities often reaching the same magnitude as their skeletal structure, it likely enhances the sinking velocity of both the cell and the materials – organic and mineral – it carries (Gowing and Coale, 1989). Still, it is likely that the fragile skeleton of large Phaeodaria is not preserved as fossils but instead dissolves before it can reach the seafloor. The contribution of deep-living Phaeodaria to fluxes, along with the susceptibility of their skeleton to dissolution, has been hypothesized to be an important factor of silica recycling in the North Pacific (Bernstein et al., 1990).

Altogether, our results suggest that mesopelagic Phaeodaria are important recyclers and producers of biogenic Si, besides organic matter, particularly in the deep ocean. Diatoms have been considered to be the main driver of the silicon cycle globally since the Mesozoic era, when they took over the control from Rhizaria and marine sponges (Conley et al., 2017). Our results therefore provide not only elements to suggest that Rhizaria, diatoms and sponges still co-dominate the silicon cycle globally, but they also provide crucial elements for the future changing oceans. Indeed, substantial changes in silica export are expected worldwide because of global warming, which are likely to lead to a subsequent decline in diatom populations (Taucher et al., 2022). Given the present results, we further explore the consequences of such changes for Rhizaria populations and their impact on biogeochemical cycles.

Implications for future ocean biogeochemistry

Rhizaria have populated the global ocean since 515 Ma according to fossil records and survived all major extinctions (Suzuki and Oba, 2015). Because of climate change, significant impacts on all oceanic regions are expected, such as seawater warming from the surface to the deep, increased stratification or decreased nutrient supply to the surface (Kwiatkowski et al., 2020). On the one hand, in future more oligotrophic oceans (Polovina et al., 2008), we can expect mixotrophic populations, representing the vast majority of the Rhizaria biomass in oligotrophic gyres and more generally widespread at low and mid latitudes (Fig. Ext. 3.3), to remain stable or to expand their habitat range globally. Indeed, these organisms, creating microenvironments of enhanced primary production to meet their carbon needs (Caron et al., 1995), will likely not be impacted by changes in this parameter in surrounding waters and may be favored by elevated temperatures (Fig. Ext. 3.5). Consequently, their importance on food webs may increase in the future. On the other hand, the fate of Phaeodaria is less certain. Since they are generalist feeders and influenced by surface chlorophyll a concentrations (Fig. Ext. 3.5), they may not be impacted by changes in upper phytoplankton community composition. Rising temperatures could lead to shorter turnover times, increasing the total carbon demand of the community. Nevertheless, the response of export flux to global changes is highly uncertain: fluxes may increase at high latitudes, whereas a decrease is expected in equatorial and upwelling areas (Henson et al., 2022). Consequently, we can expect antarctic or subarctic Phaeodaria populations to remain stable, or even become more important. In

contrast, upwelling and equatorial populations could decline following a reduced food supply. These organisms primarily inhabit the deep ocean (Fig. 3.4d), where silica concentrations exceed their requirements and where they are its exclusive users (Tréguer et al., 2021). We can therefore expect them to remain unaffected by changes in the silicon cycle and likely increase their control, leading to more biogenic Si dissolution and recycling at depth. Altogether, their ubiquity as well as the variety of their trophic modes makes Rhizaria persistent key organisms also in the future oceans, however, their impact on element turnover is likely to change, calling the need for future refinements in the quantification of their role in biogeochemical cycles.

Conclusion

Our study provides the first comprehensive assessment of the role of giant protists in the biogeochemical cycles of carbon and silicon, offering a new perspective on their significance for ocean ecology. We found that despite their relatively low biomass compared to metazoan zooplankton biomass, these protists play an important role in attenuating carbon fluxes worldwide. Mesopelagic Phaeodaria could attenuate ∼9% of the global gravitational carbon flux worldwide, diminishing the transfer efficiency through the mesopelagic layer. Furthermore, they are the sole drivers of biogenic silica production in this layer, and likely throughout the deep ocean, co-dominating the silicon cycle with diatoms and sponges worldwide. These organisms serve as essential recyclers of POC and biogenic Si, particularly in the Southern Ocean, but much remains unknown about the mechanisms by which these groups take up and metabolize organic matter and nutrients. Additionally, the abundance of Rhizaria increases as their size reduces (Stemmann and Boss, 2012). As we only considered Rhizaria whose size is >600 μm, our estimations should be regarded as conservative. The mesopelagic zone exhibits significant vertical heterogeneity, leading to variations in biological processes and organism physiology as depth changes. It is noteworthy that mesopelagic food webs do not solely depend on sinking particles. Instead, they encompass multiple pathways, including transport of organic matter by vertical migrants and lateral transport (Boyd et al., 2019), and intricate ecological interactions within the microbial, protistan and metazoan communities. While we expect little impact of climate change on overall Rhizaria populations, uncertainties remain regarding the evolution of biogeochemical processes in the mesopelagic zone and the role of Rhizaria in them.

3.1.3 Methods

Global Underwater Vision Profiler 5 dataset

We used a global UVP5 dataset compiled from 64 oceanographic cruises covering a 13-year period (2008-2021; Supplementary Table S3.1), which took place across all oceans and across a large range of oceanic structures (Fig. 3.1a). Among all profiles collected, 4,252 covered the first 200 m and 1,959 the first 1,000 m (Supplementary Table S3.1). Sampling occurred throughout the year, except at high latitudes where access is limited to boreal or austral summers (Fig. 3.1b).

The UVP5 images a water volume of ∼1 L every 5 to 20 cm of the water column during the descent part of a vertical profile. The onboard computer measures all particles larger than ∼0.1 mm, but stores vignettes for particles >0.6 mm only (Picheral et al., 2010). Upon recovery, vertical profiles are processed to extract images, which are associated with a set of metadata and morphological measurements.

Rhizaria images were classified by supervised machine learning algorithms and validated by taxonomy experts on the EcoTaxa web application (Picheral et al., 2017). In total, 167,551 Rhizaria images were validated, and classified into 18 subgroups belonging to Acantharia, Collodaria, Foraminifera, Phaeodaria and unidentified Rhizaria, following the latest classification for in situ Rhizaria images (Biard and Ohman, 2020; Fig. 3.2, Table Ext. 3.1). Phaeodaria were represented by the two abundant families Aulacanthidae and Aulosphaeridae, and by the less abundant families Cannosphaeridae, Castanellidae, Coelodendridae, Tuscaroridae, plus an additional category 'Phaeodaria_unknown'. At the lower range of the detection threshold of the UVP5, Acantharia, distinguished by their symmetric spines surrounded by a black center (Biard et al., 2016), were divided into Acantharea and 'Acantharea_like'. Collodaria were further classified into colonial specimens, solitary black and solitary globule (Biard et al., 2016). The radiolarian order Orodaria was split between the genus *Cytocladus* and other Orodaria. Foraminifera and other Rhizaria were all classified as such. Our Rhizaria specimens covered a size spectrum ranging from 0.6 mm to 20 mm, the smallest specimens belonging to Acantharea and the largest to colonial Collodaria (Fig. 3.2).

Individual biomass, carbon demand and biogenic silica production estimates

For each individual, volume was determined by first computing the Equivalent Spherical Diameter (ESD) from the area extracted by ZooProcess and then calculating the volume of the associated sphere. Volumes were also calculated by fitting a prolate ellipse to the object using the major and minor axes length, to ensure that it would not lead to significant differences, which we did not observe (Fig. Ext. 3.6). Therefore, the sphere method was chosen to estimate volume for all considered taxa.

A volume-to-carbon allometric relationship (Laget et al., 2023) was applied to individual volumes V to obtain individual carbon contents Q_{C} (in μg C cell^{-1}):

$$Q_{\mathrm{C}} = 10^{0.958} \times V^{0.455}$$

For siliceous Phaeodaria, biogenic Si contents Q_{bSi} (in μg Si cell^{-1}) were given by the following volume-to-biogenic Si allometric relationship (Llopis-Monferrer et al., 2020):

$$Q_{\mathrm{bSi}} = 10^{-4.05} \times V^{0.52}$$

Individual carbon demand (CD) for mesopelagic Phaeodaria flux-feeders was calculated from individual carbon content Q_{C} following the equation (Stukel et al., 2018):

$$CD = \frac{Q_{\mathrm{C}}}{GGE \times \tau_T}$$

with GGE the gross growth efficiency and τ_T the turnover time (in d). Assuming that turnover times are temperature-dependent with a Q_{10} of 2 (i.e., increasing the temperature by 10°C divides the turnover time by 2), we used a reference turnover time τ of 10.9 d at a temperature of 10°C from the literature (Stukel et al., 2018) for all Phaeodaria taxa considered. We also considered minimal (τ = 4.7 d) and maximal (τ = 15 d) reference turnover times. Each mesopelagic Phaeodaria specimen was assigned a temperature value coming from the World Ocean Atlas (Locarnini et al., 2018) according to its depth, location and month of sampling. The reference turnover time was adjusted to the local temperature using the formula (Biard et al., 2016):

$$\left(\frac{1}{\tau} \times \left(2^{\frac{T_{ref}-T_{obs}}{10}}\right)^{-1}\right)^{-1}$$

with T_{ref} = 10°C and T_{obs} the experienced temperature. As Phaeodaria living in the mesopelagic need to minimize their energy expenditures, we assumed GGE = 0.4 for all considered taxon (Stukel et al., 2018).

To propose a range of biogenic Si production (ρ_{Si}, in μg Si cell^{-1} d^{-1}), we considered the minimum, maximum and median from literature values (0.17, 0.54 and 1.78 nmol Si cell^{-1} d^{-1}; Llopis-Monferrer et al., 2020) and applied a Q_{10} of 2 as described above for all specimens:

$$\rho_{\mathrm{Si}_T} = \rho_{\mathrm{Si}} \times \left(2^{\frac{T_{ref}-T_{obs}}{10}}\right)^{-1}$$

with T_{ref} and T_{obs} as described above.

Environmental data

Temperature, salinity, oxygen and nutrient concentrations (i.e., silicate, phosphate and nitrate) data were extracted from the World Ocean Atlas database (Locarnini et al., 2018; Zweng et al., 2019; Garcia et al., 2019a; Garcia et al., 2019b). These data were delineated on a 1° × 1° horizontal grid over a 0-800 m depth range (as silicate, phosphate and nitrate data were not available deeper) with a monthly temporal resolution covering the years 2008 to 2019. They were averaged throughout both layer's temporal coverage and depth range. Monthly averaged surface chlorophyll-*a* data, extracted from the Copernicus database, and bathymetric data, extracted from the NOAA database (Amante and Eakins, 2009), were used for the corresponding time period. These datasets were standardized to a grid resolution of 1°. UVP5 data were matched to environmental data on the global 1° × 1° grid according to their coordinates. Profiles that could not be matched to the environmental grid were matched to the nearest cell, if any. Individual biomass, demand and production values matched to the same cell were averaged for each layer (Drago et al., 2022).

Predicting and extrapolating global distribution

To model the relationship between environmental variables and Rhizaria distributions, and ultimately predict global Rhizaria biomass distributions, we used boosted regression trees (BRTs), following a methodology developed recently (Drago et al., 2022). Briefly, BRTs function as classical regression trees linking a response (i.e., biomass, carbon demand and biogenic Si production) to predictors (i.e., environmental variables) by performing recursive binary splits (Breiman,

2017). Boosting allows the combination of successive short regression trees, which are adjusted to improve performance on observations poorly modeled by existing trees (Elith et al., 2008). They do not produce a single relationship, but instead combine relatively simple successive tree models and are thus well adapted to fit complex, nonlinear relationships between sparse species datasets and their environment, yet being robust against overfitting (Elith et al., 2008). We implemented BRTs using the R software version 4.0.3 (Team, 2020) and the `xgboost` package version 1.2.0.1 (Chen et al., 2020).

To account for spatial correlation between data points, BRTs' performance were tested using random and spatial cross-validation procedures to improve independence between the training and test sets (Hijmans, 2012). For the spatial cross-validation, data were split into 5 spatial folds according to geographical distances using the R package `blockCV` (Valavi et al., 2018). Each set consisting of 4 spatial folds was used to train the model, while the remaining fold was used for testing, repeated 20 times. We calibrated BRTs by trying various combinations of hyperparameters, including the learning rate per tree, the maximum depth of a tree, the minimum number of elements per leaf and the number of trees, to minimize predictive deviation from the test set (error reduction) and avoid overfitting (complexity minimization) (Elith* et al., 2006; Drago et al., 2022). To evaluate the models, we calculated the two-sided Pearson correlation coefficient and its associated p-value between the observed biomass and the predicted biomass. The predicted biomass was obtained as the average prediction across all repetitions for each test spatial fold. For each layer, we applied models to environmental predictors for all cells of the $1° \times 1°$ world grid to obtain maps of predicted biomass concentrations. Univariate partial dependence plots were represented to show the effect of each variable on biomass prediction, computed as the average marginal effect of the variable in the model resamples. Predicted values were integrated for each layer (in μg m^{-2}) by multiplying the mean concentration (in μg m^{-3}) for this layer by its thickness (in m). To derive global values, integrated values were multiplied by the area of each grid cell, as described in the literature (Drago et al., 2022). Regional values were obtained by partitioning world predictions using Longhurst's provinces (Longhurst, 2010). To estimate the percentage of flux attenuation, we used carbon export (i.e., out of the euphotic zone layer) values from the literature (Laws et al., 2000; Dunne et al., 2007; Nowicki et al., 2022; Clements et al., 2023) and computed the ratios of Phaeodaria carbon demand to carbon export globally and for each oceanic region.

Extended Data and Supporting information

See section 3.1.4 and 3.1.5 of this chapter.

Author Contribution Statement

TB and ML conceptualized, conceived and developed the work with input from RK, AL, LS, AR, and J-OI; RK, AR, LS, and TB contributed to data acquisition; TB manually validated all rhizarian images; ML modified the models developed by LD, TP and J-OI; ML and TB contributed substantially to the data analysis with assistance from J-OI; ML and TB created all figures; ML drafted the manuscript and all authors contributed substantially to its improvement; All authors approved the final submitted manuscript.

Data availability statement

Inputs and outputs for all models are available in the Zenodo repository https://doi.org/10.5281/zenodo.8284902. Environmental data from World Ocean Atlas are available at ncei.noaa.gov/products/world-ocean-atlas. Surface chlorophyll *a* data are available at the Copernicus database.

Code availability statement

All scripts used for results presented in this paper are available in the Zenodo repository https://doi.org/10.5281/zenodo.8284902.

Acknowledgments

We thank cruise leaders and participants who helped in the creation of the UVP5 dataset. We are grateful for the ship time provided by the respective institutions and programs. We acknowledge all the scientific programs (in particular the grant NASA OBB #80NSSC17K0568 for the EXPORTS program and NASA OBB #NNX15AE67G for the NAAMES program, AWI_PS99_00 AWI_PS124_13, METEOR/MERIAN core program & EU H2020 Project AtlantOS) involved in data acquisition. We are grateful to people who sorted images and contributed to build this dataset. We thank Michael Stukel for his advice regarding turnover time calculations and Frédéric Le Moigne for his comments on the manuscript. This work was funded by the French “Agence Nationale de la Recherche” project

RhiCycle (ANR-19-CE01-0006). RK acknowledges support via a Make Our Planet Great Again grant from the French National Research Agency (ANR) within the Programme d'Investissements d'Avenir #ANR-19-MPGA-0012 and funding from the Heisenberg Programme of the German Science Foundation #KI 1387/5-1. LS was supported by the CNRS/Sorbonne University Chair VISION to initiate the global observation. AR was funded by the PACES II (Polar Regions and Coasts in a Changing Earth System) program of the Helmholtz Association, the Federal Ministry of Education and Research of Germany (BMBF) through the projects 'Changing Arctic Transpolar System' (CATS, grant number 03F0776E) and CATS-Synthesis (grant number 03F0831D), as well as the INSPIRES programme of the Alfred Wegener Institute Helmholtz Centre for Polar and Marine Research (AWI).

3.1.4 Extended Data

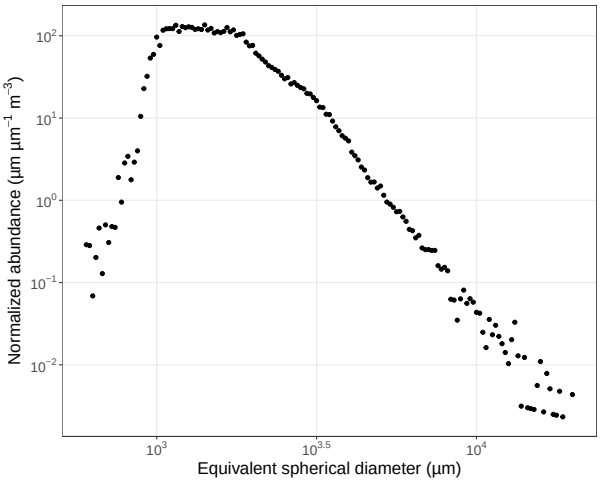

Figure Ext. 3.1: Normalized abundance size spectrum of all planktonic Rhizaria specimens considered in this study.

Table Ext. 3.1: Characteristics of Rhizaria taxa considered in this study.

Group	Taxon	Test nature	Count	Median ESD (μm)
Phaeodaria	Aulacanthidae	silicified	45,772	1,479
	Aulosphaeridae	silicified	50,728	1,799
	Cannosphaeridae	silicified	2,330	1,568
	Castanellidae	silicified	3,459	1,357
	Circoporidae	silicified	586	2,009
	Coelodendridae	silicified	7,042	2,010
	Medusettidae	silicified	642	2,880
	Phaeodaria_unknown	silicified	10,165	1,355
	Tuscaroridae	silicified	109	5,586
Acantharia	Acantharea	strontium	17,123	1,276
	Acantharea_like	strontium	887	1,364
Foraminifera	Foraminifera	calcite	4,718	2,052
Collodaria	Collodaria_colonial	naked	3,330	3,108
	Collodaria_solitaryblack	naked	7,909	1,880
	Collodaria_solitaryglobule	naked	2,935	2,521
Orodaria	Orodaria_other	silicified	44	3,535
	Cytocladus	silicified	16	7,097
Rhizaria_other	Rhizaria_like	unknown	9,756	1,481
		Total	167,551	

Table Ext. 3.2: Results of the carbon models for each Rhizaria taxon as well as for all large Rhizaria together. Stars (*) indicate significant R^2 obtained with Pearson's correlation tests (p-value <0.05).

Layer	Taxon	R^2 (random CV)	R^2 (spatial CV)	Mean integrated biomass (mg C m^{-2})	Total biomass (Tg C)
Epipelagic	Acantharia	15.3*	5.0*	1.11 ± 1.90	0.48
	Collodaria	34.6*	6.1*	3.52 ± 3.31	1.50
	Foraminifera	47.8*	1.5*	0.50 ± 0.83	0.23
	Orodaria	–	0.0	0.00 ± 0.00	0.00
	Phaeodaria	36.9*	0.1	2.15 ± 6.61	0.66
	Rhizaria_other	52.6*	0.2	0.50 ± 0.91	0.20
Mesopelagic	Acantharia	42.9*	<0.1	0.29 ± 0.49	0.10
	Collodaria	30.5*	<0.1	1.28 ± 1.41	0.46
	Foraminifera	30.4*	1.6*	0.80 ± 1.15	0.34
	Orodaria	0.9	0.0	0.02 ± 0.17	0.01
	Phaeodaria	33.3*	7.4*	21.61 ± 22.67	7.28
	Rhizaria_other	36.7*	9.4*	1.34 ± 2.04	0.42
Epipelagic	All Rhizaria	47.3*	0.1	8.84 ± 10.16	3.50
Mesopelagic	All Rhizaria	48.6*	5.4*	26.31 ± 25.98	8.93

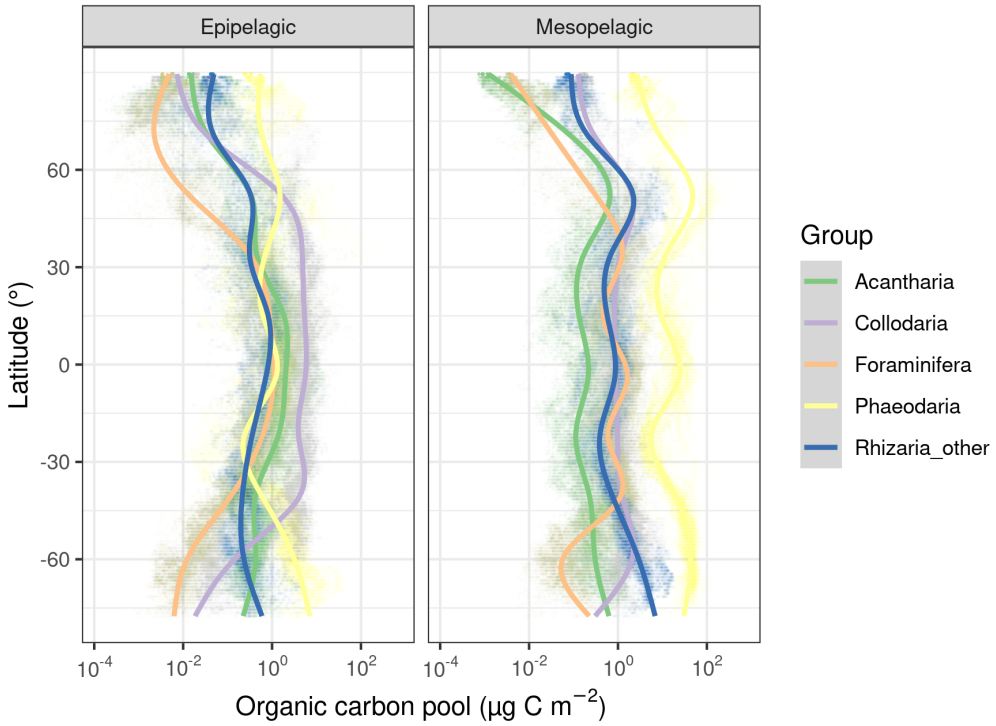

Figure Ext. 3.2: Integrated carbon biomass as a function of latitude for the epipelagic and mesopelagic layers for main Rhizaria groups. Regression curves were derived using Generalized Additive Models. Only groups whose model's R^2 calculated by random cross-validation is >0.05 are shown.

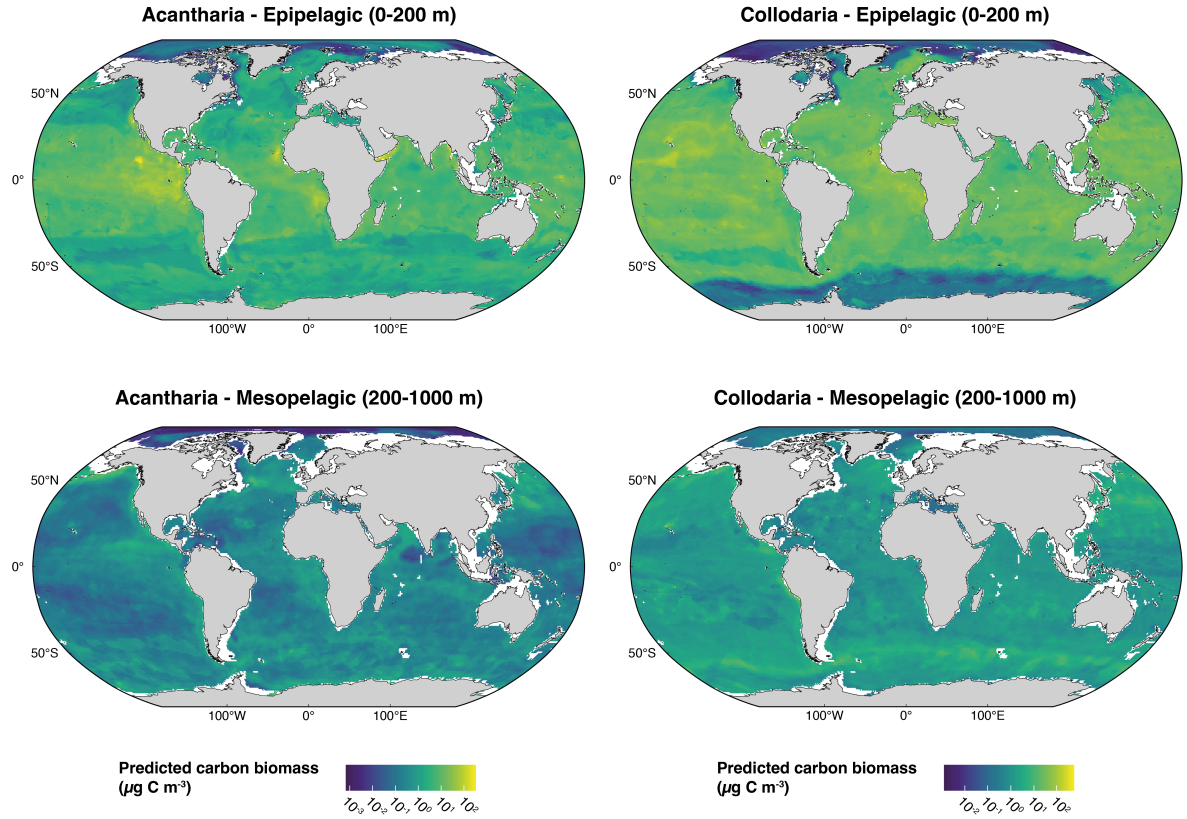

Figure Ext. 3.3: Maps of the predicted average 1° × 1° carbon concentration in the epipelagic layer (0-200 m) and in the mesopelagic layer (200-1,000 m) for Acantharia and Collodaria.

Table Ext. 3.3: Results of the models for biogenic silica (bSi) biomass and production as well as carbon (C) demand for all Phaeodaria. Stars (*) indicate significant R^2 obtained with Pearson's correlation tests (p-value <0.05) using random and spatial cross-validation (CV).

Layer	Measure	R^2 (random CV)	R^2 (spatial CV)	Total value
Epipelagic	bSi biomass	33.3*	0.12	0.33 Tg Si
	bSi production	34.0*	0.02	0.70 Tg Si y^{-1}
Mesopelagic	C demand	38.2*	10.7*	0.46 Pg C y^{-1}
	bSi biomass	32.3*	9.5*	3.91 Tg Si
	bSi production	40.6*	7.4*	3.96 Tg Si y^{-1}

Table Ext. 3.4: Global and regional carbon demand of large mesopelagic Phaeodaria.

Area	Total C demand (Pg C y^{-1})	Mean integrated demand (mg C m^{-2} d^{-1})
World	0.46	3.9 ± 3.4
Arctic	0.003	1.2 ± 0.2
Subarctic Atlantic	0.006	2.0 ± 1.2
Subarctic Pacific	0.037	13.0 ± 6.5
North Atlantic	0.026	2.9 ± 2.5
North Pacific	0.055	4.0 ± 4.7
Tropical and upwelling Atlantic	0.030	6.1 ± 3.4
Tropical and upwelling Pacific	0.073	4.1 ± 3.3
South Atlantic	0.015	2.2 ± 1.7
South Pacific	0.035	2.4 ± 2.1
Indian Ocean	0.040	2.6 ± 1.4
Southern Ocean	0.145	5.2 ± 1.9

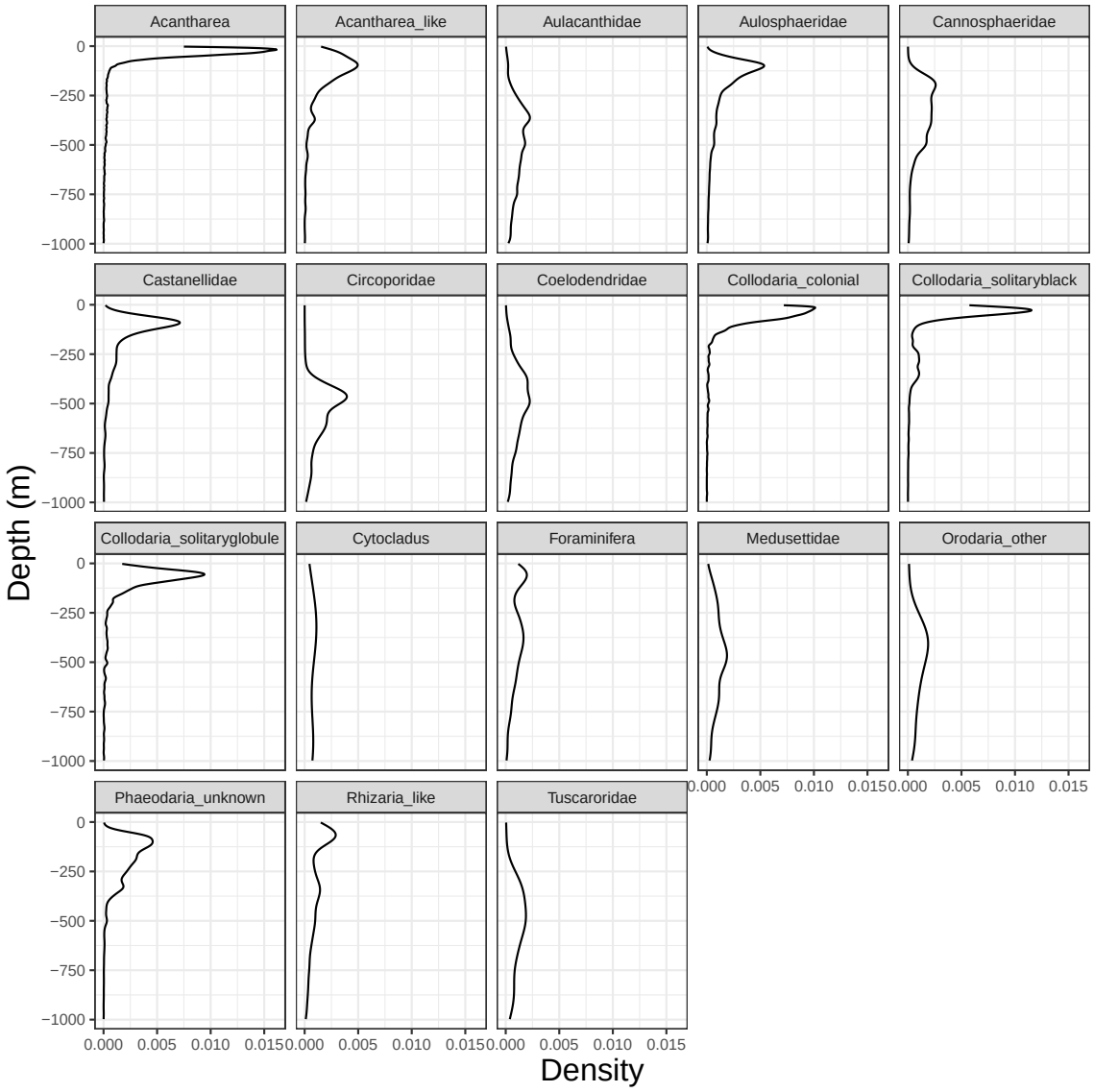

Figure Ext. 3.4: Distribution of sampled Rhizaria specimens according to depth, for each taxon considered.

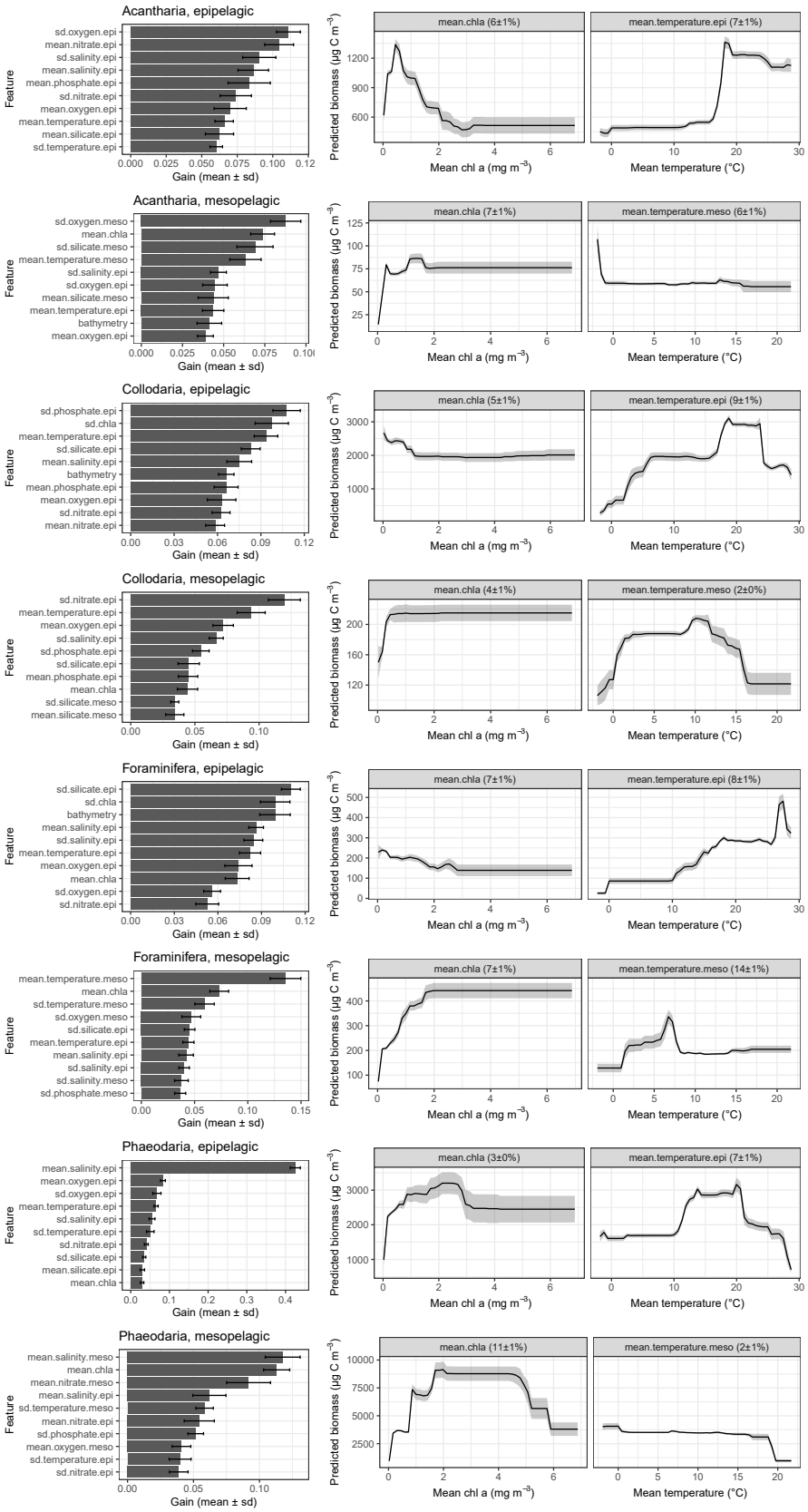

Figure Ext. 3.5: (Caption next page.)

Figure Ext. 3.5: (Previous page.) Order of importance of the 10 most important variables in the models for the epipelagic (0-200 m) and mesopelagic (200-1,000 m) layers for main Rhizaria groups (left). Partial dependence plots of the mean chlorophyll a concentration and mean temperature are shown on the right.

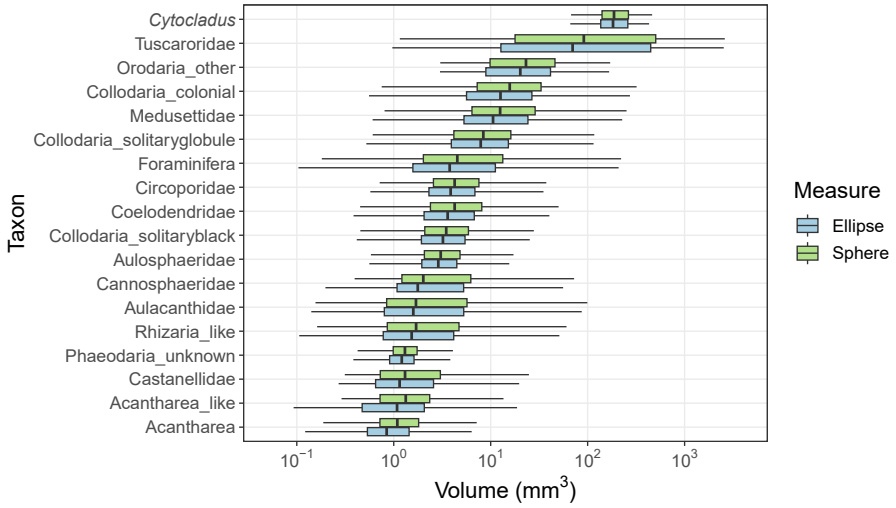

Figure Ext. 3.6: Volume distributions for each Rhizaria taxa considered when using the ellipse (blue) or sphere (green) method. Boxes' bottom and top boundaries represent the 25th and 75th percentiles. Lower whiskers stretch from the 25th percentile to the minimum value within 1.5 times the 25th percentile's inter-quartile range (IQR). Upper whiskers extend from the 75th percentile to the maximum value within 1.5 times the 75th percentile's IQR.

3.1.5 Supplementary Information

Supplementary table S1

Table S3.1: Cruise information, number of profiles in each layer and presence/absence in previous studies (Biard et al., 2016; Drago et al., 2022).

Sampling cruise name	Year	Chief scientists	Regions	Profiles 0 – 200 m	Profiles 200 – 1000 m	Biard et al. (2016)	Drago et al. (2022)
BOUM	2008	T. Moutin	Mediterranean Sea	159	29	Yes	Yes
CCELTER		M. Landry	California Upwelling	74	11	Yes	Yes
OPEREX		Z. Kolber	Northern Pacific	73	7	–	Yes

MALI	2009	M. Babin	Arctic	106	12	Yes	Yes
Tara Oceans		Tara Ocean Cons.	Mediterranean Sea	35	12	Yes	Yes
LOHAFEX		V. Smetacek	Southern Atlantic	56	24	Yes	Yes
Tara Oceans	2010	Tara Ocean Cons.	Indian Ocean, Southern Atlantic	158	51	Yes	Yes
CCELTER	2011	M. Landry	California Upwelling	56	2	–	Yes
Tara Oceans		Tara Ocean Cons.	Pacific Ocean	218	58	Yes	Yes
KEOPS II		B. Queguiner	Southern Ocean	12	–	Yes	Yes
CCELTER	2012	M. Landry	California Upwelling	60	2	–	Yes
Tara Oceans		Tara Ocean Cons.	Northern Atlantic	103	34	Yes	Yes
MSM22		P. Brandt	Equatorial Atlantic	106	80	Yes	Yes
MSM23		M. Visbeck	.	64	64	Yes	Yes
AN1304	2013	M-H. Forget	Arctic	12	–	–	Yes
Tara Oceans		Tara Ocean Cons.	.	116	21	Yes	Yes
DEWEX		P. Testor, P. Conan	Mediterranean Sea	13	12	–	Yes
MOOSE-GE		MOOSE Network	.	4	–	–	Yes
M92		S. Sommer	Peru Upwelling	16	5	–	Yes
M93		G. Lavik	.	84	31	–	Yes
M96		J. Karstensen	Equatorial Atlantic	77	56	Yes	Yes
M97		T. Tanhua	.	168	110	–	–
AN1405	2014	M-H. Forget	Arctic	27	1	–	Yes
MSM40		J. Karstensen	.	5	5	–	Yes
CCELTER		M. Landry	California Upwelling	57	7	–	Yes
M107		S. Sommer	Canary Upwelling	45	12	–	Yes
MOOSE-GE		MOOSE Network	Mediterranean Sea	4	4	–	Yes
SOMBA		L. Mortier, N. Ait Ameur, V. Taillandier	.	7	6	–	Yes
M108		R. Lampitt	Northern Atlantic	11	3	–	Yes
SARGASSO		P. Munk	.	82	–	–	Yes
M105		T. Tanhua	Equatorial Atlantic	6	4	–	Yes
PS88b		J. Hahn	.	39	39	–	Yes
M106		P. Brandt	Southern Atlantic	107	98	–	Yes
GREENEDGE IceCamp	2015	M. Babin	Arctic	29	–	–	Yes
M120		M. Dengler	Benguela Upwelling	1	–	–	–
M121		M. Frank	.	60	29	–	Yes
DY032		F. Carlotti	Mediterranean Sea	15	14	–	Yes
MOOSE-GE		MOOSE Network	.	5	4	–	Yes
CASSIOPEE		F. Marin, S. Cravatte	Eastern Pacific	13	11	–	Yes
OUTPACE		T. Moutin, S. Bonnet	.	188	18	–	Yes
P16N		J. Cross	Pacific Ocean	186	177	–	Yes
M116		M. Visbeck	Equatorial Atlantic	82	81	–	Yes
M119		P. Brandt	.	49	47	–	–
GREENEDGE	2016	M. Babin	Arctic	161	43	–	Yes
PS99		A. Rogge, A. Waite	.	19	15	–	–

CCELTER		M. Landry	California Upwelling	52	3	–	Yes
M131		P. Brandt	Benguela Upwelling	18	5	–	–
AMES II		L. Karp-Boss, E. Boss	Northern Atlantic	42	14	–	Yes
M130		M. Dengler	Equatorial Atlantic	111	95	–	–
CCELTER	2017	M. Ohman	California Upwelling	72	3	–	Yes
FLUXES I		J. Aristegui	Canary Upwelling	66	37	–	Yes
FLUXES II		J. Aristegui	.	49	47	–	–
M135		T. Tanhua	Peru Upwelling	133	108	–	Yes
M138		H. Bange	.	32	–	–	Yes
MSM60		A. Rogge, A. Waite	Southern Atlantic	123	118	–	Yes
ARCTIC	2018	A. Rogge	Arctic	107	58	–	–
IPS		M. Babin	.	7	4	–	Yes
EXPORTS		L. Karp-Boss, E. Boss	Northern Pacific	75	35	–	–
EXPORTS		A. McDonnell	.	107	105	–	–
SR1812		A. Macdonald	Southern Ocean	131	12	–	–
CCELTER	2019	M. Ohman	California Upwelling	31	28	–	Yes
CurtinUni IIOE		D. Antoine	Indian Ocean	51	26	–	–
PS124	2021	A. Rogge, M. Holtappels	Southern Ocean	77	22	–	–
Total				**4,252**	**1,959**		

3.2 Discussion

This section summarizes and discusses chapters 2 and 3.1.

3.2.1 Summary and discussion of key findings

Planktonic Rhizaria, large protists with a unique physiology

The results presented herein showed that most Rhizaria have a low carbon density, as evidenced through direct measurements of carbon content in live cells (chapter 2). With the exception of smallest taxa (<300 μm), planktonic Rhizaria have significantly lower carbon content relative to their size compared to other protists (Menden-Deuer and Lessard, 2000), aligning with prior estimates on a single Phaeodaria family (Stukel et al., 2018). As previously assumed, this low carbon density may be an adaptation to their large size (Stukel et al., 2018). Indeed, while their size and trophic role is comparable to that of metazoan zooplankton, these organisms are non-motile and do not actively hunt (Biard, 2022b). By having

a low cellular carbon density, they can thereby minimize their carbon requirements, while their large size increases their feeding efficiency, in particular in low-food environments. Likewise, we can hypothesize that the presence of a skeleton or a colonial form (for naked Collodaria, for which cells are embedded in a gelatinous matrix) is a means of maintaining their gelatinous structure. This lifestyle allows them to grow in multiple oceanic conditions, and particularly in low-food environments (Fig. 3.3).

Mixotrophic Rhizaria and the carbon cycle

Large mixotrophic Rhizaria (i.e., Acantharia, Collodaria and Foraminifera) are globally abundant, particularly at low and mid latitudes. Their distribution spans both productive and oligotrophic areas in both the epipelagic and mesopelagic layers (Fig. Ext. 3.2, Ext. 3.3). This widespread distribution was previously reported using different methodologies, through high-throughput sequencing of gene markers (Vargas et al., 2015) and a compilation of field data (Leles et al., 2017). Although the extent to which mixotrophic Rhizaria utilize phototrophy or heterotrophy remains unclear (Suzuki and Not, 2015; Biard, 2022a), these organisms use both photosymbiosis and consumption of other planktonic organisms to meet their carbon needs. They create microenvironments of concentrated primary production (Caron et al., 1995), enabled both because of the high density of photosymbionts within the host cytoplasm and the increased volume of the photosynthetic apparatus of the microalgae (Stoecker et al., 2017; Decelle et al., 2021).

Consequently, mixotrophic Rhizaria thrive particularly in the surface layer of oligotrophic waters characterized by low temperature variability (Fig. Ext. 3.3), as already reported by global (Dennett et al., 2002; Biard et al., 2016; Leles et al., 2017; Faure et al., 2019) and local studies (e.g., they contribute on average to 20-25% of total zooplankton abundance in the Indian Ocean; Davies et al., 2022). In chapter 2, although the abundance of the Nassellaria genus *Phlebarachnium* sp. (Fig. 2.2) collected in the California Current Ecosystem was not quantified, this taxon was prominent in net samples obtained from offshore locations (Fig. 2.1) while being absent in more productive coastal waters. Mixotrophic Rhizaria are non-constitutive mixotrophs, i.e., they acquire their phototrophic capacity by ingesting microalgae (Mitra et al., 2016). Among this type of mixotrophs, Rhizaria, as endosymbiotic specialists (i.e., they ingest a specific microalgae for phototrophy; Mitra et al., 2016), display distinct spatial patterns compared to

generalists (e.g., mixotrophic oligotrich ciliates) and plastidic specialists (e.g., *Mesodinium* sp.). Indeed, the contribution of the latter groups to the mixotrophic community increases towards more productive system (Leles et al., 2017). The ability of rhizarians to host numerous symbionts may explain the prevalence of such large cells in oligotrophic environments (Faure et al., 2019).

The significance of mixotrophic Rhizaria in pelagic food webs is more related to their biovolume and their overall abundance rather than to their biomass. Indeed, while their contribution to total primary production is only a few percent (Biard et al., 2016; Caron et al., 1995), their contribution in the large plankton size classes, directly available to mid-trophic levels, increases drastically (Caron et al., 1995; Stoecker et al., 2017). Mixotrophic Rhizaria are major grazers of picoplankton, dominating primary production in oligotrophic environments (Platt et al., 1983) and not available to most crustacean zooplankton. By shortcutting trophic webs, they play a crucial role in shaping the trophic structure of subtropical oligotrophic ecosystems (Decelle et al., 2015; Mitra et al., 2016). Despite both groups being widespread in the epipelagic layer (0-200 m), Collodaria were predominantly found in oligotrophic areas, while Acantharia were more associated with productive regions like upwelling zones (Fig. Ext. 3.3), as previously reported (Decelle et al., 2013; Faure et al., 2019). These differences can be explained by distinct life strategies.

The predominance of Acantharia in more productive areas can be attributed to the presence of non-mixotrophic, cyst-forming species. Indeed, cysts formed by these Acantharia can sink to bathypelagic depths, where they release 2-3 μm swarmers (Hollande et al., 1965; Decelle et al., 2012). Subsequently, juvenile Acantharia ascend to the surface and can be observed throughout the water column (Mars Brisbin et al., 2020). Cyst sinking events are thought to be triggered by high productivity associated to phytoplankton blooms. Cysts rapidly sink to the deep ocean so that juveniles can feed on the large amount of organic matter sinking from the surface (Martin et al., 2010). Cyst-forming Acantharian have been reported across a range of latitudes, with certain clades likely being endemic to deep waters (Decelle et al., 2013), accounting for the widespread distribution of Acantharia in both the epipelagic and mesopelagic layers (Fig. Ext. 3.3). However, in high latitudes, cyst-forming species may dominate, and important peak fluxes of acantharian cysts have been observed in the Icelandic Basin (Martin et al., 2010), in the North Pacific (Mars Brisbin et al., 2020) and in the Southern Ocean during austral summer (Spindler and Beyer, 1990). In these regions, they can constitute a

significant proportion to total carbon fluxes. This aligns with the observed decline of the proportion of mixotrophic rhizarians at high latitudes (Biard et al., 2016). However, we cannot distinguish mixotrophic from heterotrophic Acantharia in UVP5 images, their respective distributions could thereby not be resolved in chapter 3.1.

In contrast, Collodaria can take advantage of their colonial form to accumulate larger amounts of food and nutrients within their gelatinous extracellular matrix. While Collodaria do not form cysts (Suzuki and Not, 2015), some clades may still be endemic to the mesopelagic. Colonial Collodaria belonging to the family Collophidiidae have been reported at significant depths (e.g., Trégouboff, 1956), and their presence is also supported by DNA sequences (Not et al., 2007; Pernice et al., 2015). Biard (2015) suggested that these colonial Collodaria occupy a distinct ecological niche, possibly lacking symbionts. Interestingly, our models reveal a significant presence of Collodaria in the mesopelagic layer of the Southern Ocean, while their occurrence in the epipelagic layer remains relatively low (Fig. Ext. 3.3). This indicates that these organisms are likely exclusive inhabitants of the deep sea. Collodaria can serve as important prey for bathylagid fishes (Clarke et al., 2020), potentially playing a significant role in deep food webs.

Heterotrophic rhizarians, gatekeepers of particle flux worldwide

In chapter 3.1, we showed that >600 μm Phaeodaria, despite representing a low proportion of the total zooplankton carbon biomass, can account for 3.8 to 9.2% of gravitational carbon export (i.e., its transport out of the euphotic zone) attenuation through flux-feeding. This is about the same order of magnitude as local estimates in the California Current Ecosystem (Stukel et al., 2019). Large Phaeodaria mostly inhabit the upper mesopelagic zone, where sinking particles are abundant (Stukel et al., 2019; Biard and Ohman, 2020; Fig. Ext. 3.4). Contrasting with other zooplankton taxa, they consume fast-sinking particles rather than suspended ones (Gowing, 1986; Gowing, 1989; Stukel et al., 2019), thereby ingesting the particles most likely to transfer carbon to the deep ocean (De La Rocha and Passow, 2007). However, considering their vertical distribution patterns (Fig. Ext. 3.4), their activity also occurs in the lower epipelagic regions, which was not included in our demand calculations. For example, Aulosphaeridae have peak abundances between 100 and 200 m in the California Current Ecosystem (Zasko and Rusanov, 2005; Biard et al., 2018). Similarly, the family Castanellidae shows highest abundance between 50 and 100 m in the Eastern Pacific (Zasko

and Rusanov, 2005). Therefore, they may contribute substantially to primary production recycling in the epipelagic layer.

We showed that large Phaeodaria are mainly distributed in regions of high primary productivity, such as high latitudes and upwelling zones where they can feed upon fast-sinking articles (chapter 3.1). Indeed, oligotrophic regions are primarily characterized by small and non-biomineral-forming phytoplankton (e.g., Goericke et al., 2000; Guidi et al., 2016) and gravitational export primarily comprises small and slow-sinking particles (e.g., Richardson and Jackson, 2007). Moreover, the reduced seasonality observed in these regions means that there are no significant spring or summer pulses of export (Lampitt and Antia, 1997; Cavan et al., 2019). In upwelling areas, Phaeodaria are favored by oxygen minimum zones compared to other zooplankton taxa (Hoving et al., 2020). This is likely due to reduced metabolic rates or alternative undefined metabolism (e.g., nitrogen respiration has been observed among benthic Foraminifera and the rhizarian genus *Gromia*; Piña-Ochoa et al., 2010). Unexpectedly, we found that the impact of large flux-feeding Phaeodaria is particularly pronounced in the Southern Ocean, although previous studies reported a decline in their abundance, given the lack of data in this region (Biard et al., 2016). More investigation about their seasonal patterns and relationships with bloom events in this region is needed to refine our results. Preliminary observations from year-long UVP6 mooring data from the seasonally ice covered central Weddell Sea at 250 m showed a constant phaeodarian pool over the year (Andreas Rogge pers. comm.). Together with small Phaeodaria and Polycystinea, which were not included in our models, they could play a significant role in attenuation processes.

Although Phaeodaria are known to consume food sinking from the surface, limited information exists about their interaction with it. Small phaeodarians were observed to collect food by stretching a protoplasmic web composed of fine pseudopods and by repeatedly expanding and retracting pseudopodium-like tentacles to bring it to the cell (Nakamura et al., 2018b; Dolan and Coppola, 2023). However, this protoplasmic web surrounding the cell is more likely related to prey capture (Dolan and Coppola, 2023) and has not been observed among all Phaeodaria. The precise mechanisms by which large phaeodarians capture and ingest their food are not yet fully understood. Even less is known about how they do process ingested matter. Food is digested within digestive vacuoles, and waste is stored in the phaeodium, but the efficiency of energy transfer is still unknown (Nakamura and Suzuki, 2015). Furthermore, in chapter 3.1, we focused solely on

the carbon demand of large Phaeodaria, but not on their respiration, as recommended by Legendre and Rivkin (2008). Thus, including these values in carbon budgets should be done with caution, as ingested carbon can be recycled within mesopelagic food webs multiple times. However, respiration rates of Phaeodaria are unknown yet, and there is limited information regarding predation upon them. To gain a better understanding of their contribution to flux attenuation, an assessment of the carbon they actually respire is needed. Ultimately, some phaeodarians can contribute to carbon fluxes by evacuating waste through the production of mini-pellets (Gowing and Silver, 1985).

Important fluxes of phaeodarian mini-pellets have been reported at various locations (Gowing and Silver, 1985; Gowing, 1986; Riemann, 1989; Gonzalez, 1992; Lampitt et al., 2009). Particularly, these mini-pellets can make up the majority of carbon fluxes by small particles (Durkin et al., 2021; Leblanc et al., 2021). However, our understanding of their specific impact on carbon fluxes remains limited, and the lability of these mini-pellets, which influences their remineralization rate, remains largely unexplored. As phaeodarians are detritivores, their mini-pellets might show greater resistance to remineralization (Cavan et al., 2019). Little attenuation with depth has been observed (Durkin et al., 2021), although this could vary locally depending on their food sources. The relative impact of mini-pellets fluxes, along with phaeodarian bodies and aggregated material, in comparison with what they can remineralize needs to be addressed to shed light on the role of Phaeodaria in both modern and future oceans.

Siliceous Rhizaria in the silicon cycle

In chapter 3.1, we quantified for the first time the global mesopelagic biogenic Si production rates of large Phaeodaria. We showed that biogenic Si is actively produced in the mesopelagic layer, a zone previously considered to lack biogenic Si production (Tréguer et al., 2021), and not limited solely to the surface waters dominated by diatoms and the seafloor dominated by sponges. Siliceous Rhizaria are the most silicified pelagic organisms and exhibit important productivity at cell level (Llopis-Monferrer et al., 2020). Living in the mesopelagic layer, they could enhance the transport of silica to greater depths, particularly when incorporated into organic aggregates (Ikenoue et al., 2019). However, we can suggest a diverging role between silica-dense rhizarians, including radiolarians and phaeodarians from the family Castanellidae (Biard et al., 2018), and most phaeodarians that possess delicate and fragile skeletons. Radiolarian skeletons are abundant in ma-

rine sediments, contributing to the formation of oozes, especially in the southern ocean (Dutkiewicz et al., 2015). Radiolarian oozes participate in silica burial flux, removing silica from the marine silica cycle together with sponges and diatoms (Maldonado et al., 2019). In contrast, Phaeodaria are rarely found in sediments (Takahashi et al., 1983), which means they are not buried. This can be attributed to their porous skeleton, which is more susceptible to dissolution. Consequently, phaeodarians contribute instead to silica recycling throughout the water column down to the seafloor, enhancing the continuous circulation of silica. This role may diverge between high-latitude and low-latitude populations. Indeed, silica is often limiting in low-latitude waters, whereas the Southern Ocean exhibits the highest silica concentrations of the world ocean, although the effects of environmental conditions on rhizarian silicification process remains poorly understood. However, because of increased stratification and decreased silica supply during the Cenozoic era, low-latitude radiolarians experienced a decreasing silicification and skeleton weight (Lazarus et al., 2009). With the expected increase in water column stratification in future oceans, we can anticipate that rhizarian populations will be affected by it.

Planktonic Rhizaria in changing oceans

Chapter 3.1 briefly discussed the possible evolution of the distribution of planktonic Rhizaria with global climate-induced changes. Among these changes, sea surface warming, ocean acidification, increased stratification, and reduced nutrient supply to the upper ocean will favor certain taxa over others, impacting the structure of zooplankton communities (Richardson, 2008). Three responses of zooplankton to ocean warming have been identified (summarized in Ratnarajah et al., 2023): shifts in geographical ranges (typically polewards; e.g., Beaugrand et al., 2002), in phenological timing (Edwards and Richardson, 2004; Mackas et al., 2012) and towards smaller sizes (Daufresne et al., 2009). While the responses of major zooplanktonic groups, such as crustaceans, have been explored, research on Rhizaria remains relatively limited.

In chapter 3.1, we hypothesized that mixotrophic species may maintain a stable habitat range or even expand their geographic range, as observed for some Foraminifera (Langer et al., 2013). Indeed, Collodaria appear to be favored by increased temperatures (Fig. Ext. 3.3), although there may be a temperature threshold above which their symbiont respiration stops (Villar et al., 2018). More generally, mixotrophy could be advantageous under conditions of increased strat-

ification or temperature and diminished resources (Stoecker et al., 2017). In particular, oligotrophic-dwelling Collodaria could benefit from these changes and potentially increase in abundance. However, since mixotrophic taxa are confined to the surface ocean, their distribution may shift polewards to align with their optimal water temperature, and not towards depths. Since the pre-industrial stage, planktonic Foraminifera assemblages have been observed to shift polewards because of warming (Jonkers et al., 2019). Nevertheless, the rate of this possible expansion is unknown, as observed shifts in plankton ranges do not always follow the rate of isotherm movement (Chivers et al., 2017). In addition, the evolution of the habitat ranges of heterotrophic Rhizaria (non-mixotrophic Radiolaria and Phaeodaria) remains uncertain. In chapter 3.1 we proposed the hypothesis that the abundance of these organisms could decrease in equatorial waters but increase in the Southern Ocean. However, high-latitude regions are at risk of severe impacts from global warming, with projected sea surface temperature increases up to 10°C in the Southern Ocean within the next 300 years (Moore et al., 2018). Cold-adapted species face a greater risk of extinction due to their limited possibility to migrate and to track disappearing cold habitats (Trubovitz et al., 2020). Moreover, these organisms are unlikely to adapt to such rapid environmental changes. Phaeodaria from lower latitudes might replace the current high-latitude species. In contrast, cold-adapted phaeodarians might migrate deeper, although this would imply reduced food availability. Yet, they could still benefit from the projected increase in carbon export at higher latitudes (Henson et al., 2022). We can expect the extinction of a significant number of cold-adapted species in the next several hundred years with unknown consequences for ecosystem functioning (Trubovitz et al., 2020). In warmer waters, while some species may migrate polewards, increased stratification and decreased primary productivity may be responsible for declines in heterotrophic rhizarian populations. Indeed, declines in phaeodarian fluxes have already been observed during El Nino events, characterized by warmer waters and reduced nutrient supplies (Takahashi, 1997; Biard et al., 2018). Unlike mobile species that can adapt their spatial distribution to a certain degree, the limited mobility of Rhizaria makes them more vulnerable to environmental changes (Ratnarajah et al., 2023).

Instead of undergoing shifts in geographical ranges, rhizarian species may show phenological responses to global changes, adjusting their seasonal timing of maximal abundance. However, our models only presented predictions based on yearly averaged environmental variables and biomass values, and UVP data are yet

too scarce to infer seasonal patterns (see section 3.1.3). Our current understanding of temporality of planktonic Rhizaria remains limited. Seasonal cycling has been observed in high latitudes for small phaeodarians, such as in the Bering Sea (Ikenoue et al., 2012), as well as in the equatorial eastern Atlantic (Boltovskoy et al., 1993) and the eastern North Pacific (Takahashi, 1987). Seasonality varies among radiolarian species (see Suzuki and Not (2015) and references therein). In high latitudes, many species show no seasonal patterns despite marked seasonal cycles in environmental variables, instead being influenced by large-scale climate indices such as the Arctic Oscillation (Ikenoue et al., 2012). High-latitude rhizarians may be influenced by the availability of food. Consequently, they may respond to changes in prey phenological shifts, but responses to feeding opportunities vary among taxa (Takahashi, 1997).

A shift in size represents another response to climate warming (Daufresne et al., 2009). Potential changes in size for planktonic Rhizaria may result from various environmental factors, such as changes in water temperature, food and nutrient availability or prey size. Warmer waters can indeed affect the metabolic rates of Rhizaria, while reduced nutrient supply can limit their availability for these organisms. Such conditions could therefore lead to a shift in the size distribution of Rhizaria populations, favoring either smaller individuals, while the overall community composition remains unchanged, or smaller-sized taxa. This shift in size distribution could have implications for feeding interactions, in particular regarding the capture rate of prey or sinking particles. If smaller-sized Rhizaria become more dominant, it could result in an increased abundance of smaller consumers, potentially impacting higher trophic levels. Furthermore, as shown for copepods (Beaugrand et al., 2010), a shift towards small Rhizaria could increase the residence time of both their bodies and mini-pellets in the upper water column, diminishing their ability to export carbon to depths. However, such a shift towards smaller sizes has not been observed with increased stratification at low-latitudes during the Cenozoic era (Lazarus et al., 2009). The intricacies of factors make it difficult to predict the response of modern rhizarian populations. Furthermore, a shift towards larger species has been observed for copepods in the Southern Ocean (Takahashi and Hosie, 2020). If antarctic phaeodarians migrate deeper as suggested above, their size could increase as well (gigantism of the deep; McClain et al., 2006). For accurate predictions on the evolution of Rhizaria in response to global changes, further research is needed to better understand rhizarian ecology and their responses to environmental fluctuations.

3.2.2 Perspectives

Investigating local and temporal variability

While imaging techniques have significantly advanced our understanding of the role of rhizarians in ocean biogeochemistry (e.g., Biard et al., 2016; Stukel et al., 2018; Chapter 3.1), much is still to be done to improve model predictions. To do so, conducting smaller-scale studies in key areas is needed to refine spatial patterns and validate model predictions against observations. Such studies are yet limited to a few locations (e.g., the California Current Ecosystem; Biard et al., 2018; Stukel et al., 2018). Furthermore, investigating the temporal variability through long-term monitoring (e.g., by using UVP6 mounted on long-term moorings) will provide insights into the role of rhizarians in pelagic ecosystems and their responses to environmental changes, besides enabling to track changes in environmental conditions. Indeed, radiolarians have already proven to be valuable proxies for paleo-environmental reconstruction (De Wever et al., 2002). Refining the relationship between rhizarian communities and environmental variables will allow to improve the accuracy of both past and contemporary models and to more effectively assess their response to climate change. In addition, while some areas are well-sampled, others still lack good coverage with the UVP, such as the Southern Ocean and the Indian Ocean. I participated in a cruise in the latter, for which one of the purposes was to add data from this area to the global dataset. However, the loss of the CTD rosette with the UVP5 attached prevented data collection.

Quantifying the role of rhizarians in fluxes

A few studies showed a correlation between carbon export and the presence of Collodaria (Guidi et al., 2016; Gutierrez-Rodriguez et al., 2018), although the nature of this relationship remains unclear. Only a limited number of studies quantified the role of Rhizaria in silica and carbon fluxes (e.g., Biard et al., 2018; Ikenoue et al., 2019). Utilizing species distribution models, as undertaken in chapter 3.1, could enable the estimation of global carbon and silica fluxes, similar to recent work carried out by Knecht et al. (2023) for calcifiers (pteropods and foraminifera). However, this approach requires the refinement of parameters such as turnover times, sinking speeds, and growth rates. Additionally, our understanding of the role of their minipellets remains limited. To address this gap, it is crucial to investigate the composition and sinking speed of mini-pellets

across different geographic locations and determine the amount of carbon they can transfer through the mesopelagic layer. Still, studying the production of mini-pellets by Phaeodaria is challenged by the difficulty to culture and maintain rhizarians alive. They need to be collected in situ and could subsequently be linked to phaeodarian abundance to estimate pellet production. Studies investigating the contribution to fluxes have predominantly focused on a few specific taxa, highlighting the need to encompass the entire rhizarian community in flux assessments.

Including the whole rhizarian community

Model results presented in chapter 3.1 solely focused on Rhizaria larger than 600 μm. However, Rhizaria encompass numerous taxa smaller than 600 μm. To study these smaller taxa, alternative imaging devices like the ZooScan (Gorsky et al., 2010) and the FlowCAM can be used (Llopis Monferrer et al., 2022). Still, none of these tools provide in situ acquisition, therefore relying on net collection, which may potentially damage the delicate cells. Complementary imaging tools are necessary to accurately model the distribution of small rhizarians. Additionally, a paired approach involving DNA-metabarcoding and imaging tools can be employed to further enhance our understanding of the composition and distribution of the rhizarian community (Mars Brisbin et al., 2020; Llopis Monferrer et al., 2022). However, although small rhizarians are much more abundant than large ones, their contribution to elemental stocks can decrease significantly (Llopis Monferrer et al., 2022). Still, by likely having smaller turnover times, their contribution to element cycling may become more important and needs to be further investigated.

CHAPTER 4

In situ sinking speed of marine particles

"When I think of the floor of the deep sea, [...] I see always the steady, unremitting, downward drift of materials from above, flake upon flake, layer upon layer - a drift that has continued for hundreds of millions of years, that will go on as long as there are seas and continents.
For the sediments are the materials of the most stupendous snowfall the earth has ever seen."

R. Carson, *The Sea Around Us*

Contents

4.1 *VisuTrap*: a new method to measure in situ sinking velocity of marine particles from high throughput imaging data

Laget, M., M. Picheral, C. Catalano, L. Guidi, and T. Biard
This work is under review in *Limnology and Oceanography: Methods*.

4.1.1 Abstract

Particles sinking from the surface to the deep ocean play a key role in the biological carbon pump, whose efficiency depends on particle concentrations and sinking velocities. Over the last decade, in situ imaging has enabled critical advances in the quantification of vertical carbon fluxes. Yet, in situ velocity measurements are scarce and often inferred only from the bulk population of particles. Here, we introduce the VisuTrap, a new tool to measure in situ velocities of large marine particles. It consists of an Underwater Vision Profiler 6 (UVP6) camera inserted in a cylindro-conical sediment trap that isolates a volume of water. Continuous high frequency (1.3 Hz) image acquisition during 2-5-day quasi-Lagrangian deployments enables reconstruction of particle tracks and estimation of their in situ velocities. We detail the configuration and special UVP6 settings for this application, as well as the image processing and track analysis pipeline. Then, we present results from 2-day quasi-Lagrangian experiments at 2 sites in the Mediterranean Sea to illustrate the VisuTrap's use as a new approach to understand the dynamical behavior of marine particles in situ. Given the extensive UVP datasets available worldwide, the VisuTrap, by providing in situ velocity data, offers the possibility to refine carbon flux estimates at a global scale.

4.1.2 Introduction

Through the biological carbon pump (BCP), the ocean regulates atmospheric CO_2 concentrations (Volk and Hoffert, 1985). It exports about 5-20 Gt C each year out of the surface ocean (Laws et al., 2000; Dunne et al., 2005; Henson et al., 2011), of which about 0.2-0.5 Gt C is sequestered from the atmosphere for millennia (Guidi et al., 2015). The BCP includes several pathways of downward carbon transport, such as the gravitational settling of particles, mostly via fecal pellets and

marine snow aggregates, the advection and diffusion of dissolved and particulate organic carbon (POC) and the active transport by vertically-migrating organisms (Steinberg et al., 2000; Omand et al., 2015; Stukel et al., 2023). Among these, gravitational sinking has a crucial role in carbon export (Boyd et al., 2019; Nowicki et al., 2022; Stukel et al., 2023) and is associated with a longer remineralization length scale (Stukel et al., 2017), a process that oxidizes organic matter back into CO^2. Therefore, gravitational sinking has a higher potential to sequester carbon at great depths. It is of the utmost importance to accurately constrain the amount of carbon exported by this pathway, as it varies in time and space (Henson et al., 2012).

Nondestructive in situ imaging methods are a powerful tool to size and image marine particles and are nowadays routinely used to survey the distribution of particles and plankton with a fine spatial and temporal coverage (e.g., Stemmann et al., 2008). Among all imaging techniques currently available (Lombard et al., 2019), the Underwater Vision Profiler (UVP), in its versions 5 (Picheral et al., 2010) and 6 (Picheral et al., 2022), have permitted many coherent datasets of particle standing stocks to be acquired from intercalibrated instruments. Assuming a relationship between size and sinking velocity, these standing stocks have been used to derive particle size-based POC flux estimates (Guidi et al., 2008; Ramondenc et al., 2016). Indeed, UVP cameras provide a high sampling resolution, both vertically and horizontally. Thus, developing a methodology taking into account these data in reliable flux assessments is necessary. However, the relationship between size and sinking velocity assumed by UVP-based methods to infer POC fluxes is not straightforward, and important regional differences have been observed (Iversen and Ploug, 2010; Fender et al., 2019). Such discrepancies can be related to differences in particle type (i.e., the proportion of marine snow aggregates versus fecal pellets) or age, non-steady state particle distributions, and ultimately in situ sinking behavior.

As particle sinking velocities play an overall crucial role in the amount of POC sinking to the intermediate and deep ocean, they must be quantified adequately in order to provide accurate biogeochemical flux estimates (De La Rocha and Passow, 2007). By determining the exposure time of particles to the action of metazoans and microbes, sinking velocity impacts the depth of flux attenuation and therefore atmospheric CO2 concentrations (Kwon et al., 2009). The intricate effects of various factors such as size, morphology (McNown and Malaika, 1950; Engel et al., 2009) and composition, including the presence of mineral ballast

(Armstrong et al., 2001; Klaas and Archer, 2002) or transparent exo-polymers (Engel and Schartau, 1999), cast a shadow on the simple size-dependency of settling velocities. In addition, the properties of the ambient water the particles are sinking through also influence sinking velocities by altering the density differences with particles. Thus, as physical and biological variables (e.g., temperature, nature of sinking material because of changes in planktonic communities) are evolving with global warming, the settling velocity of the global pool of particles is expected to change simultaneously, but the direction of this change is difficult to predict (Taucher et al., 2014; Henson et al., 2022). Furthermore, particles undergo several biological and physical processes through their sinking that reshape them, such as consumption and fragmentation by zooplankton (Iversen and Poulsen, 2007), microbial activity (Arístegui et al., 2009) and physical aggregation (Burd and Jackson, 2009) or disaggregation (Alldredge et al., 1990). Consequently, it has been suggested that the bulk particle settling velocity increases with depth (Berelson, 2001), hypothetically because smaller and less compact particles would be remineralized preferentially, highlighting the need to accurately constrain sinking velocities.

Stokes' law (Stokes, 1851), giving the theoretical sinking velocity of a sphere in a fluid at low Reynolds number, is commonly used to model the sinking velocity of marine particles (Omand et al., 2020), as well as values derived from the particle size distribution (Guidi et al., 2008). However, measurements of sinking velocities range over several orders of magnitude, from a few meters to thousands of meters per day (e.g., Turner, 2002; Trull et al., 2008), and Stokes' law and size based-models alone are not sufficient to explain such variability (McDonnell and Buesseler, 2010). Adequate representation of the fractal and porous nature of marine particles can better estimate sinking velocities (Laurenceau-Cornec et al., 2020). Other approaches have estimated velocities from sediment trap data (e.g., Trull et al., 2008; McDonnell and Buesseler, 2010) or ^{210}Po-^{210}Pb profiles (Villa-Alfageme et al., 2014), but values are representative of only that particle population. Laboratory experiments have given insights into the sinking behavior of particles (Ploug et al., 2010), but a discrepancy has been observed between in situ and ex situ measurements (Williams and Giering, 2022). Indeed, attempts to measure sinking velocities of marine particles directly in situ remain scarce (Table 4.1), preventing comprehensive analyses of the sinking behavior of marine particles. Recently, cameras mounted on neutrally buoyant sediment traps provided unprecedented measures of sinking velocities in an unrestricted water column (Iversen and

Lampitt, 2020). Yet, as sinking particles undergo the influence of horizontal currents, which are orders of magnitude faster than vertical sinking, it is of the utmost importance to isolate a water volume from lateral influence, in order to understand solely the role of the vertical component. To our knowledge, only four studies actually measured in situ sinking velocities by isolating a water volume from lateral movements, either using settling columns (Diercks and Asper, 1997; Asper and Smith, 2003) or ROV-mounted settling chambers (Pilskaln et al., 1998; Nowald et al., 2009). Yet, these studies provided limited elements to fully describe marine particles' sinking behavior.

Table 4.1: Summary of existing methods to measure sinking velocities of marine particles.

Type of measurements	Reference	Method	Variables investigated
Indirect	Peterson et al. (2005); Trull et al. (2008)	Indented rotating sphere sediment traps	Composition
	Fischer and Karakaş (2009)	Time difference of fluxes at two depths measured with sediment traps	Mineral ballasting
	McDonnell and Buesseler (2010)	Sediment trap flux data combined with in situ imaging concentration data	Size
	Villa-Alfageme et al. (2014); Villa-Alfageme et al., 2016	Disequilibrium between ^{210}Po and ^{210}Pb	Size
	Kubryakov and Stanichny (2022)	Bio-Argo measurements of backscattering of small particles	
Direct	Alldredge and Gotschalk (1988); Alldredge and Gotschalk (1989)	Scuba dives	Density
	Diercks and Asper (1997); Asper and Smith (2003)	Cameras mounted on settling columns	Size, density
	Pilskaln et al. (1998); Nowald et al. (2009)	ROV-mounted settling chambers	Size, shape
	Iversen and Lampitt (2020)	Camera set on neutrally buoyant traps	Size, aspect ratio

Nonetheless, in situ settling velocity measurements are hampered by the difficulty of assembling a pool of unaltered particles, many of them too fragile to be collected (Alldredge and Gotschalk, 1988). For this reason, non-destructive in situ imaging methods appear as a powerful tool to investigate particle dynamics throughout the water column. By processing images, these instruments give detailed morphological data of particles, such as shape or gray level. In spite of the growing interest in these data in ecological (Vilgrain et al., 2021) and biogeochemical (Trudnowska et al., 2021) studies, they have seldom been used in flux assessments.

Here we present the development and test deployments of the VisuTrap, a new tool to measure in situ velocities. It is based on high frequency imaging (using the UVP6) of particles settling inside a sediment trap, whose purpose is to isolate

a water volume from lateral influence. By focusing on the vertical component of velocity, we aim to acquire a large dataset of sinking velocities that encompasses a wide variety of particles, while simultaneously accounting for their morphological properties. We expect that combining these data with the already numerous UVP particle profiles will help refine flux estimates at the global scale.

4.1.3 Material and procedures

VisuTrap setup and frame acquisition

The VisuTrap is composed of an UVP6-LP (LP for low power; Picheral et al., 2022) camera fitted onto a 149-cm high and 50-cm wide cylindro-conical sediment trap (Technicap, La Turbie, France; Fig. 4.1a). The upper cylindrical part of the VisuTrap has a height of 70.6 cm and an internal diameter of 49 cm. The lower conical section is 74.1-cm high with an internal slope of 72.15°. A metal cage holding the UVP6 and its battery is inserted outside, at the lower end of the cylindrical part. The camera unit of the UVP6 is joined via the connecting arm at a fixed distance to the light unit, which illuminates a water parcel of 180 × 151 × 23 mm (about 0.6 L) inside the trap, with a pixel resolution of 73 μm. The UVP6 is oriented side-looking (Fig. 4.1b): by doing so, the vertical component has a height of 151 mm, instead of 23 mm for its standard application. Flipping the UVP6 sideways allows a longer distance for particle tracking. The smallest dimension (23 mm) of the imaged volume corresponds therefore to the depth of field, which is highly constrained, allowing precise morphological measurements. Particles sinking into the trap are ultimately collected in a bottle (of 250 ml capacity) attached at its bottom, either filled with or free of brine. To measure the inclination of the sediment trap, DST TILT tiltmeters (StarODDI) are added on the metal cage, programmed via the dedicated software SeaStar to regularly (e.g., every second or every minute) record the x, y and z positions of the sediment trap (Supporting Information Fig. S4.1). This permits determination of its angle and roll (Supporting Information Fig. S4.2) and further corrects the track's vertical angle. In addition, each recorded frame is associated with a pressure measurement (0.1% full scale accuracy, 0.01 db resolution). To maintain the trap upright, three 9-kg lead rings are added at the bottom of the trap, whose weight is compensated by three blocks of LD2000 syntactic foam (density 420 kg m^{-3}) around the cylindrical part (Fig. 4.1a). The total air-weight of the trap and camera system is 47 kg and its water-weight is 7 kg.

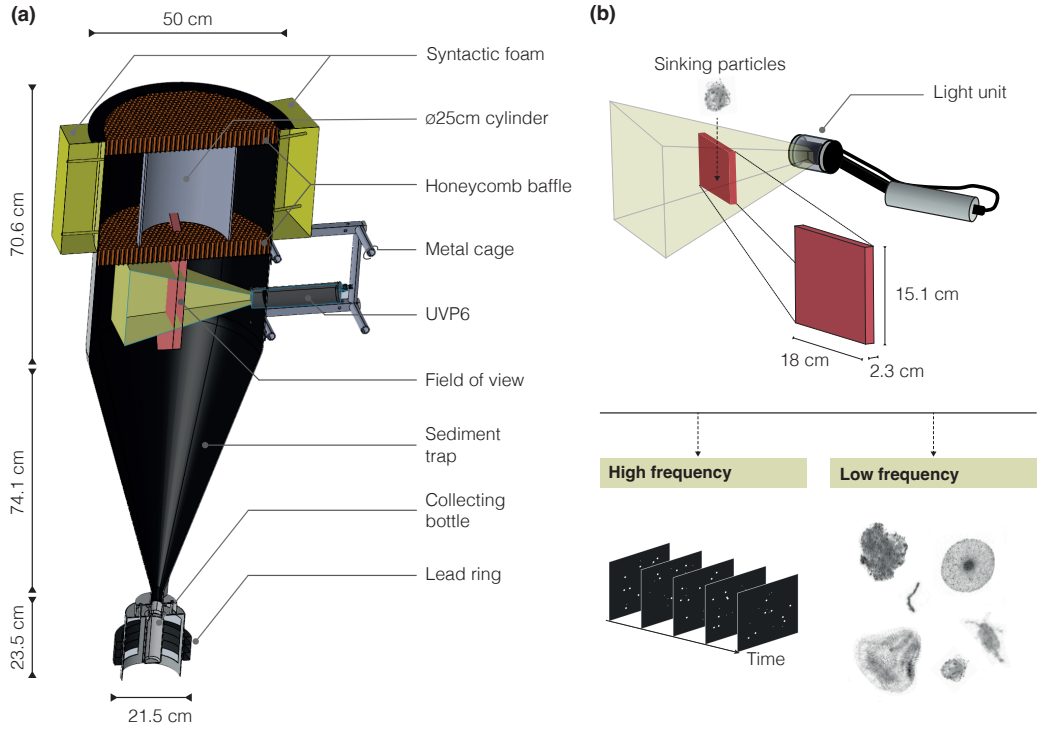

Figure 4.1: The VisuTrap setup. (**a**) Overview of the different elements of the VisuTrap, with the UVP6-LP camera set in the center inside a metal cage. (**b**) UVP6 field of view position and characteristics: a sinking particle passing through the field of view (red rectangle) is either recorded at high frequency (for tracking purpose) or at low frequency (only the particle vignette is saved).

To allow particle tracking using the UVP6, a new mode of frame acquisition was developed to record entire raw UVP6 frames without the standard segmentation into vignettes during frame acquisition (Picheral et al., 2022). This allows recording frames at a slightly higher frequency (1.3 Hz) than the standard UVP6-LP version. To store such voluminous and numerous raw frames, the UVP6 is equipped with a 1-TB microSD memory card. For long deployments (>48 h), the UVP6 is set to TIME mode (i.e., it checks for programming every 30 min and starts acquisition according to a set of parameters; Picheral et al., 2022) so that it switches every 30 minutes between two acquisition modes (Fig 4.1b): a high-frequency mode (1.3 Hz, i.e., 1 frame every 0.7 second), keeping in memory the entire raw frames; and a low-frequency mode (0.2 Hz, i.e., 1 frame every 5 seconds) keeping only vignettes of detected particles (Fig. 4.1b) and measuring particle sizes. The high-frequency mode is used to acquire tracks of particles sinking in the trap, whereas the low-frequency mode is used to measure their concentration and obtain morphometric measurements on the recorded vignettes.

By alternating between them, the UVP6 can record frames continuously for about 96 hours, being ultimately limited by memory storage. Longer deployments can still be achieved by reducing the time devoted to particle tracking, subject to the battery limits.

Hydrodynamism The primary purpose of the sediment trap is to contain a volume of water, but as oceans are dynamic with inherent tri-dimensional flows, the VisuTrap is likely to be affected by ambient motions. Therefore, ambient flows are addressed in two ways. (i) We expect horizontal currents to diverge around the trap; however, it is crucial to enhance the instrument's vertical orientation in the water column, independently of the drift tether (which is not totally vertical), in order to ensure that horizontal flows will not enter the trap (Gardner, 1985; Supporting Information Fig. S4.2). Thus, vertical orientation of the VisuTrap is ensured by the attachment of the lower bridle 1 m above the bottom of the system (the overall length of the system including bridles is 2.5 m) and the presence of three 3-kg lead rings added at the bottom of the trap, whose weight is compensated by three syntactic foam blocks (Fig. 4.1a). From two example deployments, whose sediment trap was unballasted in the first case and unballasted in the second case, we noticed a clear improvement in the angle and roll (averages of 15° for unballasted and 3° for the ballasted) of the sediment trap when we added the weights (Supporting Information Fig. S4.3). In addition, the aluminum cage holding the UVP6 serves as a tailplane and helps stabilize the trap with respect to horizontal motions. (ii) Two honeycomb meshes, 9.5-mm high with an aspect ratio of 5.26, are added at the top of the trap and just above the imaged volume (Fig. 4.1a; Supporting Information Fig. S4.4), to break currents and prevent larger organisms from entering the trap. To increase the aspect ratio of the sediment trap from 1.2 to 2.4, a 30-cm long and 25-cm diameter PVC tube is set between the two honeycomb meshes, centered on the imaged volume (Fig 4.1a; Supporting Information Fig. S4.4).

Deployment

The VisuTrap has been designed to be deployed on a drifting line during quasi-Lagrangian experiments (i.e., where the same water parcel is followed and its biogeochemical and ecological properties are sampled), typically lasting 2 to 5 days. As they provide estimation of in situ sinking velocities, VisuTrap can be deployed, for example, alongside VERTEX-style Particle Interceptor Traps (PIT;

Knauer et al., 1979), a few meters above or below the PIT array for coincident flux measurements. Once the setup is fully mounted and ready to deploy, the procedure consists of the following steps: 1) the collecting bottle (filled or free of brine) is attached at the bottom of the trap and the UVP6 is plugged to its battery, automatically starting the TIME acquisition procedure; 2) the top and bottom shackles are attached to the line. Upon recovery, the collecting bottle is removed from the bottom and can be used for further analyzes or frozen at -20°C.

Image processing

Briefly, reconstructing particle tracks consists of two main steps: 1) particle detection, i.e., obtaining the particle position on the raw frame and its morphometric properties such as size or gray level, a proxy of the object's ability to reflect UVP6 red light, possibly linked to its density; and 2) particle linking, which aims to connect particles in successive frames according to their respective positions and morphometric similarities (Fig. 4.2). Such tracking is achieved using purpose-built Python modules available upon publication, with detailed procedural steps described below.

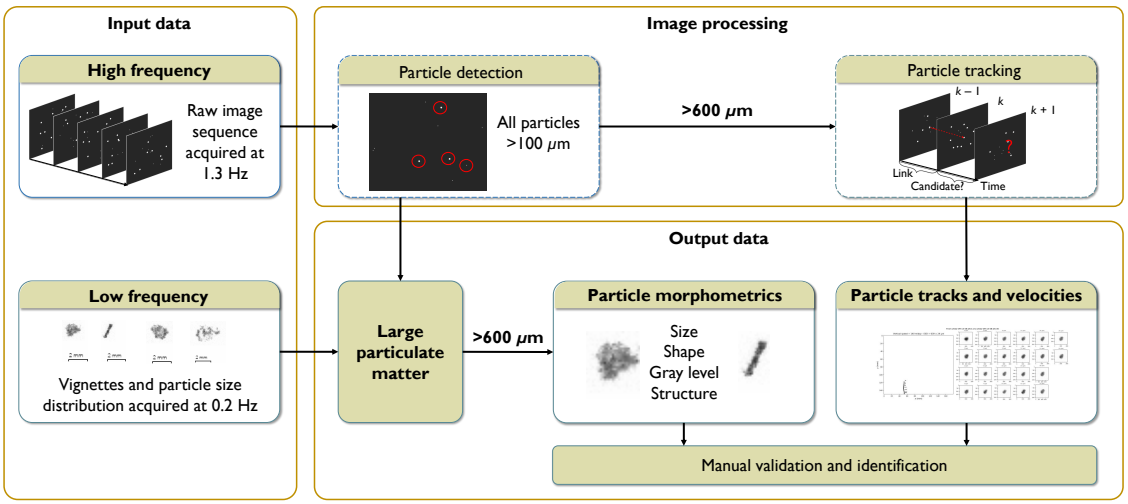

Figure 4.2: Overview of the image processing workflow for VisuTrap images. Frames recorded at high frequency are processed following two consecutive steps: particle detection and particle tracking (only for vignettes >600 μm), both generating information about particle morphometry and the corresponding tracks and velocities. Vignettes recorded at low frequency provide size spectra for particles >100 μm and particle morphometry for larger objects (>600 μm). Both vignettes and tracks are manually validated and categorized before enabling further statistical analyses.

Processing of the vignettes Sequences of particle data and vignettes acquired at low-frequency are first processed using the UVPapp and then imported to EcoPart and Ecotaxa (Picheral et al., 2017), respectively, as routinely done with standard UVP6 operations (Picheral et al., 2022).

Particle detection To detect the position of particles, monochrome frames were first converted into binary frames by applying a threshold depending on the calibration of each UVP6 (Picheral et al., 2022). Then, particle contours were extracted on each frame using the `scikit-image` Python module (Walt et al., 2014). For each particle, the area inside the contour was converted from px^2 to μm^2 using the calibration constants Aa and Exp as described in (Picheral et al., 2022). The Equivalent Spherical Diameter (ESD) was determined from the area as follows:

$$ESD = \sqrt{\frac{4 \times area}{\pi}}$$

All particles whose size is >100 μm are used to measure particle size distributions. Only particles whose size is >500 μm are used for the tracking step, as smaller particles lack sufficient details to be visually identified and compared. For each of these particles, a set of morphological descriptors (e.g., lengths of the major and minor axes, mean gray level of all its pixels, etc.) are automatically computed.

Particle tracking As the UVP6 records a large number of frames (typically from 80,000 to 170,000 frames for 40-to-85-hour long deployments), manual tracking of particles would be too time-consuming and therefore requires automation. With the development and decreasing cost of cameras, numerous particle tracking algorithms have been proposed for various applications (Meijering et al., 2012), but generally serve one specific purpose and are not adapted to the present set of frames. Indeed, the linking step is often based on a nearest neighbor association (Meijering et al., 2012), but as marine snow is composed of sets of heterogeneous particles having different velocities, this approach not suitable. Therefore, for the purpose of tracking marine particles from in situ imaging data, we developed a simple algorithm based on position and size criteria. Briefly, tracking consists of the following steps. For a frame at a given time t, we have a set of ongoing tracks and unassigned particles. For each track and particle at t, the matching

potential with each particle in the subsequent frame at $t + 1$ is assessed (Fig. 4.3); if a particle at $t + 1$ matches a track or a particle, it is linked to it; this process is repeated along the entire time series.

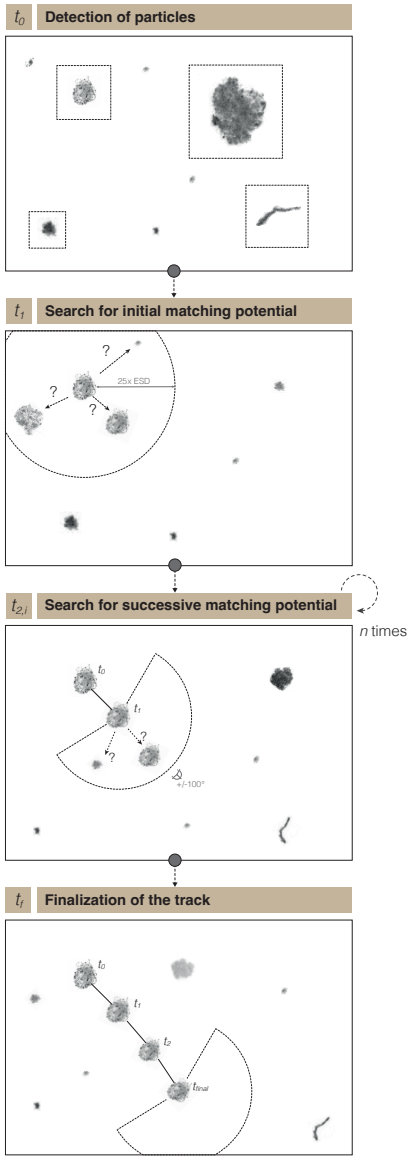

Figure 4.3: Overview of the tracking process. After an initial detection of particles (t_0), the matching potential of candidate particles located inside the circular search area (25 $\times$ particle's ESD) at t_1 is evaluated. Successive searches are then repeated by looking at potential matching particles at within $\pm$ 100° of the track's direction (t_i) until there is no more match possible (t_f).

The matching potential is evaluated as follows: (i) A search area is delimited relative to the position of the particle. If the particle begins a new track, a search circle is defined around it, whose radius is 25 times the ESD of the particle. In

any other cases, the search area is delineated from the angle of the last step $\pm$ 100°. Then, (ii) among all the particles inside the search area, the particle whose ESD is the closest to the mean ESD of the particles on the track is sought, provided it does not exceed or fall below this value by more than 20%. To provide the most reliable estimates of velocities, only tracks whose length is >3 (i.e., the particle is present on at least 4 consecutive frames) are recorded. Finally, only tracks whose mean ESD is >600 μm are retained, smaller sizes not allowing visual discrimination of the particle nature (i.e., living or not-living).

Velocity measurements Once tracks are extracted, both their absolute and vertical velocities (i.e., relative to the vertical axis only) are computed (in m d^{-1}). Absolute velocity is determined from the successive positions of the particle and the difference between the elapsed time at its final and initial positions. Vertical velocity is calculated by first correcting the mean angle, relative to the vertical axis, of the track according to the inclination of the trap (see section 'VisuTrap setup and frame acquisition' above). Tracks are classified in 3 categories depending on the motion's orientation: descending, ascending and mixed tracks (hereafter referred to as suspended). To distinguish the vertical orientation of particles, the vertical velocity U is converted into $-U$ for ascending tracks. Finally, the sinuosity index (i.e., the ratio between the track total length and the length of the beginning-end segment) and the standard deviation of the step angle, are computed as metrics of track straightness.

Data quality control

Manual checking of the tracks and data availability To visualize each particle track, a figure displaying the position of each successive position of the particle, as well as its corresponding vignettes at each time step, is generated and uploaded to EcoTaxa (Fig. 4.4). This step allows a manual sorting of tracks, in order to remove false tracks as well as swimming organism tracks from the dataset.

Influence of trap speed on velocity measurements To rule out any potential effect of sediment trap vertical oscillations and to discard potential sequences affected by trap motions, correlations between track vertical velocities and VisuTrap vertical oscillation speed, their trajectories are tested before (i.e., 30 seconds before the occurrence of the track) and during (i.e., instant velocity) a tracking episode. A moving average (window size = 3 measurements) is performed on

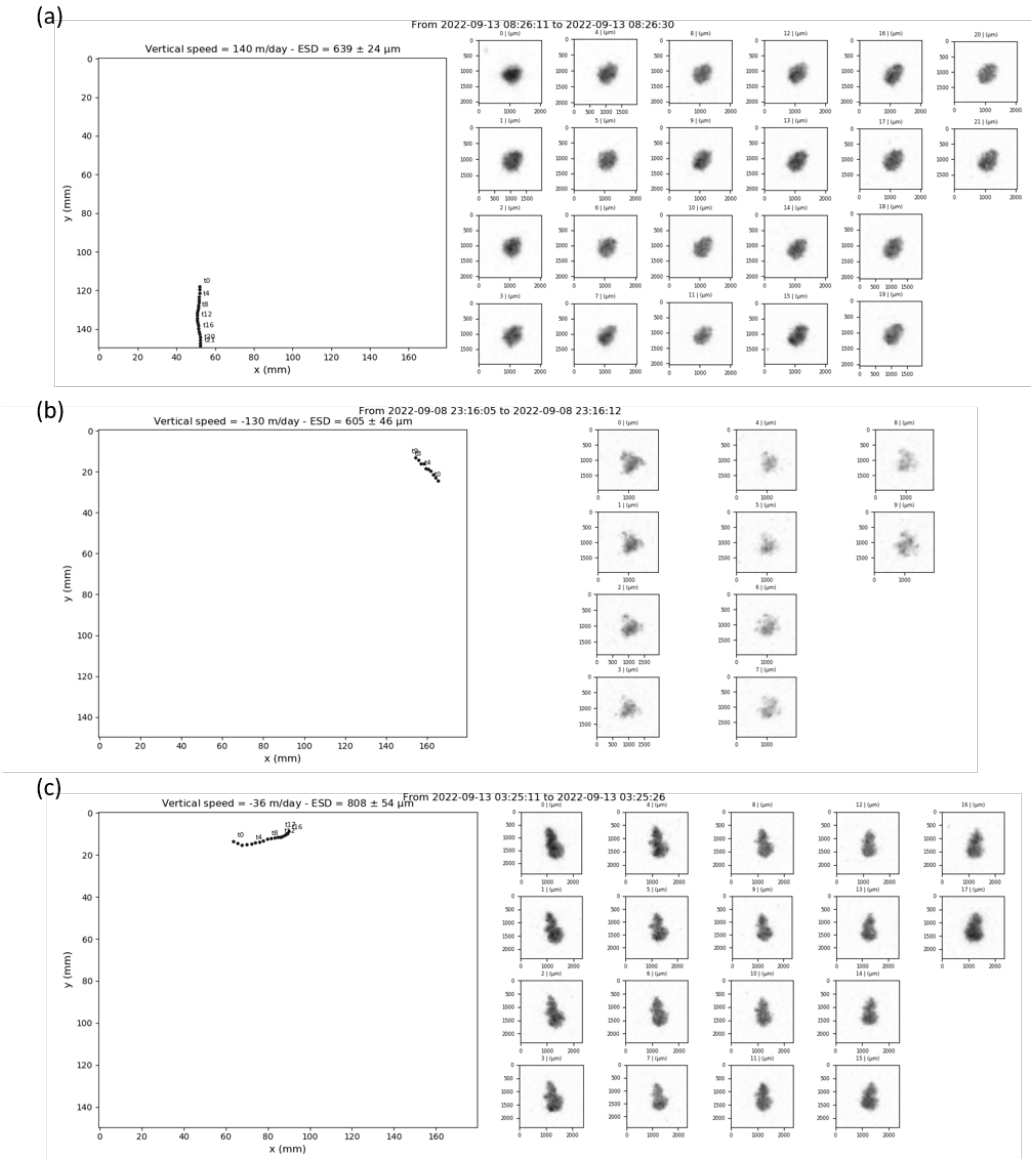

Figure 4.4: Examples of the three different types of particle tracks: (**a**) Sinking particle; (**b**) ascending particle; (**c**) suspended particle. The left panel shows the position of the particle in the UVP6 field of view at each timestep and indicates the initial and final positions. Thumbnails on the right represent the particle as it appears on frames at each timestep.

UVP6 pressure sensor data recorded alongside frames to limit the effects of sensor accuracy on depth measurements. VisuTrap vertical speed is then calculated as the depth difference divided by the time difference between two timesteps.

Data analysis procedure

All analyses described in this section were performed with R version 4.2.2 (R Core Team, 2022) and are available at https://github.com/MnnLgt/visutrap_2022_moose_ge. The package `tidyverse` (Wickham et al., 2019) was used for data handling and graphical representation.

The Normalized Abundance Size Spectrum (NASS; i.e., the particle abundance per size class, which is similar to the Normalized Biomass Size Spectrum; Platt and Denman, 1977) was used to assess the size spectrum sampled by the UVP6-LP set on the VisuTrap, as well as to compare size spectra between deployments. To do so, mean particle abundance (in # m^{-3}) for the duration of the deployment was estimated for $\log_{10}$ size classes between 100 μm and 2 mm (based on the Equivalent Spherical Diameter or ESD) and divided by the width of the class to normalize the spectrum using the `nbssr` package (https://github.com/jiho/nbssr).

To link particle velocities to particle morphology, morphological properties were first summarized into a morphological space. For that purpose, size, gray level, shape and structure of tracked particles were each described by 3 to 5 morphological variables (Supporting Information Table S4.1). A Yeo-Johnson transformation was applied to reduce skewness of their distribution (Yeo and Johnson, 2000). In an approach similar to Trudnowska et al. (2021), these variables were used to build a Principal Component Analysis (PCA) ordination, hereafter referred to as morphospace, using the package `FactoMineR` (Lê et al., 2008). This morphospace allowed us to summarize morphological information into new uncorrelated variables and to distinguish main sources of variability between particles. By that means, each particle was defined by its coordinates in the morphospace. Randomly selected particle vignettes were outlined in the morphospace using the R package `morphr` (https://github.com/jiho/morphr). This allowed a synthetic, visual interpretation of the Principal Components (PC). According to the Kaiser-Guttman criterion (Cattell, 1966), only PCs whose associated eigenvalue was greater than the mean eigenvalue were considered significant. Mean individual coordinates on each significant PC according to track types (i.e., sinking, suspended and ascending) were compared with one-way ANOVA and pairwise comparisons were made with Tukey's HSD test. Correlations between vertical velocities and particle coordinates on each significant PC were tested using Pearson's correlation test. A Holm-Bonferroni correction (Holm, 1979) was applied to p-values to take into account multiple comparisons.

4.1.4 Assessment

The following section presents example results from the MOOSE-GE 2022 cruise, which took place in the Western Basin of the Mediterranean Sea, in September 2022 aboard the N/O *Pourquoi Pas ?* (Coppola et al., 2019; Testor et al., 2022). This area is characterized by summer oligotrophy: at this time of the year, thermal stratification is strong and the surface layer is nutrient depleted, leading to low primary production. VisuTraps were set on a drifting line for two Lagrangian cycles of ca. 45 hours each. Drifting lines were deployed around LION (42.04° N 4.68° E) and DYFAMED (43.41° N 7.89° E) mooring sites (Supporting Information Fig. S4.5).

The LION mooring is located in an open-ocean deep convection zone, characterized by active winter vertical mixing that allows ventilation of deep Western Mediterranean waters (Houpert et al., 2016). The DYFAMED mooring is located in the central zone of the Ligurian Sea, where a density front at the core of the Liguro-Provençal current prevents coastal inputs (Andersen and Prieur, 2000). VisuTraps were deployed at 500 m from 8-10 September 2022 at LION and at 200 m and 500 m from 12-14 September 2022 at DYFAMED. A UVP5 camera (Picheral et al., 2010) was mounted onto the CTD rosette to quantify vertical concentrations of particles and zooplankton. The UVP5 illuminates a water volume of about 1 L and then detects and records counts of all objects (i.e., all types of particles and organisms) larger than 100 μm.

Frame recording

For each deployment, the UVP6 mounted inside the VisuTraps covered the entire cycle duration. Over the course of a cycle, the UVP6 recorded ca. 80,000 frames (Table 4.2). The number of recorded vignettes, with the low-frequency mode, was highly variable and depended on environmental conditions.

Table 4.2: Recovered data from three example deployments of the VisuTrap during the MOOSE-GE 2022 cruise and track counts of living and non-living objects.

Lagrangian cycle - Depth	Acquisition duration	Number of frames (high-frequency)	Number of vignettes (low-frequency)	# non-living objects	# living objects and dubious living objects	# false and dubious detections
Cycle 1 - 500 m	46 h	81,396	573	201	80	19
Cycle 2 - 200 m	44 h	77,545	148	51	29	1
Cycle 2 - 500 m	44 h	77,437	135	31	42	0

Size spectrum imaged by the VisuTrap

NASS were used to compare, for each deployment, the size spectrum sampled by the UVP6-LP set inside the VisuTrap and the size spectrum sampled by the UVP5 in open waters. For UVP5 vertical profiles, only data whose depth was within 10 m of the mean depth of VisuTrap deployment were used. For all deployments, slopes and intercepts of $\log_{10}$-transformed NASS differed between instruments (ANOVA: p-value <0.001 in every case). Undersampling largely increased for particles whose ESD was >300 μm (Supporting Information Fig. S4.6).

Two complementary deployments were made in February and April 2023 at the DYFAMED site. A few meters above the VisuTrap, another UVP6-LP camera was deployed to size and image particles in open waters, i.e., not constrained by the sediment trap. For both deployments, slopes of $\log_{10}$-transformed NASS did not differ between UVP6 (ANOVA: p-value = 0.21 for February and p-value = 0.29 for April; Supporting Information Fig. S4.7). Thus, differences observed with the size spectra imaged by the UVP5 is likely due to differences in instrument configuration.

Track features

During deployments, the average oscillation (Supporting Information Fig. S4.8), defined as the depth difference between two timesteps, was 0.7 $\pm$ 0.6 cm. The maximum depth amplitude for the duration of a sequence (i.e., the minimum depth subtracted from the maximum depth of the sequence) averaged 32 $\pm$ 10 cm, with a maximum amplitude of 66 cm and a minimum amplitude of 18 cm. Despite these oscillations, track vertical velocities did not show any correlation with VisuTrap speed for all deployments. The absence of significant correlations was recorded for both the instant VisuTrap speed (i.e., during the course of the track) and the mean speed 30 s before the track occurrence (Supporting Information Table S4.2, Supporting Information Fig. S4.9).

For the three deployments, a total of 283 tracks of nonliving objects (with sizes ranging from 600 to 2,200 μm ESD) were recorded (Table 4.2; Fig. 4.5a). The mean length of a track, defined as the number of frames on which the particle appears, was 8.2 $\pm$ 6.2 and the maximum length 47 (i.e., corresponding to a mean duration observation of 6.3 $\pm$ 4.8 s, and a maximum of 32.9 s). In addition to sinking particles, we also recorded tracks of ascending or seemingly suspended particles (Fig. 4.5b, 4.5c), going in all directions of the recorded field of view

(Fig. 4.5c). Ascending and suspended tracks represented a substantial, yet highly variable, proportion of the total number of tracks (Fig. 4.5a, 4.5b, 4.5c). In addition, we observed tracks of living organisms (Table 4.2), such as Rhizaria or Copepoda, which were not included in the subsequent morphological analyses.

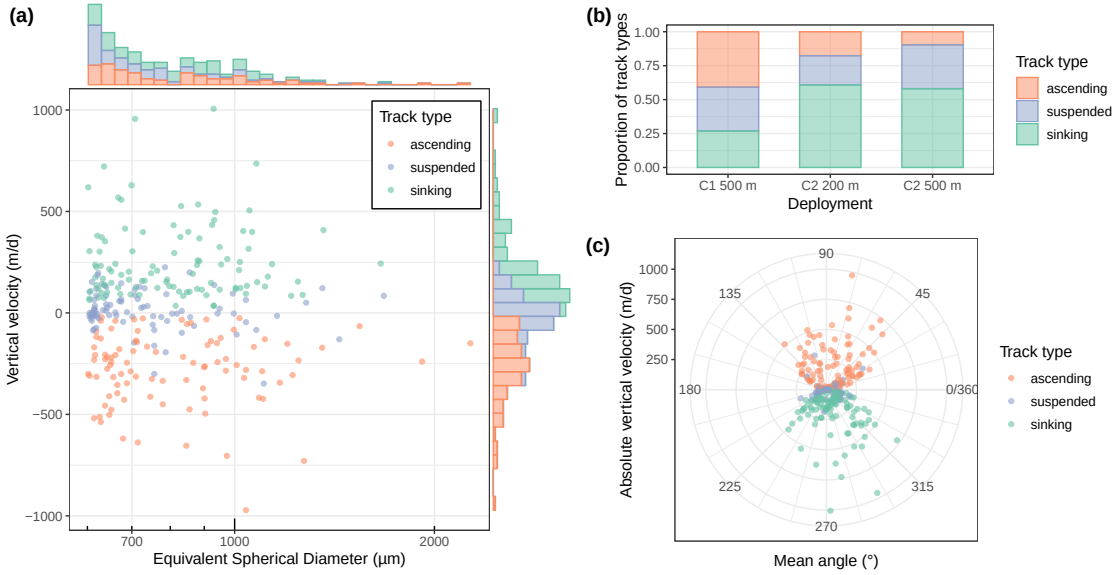

Figure 4.5: Overview of track features. (**a**) Particle size (Equivalent Spherical Diameter, ESD, in μm) as a function of vertical velocity (in m d^{-1}). Distributions of ESD and vertical velocities for each track type, are shown on the right and on top, respectively. (**b**) Proportion of track types according to deployment. (**c**) Track mean angle (i.e., overall direction, in °) versus absolute vertical velocity (in m d^{-1}).

Morphospace of tracked particles

The first three PCs of the morphospace were considered significant and explained 90.9% of the total morphological variability between particles (Fig. 4.6). As they summarize morphological descriptors, projection of individual particles onto the planes defined by these principal components eased their interpretation. PC1, explaining 47.9% of total variability, separated dark and compact particles from fluffy and light gray particles. Variables which contributed the most to this axis were associated to shape (e.g., circularity), complexity (e.g., solidity) and gray level (e.g., median of gray values) (Fig. 4.6, Supporting Information Table S4.1, Supporting Information Fig. S4.10). Thus, this PC could be summarized as "particle density and complexity", a negative value on this axis indicating a low density fluffy particle and vice versa. PC2 explained 26.8% of morphological variability. It discriminated size, with large particles on the half upper plan and

small particles on its lower half and was mainly influenced by size descriptors (area, convex area and main axes length; Fig. 4.6, Supporting Information Table S4.1, Supporting Information Fig. S4.10). PC3 explained 16.1% of variability and was related to the shape of particles, separating long and elongated particles (PC3 >0) from rounder particles (PC3 <0).

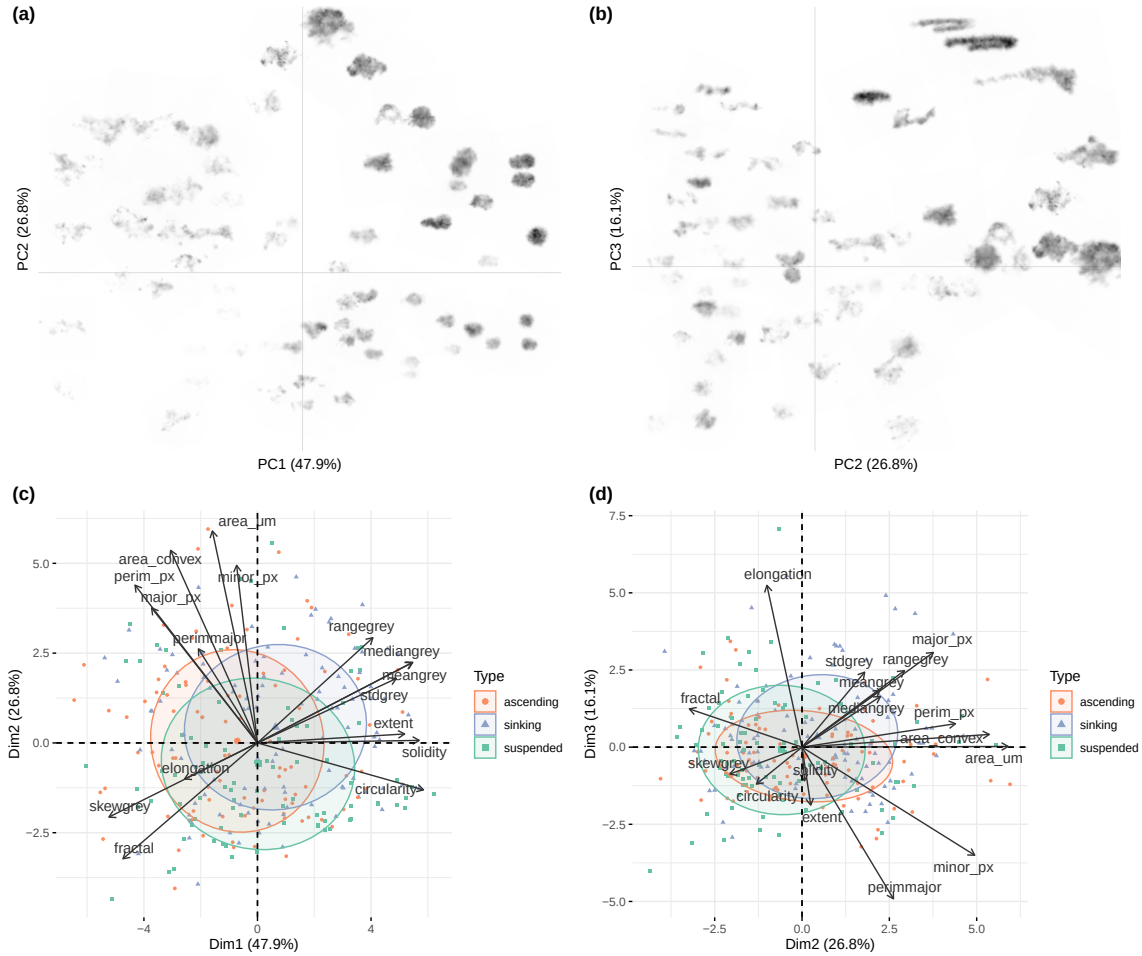

Figure 4.6: Morphospace of particles that were successfully tracked. Vignettes of randomly selected individuals are shown according to their coordinates in the plane defined by (**a**) PC1 and PC2; (**b**) PC2 and PC3. The package `morphr` was used for these representations. Correlations between PC and original variables (Supporting Information Table S4.1) are presented for (**c**) PC1 and PC2; (**d**) PC2 and PC3. The quality of representation for variables on the factorial plane is given by the length of arrows. Points represent the position of individual particles in the plane and are colored according to track type (i.e., sinking, ascending or suspended). Confidence ellipses for the centers of the categorical variable 'track type' are displayed with a threshold of 0.5.

Distribution of PCs according to track type

We observed slight differences in PC values between track types (Fig. 4.6c, 4.6d, 4.7), which were tested with one-way ANOVA and Tukey's HSD tests. Distribution of PC1 values, summarizing particle density, showed differences between sinking and ascending tracks (Tukey's HSD test: p-value = 0.001), these values being higher (thus indicating a higher density) for sinking tracks. Size, summarized by PC2, differed between suspended and sinking particles with sinking particles being larger on average than suspended ones (Tukey's HSD test: p-value = 0.002). Roundness, defined by PC3, was significantly lower (higher values of PC3) for sinking particles than for ascending ones (Tukey's HSD test: p-value = 0.016).

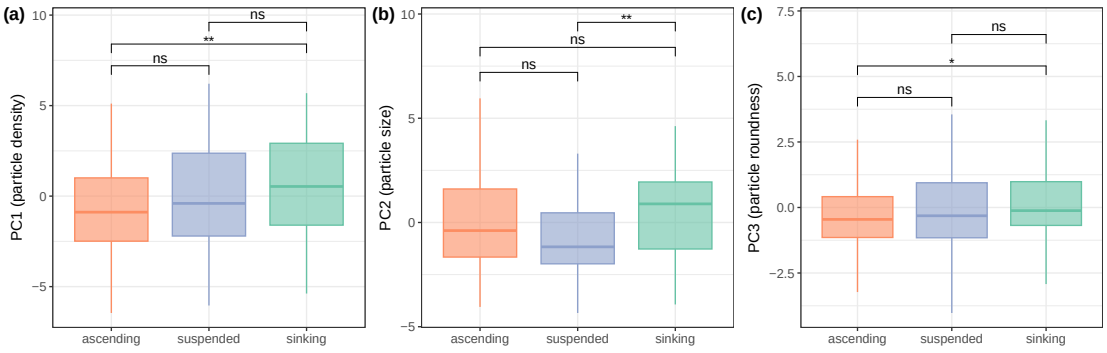

Figure 4.7: Distribution of individual scores of significant principal components according to track type: (**a**) PC1, interpreted as particle density; (**b**) PC2, summarizing particle size; (**c**) PC3, defined as particle roundness.

4.1.5 Discussion and recommendations for future directions

In situ imaging for direct particle velocity measurements

For the first time, we use the latest 6th generation of UVP to directly record in situ sinking velocities of a large spectrum of marine particles, a key variable for flux estimates (Guidi et al., 2008). The different generations of UVP through its worldwide commercialization have provided a powerful tool for studying the ecology and biogeochemistry of the ocean, allowing for studies of particle flux at various scales (e.g., Guidi et al., 2015; Ramondenc et al., 2016) without providing direct measures of sinking speeds. Thanks to its low-power consumption, allowing it to be mounted on autonomous platforms such as sediment traps, the VisuTrap-UVP6 provides a new tool to measure in situ sinking velocities. As with some other imaging methods, it is non-invasive and thus allows unaltered

particles and small planktonic organisms to be sampled, whose sinking towards the deep ocean is of paramount importance for the functioning of the BCP. The experimental design, based on quasi-Lagrangian deployment of two-to-five-days duration, makes use of the full potential of the UVP6 to investigate the dynamics of particles at high temporal resolution in a specific water mass.

A key feature of the VisuTrap is the narrow depth field (2.3 cm) of the side-looking UVP6. Indeed, a large depth of field induces more uncertainties in both size and velocity measurements: a particle close to the camera will appear larger and will seemingly move faster than the same particle located at the back (Iversen and Lampitt, 2020). Moreover, accurate size and feature measurements are of paramount importance for further flux estimates (Giering et al., 2020; Bisson et al., 2022). Such accuracy was not achieved in previous methods, because of the camera's large depth of field (ca. 10 cm; Pilskaln et al., 1998; Iversen and Lampitt, 2020). Accurate tracking of biological particles is a longstanding research area, but the numerous programs developed for this application were not adapted to record the heterogeneous speeds of marine particles. For our purpose, we developed Python modules to be used with UVP6 data, which can be integrated in a global work environment in the future. Overall, we were able to record tracks of particles for up to more than 40 frames, allowing accurate estimates of velocities relative to the vertical axis of the sediment trap.

For 134 h of deployment, a total of 283 tracks were recorded, a limited number that should be linked to oligotrophic conditions encountered during the MOOSE-GE cruise and the overall low number of vignettes recorded (Table 4.2). The size spectrum of tracked particles covered the size spectrum of the vignettes recorded by the UVP6 (600 μm - 2 mm). As an imaging-based method is necessarily limited by the optical resolution of the camera, a combination of cameras of various optical resolutions is required to cover the entire size spectrum of marine particles. In addition, size quantification, on which the tracking process relies, is limited by the 2D shape and the orientation of particles, which can ultimately lead to a mismatch and to the occlusion of a track if a particle is rotating from frame to frame. For our deployments, which occurred in relatively low-particle environments, manual sorting of tracks was not time-consuming. Still, in different environments, large numbers of tracks can be detected and we expect progress in machine learning applications (Irisson et al., 2022) to help identify particles and to reconstruct tracks in the future.

Towards a new methodology for carbon flux assessment?

The new tool VisuTrap will enable us to improve understanding of sinking marine particles by recording their in situ behavior and sinking velocities, and provides a new toolbox for studying the BCP. By taking advantage of the working environment developed around a set of numerous intercalibrated cameras, VisuTrap data can be incorporated in analyses with other data coming from UVPs in the future. As this instrument provides both velocity and morphometric measurements, we expect further efforts to decipher the variability in the velocity data, as well as to explore links between sinking velocities on the one hand, and particle concentration, morphology and size on the other. Indeed, size alone is not sufficient enough for accurate flux estimates (McDonnell and Buesseler, 2010). Instead, marine particles are distributed along a multidimensional continuum of shape, gray level, size and structure, which partly influence observed velocities. Summarizing such morphological information using dimensionality reduction methods (e.g., PCA; Vilgrain et al., 2021; Trudnowska et al., 2021) for further analyses is becoming more and more common. To take into account these multiple factors and their potential interactions, future work should take advantage of machine learning tools to implement particle vignette to velocity models.

The increasing number of particle vignettes collected by the UVP6 and their associated morphological descriptors are highly valuable information that have been underused for flux assessments. Integrating these data into new models is likely to increase the accuracy of actual flux calculations. Nevertheless, a crucial parameter is the carbon content of marine particles. Although there potentially is a link between pixel gray values of a particle (i.e., its ability to reflect UVP6 red light) and its density, no relationship has yet been established. The morphospace allowed us to distinguish particles with seemingly different densities, but a way to estimate particle composition from the vignettes alone is still lacking. Classifying tracks into various detrital types to apply size to carbon content conversion factors could in part solve this issue; however, it is still unclear how particle age, mineral ballasting or the presence of transparent exo-polymers, usually influencing the density of a particle with respect to the surrounding water, will affect morphological appearance. Although tackling such issues is challenging, imaging technologies continue to open new avenues for broadening our understanding of the biological carbon pump.

Supporting information

See section 4.1.6 of this chapter.

Author Contribution Statement

TB conceptualized the device. MP, CC and TB contributed to technological development. ML developed the code. ML and LG designed the data analysis pipeline with insights from all authors. ML wrote the manuscript with inputs from all authors.

Acknowledgments

This work was funded by the French "Agence Nationale de la Recherche" project RhiCycle (ANR-19-CE01-0006). We acknowledge the MOOSE program (Mediterranean Ocean Observing System for the Environment) coordinated by CNRS-INSU and the Research Infrastructure ILICO (CNRS-IFREMER) for participating in the MOOSE_GE cruise 2022. We acknowledge the CCE-LTER program (National Science Foundation grants OCE-1637632 and OCE-1614359) which permitted initial test deployments. Research support was provided by National Science Foundation Grant OCE-1851558 to M.R. Landry. Sampling in the Argo-Rowley Terrace Marine Park was done under Australian Government permit AU-COM2021-520 and permit PA2021-00062-1 issued by the Director of National Parks, Australia. We are grateful to the captains and crews of the N/O *Pourquoi Pas ?* and the R/V *Roger Revelle*, as well as Matthieu Bressac, Louis Petiteau and Michael Stukel who made deployments possible. We thank the Division Technique de l'INSU for lending us their inclinometers and the Plateforme d'Imagerie Quantitative de Villefranche for their technical support. We thank the Laboratoire d'Informatique, Signal et Image de la Côte d'opale for providing us the computational resources to run the analyses via the CALCULCO server, as well as Philippe Marion and Dominique Verhaghe for their helpful advice. We are grateful to Jean-Olivier Irisson for his recommendations and insightful comments on statistical analyses and to Mark Ohman for proofreading.

4.1.6 Supporting Information

Supporting Information Fig. S1

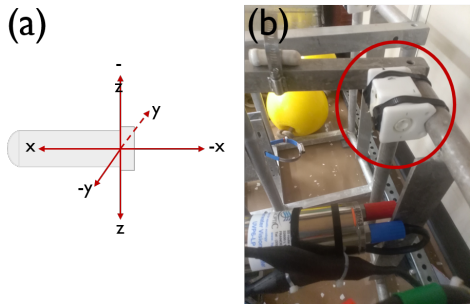

Figure S4.1: Tiltmeter for VisuTrap deployment. (**a**) Positions recorded by the tiltmeter. (**b**) Example of tiltmeter inserted in its box attached to the metal cage of the VisuTrap.

Supporting Information Fig. S2

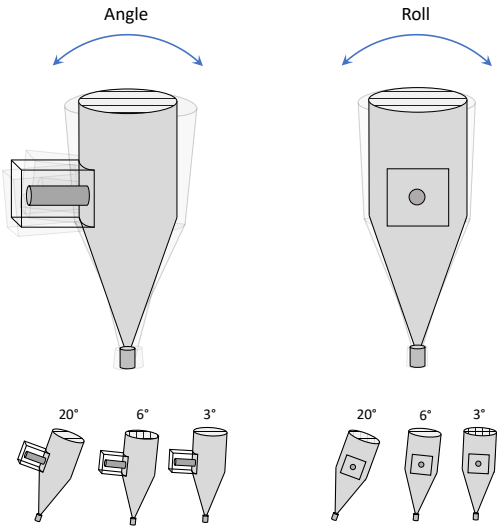

Figure S4.2: Position of the VisuTrap according to several angle and roll values. A larger angle and/or roll leads to more horizontal flow entering the trap.

Supporting Information Fig. S3

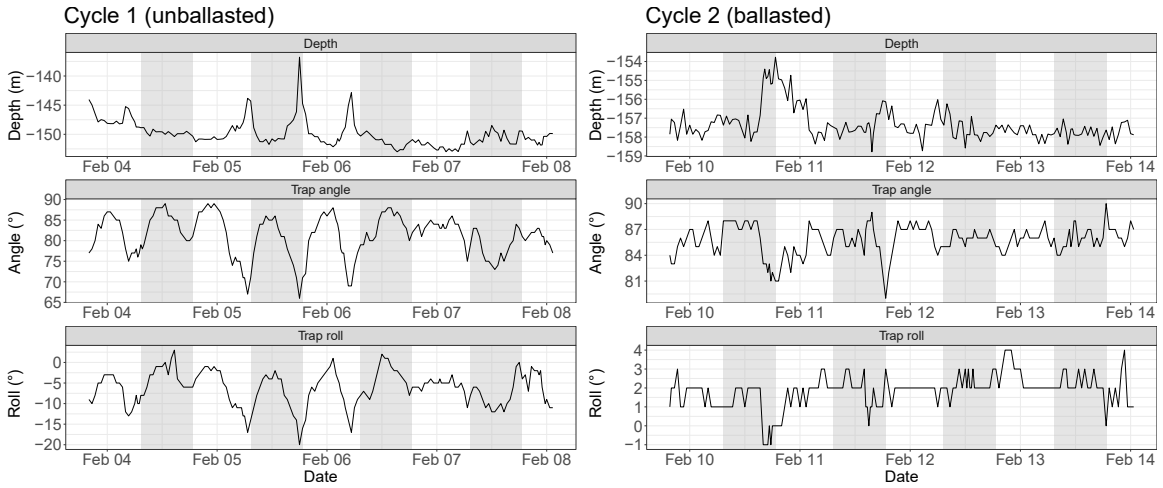

Figure S4.3: Time series of the depth, angle and roll of the VisuTrap deployed during the lagrangian cycles 1 (unballasted) and 2 (ballasted) of the BLOOFINZ cruise (Eastern Indian Ocean, February 2022). Grey ribbons indicate night periods.

Supporting Information Fig. S4

Figure S4.4: View inside the VisuTrap once the top honeycomb mesh is removed. The bottom honeycomb mesh stands above the UVP6 field of view. The PVC tube joins the two honeycomb meshes and reduces the trap aspect ratio.

Supporting Information Fig. S5

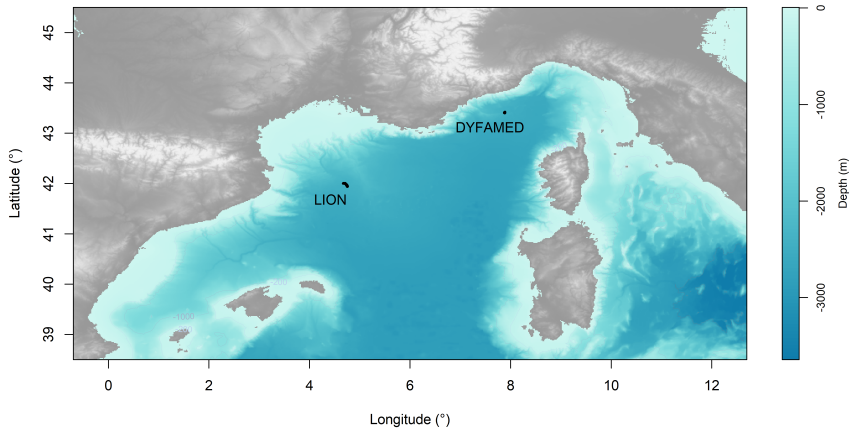

Figure S4.5: Drifting line track at LION and DYFAMED sites during the MOOSE-GE 2022 cruise in the Mediterranean Sea. Bathymetric data come from the ETOPO 2022 database hosted on the NOAA website and queried with the `marmap` R package (Pante and Simon-Bouhet, 2013).

Supporting Information Fig. S6

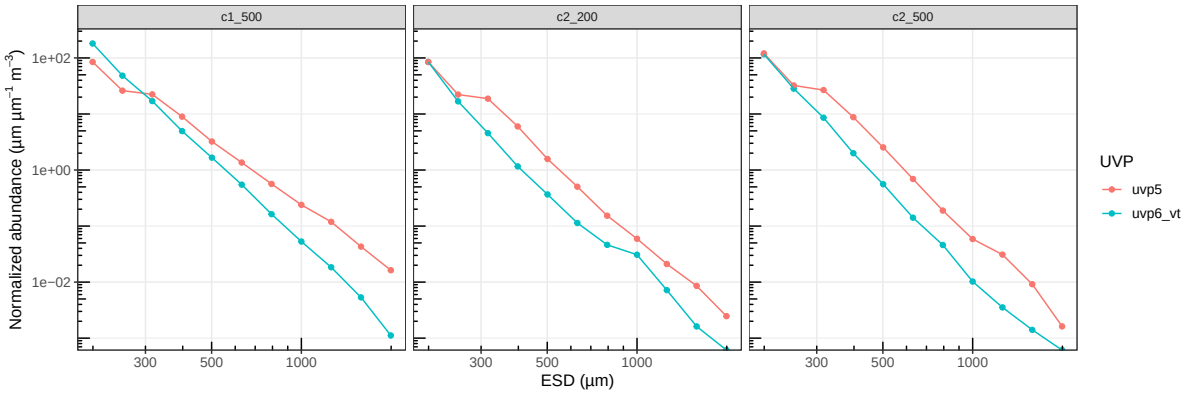

Figure S4.6: Normalized Abundance Size Spectra of particles sampled by the UVP6 inserted in the VisuTrap and by the UVP5 in open waters, for all three deployments during the MOOSE-GE 2022 cruise. For UVP5 data, only those whose depth was between the mean depth of VisuTrap deployment more or less 10 m were used.

Supporting Information Fig. S7

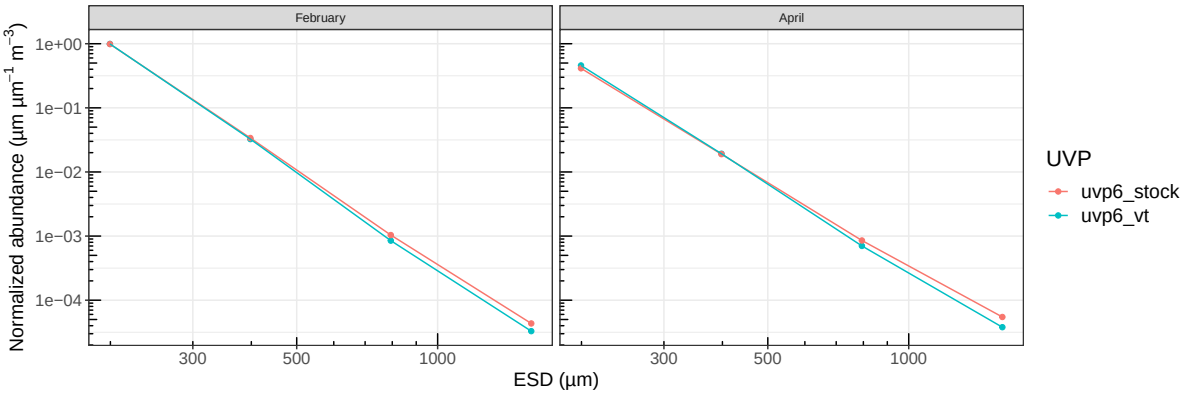

Figure S4.7: Normalized Abundance Size Spectra of particles sampled by the UVP6 inserted in the VisuTrap and by the UVP6 sampling a few meters above the VisuTrap in open waters, for two deployments in February and April 2023 at DYFAMED.

Supporting Information Fig. S8

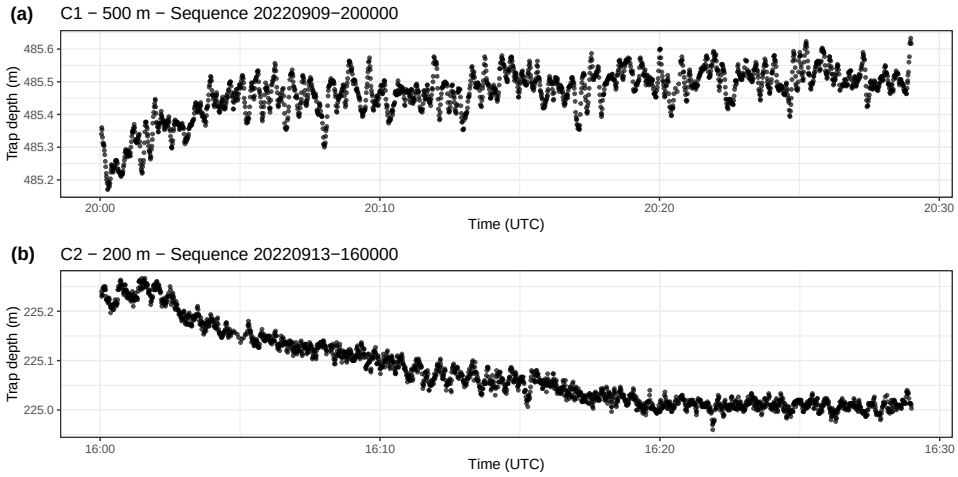

Figure S4.8: Examples of depth variations of the VisuTrap with time, for 2 30-minute sequences during (**a**) cycle 1 at 500 m depth and (**b**) cycle 2 at 200 m depth.

Supporting Information Fig. S9

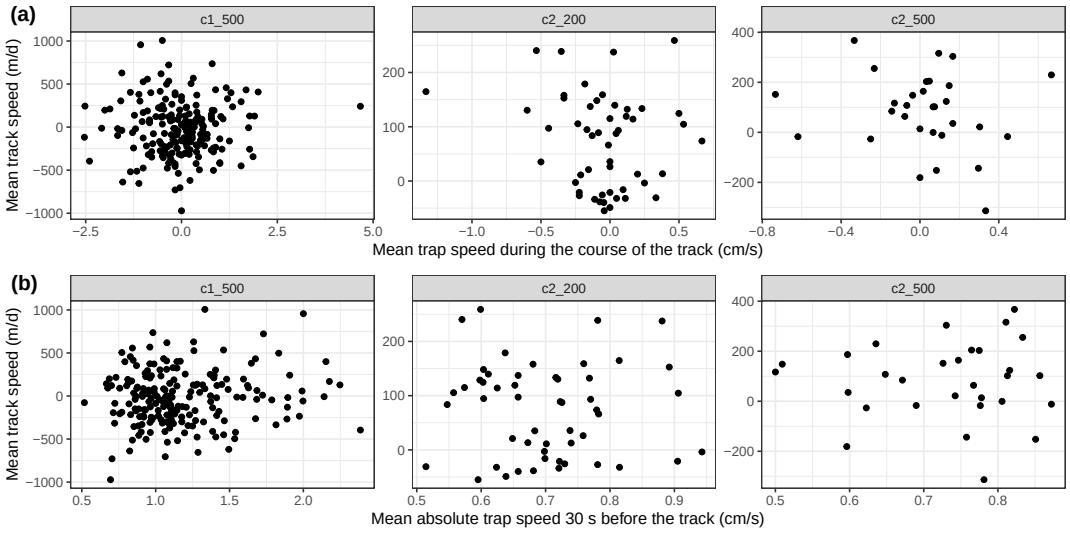

Figure S4.9: Track vertical velocities versus VisuTrap vertical oscillation speed (**a**) before (i.e., 30 seconds before the occurrence of the track) and (**b**) during their course (i.e., instant velocity), for each deployment.

Supporting Information Fig. S10

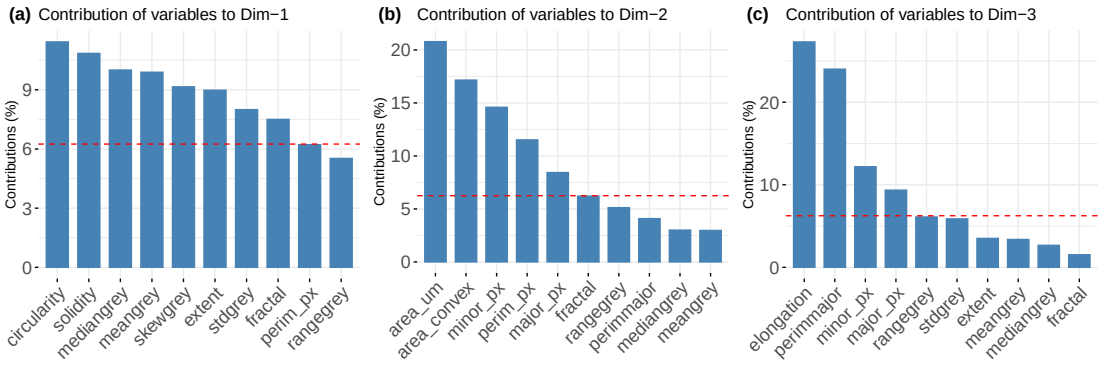

Figure S4.10: Contribution of the initial morphological variables to the three significant axes of the PCA performed on tracked particles. Contribution of variables to (**a**) PC1, (**b**) PC2, (**c**) PC3. Red lines show the mean contribution.

Supplementary table S1

Table S4.1: Particle morphological descriptors computed by scikit-image *regionprops* function and used to perform PCA.

Type	Parameter	Description
Size	Area	Number of pixels of the object
	Convex area	Number of pixels of the smallest convex polygon that encloses the object
	Perimeter	Perimeter of the object
	Major axis length	Length of the major axis of the ellipse fitted on the object
	Minor axis length	Length of the minor axis of the ellipse fitted on the object
Color	Mean grey	Mean grey level value
	Median grey	Median grey level value
	Std grey	Standard deviation of grey level values
	Skew grey	Skewness of the histogram of grey level values
	Range grey	Maximum grey level value − minimum grey level value
Shape	Circularity	1 indicates a perfect circle, decreases as object moves away from a circle
	Elongation	Major axis length to minor axis length ratio
	Extent	Ratio of pixels of the object to pixels in the total object bounding box
Complexity	Perim/Major	Perimeter to major axis length ratio
	Solidity	Ratio of object area to convex hull area
	Fractal dimension	Fractal dimension of the object as defined in Maggi and Winterwerp (2004) and Many et al. (2019)

Supplementary table S2

Table S4.2: *p*-value of correlation tests between track speeds on one hand, and averaged trap speed during the track and from 30 s to the beginning of the trap.

Deployment	Mean trap speed during the course of the track	Mean trap speed 30 s before the track
C1 - 500 m	0.93	0.51
C2 - 200 m	0.23	0.75
C2 - 500 m	0.54	0.90

4.2 In situ imaging sheds light on particle sinking speeds in the North Atlantic

Laget, M., M. Picheral, C. Catalano, L. Guidi, and T. Biard. In preparation.

4.2.1 Introduction

The biological carbon pump (BCP) is a crucial process in the global carbon cycle, exerting far-reaching impacts on atmospheric CO_2 levels and on the Earth's climate system (Sarmiento and Toggweiler, 1984; Kwon et al., 2009). This process involves the biological production of organic material in the surface ocean through photosynthesis and its subsequent downward transport to depths, resulting in atmospheric CO_2 trapping in oceanic waters (Volk and Hoffert, 1985). As organic particles are transported towards the deep ocean, they undergo diverse transformations through interactions with organisms, whether associated with particles or existing freely in the water, ultimately leading to the remineralization of most organic carbon back into CO_2. Only a minor fraction (1-3%; Lampitt et al., 2010) of carbon is eventually sequestered from the atmosphere for long time periods. Although sequestered carbon can be found throughout the water column as refractory material (Legendre and Le Fèvre, 1992), most of it is stored at depths >1000 m (Primeau, 2005; Lampitt et al., 2008a; Passow and Carlson, 2012). Among the mechanisms leading to downward transport, gravitational sinking of particles play a key role in carbon export and sequestration (Stukel et al., 2017; Boyd et al., 2019; Stukel et al., 2023).

Gravitational flux declines exponentially with increasing depth (Martin et al., 1987), with most of this decline occurring within the mesopelagic layer (Arístegui et al., 2005; Robinson et al., 2010). However, the transfer efficiency, defined as the fraction of organic carbon exiting the mesopelagic layer, is highly variable spatially (Buesseler et al., 2007; Henson et al., 2012; Guidi et al., 2015). Indeed, it depends on the nature of sinking material and the remineralization processes it is exposed to. The faster a particle sinks, the more likely it is to reach great depths before its carbon is completely respired (De La Rocha and Passow, 2007). This feature results from its individual characteristics and from the properties of the surrounding seawater.

Marine particle pools encompass individual dead cells or carcasses, aggregates,

fecal pellets, or a mixture of these, spanning a size spectrum from a few micrometers to several millimeters (Alldredge and Silver, 1988; Stemmann and Boss, 2012). A particle can be composed of various organic (e.g., lipids, carbohydrates) and mineral elements (e.g., calcium carbonate, biogenic silica), thereby influencing its morphological properties such as its structure, shape and density. Consequently, marine particles exhibit high morphological diversity, being shaped by the nature of material produced in the surface layer and its inhabitants. Interestingly, these various types of particles have been shown to have different contributions to carbon export (Durkin et al., 2021; Trudnowska et al., 2021). Furthermore, these morphological variations have been linked to a broad range of sinking speeds, ranging from 2 m d^{-1} to 2700 m d^{-1} (e.g., Alldredge and Gotschalk, 1988; Turner, 2002; Iversen and Lampitt, 2020). To analyze this continuous, multi-dimensional spectrum of properties and their distribution within a particle pool, alongside their sinking speeds, a comprehensive set of measurements that can effectively quantify them is needed.

In situ optical devices have yielded extensive data on particle size distribution, concentration and biovolume (Stemmann and Boss, 2012). Among the range of optical instruments available (summarized in Lombard et al., 2019), the Underwater Vision Profiler (UVP; Picheral et al., 2010; Picheral et al., 2022) are in situ camera counting and sizing particles above 100 μm, while also recording individual images of particles larger than 600 μm. By doing so, it provides numerous quantitative measurements of size, shape, gray level, and structural properties (e.g., fractal dimension) of large particles. In its latest version featuring a reduced size, the UVP6 can be integrated onto autonomous platforms (e.g., floats, mooring, etc.), allowing greater flexibility (Picheral et al., 2022). While in situ imaging systems can offer an increasing number of detailed morphological data of encountered particles, their application in biogeochemical studies are still limited (Trudnowska et al., 2021). Moreover, no investigation of relationships between morphological variables and sinking speeds using the UVP6 has been conducted so far.

Here, we use the VisuTrap (chapter 4.1), a sediment trap equipped with an UVP6, to record the sinking velocity of marine particles along their morphological properties. Unlike the standard UVP6 solely recording particle images, it here records the complete imaged volume, enabling the measurement of marine particle sinking velocity while simultaneously recording their morphological characteristics. Our objective is to characterize the morphological structure of

the particle pool and its sinking behavior following a summer bloom in the North Atlantic. Seasonal phytoplankton blooms, followed by large pulses of organic matter, are a key element for carbon export in this region, whose magnitude is further enhanced by the presence of oceanic fronts (Allen et al., 2005). Studying the characteristics and the fate of this intense pulse of primary production is necessary for our understanding of the biological carbon pump in this region. We hypothesize that sinking speeds are influenced by particle morphology, environmental conditions, and ecosystem state and we aim to explore the relationships between them.

4.2.2 Material and methods

Cruise design and sampling strategy

Data were collected around the Porcupine Abyssal Plain Sustained Observatory (PAP-SO; 49° N, 16.5° W; Fig. 4.8) in the northeast Atlantic during the APERO cruise which took place from June, 6th to July, 18th 2023 onboard the N/O *Pourquoi Pas ?*. The sampling strategy was based on quasi-Lagrangian experiments (referred to as 'cycles') lasting 3 to 5 days each. During each cycle, a targeted water parcel was extensively sampled, with a 1 km surface-tethered drifting line following the water mass. A total of five cycles were performed (Fig. 4.8), covering various oceanic conditions. While cycle 1 sampled an anticyclonic eddy, cycles 2, 3 and 5 sampled a cyclonic eddy, but with contrasted productivity (Supplementary Information Table S4.3). Cycle 2 exhibited the highest productivity of the cruise overall. Cycle 5 sampled within the same eddy as cycle 2, but with reduced productivity as it occurred 3 weeks later. Finally, cycle 4 occurred at a front between two cyclonic (cycle 2) and anticyclonic eddies.

Environmental data

A CTD (Sea Bird Scientific 911+) mounted on a rosette was used to perform vertical profiles of hydrographic parameters during each cycle, including conductivity, temperature, pressure, fluorescence and oxygen concentration. A UVP6-HF (Picheral et al., 2022) was mounted on the rosette to simultaneously perform vertical profiles of >100 μm particle abundance.

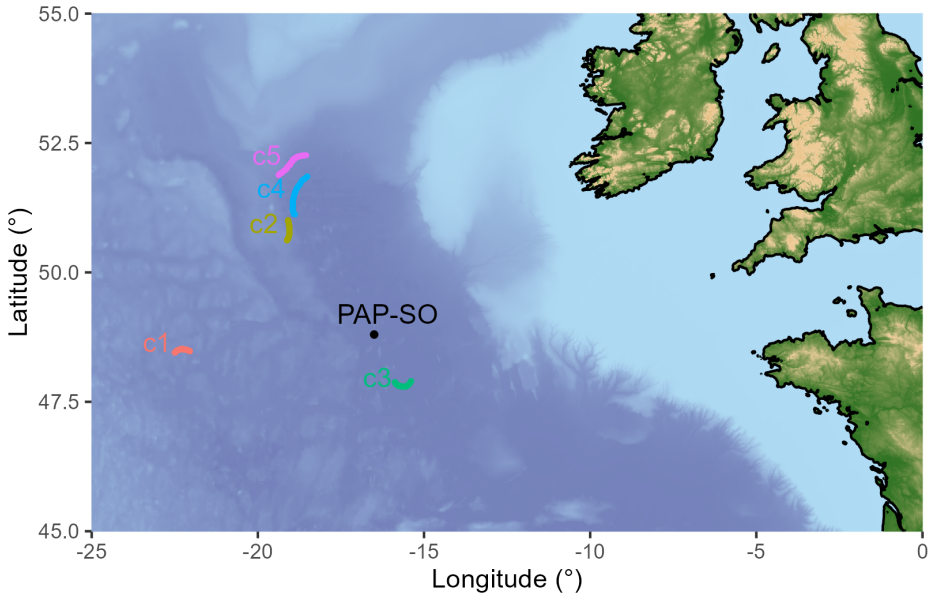

Figure 4.8: Drifting line tracks during the APERO cruise around the Porcupine Abyssal Plain Sustained Observatory (PAP-SO). Bathymetric data come from the ETOPO 2022 database hosted on the NOAA website and queried with the `marmap` R package (Pante and Simon-Bouhet, 2013).

VisuTrap deployment, image recording and image processing

Four VisuTrap (chapter 4.1) were deployed on the drifting line. One VisuTrap was deployed at 100 m and another at 200 m, while two were deployed side by side at 500 m. VisuTrap were deployed at 100 m only during cycles 2 and 4. Briefly, the VisuTrap comprises a UVP6-LP camera (Picheral et al., 2022) inserted within a cylindro-conical sediment trap (chapter 4.1). The UVP6 camera is oriented sideward, allowing for successive recordings of the same sinking particle every 0.7 s (i.e., 1.3 Hz frequency). The UVP6 alternated between two modes: recording full frames without segmentation during acquisition to subsequently conduct particle tracking, and its regular mode to obtain particle size distribution and concentration. Starmon (Star Oddi) were used to record the angle and roll of sediment traps at each depth, and thus correct track angle and speed along the vertical axis. All vignettes recorded during the low-frequency steps were processed using the UVPapp software. For high-frequency acquisition of raw images, particle tracking was performed based on particle size similarity and relative positions as previously described (chapter 4.1). Particle data were imported into the EcoPart application, while both vignettes and particle tracks were imported into the EcoTaxa application (Picheral et al., 2017) for classification and removal

of false tracks as well as tracks of living organisms.

Data analysis

All analyses were performed using the R software version 4.2.2 (R Core Team, 2022) and the packages `tidyverse` (Wickham et al., 2019) and `plyr` (Wickham, 2011) for data manipulation.

CTD data were handled and cleaned using the packages `oce` (Kelley and Richards, 2023) and `castr` (https://github.com/jiho/castr). Normalized abundance size spectra (NASS) on UVP6 mounted on the CTD rosette were computed using the `nbssr` package (https://github.com/jiho/nbssr).

Following the approach by Trudnowska et al. (2021), we conducted a Principal Component Analysis (PCA) using a set of 16 morphological variables associated to size, shape, grey level, and complexity, with 3 to 5 variables within each category (Supporting Information Table S4.4). After a Yeo-Johnson transformation (Yeo and Johnson, 2000), this PCA was applied to the 117,690 particle vignette data (i.e., after having removed zooplankton) recorded for all depths during all cycles. The aim was to establish a morphospace and project the data into a reduced-dimensional space to investigate morphological diversity. Principal Components (PCs) were considered significant if their eigenvalue was superior to the average eigenvalue (>1; Kaiser-Guttman criterion; Cattell, 1966). The morphospace was built and plotted using the morphr package (https://github.com/jiho/morphr). Subsequently, a *k*-means clustering was performed on the particle coordinates on the significant PCs – to retain most of the variance while reducing data dimension – to define particle morphotypes.

To ensure that trap movements had no impact on sinking speeds of particles, we tested for correlations between particle speeds and VisuTrap vertical oscillations both during and before the track occurrence. To reduce uncertainty of sinking speed measurements, we removed tracks for which particles appeared in less than 6 subsequent images. Additionally, tracks displaying a sinuosity index (defined as the ratio between the track total length and the length of the beginning-end segment) at the tail end of its distribution were removed from the analysis. Each track was then associated with a set of environmental values, using the nearest CTD measurement in terms of both time and depth.

Particles forming a track were projected onto the morphospace, and subsequently, each track was assigned a morphotype using *k*-means algorithm. To evaluate differences in sinking speeds across morphotypes, we conducted an anal-

ysis of variance (ANOVA) followed by Tukey post-hoc tests on $\log_{10}$-transformed data, considering each cycle and depth together and then separately.

Environmental variables, including oxygen, temperature, seawater potential density, salinity, large particle abundance and chlorophyll *a* (Chl *a*), were integrated into a new PCA using the `FactoMineR` package (Lê et al., 2008) after a Yeo-Johnson transformation to meet the normality assumption. Sinking speeds were projected as a supplementary quantitative variable to help visualize correlations with PCs. We computed Pearson's correlation coefficients to test the relationship between sinking speeds and significant PCs.

Then, we used Boosted Regression Trees (BRTs) to evaluate our capacity to predict sinking speeds from morphological and environmental predictors. Briefly, BRTs model the relationship between a response variable (sinking speed) and predictors (morphological and environmental variables) by successively combining short regression trees to enhance predictive performance. They offer several advantages, including their ability to handle a large number of categorical or continuous variables, the capability to select relevant explanatory variables, the absence of assumptions regarding the nature of the relationship between predictors and the response variable, and the incorporation of interactions among predictors (Elith* et al., 2006). Thus, they are a suitable choice since the relationships between predictors and sinking speeds, as well as their interactions, remain unknown. BRTs' statistics R^2 was calculated as the squared Pearson's correlation coefficient between observed and predicted values.

Lastly, we estimated particle flux for each morphotype at each depth and for each cycle. To do so, particle abundance for each morphotype (in # m^{-3}) was converted to carbon concentration (in mg C m^{-3}) using equations described in Durkin et al. (2021) (see Supporting Information Table S4.4 for details). Then, we multiplied carbon concentration for a given deployment (obtained with the standard UVP6 acquisition mode) by the morphotype's median sinking speed for the same deployment.

- In the future, this will be compared to fluxes estimated from BRTs developed above and from the method from (Guidi et al., 2008).

4.2.3 Results

Environmental conditions

Cycle 2 (C2), occurring in a cyclonic eddy, was the most productive cycle sampled (1.34 μg Chl *a* L^{-1} averaged at the DCM; Supporting Information Fig. S4.11a), followed by the anticyclonic eddy C1 (1.21 Chl *a* μg L^{-1}; Supporting Information Fig. S4.11a). Average Chl *a* concentration at the DCM was the lowest during cycle 5 (0.25 μg L^{-1}), which took place in the same eddy that C2 but about 20 days later. C3 was characterized by low Chl *a* concentrations and cycle 4 by high Chl *a* concentrations. Particle abundance, measured by the UVP6-HF mounted on the CTD rosette, reached the cruise maximum during C2 near the DCM (300-450 # L^{-1}; Supporting Information Fig. S4.11b). C5 showed high particle concentrations at the surface (250-400 # L^{-1}), which sharply declined with depth (Supporting Information Fig. S4.11b). Although C1 displayed high Chl *a* concentrations, it exhibited low particle concentrations (130-200 # L^{-1}), but with a smooth decline with depth. During C3 and C4, maximum particle concentration was the highest at the surface but quickly decreased with depth (Supporting Information Fig. S4.11b). C2 had the highest proportion of large particles, decreasing with depth (NASS slope -0.9 at 100 m, -1.2 at 200 m and -2.0 at 500 m). Slopes were higher at all depths and similar for C3, C4 and C5.

Particle morphological properties

To investigate morphological diversity, a PCA was performed on vignettes data acquired with the VisuTrap's UVP6 in their standard acquisition mode, to summarize the 16 morphological variables (Supporting Information Table S4.4) into a few easily interpretable variables. The first four PCs were significant based on the Kaiser-Guttman criterion, accounting for 89.7% of the total variance within the dataset. PC1 alone captured 44.9% of the total variance and segregated particles based on their size (Fig. 4.9a), with larger particles on the right hand side of the plane (i.e., PC1>0) and smaller particles on the left hand side (i.e., PC1<0). Hence, this PCs was mostly driven by size-related variables such as perimeter and convex area (Supporting Information Fig. S4.12). PC2, explaining 25.4% of the total variance, opposed darker and more compact particles (i.e., PC2>0) to lighter and more loosely structured ones (i.e., PC2<0; Fig. 4.9a). It was mostly influenced by grey-related variables (e.g., skewgrey, mediangrey; Supporting Information Table S4.4) and minor axis length (Supporting Information Fig. S4.12).

PC3 accounted for 12.4% of the variance and was primarily driven by elongation, the ratio of the perimeter length to the major axis length, along with grey variables (e.g., cvgrey, mediangrey; Supporting Information Table S4.4, Fig. S4.12). It separated elongated and dark particles from rounder and lighter ones (Fig. 4.9a). PC4, mostly influenced by the kurtosis of grey pixels (Supporting Information Fig. S4.12), explained 7.0% of the variance and opposed particles with an homogeneous structure (i.e., PC4<0) to those with a more heterogeneous structure (i.e., PC4>0; Fig. 4.9a).

Based on the *k*-means clustering algorithm performed on the coordinates of particles along the first four axes of the PCA, we defined four morphological morphotypes (Fig. 4.9b), named following Trudnowska et al. (2021). Particle aspects and morphological metrics are displayed in Supporting Information Fig. S4.13. Morphotype 1 "Fluffy", consisted of fluffy, i.e., loose medium-sized particles (mean ESD = 1,000 μm, mean circularity = 0.71). Morphotype 2 "Flakes" included small flake-type particles with a homogeneous structure and a round shape (mean ESD = 695 μm, mean solidity = 0.89, mean circularity = 0.85). Morphotype 3 "Elongated" comprised elongated particles (mean ESD = 756 μm, mean elongation = 2.31, mean circularity = 0.47). Morphotype 4 "Agglomerated" comprised large, heterogeneous and loose agglomerated structures (mean ESD = 1,562 μm, mean elongation = 1.95, mean solidity = 0.76, mean circularity = 0.40).

C2, with the highest particle abundance overall (Supporting Information Fig. S4.11), was dominated by flakes and elongated particles at 100 m and by flakes at 200 and 500 m (Fig. 4.9c). C1, characterized by low particle abundances, showed a high proportion of flake particles at 200 m, which decreased at 500 m (Fig. 4.9d). In contrast, for all other cycles, the proportion of flake particles increased with depth. The proportion of agglomerated particles was low during C1, C2 and C3 but was consistently higher during C4 (frontal zone) and C5 (Fig. 4.9d), the latter occurring in the same eddy as C2 but 20 days later, likely characterizing older particles.

- To refine these observations, data from the UVP6 mounted on the CTD rosette will be used 1) to check if there is any bias leading to an over- or undercollection of certain morphotypes - as it was shown previously that particle size spectra slopes were the same 2) to refine changes in particle morphology with depth.

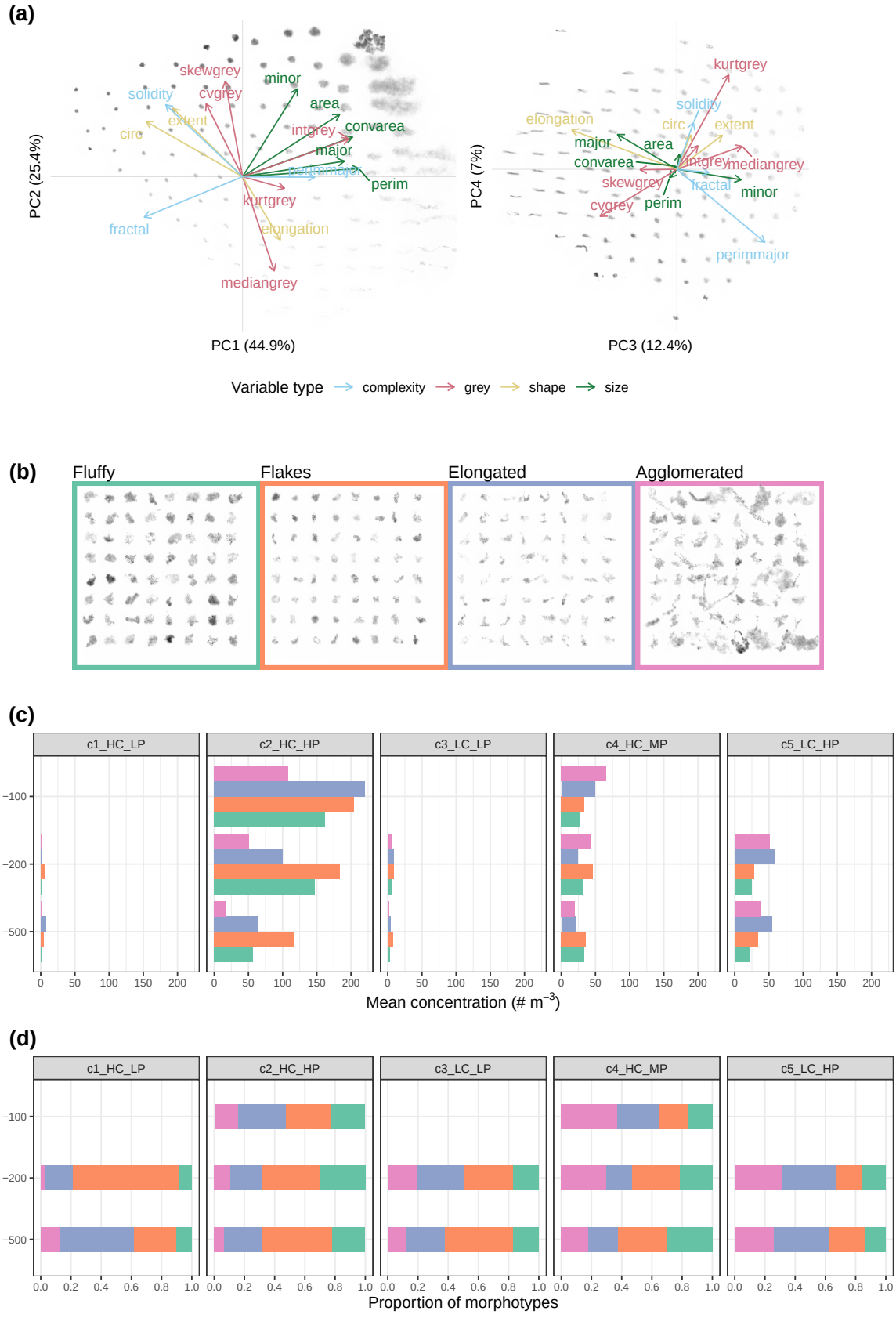

Figure 4.9: (Caption next page.)

Figure 4.9: (Previous page.) Description of particle morphology and distribution, recorded with the VisuTrap, among cycles. (**a**) Principal Component Analysis of the 16 morphological descriptors of particles. The four significant principal components (PCs) are represented with PC1 and PC2 on the left and PC3 and PC4 on the right with the percentage of variance explained by each PC between parentheses. Colored arrows show correlations between descriptors and each PC, with each color representing a type of morphological descriptors. Randomly chosen example images are displayed according to their coordinates on each plane using the `morphr` package. Morphological descriptors are described in (Supporting Information Table S4.4). (**b**) Randomly chosen example images for each morphological cluster (morphotype) determined from the *k*-means algorithm. Morphotypes were named after Trudnowska et al. (2021). (**c**) Mean particle abundance for each morphotype, cycle and depth as determined from vignette data. (**d**) Distribution of morphotypes, for each cycle and depth. LP, MP and HP stand for low, medium and high particle abundance respectively. LC and HC stand for low and high chlorophyll *a* concentration.

Particle sinking speeds

From an initial dataset of 22,150 sinking tracks with a particle appearing in at least 4 images, and after removing false tracks, tracks associated with living organisms, sequences with high VisuTrap oscillations, and sinuous tracks, we acquired a total of 8,942 individual measurements of particle sinking speeds with particles appearing in a minimum of 6 images (i.e, >5 s; Table 4.3). For all sequences considered, no correlation with trap vertical speed nor acceleration was observed (Kendall's τ correlation test: p-value <0.05). The majority of tracks (7,225) were recorded during C2, which showed the highest particle abundance. Particle ESD ranged from 570 μm to 6,625 μm (averaging 924 $\pm$ 434 μm). Sinking speeds ranged between 4 and 1,104 m d^{-1} (averaging 301 $\pm$ 165 m d^{-1}). We observed significant differences in sinking speeds between sampled depths for C2, C3 and C4 (Supporting Information Fig. S4.14).

Table 4.3: Number of tracks recorded and particle characteristics for each cycle at each depth. Particle Equivalent Spherical Diameter (ESD) and sinking speed are expressed in mean ± sd. LP, MP and HP stand for low, medium and high particle abundance respectively. LC and HC stand for low and high chlorophyll *a* concentration.

Cycle	Depth	n	Particle ESD (μm)	Particle sinking speed (m d^{-1})
C1 (HC-LP)	200	41	711 ± 110	405 ± 173
	500	12	698 ± 64	317 ± 167
C2 (HC-HP)	100	4,036	885 ± 285	259 ± 129
	200	1,962	888 ± 324	324 ± 178
	500	1,227	812 ± 273	295 ± 148
C3 (LC-LP)	200	68	1,168 ± 707	313 ± 174
	500	42	928 ± 590	523 ± 232
C4 (HC-MP)	100	187	1,282 ± 914	308 ± 167
	200	289	1,197 ± 771	408 ± 220
	500	428	1,111 ± 694	356 ± 182
C5 (LC-HP)	200	386	1,165 ± 704	395 ± 206
	500	264	1,085 ± 804	390 ± 198
Total		8,942		

Relationships between particle sinking speeds, morphology and environmental variables

Sinking speeds showed significant correlations (Kendall's τ correlation test, p-value <0.05) with all morphological variables considered, except with extent and Perim/Major. However, these correlations were very weak (absolute τ value <0.1).

We then assigned a morphotype to each particle forming a track and compared the distribution of sinking speeds among morphotypes. All cycles and depths considered together, we did not observe significant differences between elongated, fluffy and flake-like particles (one-way ANOVA and Tukey post-hoc tests: p-value >0.05). Only agglomerates, characterized by a large size and a heterogeneous structure, showed on average higher sinking speeds with all other morphotypes at 100 during C2 (one-way ANOVA and Tukey post-hoc tests: p-value <0.0001; Supporting Information Fig. S4.15). Then, we looked at the correlation between particle area and sinking speed for each morphotype separately. We observed a weak positive correlation with particle area for the agglomerated morphotype only (Kendall's τ = 0.10, p-value <0.0001).

As we recorded a limited number of tracks as well as low particle concentration for C1 and C3, the following analyses are focused on C2, C4 and C5. Multiple

significant differences in sinking speed distributions were observed for the same morphotype across cycles (Fig. 4.10). On average, at 200 and 500 m, particle sinking speeds were almost always lower for all morphotypes during C2 (cyclonic eddy with high Chl *a* and high particle abundance) than during C4 (frontal zone with high Chl *a* and medium particle concentrations) and C5 (cyclonic eddy with decreased Chl *a* concentration but high particle abundance). At 100 m, only elongated particles and flakes had a higher speed during C4 than C2.

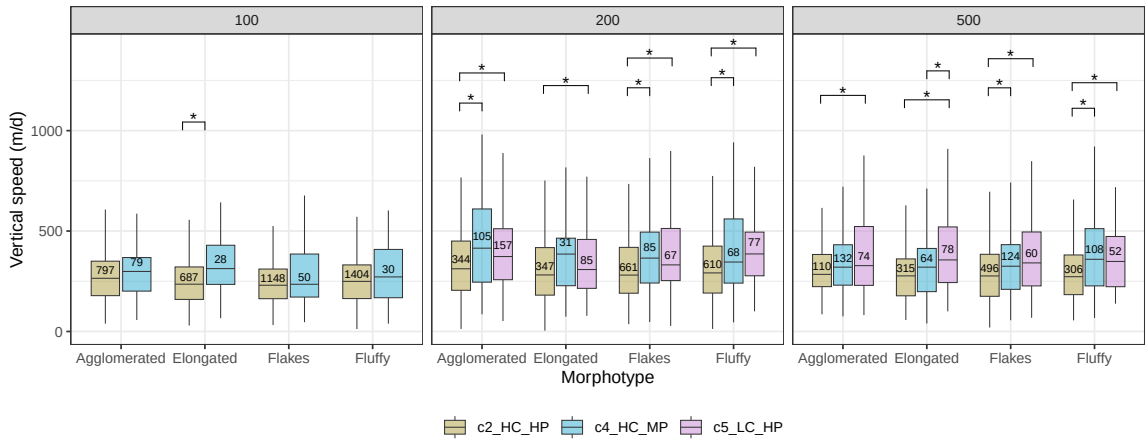

Figure 4.10: Differences in sinking speed distribution within particle morphotypes according to cycle and depth. MP and HP stand for medium and high particle abundance respectively. LC and HC stand for low and high chlorophyll *a* concentration. The boxes' bottom and top boundaries represent the 25th and 75th percentiles respectively. Lower and upper whiskers stretch from the 25th and 75th percentile to the minimum and maximum value within 1.5 times the percentile's inter-quartile range (IQR). Numbers show the number of tracks for each boxplot. An analysis of variance followed by Tukey post-hoc tests identified differences in sinking speeds between some morphotypes (*: *p*-value <0.5).

Subsequently, we performed a PCA on environmental variables associated with each tracked particle, and projected its sinking speed onto the resulting PCA space (Fig. 4.11). PC1 was related to depth, with tracks recorded at 500 m on the right hand side of the plane (PC1<0) and tracks recorded at 100 on the left hand side (PC1>0). This PC was mostly driven by seawater density (sigmaTheta), oxygen and temperature (Fig. 4.11a). PC2 was mostly driven by salinity, particle abundance (LPM) and to a lower extent temperature and Chl *a* concentration. It separated tracks occurring at low or medium particle concentration (PC2<0; especially during cycles 3, 4 and 5) to those occurring at high particle concentration (PC2>0; Fig. 4.11b). Sinking speed showed a weak but significant negative correlation with PC1 (Pearson correlation coefficient: -0.13, *p*-value <0.0001) and PC2 (Pearson

correlation coefficient: -0.14, p-value <0.0001), and therefore a positive correlation with depth and with cycles 3, 4 and 5.

- To complement these analyses, additional variables will be added, such as pigment and community composition data. Such variables will give knowledge about particle composition (e.g., presence of ballasting minerals, formation of specific compounds...) that defines particle density.

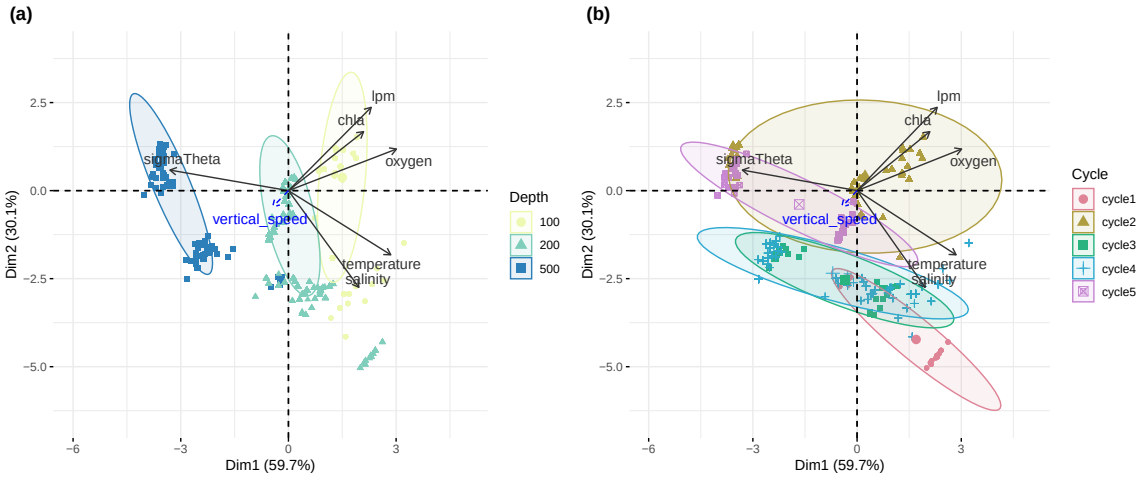

Figure 4.11: Principal Component Analysis of six environmental variables. The two significant principal components (PCs) are represented with the percentage of variance explained by each PC between parentheses. Black arrows show the correlations between original variables and each PC. Blue arrows show the correlations between sinking speeds and each PC. Confidence ellipses for the barycenters of the categorical variable 'track type' are displayed with a threshold of 0.9. Points represent the position of individual particles in the factorial plane and are colored according to (**a**) track depth (**b**) track cycle.

To assess our ability to predict particle sinking speeds using morphological and environmental variables, we developed BRTs to identify the most significant predictors which can explain and predict this variability. To do so, morphological variables showing a significant correlation with sinking speed were used (see above). We also included the six environmental variables used for the PCA plus exact trap depth. We constructed BRTs including particles recorded at all depths (R^2 = 10.6%, p-value <0.0001; Supporting Information Fig. S4.16). Variables that explained most of the variability were depth (26.7%), oxygen (10.5%), particle abundance (9.0%) and Chl *a* concentration (8.8%). When considering only morphological variables, R^2 was not significant (p-value >0.05).

To remove the effect of depth, we performed BRTs on tracks recorded at each depth separately. At 100 m (R^2 = 7.63%, p-value <0.0001), variables that explained

most of the variability were Chl *a* concentration (11.7%), median grey level of each particle (11.5%), seawater density (10.8%) and particle abundance (10.1%). At 200 m (R^2 = 5.33%, p-value = 0.0001), variability was mostly driven by particle abundance (12.5%), oxygen concentration (11.2%) and fractal dimension (7.1%). At 500 m (R^2 = 13.6%, p-value <0.0001), oxygen concentration (20.0%) primarily drove variability, followed by seawater density (8.4%).

Particle flux

Using median sinking speed for each morphotype measured above, we estimated carbon flux for each morphotype, cycle and depth using carbon-to-volume relationships described in Supporting Information Table S4.5. Total carbon flux was highest during C2 (145 ± 84 mg C m^{-2} d^{-1} at 200 m) and lowest during C1 (2 ± 1 mg C m^{-2} d^{-1} at 200 m). It was highest at 200 m during C4 (132 ± 83 mg C m^{-2} d^{-1}) and C5 (130 ± 66 mg C m^{-2} d^{-1}). Estimated carbon flux of agglomerated particles sharply decreased between 200 m and 500 m, but this decline was less pronounced during C5 (Fig. 4.12). Carbon flux of fluffy particles decreased little with depth except for C2. Carbon flux of flakes was highest at 200 m during C2 and C4 and decreased slightly at between 200 and 500 m. Carbon flux of elongated particles decreased with depth for C2 and C4, but increased between 200 and 500 during C5.

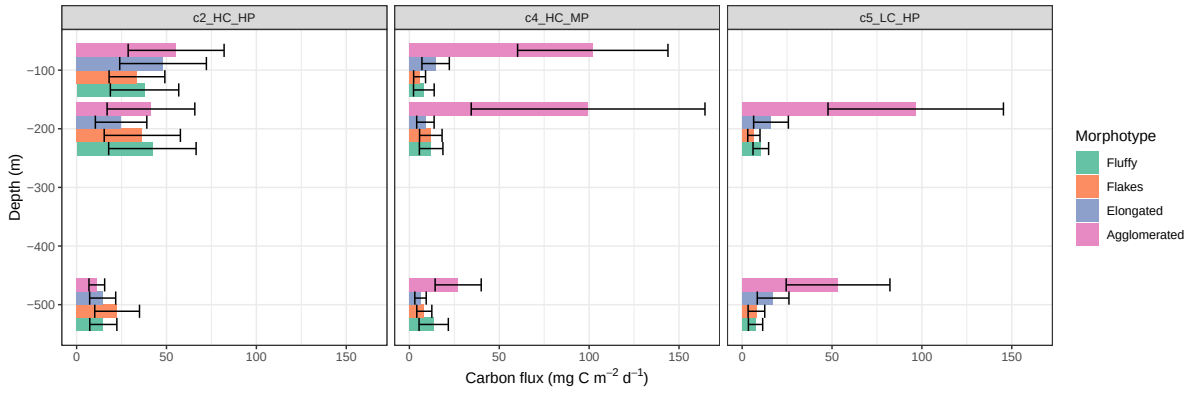

Figure 4.12: Carbon flux for each morphotype and depth, for cycles 2, 4 and 5 from VisuTrap data. Fluxes were calculated as the median sinking speed times carbon concentration at each depth. MP and HP stand for medium and high particle abundance respectively. LC and HC stand for low and high chlorophyll *a* concentration. Error bars are calculated as median carbon flux ± median absolute deviation times carbon concentration for each morphotype at each depth.

4.2.4 Discussion

The sinking speed and flux of marine particles in the North Atlantic

Using in situ cameras mounted onto sediment traps and deployed along a drifting line, we successfully measured the sinking speed of 8,942 marine particles (size 0.6-6.6 mm) under diverse oceanic conditions during a summer phytoplankton bloom. We observed an extensive range of sinking speeds, spanning from a few meters per day to >1,000 m d^{-1}, with a significant fraction settling between 200 and 350 m d^{-1}. This range is consistent with observations obtained using various methodology, including in situ measurements (e.g., Alldredge and Gotschalk, 1988; Peterson et al., 2005; Trull et al., 2008; Iversen and Lampitt, 2020). In particular, these ranges of velocity have been observed during a bloom period in the Mediterranean Sea (Peterson et al., 2005) and at the same location (Villa-Alfageme et al., 2014; Villa-Alfageme et al., 2016). However, lower sinking speeds have also been estimated during a bloom period, for example in the subpolar North Atlantic (76 m d^{-1}; Briggs et al., 2011), in Arctic waters (38 m d^{-1}; Trudnowska et al., 2021), but estimated for the bulk particle population. Such variations may be attributed to the nature of the ecosystem or to methodological differences in the proportion of fast- and slow-sinking particles recorded.

As the cyclonic eddy C2 evolved to a less productive C5, we noticed an increase in speeds at 200 m: 324 $\pm$ 178 and 395 $\pm$ 206 m d^{-1} respectively. A dramatic increase in average sinking speeds was previously reported in a one-week interval at PAP (Villa-Alfageme et al., 2016). This shift was hypothetically attributed to the formation of large and fast-sinking diatom aggregates during the bloom period. While the number of particles was higher during C2, a shift in morphology from flakes to elongated and agglomerated particles occurred as this cyclonic eddy evolved toward C5. Despite the diversity of particles within this morphotype, its dominance could potentially be attributed to an influx of fast-sinking fecal pellets because of an increased zooplankton feeding activity following the bloom. Additionally, larger particles and a higher proportion of agglomerated particles characterized this post-bloom period.

Carbon fluxes of agglomerated particles dominated during C4 and C5 compared to C2, which is easily explained by an increased particle size during C4 and C5. Flakes-mediated fluxes decreased little with depth, likely because these particles are more refractory and less degraded than other morphotypes. Total POC flux (including fast and slow sinking particles) at the base of the mixed layer

at PAP using the Marine Snow Catcher was estimated to be 146 ± 26 mg C m^{-2} d^{-1} (Riley et al., 2012), which is close to fluxes estimated at 200 m during C2, C4 and C5. Using radioisotopes, POC flux was estimated to be 64 mg C m^{-2} d^{-1} at 100 m (Thomalla et al., 2008), which is close to measurements at 100 m during C4 (130 ± 59 mg C m^{-2} d^{-1}), and 207 mg C m^{-2} d^{-1} at 100 m (Lampitt et al., 2008b). Thus, our POC flux estimates fall within the range measured from various techniques, except during C1 and C3 where POC fluxes were exceptionally low given oceanic conditions. In addition to the sinking speed measurements, we were also able to measure various particle morphological characteristics, enabling us to explore the relationships between these data and sinking speeds.

- Estimated fluxes will be compared to fluxes measured from sediment traps. To investigate the type of particle and the presence of fecal pellets within each morphotype, more investigation of particle types and zooplankton community for each cycle will be done using data from the UVP6-HF.

Factors influencing sinking speeds

Our findings suggest a weak impact of particle morphology on sinking speeds overall. Indeed, only agglomerated particles showed distinct sinking speed distributions compared to other morphotypes. However, it is important to note that morphotypes defined on UVP images in fact encompass a broad diversity of particles. For example, the elongated morphotype comprises particles such as fecal pellets, but can also include diatom-chains or phytoplankton colonies (Trudnowska et al., 2021) which can explain the broad range of measured sinking speeds. Our undertaken approach, using a PCA to resume numerous morphological variables into a few interpretable variables (Trudnowska et al., 2021), offers an alternative to the time-consuming manual categorization of particles into predefined groups (e.g., Durkin et al., 2021). However, our dataset encompasses particles of varying composition and age. As such, we observed little effect of particle size, even among the same morphotype, which aligns with previous observations (Nowald et al., 2009; Iversen and Lampitt, 2020). The effect of particle shape was not apparent through correlation analyses, which was already observed in prior studies (Laurenceau-Cornec et al., 2015; Iversen and Lampitt, 2020). We also observed little effect of particles' grey level. Although no direct relationship exists, grey level values can be seen as a proxy for particle density – darker appearances implying denser and more compact structures. Excess density, re-

sulting from particle composition and compactness, can substantially increase sinking velocities (Ploug et al., 2008). However, such an effect was weakly captured from UVP images. Laurenceau-Cornec et al. (2015) demonstrated that chemical composition and phytoplankton cell characteristics predominantly account for variations in sinking velocities, yet these parameters necessitate additional measurements beyond those provided by the UVP. While the UVP provides 2D shape measurements of size, shape and structure, it lacks the ability to provide insight into a particle's composition, internal structure, and 3D shape – which can substantially differ among particles of similar 2D appearances. This is especially true for large particles, but the smaller a particle appears, the less morphological details it will have. Additionally, although the ballast effect may increase the density of a particle and thus its sinking speed (e.g., Iversen and Ploug, 2010), the UVP cannot distinguish the presence of ballasting minerals. Other factors like aggregation processes and particle stickiness can exert influence on sinking speeds by modifying their structure and density, but are difficult to measure. Aggregation processes depend on phytoplankton cell stickiness or their ability to produce compounds such as transparent exopolymers, which are species-specific (Crocker and Passow, 1995) and depends on cell physiology and the availability of nutrients (Kiørboe et al., 1990), emphasizing the need to include data relative to phytoplankton communities in analyses.

The factor explaining most of sinking speed variations was the depth at which particles were recorded. The observed negative correlations with Chl *a* and oxygen concentrations may in fact result from the observed positive correlation with depth. Such increase in particle speed with depth was observed between in the upper 500 m at PAP (Villa-Alfageme et al., 2016), but also off California (Pilskaln et al., 1998), and at substantially greater depths (from 100-2,200 to 2,200-3,500 m) in the Equatorial Pacific and the Arabian Sea (Berelson, 2001). However, this trend was not observed across all cycles and is not always reported (Nowald et al., 2009). During C2 and C4, the highest average speeds were recorded at 200 m rather than at 500 m. This contrasts with a consistent increase in sinking speeds with depth across the North Atlantic throughout the year (Villa-Alfageme et al., 2016). Decrease in particle size with depth was observed but not for all cycles. Therefore, such relationship should be taken with caution and additional factors may be responsible for the observed increase with depth, such as repackaging, disaggregation or a loss of low-density, slow-sinking particles (Nowald et al., 2009). Indeed, the proportion of flakes, which are likely to be more compact,

increased with depth for all cycles except C1. As a particle sinks, water going through could modify its structure and compact it (Guidi et al., 2008), but this effect would depend on the original structure of the particle as it forms. Furthermore, we can hypothesize that oxygen levels, influencing metabolic activity of particles, might be responsible for the production of compounds impacting a particle density. Temperature and salinity effects, two parameters that determine seawater viscosity, were weak. A strong effect of temperature was previously shown (Bach et al., 2012), but the range of temperatures considered (extending over 9°C) was larger than ours (temperatures ranged between 7°C and 12.5°C). In addition to decreasing seawater viscosity, an increase in temperature can fasten the remineralization process of the lighter organic fraction within particles. As a result, only fast-sinking particles may reach the mesopelagic zone (Villa-Alfageme et al., 2016). Therefore, peaks in sinking speeds observed at 200 m during C2 and C4 could be attributed to the formation of fast-sinking aggregates in the upper mesopelagic zone, which could be fragmented at greater depths. In contrast, the increase in sinking speeds between 200 and 500 m during C3 could indicate a higher degree of remineralization (Berelson, 2001).

To refine our explanations of sinking speeds, additional variables are needed. Surface communities, which exert an influence on aggregate composition and structure, influence initial particle sinking speeds exiting the euphotic zone and clear differences were observed between PAP (temperate ecosystem) and BATS (oligotrophic ecosystem) (Villa-Alfageme et al., 2016). Berelson (2001) noted that particle sinking speed is negatively correlated with surface primary production, which may be related to dominant phytoplankton taxa. They further observed a steeper percent organic carbon decrease associated with more important changes in sinking speeds with depth. Indeed, zooplankton grazing and microbial activities, associated with the loss of slow-sinking particles and the organic fraction in larger particles. This underscores the importance of linking our results to phytoplankton communities, particularly in terms of how they relate to particle properties and the ability to form fast-sinking aggregates. Such data will shed light on the observed sinking speeds and will help flux estimates from UVP data.

In situ imaging and flux estimates

Compared to classical flux measurement methods, the UVP presents numerous advantages. It provides measurements at the level of individual particles, encompassing a broad size range (0.1 - 2.6 mm for size measurements; Lombard et al.,

2019. UVP profiles are characterized by enhanced temporal and spatial resolution than sediment traps and radiochemical tracers. The UVP5 has notably been used to infer particle fluxes based on particle size distribution, assuming that sinking speeds can be estimated through a power law that depends on particle size (Guidi et al., 2008). However, achieving this estimation requires fine tuning of power-law exponents using sediment trap or thorium data, given that substantial variations have been observed across different oceanic regions (Iversen et al., 2010; Fender et al., 2019). In addition, as shown in this study and previously (Laurenceau-Cornec et al., 2015; Iversen and Lampitt, 2020), the relationship between size and sinking speed is not straightforward and accurate estimations are needed for flux estimates using the UVP. Here, we used a modified version of the UVP6 to derive particle flux not only of the bulk population, but for diverse morphotypes across various environmental conditions. While we show that sinking speeds cannot yet be well predicted from UVP images, improving such an approach is necessary. Indeed, particle diversity must be considered in flux estimates to improve assessment of their respective contribution, but trade-offs have to be found to avoid overly time-consuming approaches. Statistical methods have helped to investigate their diversity (Trudnowska et al., 2021); however, particle classification needs to be improved. Classifying particles into broad categories (e.g., aggregates, long fecal pellets, short fecal pellets), for which particles can be expected to be of similar composition, and then performing morphological analyses may uncover relationships between sinking speeds and morphology. Lastly, although this task is challenging, linking particle images to composition or a range of densities will be required in the future to improve flux estimates using in situ imaging.

Author contribution

ML and TB designed the work with inputs from MP, CC, LG. TB and CC acquired data. ML validated most images with assistance from TB. ML wrote the code and performed data analysis.

4.2.5 Supporting Information

Supplementary tables

Table S4.3: Type of water mass sampled during each cycle.

Cycle	Type of water mass
C1	anticyclonic eddy
C2	cyclonic eddy
C3	cyclonic eddy
C4	front
C5	cyclonic eddy

Table S4.4: Particle morphological descriptors used to perform PCA.

Type	Parameter (*variable name*)	Description
Size	Area (*area*)	Number of pixels of the object
	Convex area (*convarea*)	Number of pixels of the smallest convex polygon that encloses the object
	Perimeter (*perim*)	Perimeter of the object
	Major axis length (*major*)	Length of the major axis of the ellipse fitted on the object
	Minor axis length (*minor*)	Length of the minor axis of the ellipse fitted on the object
Color	Median grey (*mediangrey*)	Median grey level values
	Coefficient of variation grey (*cvgrey*)	Ratio of the standard deviation to the mean grey level values
	Integral grey (*intgrey*)	Sum of all grey level values
	Skewness grey (*skewgrey*)	Skewness of the histogram of grey level values
	Kurtosis grey (*kurtgrey*)	Kurtosis of the histogram of grey level values
Shape	Circularity (*circ*)	1 indicates a perfect circle, decreases as object moves away from a circle
	Elongation (*elongation*)	Major axis length to minor axis length ratio
	Extent (*extent*)	Ratio of pixels of the object to pixels in the total object bounding box
Complexity	Perim/Major (*perimmajor*)	Perimeter to major axis length ratio
	Solidity (*solidity*)	Ratio of object area to convex hull area
	Fractal dimension (*fractal*)	Fractal dimension of the object as defined in Maggi and Winterwerp (2004) and Many et al. (2019)

Table S4.5: Equations used to convert particle volume V to carbon content Q_{C}. Equations come from Durkin et al. (2021).

Morphotype	Equation
Agglomerated	$Q_{\mathrm{C}} = 0.1^{-9} \times V^{0.8}$
Elongated	$Q_{\mathrm{C}} = 0.1^{-9} \times V^{0.83}$
Flakes	$Q_{\mathrm{C}} = 0.1^{-9} \times V^{0.83}$
Fluffy	$Q_{\mathrm{C}} = 0.1^{-9} \times V^{0.8}$

Supplementary figures

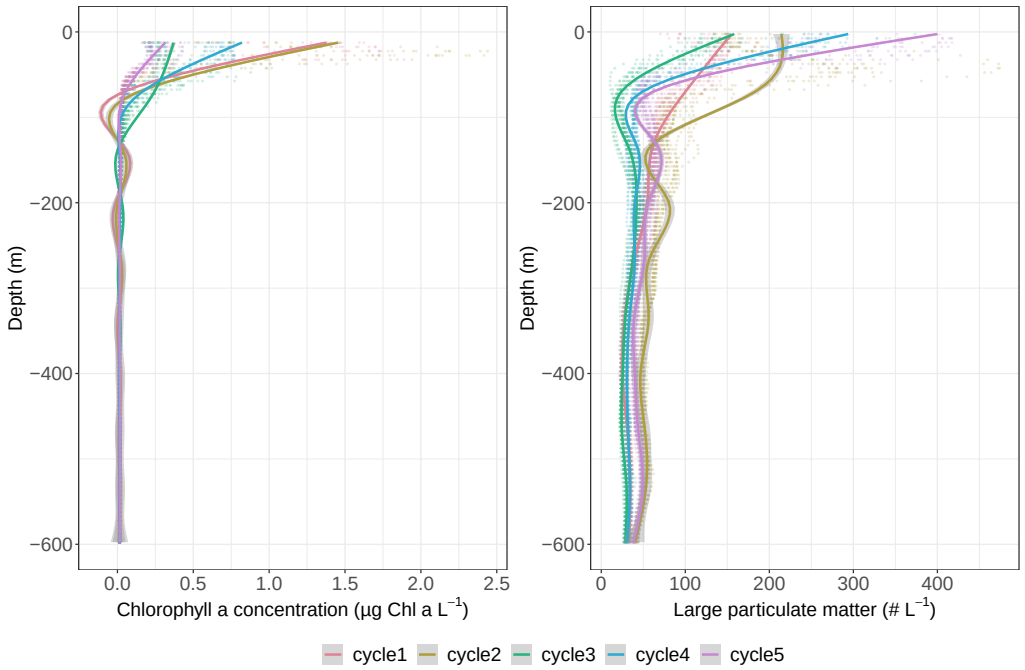

Figure S4.11: Vertical profiles of (**a**) chlorophyll *a* concentration and (**b**) particle abundance using the UVP6-HF. Smoothing was derived using Generalized Additive Models for each cycle.

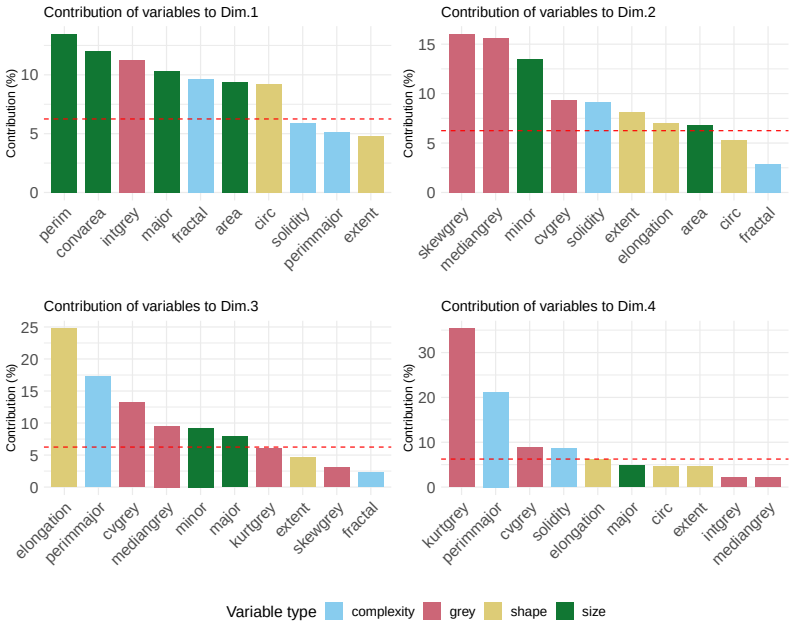

Figure S4.12: Contribution of the 10 morphological variables that contributed the most to each of the four significant axes of the Principal Component Analysis conducted on particle vignettes. Red lines show the mean contribution of all variables.

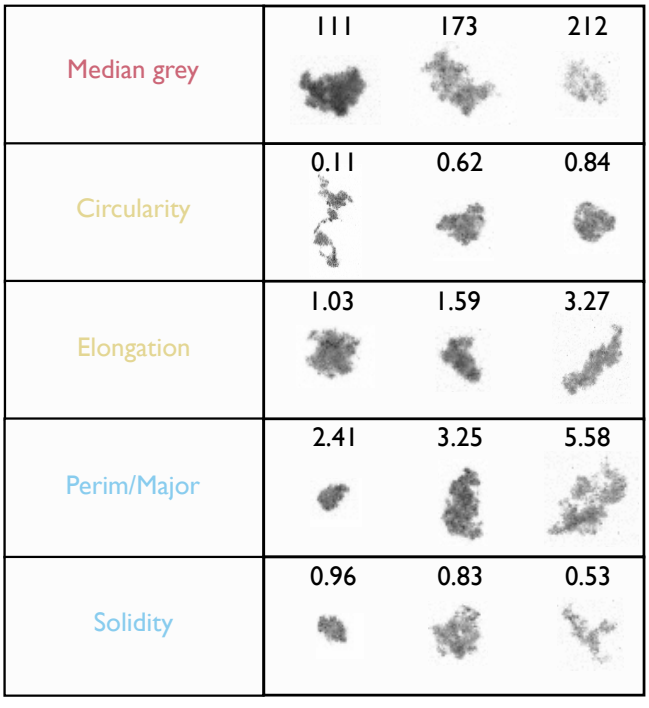

Figure S4.13: Example values and particle aspect for a few morphological variables considered. Each variable is associated with a particle property: grey level (red), shape (yellow), complexity (blue).

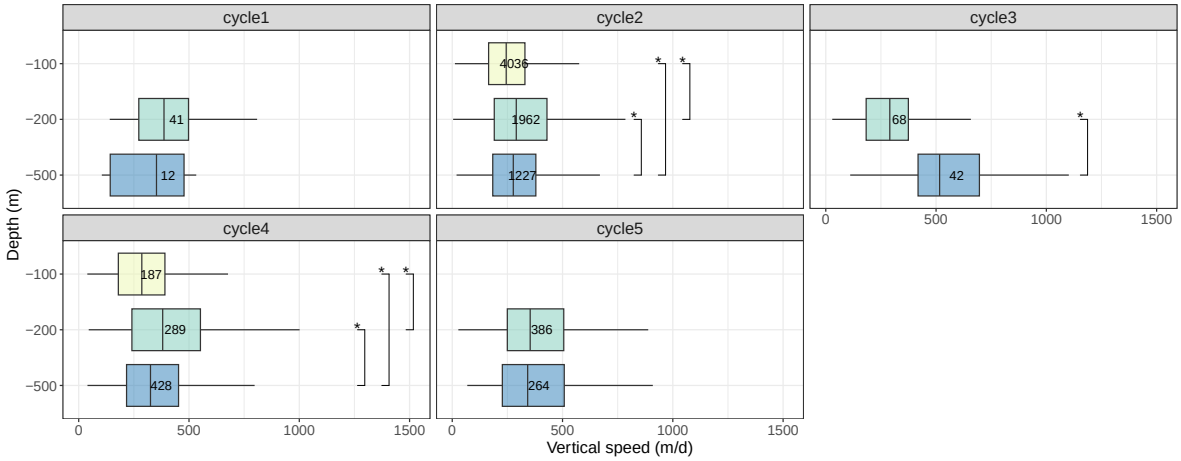

Figure S4.14: Sinking speed distribution according to cycle and depth. The boxes' bottom and top boundaries represent the 25th and 75th percentiles respectively. Lower and upper whiskers stretch from the 25th and 75th percentile to the minimum and maximum value within 1.5 times the percentile's inter-quartile range. Numbers show the number of tracks for each boxplot. An analysis of variance followed by Tukey post-hoc tests identified differences in sinking speeds between some morphotypes (*: p-value <0.05). Numbers indicate the number of observations per boxplot.

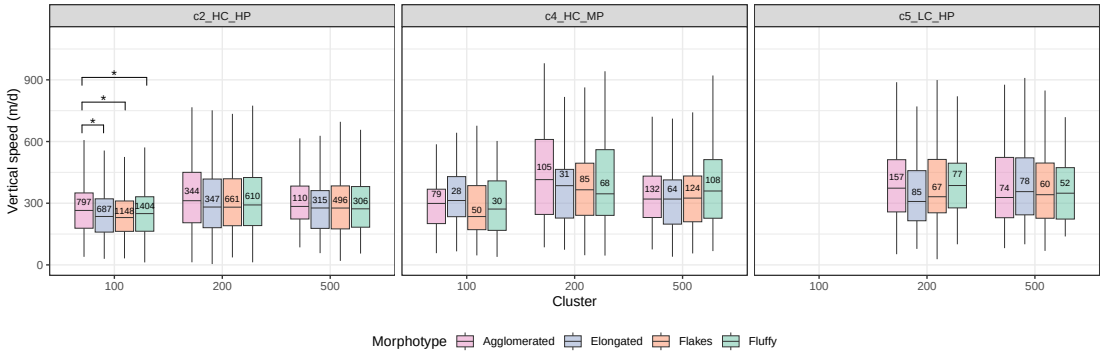

Figure S4.15: Differences in sinking speed distribution between particle morphotypes according to cycle and depth. The boxes' bottom and top boundaries represent the 25th and 75th percentiles respectively. Lower and upper whiskers stretch from the 25th and 75th percentile to the minimum and maximum value within 1.5 times the percentile's inter-quartile range. Numbers show the number of tracks for each boxplot. An analysis of variance followed by Tukey post-hoc tests identified differences in sinking speeds between some morphotypes (*: p-value <0.05). Numbers indicate the number of observations per boxplot.

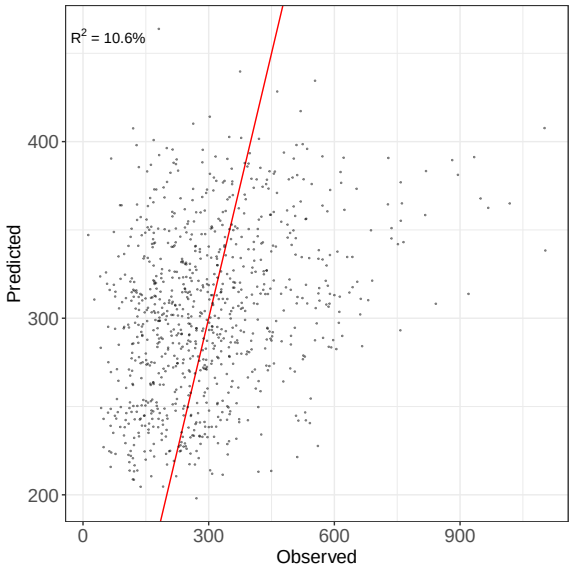

Figure S4.16: Observed versus predicted sinking speeds (m d^{-1}) from boosted regression trees.

4.3 Discussion

4.3.1 Methodological considerations

This chapter was focused on measuring particle sinking speeds in situ, with the aim of untangling factors that influence this parameter, crucial for understanding carbon transfer to the deep ocean. We took advantage of the UVP6 versatility, which can be mounted on various platforms (Picheral et al., 2022). However, during the development of the VisuTrap, we had to face several challenges and additional developments are still needed.

Development of the VisuTrap

A common issue of sediment traps is hydrodynamic bias, wherein the movement of water affects particle collection efficiency, in particular in the upper ocean. Several studies have shown the impact of trap geometry, current velocity, sediment trap tilt, and the design of baffles on particle collection and flux estimates (Gardner, 1980; Gardner, 1985; Honjo et al., 1992). Thus, ensuring the verticality and the stability of the sediment trap line was a key aspect to consider. To improve VisuTrap stability, we added weights at its bottom (Fig. 4.1), reducing its angle and roll values (Fig. S4.3), so that lateral currents diverge around it rather than enter it. In addition, the honeycomb mesh on the top of the trap is expected to

minimize hydrodynamics inside. As keeping minimal hydrodynamics is crucial for accurate speed measurements, we investigated the effect of two trap interior designs on particle size spectra and speeds. The VisuTrap was initially designed with a single honeycomb mesh on top and no internal PVC tube. The design described in section 4.1 was chosen after comparing two designs in order to minimize hydrodynamics inside the trap. The design of the VisuTrap was constrained by the shape of the camera: the opening needed to be wide enough to center the image volume within the trap and to circumvent wall effects. However, this large aperture led to a low height:width aspect ratio (3:1). Reducing this aspect ratio is known to increase the turbulence inside sediment traps and to decrease collection efficiency when lateral currents are strong (Hargrave and Burns, 1979). To investigate this effect, we deployed two VisuTraps side by side to ensure identical flow conditions. One VisuTrap featured two honeycomb meshes (height: 9.5 mm, aspect ratio 5.26) connected by a PVC tube, as described in section 4.1. The other VisuTrap had a single mesh on its top and lacked an internal PVC tube. As a result, the height:width aspect ratio decreased from 2.4 to 1.2 in the absence of the PVC tube. We observed that the presence of two honeycomb meshes increased track straightness. The final VisuTrap design slightly undertraps large particles, although this was not always observed as previously shown in section 4.1, but collect more particles in total than the single-meshed design. Trapping efficiency in sediment traps is influenced by their height:width ratio, with lower ratios corresponding to reduced efficiency (Gardner, 1980). Deeply penetrating baffles can result in an overtrapping of particles <63 μm (Gardner, 1980), but this size fraction is not within the size range covered by the UVP6. Particle tracks were longer (i.e., a particle appeared on more images) on average with the final design, staying longer in the field of view of the UVP6, likely because of less hydrodynamics inside the VisuTrap. An advantage of the VisuTrap is that particle concentration and size spectrum can be compared with other UVP deployments, in particular with the UVP6 mounted on the CTD rosette. By integrating the UVP6 on a sediment trap, we are now able to capture images of particle sinking inside the trap, and thus to measure and quantify various properties aside their speed.

Image analysis

The UVP6 records morphological properties of particles, but it is important to mention that these measurements can vary significantly for a single particle. The

2D shape or structure of a particle may change as they rotate during their sinking, resulting in a range of morphological values along their track. While we calculate an average morphological value, depending on how the particle is recorded, this value may reflect a peculiar particle position. For example, although we took care to remove these tracks, we observed particles displaying a lighter appearance in the initial or final frames of its track, coinciding with their entry or exit from the field of view. This is especially true for large particles. Regarding small particles (<1 mm), morphological data are likely to be less accurate. Additionally, grey level values may vary depending on whether the particle is located in front of or in the back of the field of view. To further refine morphological variability, morphological properties measured by the UVP should be compared to morphological measurements performed by other tools (e.g., Durkin et al., 2021) at the same location. This could help to shed light on the evolution of particle morphology and speed with depth.

Additionally, the UVP6 mounted on the VisuTrap acquires images from the side, unlike when it is mounted on a CTD rosette. Thus, it allows to determine the orientation of particles and organisms relative to the vertical plane. Although this aspect was not explored in this chapter, particle sinking dynamics could be further explored. Recent studies with optical system that acquires images from the side have investigated preferential cell orientation of Collodaria and Phaeodaria (Panaïotis et al., unpubl.) and Foraminifera (Gaskell et al., 2019). This could provide insights into the dynamics of marine particles' movement through the water column and their interaction with the surrounding environment.

While retaining full images is memory-consuming and can limit deployment duration, especially on fixed platforms for long-term deployments, processing images in real-time to extract particle vignettes and positions can reduce acquisition frequency, particularly when dealing with images containing numerous particles. This approach may be feasible in low particle density environments. Therefore, it is essential for data management and storage protocols to account for the large number of images generated and deployments on long-term mooring would require adaptation.

4.3.2 Particle behavior

In our results, although they were not considered in chapter 4.2, we observed a significant number of suspended and ascending particles. This was unexpected,

as it is generally assumed that particles entering a sediment trap sink. While we could expect some particles to be resuspended due to hydrodynamics, it is noteworthy that particles were observed ascending or suspended for over 30 seconds, suggesting that they remained within the UVP6 field of view (about 2 cm thick) and likely experienced minimal hydrodynamic forces. In fact, both biotic and abiotic processes continuously influence particle dynamics, and particles can shift between different types of movement (Baumas and Bizic, 2023). However, these pools of particles, and in particular the ascending one, have received little attention previously. They can be attributed to the suspension of strongly degraded particles stopping their descent (Baumas and Bizic, 2023). Indeed, zooplankton can transform large sinking particles into small, non-sinking particles (e.g., Briggs et al., 2020), and a significant number of swimmers were observed in VisuTrap data. Additionally, microbial degradation can alter fractal dimension (Guidi et al., 2008), and physical shear can erode the surface of a particle (see Baumas and Bizic, 2023, and references therein). Such transformations are likely to not be detected through image analysis and may result in little variation in particle properties.

4.3.3 Perspectives

UVP6 embedded on a float

During the APERO cruise, another UVP6 was mounted on a Twilight Zone Explorer float (Fig. 4.13). This design has the advantage to reduce sediment trap hydrodynamics bias, but the absence of the sediment trap may induce strong effects of lateral currents. The float aimed to stop at 100, 200, and 500 m. At the beginning of each cycle, the float descended to the programmed depth to remain there for a predefined period of time, then descended to the next depth. However, a buoyancy adjustment issue occurred, and the float could not stabilize at its target depth, continuously descending or ascending (Fig. 4.14a). Firmware bugs prevented real-time updates of pressure data, and accurate pressure measurements were only recorded every minute (Fig. 4.14b). To fully exploit this data, it will be necessary to decouple particle speed from float speed.

Temporal aspect

An aspect that was not addressed in this thesis are small-scale temporal variations. By recording at a relatively high temporal resolution (although not the highest

Figure 4.13: Deployment of the Twilight Zone Explorer float during the APERO cruise.

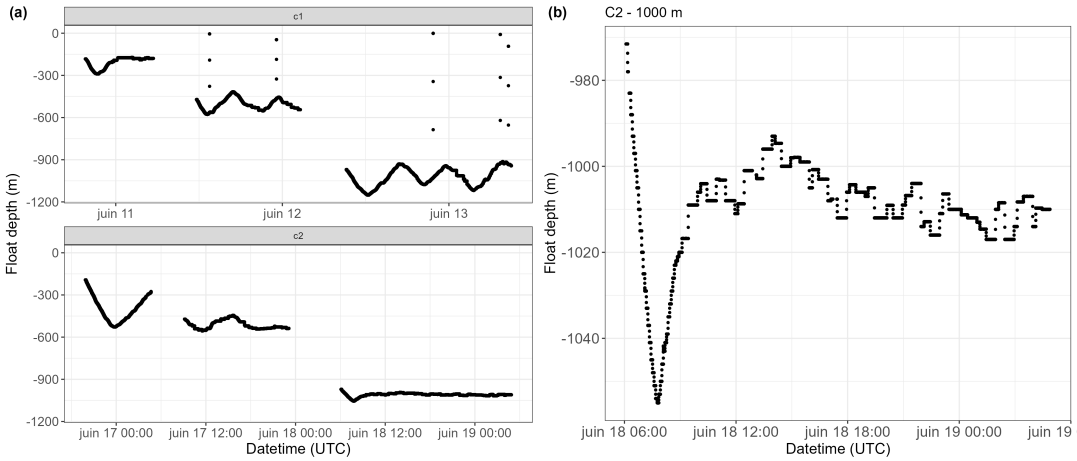

Figure 4.14: Float depth variations. (**a**) Float depth when the UVP6 is recording images for cycles 1 and 2. (**b**) Float depth during cycle 2, during its stop at 1,000 m. Depths are smoothed using a moving average with a window size of 3.

for in-situ imaging devices), we may be able to capture small-scale events (e.g., large pulse events) at discrete depths. For example, particle abundance and total biovolume decreased during cycle 2 of the APERO cruise at 200 m (Fig. 4.15). Such information would be useful to identify potential drivers of such events (e.g., rhizarians, Lampitt et al., 2009) and to investigate conditions of their occurrence.

Estimating carbon fluxes from in situ imaging

As stated previously, refining sinking speed calculations in flux estimates using in-situ imaging devices is necessary. To achieve this, two approaches can be considered using VisuTrap data. We can calculate an average sinking speed for each cluster, or predict the sinking speed of a particle using various morphological and environmental predictors. However, little differences were observed in sinking

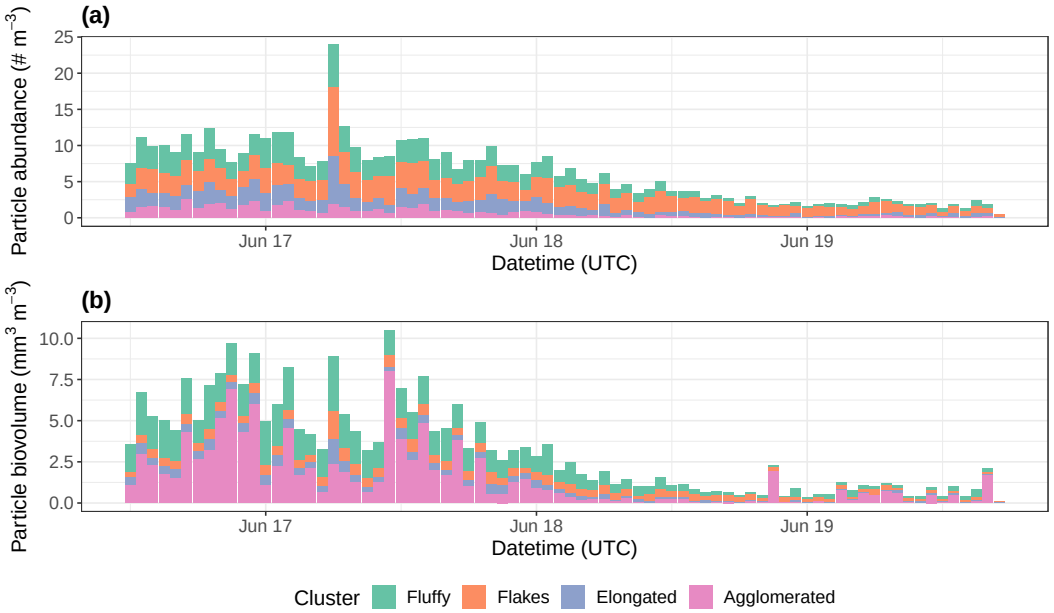

Figure 4.15: Hourly variation in (**a**) particle abundance and (**b**) total particle biovolume during cycle 2 (from Jun. 16th to Jun. 19th 2023, characterized by high chlorophyll *a* concentration and high particle abundance, Fig. S4.11) at 200 m of the APERO cruise which took place in the North Atlantic.

speeds among particle morphotypes, and predictions based on morphological and environmental variables were not accurate. In my view, the particle classification process need to be refined in the future. Given the extensive datasets collected, an automated approach using PCA and statistical clustering has the advantage to be more efficient. Still, morphotypes contain heterogeneous particles. A hybrid approach involving classification in pre-defined particle categories (such as done by Durkin et al., 2021) would give additional information regarding the characteristics of morphotypes. If I were to do it again, I would take a different approach by manually classifying particle tracks into broad categories (e.g., fibers, fecal pellets). Then, I would conduct morphological analyses and investigate the relationship with sinking speed for each particle category. For example, fecal pellets composition can vary depending on the taxa involved and the type of food they consume (Atkinson et al., 2012). The relationship between these variations and the morphological differences captured in images is likely to differ from that observed for phytoplankton aggregates. To go further, UVP6 vertical profiles can be used to determine attenuation profiles of each particle category, as clear differences between them has been observed. By comparing these profiles with sinking speeds, we could gain insights into alteration processes occurring for

each particle category. In addition, changes in particle morphology distribution with depth could provide further insights into particle transformations. Finally, these data need to be compared with flux measurements to ensure their reliability. Although we lack a carbon conversion factor based on morphological properties for UVP images, flux values from sediment traps can be used to calibrate imaging observations and convert particle flux to POC flux. Overall, developing further imaging-based approaches is crucial as they can resolve higher spatial and temporal variability. In the future, datasets from long-term research programs such as CCE-LTER, which has already permitted to collect a substantial amount of UVP data covering various conditions but whose morphological data have seldom been used, will be of great interest to investigate variations over different time scales and to relate images to environmental conditions and community composition.

Additional datasets

Additional datasets were collected in various locations, including the Pacific Ocean during the CCE-LTER P2107 cruise, the Eastern Indian Ocean as part of the BLOOFINZ cruise, and at DYFAMED in the Mediterranean Sea through a short monthly time series. Although results from these datasets are not presented in this dissertation, data from contrasting ecosystems and different plankton communities may shed further light on particle flux and particle morphological properties.

CHAPTER 5

Conclusion

"Alors, qu'allons-nous faire de l'océan ?"

A. Conti, *L'océan, les bêtes et les hommes*

Summary of the thesis

The main results of the thesis are the following:

- In **chapter 2**, I established an allometric relationship linking planktonic Rhizaria cell volume to carbon and nitrogen content, encompassing numerous taxa and a broad size range (200 μm - 9 mm). This provided experimental evidence that Rhizaria have a low carbon density, likely related to their ecological niches. Contrastingly, no relationship between size and biogenic Si production rates was found.
- In **chapter 3**, I conducted a global census of the carbon and biogenic Si biomass of Rhizaria on the one hand, and assessed the global carbon demand and biogenic Si production rates of Phaeodaria on the other hand. I particularly showed that mesopelagic Phaeodaria could intercept 3.8 to 9.2% of gravitational export globally, and 11.2 and 23.4% in the Southern Ocean. Such values may help to refine carbon and silica global budgets in the future.
- In **chapter 4**, I introduced a novel method for in situ measurement of marine particle sinking speeds using the UVP6, a recent, widely-used camera. I investigated links between particle morphological properties, sinking speeds and environmental conditions, and showed that variations in sinking speeds were more related to environmental conditions than to particle morphology. This can be explained by the fact that environmental conditions influence community structure and thus particle composition. While it was not directly related to Rhizaria, the work undertaken in this chapter advocates for including particle characteristics, beyond size, in flux estimates.

Concluding remarks

The overarching approach that guided the work presented in this thesis can be summarized as follows: 'What insights can we gain about the functioning of oceanic biogeochemical cycles from particle-scale observations?'. To this end, most of the work presented in this thesis relied on the analysis of extensive in situ imaging datasets, which provide detailed information about individual particles and planktonic organisms in the ocean. While the cost of imaging tools has decreased, they have become more effective and collect an increasing volume of

data, offering valuable insights into ocean biogeochemistry. These instruments can be associated with the numerous oceanographic sensors available, either ship-deployed or mounted on autonomous platforms, bringing a large amount of contextual data with an increased spatial and temporal coverage. However, numerous challenges are yet to be overcome in the future to constrain the biological gravitational pump. While we commonly assess two ends of a spectrum, i.e., we provide measurements from a given location and timestamp, and use large-scale models, gaps remain regarding what is in between, yet various spatial and temporal scales may be relevant for different processes. Observations remain heterogeneously distributed and relatively scarce on the scale of oceans. Thus, numerical and modeling tools become necessary to extract and scale up meaningful patterns from such datasets. Understanding their structure is essential, and while questions can emerge through data mining, it is also important to formulate informed hypotheses through collaborative efforts involving researchers from diverse backgrounds, all while keeping experimental and fieldwork aspects in perspective. In addition, to make the most of such datasets, it becomes crucial to enhance data management protocols and develop a set of best practices to ensure reproducibility of results and to allow data and code sharing. Addressing these challenges is essential for advancing our knowledge of ocean biogeochemistry and its evolution with global changes.

Résumé détaillé en français

Introduction et objectifs

L'océan mondial joue un rôle crucial dans la régulation du climat et la production d'oxygène, ayant absordé 90 % de la chaleur gagnée par la Terre depuis les années 1970 (Cheng et al., 2017) ainsi qu'une partie du dioxyde de carbone (CO_2) atmosphérique relâché par les activités humaines (Friedlingstein et al., 2022). La zone pélagique (Fig. 1.1), constituant la plus grande partie du volume océanique, est définie par de forts gradients de lumière, de température et de pression. Le plancton, composé d'une grande diversité d'organismes dérivant avec les courants marins, est omniprésent dans ces écosystèmes. Il contribue au cycle du carbone d'une part par la photosynthèse dans la zone épipélagique (couche dans laquelle 99 % de la lumière du soleil est absorbée) à l'origine de la production de matière organique, et d'autre part par la consommation, le recyclage, et le transfert vers les niveaux trophiques supérieurs de cette matière organique. En particulier, la pompe biologique de carbone transporte la matière organique de la surface à l'océan profond, influençant les niveaux de CO_2 atmosphérique (Volk and Hoffert, 1985; Kwon et al., 2009; Turner, 2015; Fig. 1.3). L'action biologique des communautés de surface et profondes détermine la nature des particules qui participent à cet export (Buesseler et al., 2007; Steinberg et al., 2008b). Notamment, la vitesse de sédimentation des particules affecte les flux de carbone vers l'océan profond et sa capacité à séquestrer le CO_2 (De La Rocha and Passow, 2007). Parmi les organismes planctoniques, les protistes hétérotrophes et mixotrophes, tels que les Rhizaria, jouent un rôle dans ces processus (e.g., Biard et al., 2016), mais qui reste encore relativement peu étudié.

Les Rhizaria sont des organismes eucaryotes unicellulaires classés dans le supergroupe SAR (Stramenopila, Alveolata, Rhizaria; Keeling and Burki, 2019). Cette thèse porte sur deux taxon de Rhizaria planctoniques : les Radiolaria et les Phaeodaria. Les Radiolaria possède un squelette minéral composé de sulfate de strontium ou de silice biogène, tandis que les Phaeodaria possèdent tous un squelette de silice biogène de structure poreuse (Suzuki and Not, 2015; Nakamura and Suzuki, 2015). Ces organismes présentent des structures et des caractéristiques écologiques variées. Les Rhizaria couvrent un large spectre de tailles (de quelques dizaines de μm jusqu'à plusieurs mm) et occupent différentes niches écologiques, étant particulièrement présents en milieu oligotrophe. Beaucoup de Radiolaria sont mixotrophes, abritant des symbiotes algaux photosynthétiques et étant en même temps capables de capturer des proies ou des particules (Suzuki

and Not, 2015). Cependant, les Phaeodaria sont strictement hétérotrophes et sont détritivores, se nourrissant du flux de particules qui sédimentent (Gowing, 1986; Gowing, 1989). Leur distribution est influencée par des facteurs tels que la disponibilité de la nourriture, la température et la stratification de la colonne d'eau (Biard and Ohman, 2020). Ils contribuent aux flux verticaux de carbone et de silice (e.g., Biard et al., 2016; Ikenoue et al., 2019), en plus de permettre l'agrégation et le transport de particules (Ikenoue et al., 2019). Cependant, leur abondance et leur biomasse ont longtemps été sous-estimées en raison de leurs structures fragiles et, de ce fait, de la difficulté à les échantillonner. Les récents développements en imagerie in situ, méthode non destructive pour ces organismes, ont mis en lumière leur contribution aux stocks de carbone (Biard et al., 2016), mais aussi aux flux de silice (Biard et al., 2018) et à l'atténuation des flux de carbone (Stukel et al., 2019). Néanmoins, les estimations de biomasse manquent d'un facteur de conversion volume :carbone adéquat et les études portant sur la contribution des Rhizaria aux processus biogéochimiques restent limitées.

Pour échantillonner les Rhizaria, les filets à plancton permettent de collecter des spécimens, mais ne permettent pas une estimation précise de l'abondance de ces organismes fragiles qui sont souvent abîmés par ces instruments. Les outils d'imagerie in situ tels que l'Underwater Vision Profiler (UVP ; Picheral et al., 2010; Picheral et al., 2022), permettent d'enregistrer une image de l'organisme, des mesures de sa taille, ainsi qu'un ensemble de métadonnées telle que la position géographique et la profondeur d'échantillonnage. De ce fait, ils permettent des estimations plus fines de l'abondance des organismes planctoniques, notamment des plus fragiles comme les Rhizaria. Afin de mieux quantifier le rôle de ces derniers dans les cycles biogéochimiques, il est nécessaire d'estimer des paramètres biogéochimiques tels que leur concentration, leur masse carbonée et siliceuse pour les organismes silicifiants, leur demande en carbone et leur vitesse de sédimentation. En particulier, la vitesse de sédimentation des particules marines est cruciale pour comprendre les flux verticaux, mais ce paramètre est souvent estimé à partir de la taille seule de la particule, omettant le rôle d'autres paramètres morphologiques tels que la structure ou la forme, ou est mesuré en laboratoire. Ainsi, afin de mieux définir le rôle des Rhizaria dans les cycles biogéochimiques, les objectifs de la thèse sont les suivants :

1. Mesurer le contenu en carbone et la production de silice biogène de divers taxons de Rhizaria ;

2. Réévaluer la biomasse mondiale en carbone et en silice biogène des Rhizaria, ainsi qu'estimer leur demande en carbone et leur production de silice biogène ;

3. Développer une méthodologie pour mesurer les vitesses de sédimentation à partir de l'imagerie in situ et étudier les liens avec la morphologie des particules.

Composition cellulaire et taux d'absorption du silicium des Rhizaria

Afin d'estimer la biomasse du plancton à grande échelle, il est nécessaire de connaître leurs contenus élémentaires à l'échelle de l'organisme. Les relations d'allométrie relient les traits morphologiques des organismes, tels que leur taille, à leurs traits fonctionnels sur plusieurs ordres de grandeur et sont utilisées pour presque toutes les formes de vie (Brown et al., 2002). Des relations allométriques reliant les teneurs individuelles en carbone (Q_C) et en azote (Q_N) au volume cellulaire ont été développées pour les diatomées et divers protistes. Cependant, elles sont susceptibles de surestimer la composition élémentaire de protistes tels que les Rhizaria (Menden-Deuer and Lessard, 2000). Ces dernières années, des études ont montré l'importance des Rhizaria dans les cycles biogéochimiques océaniques.

Ce super-groupe eucaryote, qui comprend les Radiolaria et les Phaeodaria, représente une part importante de la biomasse zooplanctonique et contribue à l'export de carbone et de silice biogène (e.g., Biard et al., 2016 ; Guidi et al., 2016 ; Biard et al., 2018). Pourtant, les estimations précises de leur biomasse sont entravées par une faible connaissance de leur composition élémentaire, ce qui contraste avec les relations allométriques carbone/volume bien établies pour les protistes plus petits. Les objectifs de cette étude sont d'étudier les liens entre la taille des organismes d'une part, et leur contenu élémentaire ainsi que leur production de silice d'autre part. L'écologie des Rhizaria est ensuite discutée de ces résultats.

Pour cela, nous avons collecté des spécimens de Rhizaria en 2019 dans la rade de Villefranche-sur-mer et lors de la campagne P2107 dans le courant de Californie dans des conditions environnementales variées (eutrophe-oligotrophe).

Ceux-ci ont été collectés à l'aide de filets à plancton de la surface jusque dans la zone mésopélagique. Ces spécimens ont été isolés sous microscope et plusieurs individus appartenant au même taxon (selon la classification de Suzuki and Not (2015) pour les Radiolaria et de Nakamura and Suzuki (2015) pour les Phaeodaria) ont été regroupés ensemble. En parallèle, chaque spécimen a été photographié et assigné à une forme géométrique simple afin d'obtenir une estimation de son volume. Les groupes d'individus ont été filtrés et les filtres analysés à l'aide d'un analyseur C/N pour le contenu élémentaire. L'analyse de la production de silice a été faite à l'aide du radioisotope ^{32}Si (voir Llopis-Monferrer et al. (2020) et références associées). Les données obtenues ont ensuite été combinées avec des données de la littérature (Mansour et al., 2021).

Pour analyser le lien entre la taille d'une part, et les contenus élémentaires et la production de silice biogène d'autre part, des régressions linéaires sur les données transformées en $\log_{10}$ ont été effectuées. Les contenus en carbone Q_{C} (μg C mm^{-3}) et en azote Q_{N} (μg N mm^{-3}) peuvent être prédits à partir du volume V (mm^3) à partir des relations suivantes :

$$Q_{\mathrm{C}} = 9.078 \times V^{0.455}$$

$$Q_{\mathrm{N}} = 1.435 \times V^{0.477}$$

Dans les deux cas, R^2 est supérieur à 0.75, ce qui indique que le volume explique une large part de la variabilité du contenu élémentaire (Fig. 2.3). La pente de l'allométrie liant V et Q_{C} (0.455) est significativement inférieure (test t de Student : p-value <0.0001) à celle établie précédemment pour un ensemble de protistes (0.939 ; Menden-Deuer and Lessard, 2000). Ces résultats indiquent que les Rhizaria, particulièrement les plus gros, ont une faible teneur en carbone et que la relation établie pour d'autres protistes peut surestimer Q_{C} de plusieurs ordres de grandeur.

Toutefois, nous observons que les densités en carbone (μg C mm^{-3}) des différents taxons considérés varient sur quatre ordres de grandeur. Cela a plusieurs implications concernant leur stratégie écologique. Tout d'abord, nous observons que les taxons vivant dans un environnement pauvre en nourriture sont les moins denses en carbone. Les taxons photosymbiotiques (Collodaria et *Phlebarachnium* sp.), retrouvés en surface principalement dans les gyres oligotrophes, ont une faible densité en carbone. Cela peut leur permettre d'augmenter la taille de leur

matrice gélatineuse ectoplasmique et ainsi d'abriter plus de symbiontes. Les taxons vivant dans la zone mésopélagique (majoritairement des Phaeodaria) ont également une faible densité en carbone. Ceux-ci dépendent du flux de neige marine provenant de la surface pour se nourrir. Dès lors, une manière d'augmenter leur taux d'interception est d'augmenter leur taille. Ainsi, une faible densité en carbone pourrait compenser pour cette augmentation de taille et permettre à ces organismes de vivre dans la zone mésopélagique pauvre en nourriture. Un autre avantage de cette faible densité en carbone est que cela rend l'organisme moins nutritif et donc potentiellement moins attractif pour ses prédateurs (Kiørboe, 2013), bien que peu soit encore connu sur la pression de prédation exercée sur les Rhizaria (voir Biard, 2022a). Enfin, comme suggéré par Stukel et al. (2018), cette faible densité en carbone peut également compenser le poids du squelette et permettre à l'organisme de maintenir une flottabilité neutre. En effet, certains taxons occupent des niches écologiques limitées dans la colonne d'eau (Biard and Ohman, 2020) et cela pourrait leur permettre de rester dans leur optimum écologique.

A partir des mesures de contenu en carbone, azote et silice, nous avons estimé les vitesses de sédimentation théoriques à partir de la loi de Stokes (Stokes, 1851). Une grande variabilité existe entre les différents taxons et on peut distinguer deux groupes : un groupe à vitesse de sédimentation élevée (>1000 m j^{-1}) et un groupe à vitesse de sédimentation faible à modérée (30-200 m j^{-1}). On observe notamment que les taxons Orodaria et Spumellaria (Radiolaria) ont une vitesse de sédimentation bien plus élevée que les Phaeodaria de taille équivalente, qui peut s'expliquer par la différence dans la structure du squelette, plus poreux chez les Phaeodaria. Toutefois, on observe que certaines familles de Phaeodaria qui sont plus denses en silice (e.g., Castanellidae) ont également une vitesse de sédimentation importante. Ainsi, ces taxons pourraient exporter efficacement le carbone organique et la silice vers l'océan profond à leur mort. De l'autre côté, les squelettes les plus délicats de certaines familles de Phaeodaria se dissoudront probablement entièrement lors de leur sédimentation et n'atteindront jamais le fond de l'océan.

A l'inverse de Q_{C} et Q_{N}, la production de silice n'est liée que faiblement à la taille. Un lien faible avec la concentration en acide silicique est également observé. Ainsi, on peut faire l'hypothèse que plusieurs paramètres, à la fois propres à la cellule et environnementaux, influencent cette production. Nos valeurs de production de silice sont plus faibles que celles de la littérature (Llopis-Monferrer

et al., 2020). Toutefois, la dynamique de la production de silice par les Rhizaria, de même que leur cycle de vie, est encore inconnue. S'ils possèdent les transporteurs du silicium SIT-L (Marron et al., 2016), leur nombre ainsi que l'affinité de ceux-ci avec la silice dissoute reste inconnue.

Cette étude apporte des outils simples, facilement implémentables dans des modèles écologiques ou biogéochimiques, pour estimer la biomasse des Rhizaria planctonique à partir de leur taille. Ainsi, les équations obtenues peuvent par exemple être appliquées sur des données d'imagerie automatisée qui permettent d'obtenir la taille des organismes à partir des images.

Rhizaria et cycles biogéochimiques à échelle globale

Les Rhizaria planctoniques sont abondants dans la zone mésopélagique, située juste sous la zone épipélagique (Stukel et al., 2018; Biard and Ohman, 2020). La zone mésopélagique, ou zone crépusculaire, est une zone de transition entre l'océan de surface et l'océan profond et joue un rôle crucial dans le transfert de matière, tant organique que minérale, vers les profondeurs. Notamment, les organismes mésopélagiques consomment près de 90 % de la matière organique exportée de l'océan de surface (Robinson et al., 2010). Néanmoins, ceux-ci restent bien moins étudiés que ceux de la zone épipélagique - du fait de difficultés d'accès et d'en rapporter des organismes intacts. Évaluer la biomasse des organismes qui s'y trouvent ainsi que les processus dans lequels ils sont impliqués est cependant essentiel pour affiner les budgets biogéochimiques.

Nous avons ici utilisé un jeu de données global collecté in situ entre 2008 et 2021, contenant des informations sans précédent sur la distribution et l'abondance des Rhizaria. Il se compose de 4 252 profils verticaux acquis avec l'UVP5 (Picheral et al., 2010) jusqu'à une profondeur de 1 000 m (Fig. 3.1, Table S3.1). L'UVP5 enregistre une image de chaque organisme rencontré de plus de 0,6 mm, permettant une mesure de la taille et une identification à un niveau taxonomique allant de l'ordre au genre. Avec des diamètres sphériques équivalents allant de 0,6 mm à 20 mm (excluant donc les Rhizaires plus petits; Fig. Ext. 3.1), les 167 551 images de Rhizaires manuellement identifiées et validées via la plateforme EcoTaxa (Picheral et al., 2017) couvrent 18 catégories taxonomiques (dont les critères d'identification sont définis dans Biard and Ohman, 2020) incluses dans les Acantharia, les Collodaria, les Foraminifera, les Phaeodaria et autres Rhizaria (Figure 3.2, Table Ext. 3.1). Nous appliquons la relation d'allométrie développée

précédemment (Laget et al., 2023), afin de déterminer le contenu en carbone à partir de la taille des organismes. Nous utilisons également une relation d'allométrie pour estimer le contenu en silice des Phaeodaria (Llopis-Monferrer et al., 2020). En plus de leur contribution aux stocks d'éléments, nous étudions également leur rôle dans les processus biogéochimiques en estimant la demande en carbone des Phaeodaria mésopélagique (d'après la formule de Stukel et al., 2018) et la production de silice biogène (Llopis-Monferrer et al., 2020). En associant chacune des 167 551 images de Rhizaria à un ensemble de valeurs environnementales, nous quantifions ces processus sur une grille mondiale de $1° \times 1°$ en utilisant des arbres de régression boostés. Enfin, nous comparons les demandes en carbone à des valeurs d'export (i.e., de transport hors de la zone épipélagique) provenant de la littérature (Laws et al., 2000; Dunne et al., 2007; Nowicki et al., 2022).

Nous montrons que la biomasse en carbone mondiale des Rhizaria >0,6 mm dans les 1 000 premiers mètres est inférieure aux estimations précédentes (Biard et al., 2016; Drago et al., 2022), mais leur contribution à l'abondance du mésozooplancton reste substantielle (31 %; Biard et al., 2016). La distribution des Rhizaria varient entre les groupes mixotrophes et hétérotrophes. Les mixotrophes (Acantharia, Collodaria, Foraminifera) dominent dans la couche épipélagique, en particulier dans les régions intertropicales et les gyres subtropicaux oligotrophes. En revanche, les Phaeodaria sont plus abondants dans la zone mésopélagique, où ils jouent un rôle crucial dans l'atténuation du flux de carbone, interceptant potentiellement 3,8 à 9,2 % du flux de carbone gravitationnel exporté de la zone épipélagique. Ce rôle est particulièrement marqué dans l'océan Austral où ils pourraient intercepter de 11,2 à 23,4 % du carbone exporté de la couche épipélagique. Ces résultats mettent en lumière le rôle inattendu de ces protistes dans l'atténuation des flux de carbone et l'importance de les considérer dans les budgets de carbone globaux. De plus, nous montrons que les Phaeodaria sont les uniques producteurs et recycleurs de silice biogène dans la zone mésopélagique. De ce fait, ils co-dominent le cycle du silicium avec les diatomées et les éponges. Ainsi, les Rhizaria pourraient jouer un rôle important dans les écosystèmes océaniques futurs, notamment dans le contexte du changement climatique en cours.

En effet, les impacts du changement climatique sur les régions océaniques, notamment le réchauffement, la stratification et les changements dans les quantités de nutriments, sont connus (Kwiatkowski et al., 2020). Dans les océans oligotrophes, on peut s'attendre à ce que les communautés de Rhizaria mixotrophes restent stables ou s'étendent en raison de leur capacité à créer des microenviron-

nements favorisant une production primaire élevée, ce qui pourrait accroître leur importance dans les réseaux trophiques. Les communautés de Phaeodaria dans les régions antarctiques et subarctiques pourraient rester stables, voire croître, tandis que celles des zones d'upwelling pourraient décliner en raison d'une diminution des flux de carbone, donc de leur source de nourriture. Ainsi, leur impact sur le cycle des éléments pourrait évoluer, d'où la nécessité d'études approfondies sur leur rôle dans les cycles biogéochimiques.

Vitesses de sédimentation des particules marines mesurées in situ

Les particules qui sédimentent de la surface jusqu'aux profondeurs océaniques par l'action gravitationnelle jouent un rôle clé dans la pompe biologique du carbone, l'efficacité de cette dernière dépendant des concentrations en particules et de leur vitesse de chute (De La Rocha and Passow, 2007). Cependant, quantifier avec précision la vitesse de sédimentation des particules est difficile en raison de la nature très hétérogène des particules marines (e.g., agrégats de neige marine, pelotes fécales, carcasses d'organismes...) et de leur diversité de taille, de composition et de structure (Alldredge and Silver, 1988; Turner, 2002). Les mesures in situ de la vitesse sont rares et souvent déduites uniquement de la population de particules étudiée (e.g., Trull et al., 2008; Villa-Alfageme et al., 2014). Ces dernières années, l'imagerie in situ a permis des avancées critiques dans la quantification des flux verticaux de carbone, à l'aide de l'UVP (Guidi et al., 2008). Toutefois, les estimations actuelles des vitesses de chute et de flux de particules à partir de cet outil se basent uniquement sur la taille de ces dernières et ne prennent pas en compte leur diversité morphologique. Pourtant, leur caractère non destructif et leur capacité à échantillonner avec une meilleure couverture spatiale et temporelle que les outils actuels de mesure de flux (e.g., pièges à sédiments) offrent des opportunités pour mesurer les flux de particules avec une plus haute résolution. Nous introduisons ainsi le VisuTrap, un nouvel outil pour mesurer les vitesses in situ des grandes particules marines.

Le VisuTrap consiste en une caméra UVP6 (Picheral et al., 2022) insérée dans un piège à sédiments cylindro-conique qui emprisonne un volume d'eau. L'acquisition continue d'images à haute fréquence (1,3 Hz) pendant des déploiements quasi-lagrangiens de 2 à 5 jours sur une ligne dérivante permet la reconstruction

des trajectoires des particules et l'estimation de leurs vitesses in situ. Pour cela, les séries d'images sont analysées à l'aide de modules de *tracking* spécialement développés pour cette application. Dans un premier temps, les particules sont détectées sur les images à l'aide d'une segmentation par seuil. Ensuite, la morphologie et la position des particules se trouvant sur des images successives sont comparées afin de lier ensemble les particules ayant la plus grande probabilité d'être les mêmes. Une fois les trajectoires des particules obtenues, leur vitesse de sédimentation est calculée. Cet outil permet donc d'obtenir à la fois des données morphologiques sur les particules (taille, niveau de gris, forme et structure) et leur vitesse de sédimentation. Compte tenu des vastes ensembles de données UVP disponibles dans le monde entier, le VisuTrap, en fournissant des données de vitesse in situ, offre la possibilité d'affiner les estimations des flux de carbone à l'échelle mondiale.

Ensuite, le VisuTrap a été déployé lors de la campagne APERO ayant eu lieu dans l'Atlantique Nord en 2023 pendant le bloom estival. Il a été ainsi déployé sur la ligne dérivante à 3 profondeurs (100, 200 et 500 m) lors de cinq cycles lagrangiens couvrant des conditions océanographiques variées (eddy cyclonique, eddy anticyclonique, front). Les données acquises ont permis de collecter un jeu de données sans précédent de 8 942 trajectoires de particules qui sédimentent, incluant leur vitesse de sédimentation et leurs caractéristiques morphologiques. En étudiant le lien entre ces vitesses de sédimentation, les caractéristiques morphologiques et les conditions environnementales, nous montrons un lien significatif mais faible avec la morphologie. En revanche, nous observons que les vitesses de sédimentation augmentent avec la profondeur des déploiements. De futures comparaisons avec d'autres systèmes de mesure de vitesses utilisés pendant la campagne permettront de mettre en lumière les observations avec les conditions océaniques et la structure des communautés planctoniques de surface et profondes.

Conclusion

L'objectif de cette thèse était d'étudier le rôle des Rhizaria planctoniques, des protistes ubiquistes, dans les cycles biogéochimiques du carbone et du silicium. Les principaux résultats de la thèse sont les suivants :

- Dans le **chapitre 2**, J'ai établi une relation allométrique reliant le volume

cellulaire des Rhizaria planctoniques à la teneur en carbone et en azote, englobant de nombreux taxons et couvrant une large gamme de tailles (200 mum - 9 mm). Cela a permis de prouver expérimentalement que les Rhizaria ont une faible densité de carbone, probablement liée à leurs niches écologiques. En revanche, aucune relation n'a été établie entre la taille et les taux de production de silice biogène.

- Le chapitre **chapitre 3** a permis un recensement mondial de la biomasse en carbone des Rhizaria planctoniques en général, ainsi que de la biomasse en silice biogène des Phaeodaria. Nous avons également évalué la demande globale en carbone des Phaeodaria mésopélagiques et leurs taux de production de silice biogène. Nous avons notamment montré que les Phaeodaria mésopélagiques pourraient intercepter de 3,8 à 9,2 % du flux de carbone gravitationnel à l'échelle mondiale, et en particulier de 11,2 à 23,4 % dans l'océan Austral. Ces valeurs ont pour objectifs de contribuer à affiner les budgets globaux de carbone et de silice pour de futures études.

- Dans le chapitre **chapitre 4**, j'ai introduit une nouvelle méthode de mesure in situ des vitesses de sédimentation des particules marines à l'aide de l'UVP6. J'ai étudié les liens entre les propriétés morphologiques des particules, les vitesses de sédimentation et les conditions environnementales, et j'ai montré que les variations des vitesses de sédimentation étaient davantage liées aux conditions environnementales qu'à la morphologie des particules. Cela peut s'expliquer par le fait que les conditions environnementales influencent la structure de la communauté et donc la composition des particules. Bien qu'ils ne soient pas directement liés aux Rhizaria, les travaux entrepris dans ce chapitre plaident en faveur de l'inclusion des caractéristiques des particules, au-delà de la taille, dans les estimations de flux.

L'approche générale de cette thèse peut être résumée comme suit : "Quelles informations pouvons-nous obtenir sur le fonctionnement des cycles biogéochimiques océaniques à partir d'observations à l'échelle des particules ?". À cette fin, la majeure partie du travail présenté ici s'est appuyée sur l'analyse de grands jeux de données d'imagerie in situ, offrant des mesures détaillées au niveau de la particule individuelle et permettant d'explorer la diversité morphologique à la fois parmi les organismes planctoniques et les particules. Ces instruments,

tout en devenant plus efficaces et collectant une quantité accrue de données, fournissent des informations précieuses sur la biogéochimie océanique. Cependant, de nombreux défis restent à relever à l'avenir pour mieux comprendre la pompe gravitationnelle biologique. Alors que nous étudions généralement les deux extrémités d'un spectre, c'est-à-dire que nous fournissons des mesures ponctuelles et utilisons des modèles à grande échelle, des lacunes subsistent pour diverses échelles spatiales et temporelles. Les observations demeurent hétérogènes et relativement rares à l'échelle des océans. Ainsi, des outils numériques et de modélisation deviennent nécessaires pour extraire des signaux à partir de ces ensembles de données. Comprendre la structure de ces derniers est essentiel, et bien que des questions puissent émerger grâce au *data mining*, il est important de formuler des hypothèses éclairées grâce à des efforts collaboratifs impliquant des chercheurs de divers horizons, tout en gardant à l'esprit les aspects expérimentaux et de terrain. De plus, pour tirer le meilleur parti de ces données, il devient crucial d'améliorer les protocoles de gestion des données et de développer un ensemble de meilleures pratiques pour garantir la reproductibilité des résultats et permettre le partage des données et du code. S'attaquer à ces défis est essentiel pour faire progresser notre connaissance de la biogéochimie océanique et de ses évolutions.

Bibliography

Abràmoff, M. D., P. J. Magalhães, and S. J. Ram (2004). Image processing with ImageJ. In: *Biophotonics international* 11.7, pp. 36–42 (cit. on p. 52).

Adl, S. M. et al. (2018). Revisions to the Classification, Nomenclature, and Diversity of Eukaryotes. In: *Journal of Eukaryotic Microbiology*. DOI: 10.1111/jeu.12691 (cit. on p. 26).

Alldredge, A. and C. Gotschalk (1989). Direct observations of the mass flocculation of diatom blooms: characteristics, settling velocities and formation of diatom aggregates. In: *Deep Sea Research Part A. Oceanographic Research Papers* 36.2, pp. 159–171. DOI: 10.1016/0198-0149(89)90131-3 (cit. on p. 134).

Alldredge, A. L. and C. Gotschalk (1988). In situ settling behavior of marine snow 1. In: *Limnology and Oceanography* 33.3, pp. 339–351. DOI: 10.4319/lo.1988.33.3.0339 (cit. on pp. 134, 159, 172).

Alldredge, A. L., T. C. Granata, C. C. Gotschalk, and T. D. Dickey (1990). The physical strength of marine snow and its implications for particle disaggregation in the ocean. In: *Limnology and Oceanography* 35.7, pp. 1415–1428 (cit. on pp. 21, 133).

Alldredge, A. L. and M. W. Silver (1988). Characteristics, dynamics and significance of marine snow. In: *Progress in oceanography* 20.1, pp. 41–82 (cit. on pp. 21, 159, 201).

Allen, J. T., L. Brown, R. Sanders, C Mark Moore, A. Mustard, S. Fielding, M. Lucas, M. Rixen, G. Savidge, S. Henson, et al. (2005). Diatom carbon export enhanced by silicate upwelling in the northeast Atlantic. In: *Nature* 437.7059, pp. 728–732 (cit. on p. 160).

Amante, C. and B. W. Eakins (2009). ETOPO1 arc-minute global relief model: procedures, data sources and analysis. In: (cit. on p. 105).

Aminot, A. and R. Kérouel (2007). Dosage automatique des nutriments dans les eaux marines: méthodes en flux continu. Editions Quae (cit. on p. 51).

Andersen, K. H., D. L. Aksnes, T. Berge, Ø. Fiksen, and A. Visser (2015). Modelling emergent trophic strategies in plankton. In: *Journal of Plankton Research* 37.5, pp. 862–868 (cit. on p. 46).

Andersen, V. and L. Prieur (2000). One-month study in the open NW Mediterranean Sea (DYNAPROC experiment, May 1995): overview of the hydrobiogeochemical structures and effects of wind events. In: *Deep Sea Research Part I: Oceanographic Research Papers* 47.3, pp. 397–422 (cit. on p. 144).

Anderson, O. R. (1983). Radiolaria. New York, NY: Springer New York. ISBN: 9781461255369 (cit. on pp. 27, 31, 70).

Anderson, O. R., P. Bennett, and M. Bryan (1989). Experimental and observational studies of radiolarian physiological ecology: 3. Effects of temperature, salinity and light intensity on the growth and survival ofSpongaster tetras tetras maintained in laboratory culture. In: *Marine Micropaleontology* 14.4, pp. 275–282 (cit. on p. 68).

Arístegui, J., C. M. Duarte, J. M. Gasol, and L. Alonso-Sáez (2005). Active mesopelagic prokaryotes support high respiration in the subtropical northeast Atlantic Ocean. In: *Geophysical Research Letters* 32.3 (cit. on p. 158).

Arístegui, J., J. M. Gasol, C. M. Duarte, and G. J. Herndld (2009). Microbial oceanography of the dark ocean's pelagic realm. In: *Limnology and Oceanography* 54.5, pp. 1501–1529. DOI: 10.4319/lo.2009.54.5.1501 (cit. on p. 133).

Armstrong, R. A., C. Lee, J. I. Hedges, S. Honjo, and S. G. Wakeham (2001). A new, mechanistic model for organic carbon fluxes in the ocean based on the quantitative association of POC with ballast minerals. In: *Deep Sea Research Part II: Topical Studies in Oceanography* 49.1-3, pp. 219–236. DOI: 10.1016/s0967-0645(01)00101-1 (cit. on pp. 23, 133).

Asper, V. L. and W. O. Smith (2003). Abundance, distribution and sinking rates of aggregates in the Ross Sea, Antarctica. In: *Deep Sea Research Part I: Oceanographic Research Papers* 50.1, pp. 131–150 (cit. on p. 134).

Atkinson, A., K. Schmidt, S. Fielding, S Kawaguchi, and P. Geissler (2012). Variable food absorption by Antarctic krill: Relationships between diet, egestion rate and the composition and sinking rates of their fecal pellets. In: *Deep Sea Research Part II: Topical Studies in Oceanography* 59, pp. 147–158 (cit. on p. 186).

Aumont, O., C. Éthé, A. Tagliabue, L. Bopp, and M. Gehlen (2015). PISCES-v2: an ocean biogeochemical model for carbon and ecosystem studies. In: *Geoscientific Model Development Discussions* 8.2, pp. 1375–1509 (cit. on p. 21).

Azam, F. (1998). Microbial Control of Oceanic Carbon Flux: The Plot Thickens. In: *Science* 280.5364, pp. 694–696. DOI: 10.1126/science.280.5364.694 (cit. on p. 19).

Bach, L. T., U. Riebesell, S. Sett, S. Febiri, P. Rzepka, and K. G. Schulz (2012). An approach for particle sinking velocity measurements in the 3–400 μm size range and considerations on the effect of temperature on sinking rates. In: *Marine Biology* 159.8, pp. 1853–1864. DOI: 10.1007/s00227-012-1945-2 (cit. on pp. 22, 175).

Baines, S. B., B. S. Twining, M. A. Brzezinski, D. M. Nelson, and N. S. Fisher (2010). Causes and biogeochemical implications of regional differences in silicification of marine diatoms. In: *Global Biogeochemical Cycles* 24.4 (cit. on pp. 53, 65, 75).

Baltar, F., J. Arístegui, J. M. Gasol, E. Sintes, and G. J. Herndl (2009). Evidence of prokaryotic metabolism on suspended particulate organic matter in the dark waters of the subtropical North Atlantic. In: *Limnology and Oceanography* 54.1, pp. 182–193 (cit. on p. 22).

Baltar, F., J. Arístegui, E. Sintes, J. M. Gasol, T. Reinthaler, and G. J. Herndl (2010). Significance of non-sinking particulate organic carbon and dark CO2 fixation to heterotrophic carbon demand in the mesopelagic northeast Atlantic. In: *Geophysical research letters* 37.9 (cit. on p. 22).

Bass, D. and T. Cavalier-Smith (2004). Phylum-specific environmental DNA analysis reveals remarkably high global biodiversity of Cercozoa (Protozoa). In: *International journal of systematic and evolutionary microbiology* 54.6, pp. 2393–2404 (cit. on p. 26).

Baumas, C. M. and M. Bizic (2023). Did you say marine snow? Zooming into different types of organic matter particles and their importance in the open ocean carbon cycle. In: (cit. on p. 184).

Baumas, C. M., F. A. Le Moigne, M. Garel, N. Bhairy, S. Guasco, V. Riou, F. Armougom, H.-P. Grossart, and C. Tamburini (2021). Mesopelagic microbial carbon production correlates with diversity across different marine particle fractions. In: *The ISME Journal* 15.6, pp. 1695–1708 (cit. on p. 22).

Beaugrand, G., M. Edwards, and L. Legendre (2010). Marine biodiversity, ecosystem functioning, and carbon cycles. In: *Proceedings of the National Academy of Sciences* 107.22, pp. 10120–10124. DOI: 10.1073/pnas.0913855107 (cit. on p. 125).

Beaugrand, G., P. C. Reid, F. Ibanez, J. A. Lindley, and M. Edwards (2002). Reorganization of North Atlantic marine copepod biodiversity and climate. In: *Science* 296.5573, pp. 1692–1694 (cit. on p. 123).

Beers, J. R. and G. L. Stewart (1970). Numerical abundance and estimated biomass of microzooplankton. In: *The ecology of the plankton off La Jolla, California, in the period April through September, 1967*. Ed. by J. D. H. Strickland, pp. 67–87 (cit. on pp. 31, 48).

Berelson, W. M. (2001). Particle settling rates increase with depth in the ocean. In: *Deep Sea Research Part II: Topical Studies in Oceanography* 49.1-3, pp. 237–251. DOI: 10.1016/s0967-0645(01)00102-3 (cit. on pp. 22, 133, 174, 175).

Bernstein, R. E., P. R. Betzer, and K. Takahashi (1990). Radiolarians from the western North Pacific Ocean: a latitudinal study of their distributions and fluxes. In: *Deep Sea Research Part A. Oceanographic Research Papers* 37.11, pp. 1677–1696. DOI: 10.1016/0198-0149(90)90071-3 (cit. on p. 100).

Biard, T. (2015). Diversité, biogéographie et écologie des Collodaires (Radiolaires) dans l'océan mondial. PhD thesis. Paris 6 (cit. on p. 120).

— (2022a). Diversity and ecology of Radiolaria in modern oceans. In: *Environmental Microbiology* (cit. on pp. 26, 28, 46, 47, 69, 96, 118, 198).

— (2022b). Rhizaria. In: *eLS* 2, pp. 1–11 (cit. on pp. 46, 90, 91, 117).

Biard, T., J. W. Krause, M. R. Stukel, and M. D. Ohman (2018). The Significance of Giant Phaeodarians (Rhizaria) to Biogenic Silica Export in the California Current Ecosystem. In: *Global Biogeochemical Cycles* 32.6, pp. 987–1004. DOI: 10.1029/2018gb005877 (cit. on pp. 23, 24, 32, 33, 37, 47, 48, 53, 57, 59, 60, 64, 66, 73, 74, 82, 91, 99, 120, 122, 124, 126, 195, 196).

Biard, T. and M. D. Ohman (2020). Vertical niche definition of test-bearing protists (Rhizaria) into the twilight zone revealed by in situ imaging. In: *Limnology and Oceanography* 65.11, pp. 2583–2602. DOI: 10.1002/lno.11472 (cit. on pp. 28–30, 36, 41, 47, 62, 64, 69, 90, 92, 93, 98, 103, 120, 195, 198, 199).

Biard, T., L. Pillet, J. Decelle, C. Poirier, N. Suzuki, and F. Not (2015). Towards an Integrative Morpho-molecular Classification of the Collodaria (Polycystinea, Radiolaria). In: *Protist* 166.3, pp. 374–388. DOI: 10.1016/j.protis.2015.05.002 (cit. on p. 28).

Biard, T., L. Stemmann, M. Picheral, N. Mayot, P. Vandromme, H. Hauss, G. Gorsky, L. Guidi, R. Kiko, and F. Not (2016). In situ imaging reveals the biomass of giant protists in the global ocean. In: *Nature* 532.7600, pp. 504–507. DOI: 10.1038/nature17652 (cit. on pp. 31, 36, 47, 62, 64, 91–93, 96, 103, 104, 115, 118–121, 126, 194–196, 200).

Bisson, K. M., R. Kiko, D. A. Siegel, L. Guidi, M. Picheral, E. Boss, and B. Cael (2022). Sampling uncertainties of particle size distributions and derived fluxes. In: *Limnology and Oceanography: Methods* 20.12, pp. 754–767 (cit. on p. 149).

Blanchard, J. L., R. F. Heneghan, J. D. Everett, R. Trebilco, and A. J. Richardson (2017). From Bacteria to Whales: Using Functional Size Spectra to Model Marine Ecosystems. In: *Trends in Ecology & Evolution* 32.3, pp. 174–186. DOI: 10.1016/j.tree.2016.12.003 (cit. on p. 46).

Boltovskoy, D. (2017). Vertical distribution patterns of Radiolaria Polycystina (Protista) in the World Ocean: living ranges, isothermal submersion and settling shells. In: *Journal of Plankton Research* 39.2, pp. 330–349. DOI: 10.1093/plankt/fbx003 (cit. on p. 65).

Boltovskoy, D., V. A. Alder, and A. Abelmann (1993). Annual flux of Radiolaria and other shelled plankters in the eastern equatorial Atlantic at 853 m: seasonal variations and polycystine species-specific responses. In: *Deep Sea Research Part I: Oceanographic Research Papers* 40.9, pp. 1863–1895 (cit. on p. 125).

Boltovskoy, D. and N. Correa (2016). Biogeography of Radiolaria Polycystina (Protista) in the World Ocean. In: *Progress in Oceanography* 149, pp. 82–105. DOI: 10.1016/j.pocean.2016.09.006 (cit. on p. 47).

Bottazzi, E. M. and M. G. Andreoli (1982). Distribution of adult and juvenile Acantharia (Protozoa Sarcodina) in the Atlantic Ocean. In: *Journal of Plankton Research* 4.4, pp. 757–777 (cit. on p. 31).

Boyd, P. W., H. Claustre, M. Levy, D. A. Siegel, and T. Weber (2019). Multi-faceted particle pumps drive carbon sequestration in the ocean. In: *Nature* 568.7752, pp. 327–335. DOI: 10.1038/s41586-019-1098-2 (cit. on pp. 19, 20, 90, 102, 132, 158).

Brandão, M. C., F. Benedetti, S. Martini, Y. D. Soviadan, J.-O. Irisson, J.-B. Romagnan, A. Elineau, C. Desnos, L. Jalabert, A. S. Freire, et al. (2021). Macroscale patterns of oceanic zooplankton composition and size structure. In: *Scientific reports* 11.1, pp. 1–19 (cit. on pp. 31, 93).

Breiman, L. (2017). Classification and regression trees. Routledge (cit. on p. 105).
Briggs, N., G. Dall'Olmo, and H. Claustre (2020). Major role of particle fragmentation in regulating biological sequestration of CO2 by the oceans. In: *Science* 367.6479, pp. 791–793. DOI: 10.1126/science.aay1790 (cit. on p. 184).
Briggs, N., M. J. Perry, I. Cetinić, C. Lee, E. D'Asaro, A. M. Gray, and E. Rehm (2011). High-resolution observations of aggregate flux during a sub-polar North Atlantic spring bloom. In: *Deep Sea Research Part I: Oceanographic Research Papers* 58.10, pp. 1031–1039 (cit. on p. 172).
Brown, J. H., V. K. Gupta, B.-L. Li, B. T. Milne, C. Restrepo, and G. B. West (2002). The fractal nature of nature: power laws, ecological complexity and biodiversity. In: *Philosophical Transactions of the Royal Society of London. Series B: Biological Sciences* 357.1421. Ed. by R. V. Solé and S. A. Levin, pp. 619–626. DOI: 10.1098/rstb.2001.0993 (cit. on pp. 46, 196).
Brzezinski, M. A. (1985). The Si: C: N ratio of marine diatoms: interspecific variability and the effect of some environmental variables 1. In: *Journal of Phycology* 21.3, pp. 347–357 (cit. on p. 64).
Buesseler, K. O. et al. (2007). Revisiting Carbon Flux Through the Ocean's Twilight Zone. In: *Science* 316.5824, pp. 567–570. DOI: 10.1126/science.1137959 (cit. on pp. 17, 20, 23, 158, 194).
Burd, A. B. and G. A. Jackson (2009). Particle Aggregation. In: *Annual Review of Marine Science* 1.1, pp. 65–90. DOI: 10.1146/annurev.marine.010908.163904 (cit. on pp. 22, 133).
Burd, A. B. et al. (2010). Assessing the apparent imbalance between geochemical and biochemical indicators of meso- and bathypelagic biological activity: What the @$♯! is wrong with present calculations of carbon budgets? In: *Deep Sea Research Part II: Topical Studies in Oceanography* 57.16, pp. 1557–1571. DOI: 10.1016/j.dsr2.2010.02.022 (cit. on p. 21).
Burki, F., A. J. Roger, M. W. Brown, and A. G. Simpson (2020). The new tree of eukaryotes. In: *Trends in ecology & evolution* 35.1, pp. 43–55 (cit. on p. 26).
Burki, F., K. Shalchian-Tabrizi, M. Minge, Å. Skjæveland, S. I. Nikolaev, K. S. Jakobsen, and J. Pawlowski (2007). Phylogenomics Reshuffles the Eukaryotic Supergroups. In: *PLoS ONE* 2.8. Ed. by G. Butler, e790. DOI: 10.1371/journal.pone.0000790 (cit. on p. 25).
Cachon, J, M Cachon, and K. Estep (1990). Phylum Actinopoda (Classes Polycystina (= Radiolaria) and Phaeodaria. In: *Handbook of protoctista*. Jones and Bartlett Boston, pp. 334–346 (cit. on p. 27).
Cachon, J. and M. Cachon (1973). Systèmes microtubulaires de l'astropyle et des parapyles de Phaeodariés. In: *Archiv für Protistenkunde* 115, pp. 324–335 (cit. on p. 27).
Cachon-Enjumet, M. (1961). Contribution à l'étude de radiolaires Phaeodariés. PhD thesis. Alger (cit. on p. 29).
Caron, D. A., A. F. Michaels, N. R. Swanberg, and F. A. Howse (1995). Primary productivity by symbiont-bearing planktonic sarcodines (Acantharia, Radiolaria, Foraminifera) in surface waters near Bermuda. In: *Journal of Plankton Research* 17.1, pp. 103–129. DOI: 10.1093/plankt/17.1.103 (cit. on pp. 101, 118, 119).
Casey, R. E. (1966). A seasonal study on the distribution of polycystine radiolarians from waters overlying the Catalina Basin, Southern California. University of Southern California (cit. on p. 29).
Cattell, R. B. (1966). The scree test for the number of factors. In: *Multivariate behavioral research* 1.2, pp. 245–276 (cit. on pp. 143, 162).
Cavalier-Smith, T. (2002). The phagotrophic origin of eukaryotes and phylogenetic classification of Protozoa. In: *International journal of systematic and evolutionary microbiology* 52.2, pp. 297–354 (cit. on p. 25).
Cavan, E., E. Laurenceau-Cornec, M. Bressac, and P. Boyd (2019). Exploring the ecology of the mesopelagic biological pump. In: *Progress in Oceanography* 176, p. 102125. DOI: 10.1016/j.pocean.2019.102125 (cit. on pp. 20, 21, 121, 122).
Chen, T. et al. (2020). xgboost: Extreme Gradient Boosting. R package version 1.2.0.1. URL: https://CRAN.R-project.org/package=xgboost (cit. on p. 106).
Cheng, L., K. E. Trenberth, J. Fasullo, T. Boyer, J. Abraham, and J. Zhu (2017). Improved estimates of ocean heat content from 1960 to 2015. In: *Science Advances* 3.3, e1601545 (cit. on pp. 15, 194).

Chivers, W. J., A. W. Walne, and G. C. Hays (2017). Mismatch between marine plankton range movements and the velocity of climate change. In: *Nature communications* 8.1, p. 14434 (cit. on p. 124).

Claquin, P., A. Leynaert, A. Sferratore, J. Garnier, and O. Ragueneau (2006). Physiological Ecology of Diatoms Along the River–Sea Continuum. In: *The Silicon Cycle. Human Perturbations and Impacts on Aquatic Systems*, pp. 121–138 (cit. on p. 67).

Clarke, L. J., R. Trebilco, A. Walters, A. M. Polanowski, and B. E. Deagle (2020). DNA-based diet analysis of mesopelagic fish from the southern Kerguelen Axis. In: *Deep Sea Research Part II: Topical Studies in Oceanography* 174 (cit. on p. 120).

Clements, D., S Yang, T Weber, A. McDonnell, R. Kiko, L Stemmann, and D Bianchi (2023). New Estimate of Organic Carbon Export From Optical Measurements Reveals the Role of Particle Size Distribution and Export Horizon. In: *Global Biogeochemical Cycles* 37.3, e2022GB007633 (cit. on pp. 19, 106).

Conley, D. J., P. J. Frings, G. Fontorbe, W. Clymans, J. Stadmark, K. R. Hendry, A. O. Marron, and C. L. D. L. Rocha (2017). Biosilicification Drives a Decline of Dissolved Si in the Oceans through Geologic Time. In: *Frontiers in Marine Science* 4. DOI: 10.3389/fmars.2017.00397 (cit. on p. 101).

Coppola, L., P. Raimbault, L. Mortier, and P. Testor (2019). Monitoring the environment in the northwestern Mediterranean Sea. In: *Eos, Transactions American Geophysical Union* 100 (cit. on p. 144).

Cram, J. A., T. Weber, S. W. Leung, A. M. P. McDonnell, J.-H. Liang, and C. Deutsch (2018). The Role of Particle Size, Ballast, Temperature, and Oxygen in the Sinking Flux to the Deep Sea. In: *Global Biogeochemical Cycles* 32.5, pp. 858–876. DOI: 10.1029/2017gb005710 (cit. on p. 21).

Crocker, K. M. and U. Passow (1995). Differential aggregation of diatoms. In: *Marine ecology progress series. Oldendorf* 117.1, pp. 249–257 (cit. on p. 174).

Daufresne, M., K. Lengfellner, and U. Sommer (2009). Global warming benefits the small in aquatic ecosystems. In: *Proceedings of the National Academy of Sciences* 106.31, pp. 12788–12793 (cit. on pp. 123, 125).

Davies, C. H., L. E. Beckley, and A. J. Richardson (2022). Copepods and mixotrophic Rhizaria dominate zooplankton abundances in the oligotrophic Indian Ocean. In: *Deep Sea Research Part II: Topical Studies in Oceanography* 202, p. 105136 (cit. on p. 118).

Davies, T. K., S. Martin, C. Mees, E. Chassot, and D. M. Kaplan (2012). A review of the conservation benefits of marine protected areas for pelagic species associated with fisheries. In: *International Seafood Sustainability Foundation, McLean, Virginia, USA* (cit. on p. 15).

De La Rocha, C. L. and U. Passow (2007). Factors influencing the sinking of POC and the efficiency of the biological carbon pump. In: *Deep Sea Research Part II: Topical Studies in Oceanography* 54.5-7, pp. 639–658. DOI: 10.1016/j.dsr2.2007.01.004 (cit. on pp. 21, 120, 132, 158, 194, 201).

De Wever, P., P. Dumitrica, J. P. Caulet, C. Nigrini, and M. Caridroit (2002). Radiolarians in the sedimentary record (cit. on pp. 26, 47, 126).

Decelle, J., I. Probert, L. Bittner, Y. Desdevises, S. Colin, C. de Vargas, M. Gali, R. Simo, and F. Not (2012). An original mode of symbiosis in open ocean plankton. In: *Proceedings of the National Academy of Sciences* 109.44, pp. 18000–18005. DOI: 10.1073/pnas.1212303109 (cit. on pp. 28, 119).

Decelle, J., S. Colin, and R. A. Foster (2015). Photosymbiosis in Marine Planktonic Protists. In: *Marine Protists*. Springer Japan, pp. 465–500. DOI: 10.1007/978-4-431-55130-0_19 (cit. on pp. 47, 91, 96, 119).

Decelle, J., P. Martin, K. Paborstava, D. W. Pond, G. Tarling, F. Mahé, C. de Vargas, R. Lampitt, and F. Not (2013). Diversity, Ecology and Biogeochemistry of Cyst-Forming Acantharia (Radiolaria) in the Oceans. In: *PLoS ONE* 8.1. Ed. by L. J. Stal, e53598. DOI: 10.1371/journal.pone.0053598 (cit. on p. 119).

Decelle, J., G. Veronesi, C. LeKieffre, B. Gallet, F. Chevalier, H. Stryhanyuk, S. Marro, S. Ravanel, R. Tucoulou, N. Schieber, et al. (2021). Subcellular architecture and metabolic connection in

the planktonic photosymbiosis between Collodaria (radiolarians) and their microalgae. In: *Environmental Microbiology* 23.11, pp. 6569–6586 (cit. on p. 118).

Dennett, M. R., D. A. Caron, A. F. Michaels, S. M. Gallager, and C. S. Davis (2002). Video plankton recorder reveals high abundances of colonial Radiolaria in surface waters of the central North Pacific. In: *Journal of Plankton Research* 24.8, pp. 797–805 (cit. on pp. 31, 118).

DeVries, T., F. Primeau, and C. Deutsch (2012). The sequestration efficiency of the biological pump. In: *Geophysical Research Letters* 39.13, n/a–n/a. DOI: 10.1029/2012gl051963 (cit. on p. 19).

Diercks, A.-R. and V. L. Asper (1997). In situ settling speeds of marine snow aggregates below the mixed layer: Black Sea and Gulf of Mexico. In: *Deep Sea Research Part I: Oceanographic Research Papers* 44.3, pp. 385–398 (cit. on p. 134).

Dolan, J. R., M. Ciobanu, S. Marro, and L. Coppola (2017). An exploratory study of heterotrophic protists of the mesopelagic Mediterranean Sea. In: *ICES Journal of Marine Science* 76.3. Ed. by R. Ji, pp. 616–625. DOI: 10.1093/icesjms/fsx218 (cit. on p. 30).

Dolan, J. R. and L. Coppola (2023). Phaeogromids of the mesopelagic marine plankton: Temporal variability of concentrations and observations of feeding structures of four species from the mesopelagic in the Mediterranean Sea. In: *Journal of Eukaryotic Microbiology*, e12962 (cit. on p. 121).

Drago, L., T. Panaïotis, J.-O. Irisson, M. Babin, T. Biard, F. Carlotti, L. Coppola, L. Guidi, H. Hauss, L. Karp-Boss, et al. (2022). Global Distribution of Zooplankton Biomass Estimated by In Situ Imaging and Machine Learning. In: *Frontiers in Marine Science* 9 (cit. on pp. 31, 32, 41, 64, 91–93, 105, 106, 115, 200).

Ducklow, H., D. Steinberg, and K. Buesseler (2001). Upper Ocean Carbon Export and the Biological Pump. In: *Oceanography* 14.4, pp. 50–58. DOI: 10.5670/oceanog.2001.06 (cit. on pp. 21, 46).

Dunne, J. P., R. A. Armstrong, A. Gnanadesikan, and J. L. Sarmiento (2005). Empirical and mechanistic models for the particle export ratio. In: *Global Biogeochemical Cycles* 19.4 (cit. on p. 131).

Dunne, J. P., J. L. Sarmiento, and A. Gnanadesikan (2007). A synthesis of global particle export from the surface ocean and cycling through the ocean interior and on the seafloor. In: *Global Biogeochemical Cycles* 21.4 (cit. on pp. 95, 97, 106, 200).

Duret, M. T., R. S. Lampitt, and P. Lam (2019). Prokaryotic niche partitioning between suspended and sinking marine particles. In: *Environmental microbiology reports* 11.3, pp. 386–400 (cit. on p. 22).

Duret, M. T., R. S. Lampitt, and P. Lam (2020). Eukaryotic influence on the oceanic biological carbon pump in the Scotia Sea as revealed by 18S rRNA gene sequencing of suspended and sinking particles. In: *Limnology and Oceanography* 65.S1. DOI: 10.1002/lno.11319 (cit. on pp. 24, 33).

Durkin, C. A., K. O. Buesseler, I. Cetinić, M. L. Estapa, R. P. Kelly, and M. Omand (2021). A visual tour of carbon export by sinking particles. In: DOI: 10.1101/2021.02.16.431317 (cit. on pp. 34, 122, 159, 163, 173, 178, 183, 186).

Dutkiewicz, A., R. D. Müller, S. O'Callaghan, and H. Jónasson (2015). Census of seafloor sediments in the world's ocean. In: *Geology* 43.9, pp. 795–798. DOI: 10.1130/g36883.1 (cit. on p. 123).

Edgcomb, V. P. (2016). Marine protist associations and environmental impacts across trophic levels in the twilight zone and below. In: *Current Opinion in Microbiology* 31, pp. 169–175. DOI: 10.1016/j.mib.2016.04.001 (cit. on p. 24).

Edwards, K. F., M. K. Thomas, C. A. Klausmeier, and E. Litchman (2012). Allometric scaling and taxonomic variation in nutrient utilization traits and maximum growth rate of phytoplankton. In: *Limnology and Oceanography* 57.2, pp. 554–566 (cit. on p. 66).

Edwards, M. and A. J. Richardson (2004). Impact of climate change on marine pelagic phenology and trophic mismatch. In: *Nature* 430.7002, pp. 881–884 (cit. on p. 123).

Elith*, J., C. H. Graham*, R. P. Anderson, M. Dudík, S. Ferrier, A. Guisan, R. J. Hijmans, F. Huettmann, J. R. Leathwick, A. Lehmann, et al. (2006). Novel methods improve prediction of species' distributions from occurrence data. In: *Ecography* 29.2, pp. 129–151 (cit. on pp. 106, 163).

Elith, J., J. R. Leathwick, and T. Hastie (2008). A working guide to boosted regression trees. In: *Journal of animal ecology* 77.4, pp. 802–813 (cit. on p. 106).

Engel, A. and M. Schartau (1999). Influence of transparent exopolymer particles (TEP) on sinking velocity of Nitzschia closterium aggregates. In: *Marine Ecology Progress Series* 182, pp. 69–76 (cit. on p. 133).

Engel, A., J. Szlosek, L. Abramson, Z. Liu, and C. Lee (2009). Investigating the effect of ballasting by CaCO3 in Emiliania huxleyi: I. Formation, settling velocities and physical properties of aggregates. In: *Deep Sea Research Part II: Topical Studies in Oceanography* 56.18, pp. 1396–1407 (cit. on pp. 21, 132).

Erez, J., K. Takahashi, and S. Honjo (1982). In-situ dissolution experiment of radiolaria in the central North Pacific ocean. In: *Earth and Planetary Science Letters* 59.2, pp. 245–254. DOI: 10.1016/0012-821x(82)90129-7 (cit. on pp. 27, 33, 66, 99).

Faillettaz, R., M. Picheral, J. Y. Luo, C. Guigand, R. K. Cowen, and J.-O. Irisson (2016). Imperfect automatic image classification successfully describes plankton distribution patterns. In: *Methods in Oceanography* 15, pp. 60–77 (cit. on p. 29).

Faure, E., F. Not, A.-S. Benoiston, K. Labadie, L. Bittner, and S.-D. Ayata (2019). Mixotrophic protists display contrasted biogeographies in the global ocean. In: *The ISME Journal* 13.4, pp. 1072–1083. DOI: 10.1038/s41396-018-0340-5 (cit. on pp. 118, 119).

Fender, C. K., T. B. Kelly, L. Guidi, M. D. Ohman, M. C. Smith, and M. R. Stukel (2019). Investigating Particle Size-Flux Relationships and the Biological Pump Across a Range of Plankton Ecosystem States From Coastal to Oligotrophic. In: *Frontiers in Marine Science* 6. DOI: 10.3389/fmars.2019.00603 (cit. on pp. 22, 132, 176).

Field, C. B., M. J. Behrenfeld, J. T. Randerson, and P. Falkowski (1998). Primary production of the biosphere: integrating terrestrial and oceanic components. In: *science* 281.5374, pp. 237–240 (cit. on pp. 16, 23).

Fiksen, Ø., M. J. Follows, and D. L. Aksnes (2013). Trait-based models of nutrient uptake in microbes extend the Michaelis-Menten framework. In: *Limnology and oceanography* 58.1, pp. 193–202 (cit. on p. 67).

Finkel, Z. V., J. Beardall, K. J. Flynn, A. Quigg, T. A. V. Rees, and J. A. Raven (2009). Phytoplankton in a changing world: cell size and elemental stoichiometry. In: *Journal of Plankton Research* 32.1, pp. 119–137. DOI: 10.1093/plankt/fbp098 (cit. on p. 64).

Finkel, Z. V., J. Beardall, K. J. Flynn, A. Quigg, T. A. V. Rees, and J. A. Raven (2010). Phytoplankton in a changing world: cell size and elemental stoichiometry. In: *Journal of plankton research* 32.1, pp. 119–137 (cit. on p. 46).

Fischer, G. and G Karakaş (2009). Sinking rates and ballast composition of particles in the Atlantic Ocean: implications for the organic carbon fluxes to the deep ocean. In: *biogeosciences* 6.1, pp. 85–102 (cit. on p. 134).

Flynn, K. J., D. O. F. Skibinski, and C. Lindemann (2018). Effects of growth rate, cell size, motion, and elemental stoichiometry on nutrient transport kinetics. In: *PLoS Computational Biology* 14.4. Ed. by N. L. Komarova, e1006118. DOI: 10.1371/journal.pcbi.1006118 (cit. on p. 67).

Flynn, K., D. Stoecker, A Mitra, J. Raven, P. Glibert, P. Hansen, E Granéli, and J. Burkholder (2013). A case of mistaken identification: the importance of mixotrophy and the clarification of plankton functional-classification. In: *J. Plankton Res* 35, pp. 3–11 (cit. on p. 24).

Francois, R., S. Honjo, R. Krishfield, and S. Manganini (2002). Factors controlling the flux of organic carbon to the bathypelagic zone of the ocean. In: *Global Biogeochemical Cycles* 16.4, pp. 34–1–34–20. DOI: 10.1029/2001gb001722 (cit. on pp. 19, 20, 23).

Friedlingstein, P., M. W. Jones, M. O'Sullivan, R. M. Andrew, D. C. Bakker, J. Hauck, C. Le Quéré, G. P. Peters, W. Peters, J. Pongratz, et al. (2022). Global carbon budget 2021. In: *Earth System Science Data* 14.4, pp. 1917–2005 (cit. on pp. 15, 194).

Ganachaud, A. and C. Wunsch (2000). Improved estimates of global ocean circulation, heat transport and mixing from hydrographic data. In: *Nature* 408.6811, pp. 453–457 (cit. on p. 15).

Garcia, H., K. Weathers, C. Paver, I Smolyar, T. Boyer, M. Locarnini, M. Zweng, A. Mishonov, O. Baranova, D Seidov, et al. (2019a). World Ocean Atlas 2018, volume 3: Dissolved Oxygen, Apparent Oxygen Utilization, and Dissolved Oxygen Saturation. In: (cit. on p. 105).

Garcia, H., K. Weathers, C. Paver, I Smolyar, T. Boyer, M. Locarnini, M. Zweng, A. Mishonov, O. Baranova, D Seidov, et al. (2019b). World ocean atlas 2018, volume 4: Dissolved inorganic nutrients (phosphate, nitrate and nitrate+ nitrite, silicate). In: (cit. on p. 105).

Gardner, W. D. (1980). Field assessment of sediment traps. In: *J. mar. Res* 38.1, pp. 41–52 (cit. on pp. 181, 182).

— (1985). The effect of tilt on sediment trap efficiency. In: *Deep Sea Research Part A. Oceanographic Research Papers* 32.3, pp. 349–361 (cit. on pp. 137, 181).

Gaskell, D. E., M. D. Ohman, and P. M. Hull (2019). Zooglider-based measurements of planktonic foraminifera in the California Current System. In: *Journal of Foraminiferal Research* 49.4, pp. 390–404 (cit. on p. 183).

Giering, S. L. C., B. Hosking, N. Briggs, and M. H. Iversen (2020). The Interpretation of Particle Size, Shape, and Carbon Flux of Marine Particle Images Is Strongly Affected by the Choice of Particle Detection Algorithm. In: *Frontiers in Marine Science* 7. DOI: 10.3389/fmars.2020.00564 (cit. on p. 149).

Goericke, R, R. Olson, and A Shalapyonok (2000). A novel niche for Prochlorococcus sp. in low-light suboxic environments in the Arabian Sea and the Eastern Tropical North Pacific. In: *Deep Sea Research Part I: Oceanographic Research Papers* 47.7, pp. 1183–1205 (cit. on p. 121).

Gonzalez, H. E. (1992). Distribution and abundance of minipellets around the Antarctic peninsula. Implications for protistan feeding behaviour. In: *Marine Ecology Progress Series* 90, pp. 223–236 (cit. on pp. 28, 29, 34, 96, 98, 122).

Gorsky, G, M Picheral, and L Stemmann (2000). Use of the Underwater Video Profiler for the study of aggregate dynamics in the North Mediterranean. In: *Estuarine, Coastal and Shelf Science* 50.1, pp. 121–128 (cit. on p. 36).

Gorsky, G., M. D. Ohman, M. Picheral, S. Gasparini, L. Stemmann, J.-B. Romagnan, A. Cawood, S. Pesant, C. García-Comas, and F. Prejger (2010). Digital zooplankton image analysis using the ZooScan integrated system. In: *Journal of plankton research* 32.3, pp. 285–303 (cit. on p. 127).

Gowing, M. M. (1989). Abundance and feeding ecology of Antarctic phaeodarian radiolarians. In: *Marine Biology* 103.1, pp. 107–118. DOI: 10.1007/bf00391069 (cit. on pp. 27, 28, 33, 34, 91, 97, 98, 120, 195).

Gowing, M. M. (1986). Trophic biology of phaeodarian radiolarians and flux of living radiolarians in the upper 2000 m of the North Pacific central gyre. In: *Deep Sea Research Part A. Oceanographic Research Papers* 33.5, pp. 655–674. DOI: 10.1016/0198-0149(86)90059-2 (cit. on pp. 27, 28, 34, 47, 63, 68, 91, 97, 98, 120, 122, 195).

— (1993). Seasonal radiolarian flux at the VERTEX North Pacific time-series site. In: *Deep Sea Research Part I: Oceanographic Research Papers* 40.3, pp. 517–545. DOI: 10.1016/0967-0637(93)90144-r (cit. on p. 33).

Gowing, M. M. and W. N. Bentham (1994). Feeding ecology of phaeodarian radiolarians at the VERTEX North Pacific time series site. In: *Journal of Plankton Research* 16.6, pp. 707–719. DOI: 10.1093/plankt/16.6.707 (cit. on p. 28).

Gowing, M. M. and S. L. Coale (1989). Fluxes of living radiolarians and their skeletons along a northeast Pacific transect from coastal upwelling to open ocean waters. In: *Deep Sea Research Part A. Oceanographic Research Papers* 36.4, pp. 561–576. DOI: 10.1016/0198-0149(89)90006-x (cit. on p. 100).

Gowing, M. M. and D. L. Garrison (1992). Abundance and feeding ecology of larger protozooplankton in the ice edge zone of the Weddell and Scotia Seas during the austral winter. In: *Deep Sea Research Part A. Oceanographic Research Papers* 39.5, pp. 893–919. DOI: 10.1016/0198-0149(92)90128-g (cit. on p. 29).

Gowing, M. M. and M. W. Silver (1985). Minipellets: A new and abundant size class of marine fecal pellets. In: *Journal of Marine Research* 43.2, pp. 395–418. DOI: 10.1357/002224085788438676 (cit. on pp. 34, 98, 122).

Guidi, L., G. A. Jackson, L. Stemmann, J. C. Miquel, M. Picheral, and G. Gorsky (2008). Relationship between particle size distribution and flux in the mesopelagic zone. In: *Deep Sea Research Part I: Oceanographic Research Papers* 55.10, pp. 1364–1374. DOI: 10.1016/j.dsr.2008.05.014 (cit. on pp. 22, 36, 132, 133, 148, 163, 175, 176, 184, 201).

Guidi, L., L. Legendre, G. Reygondeau, J. Uitz, L. Stemmann, and S. A. Henson (2015). A new look at ocean carbon remineralization for estimating deepwater sequestration. In: *Global Biogeochemical Cycles* 29.7, pp. 1044–1059. DOI: 10.1002/2014gb005063 (cit. on pp. 20, 131, 148, 158).

Guidi, L., L. Stemmann, G. A. Jackson, F. Ibanez, H. Claustre, L. Legendre, M. Picheral, and G. Gorskya (2009). Effects of phytoplankton community on production, size, and export of large aggregates: A world-ocean analysis. In: *Limnology and Oceanography* 54.6, pp. 1951–1963. DOI: 10.4319/lo.2009.54.6.1951 (cit. on p. 20).

Guidi, L. et al. (2016). Plankton networks driving carbon export in the oligotrophic ocean. In: *Nature* 532.7600, pp. 465–470. DOI: 10.1038/nature16942 (cit. on pp. 22, 33, 47, 121, 126, 196).

Gutierrez-Rodriguez, A., M. R. Stukel, A. L. dos Santos, T. Biard, R. Scharek, D. Vaulot, M. R. Landry, and F. Not (2018). High contribution of Rhizaria (Radiolaria) to vertical export in the California Current Ecosystem revealed by DNA metabarcoding. In: *The ISME Journal* 13.4, pp. 964–976. DOI: 10.1038/s41396-018-0322-7 (cit. on pp. 33, 47, 126).

Haeckel, E. (1866). Generelle Morphologie der Organismen. Allgemeine Grundzüge der organischen Formen-Wissenschaft, mechanisch begründet durch die von C. Darwin reformirte Descendenz-Theorie, etc. Vol. 1 (cit. on p. 24).

— (1887). Report on the Radiolaria collected by HMS Challenger during the years 1873–1876. In: *Report on the Scientific Results of the Voyage of H.M.S. Challenger During the Years 1873–1876*. Ed. by C. W. Thompson. Vol. 18, pp. 1–1803 (cit. on p. 26).

Hannides, C. C., J. C. Drazen, and B. N. Popp (2015). Mesopelagic zooplankton metabolic demand in the North Pacific Subtropical Gyre. In: *Limnology and Oceanography* 60.2, pp. 419–428 (cit. on p. 98).

Hargrave, B. T. and N. M. Burns (1979). Assessment of sediment trap collection efficiency. In: *Limnology and Oceanography* 24.6, pp. 1124–1136 (cit. on p. 182).

Hays, G. C. (2003). A review of the adaptive significance and ecosystem consequences of zooplankton diel vertical migrations. In: *Migrations and Dispersal of Marine Organisms: Proceedings of the 37 th European Marine Biology Symposium held in Reykjavík, Iceland, 5–9 August 2002*. Springer, pp. 163–170 (cit. on p. 17).

Hedges, J. I., J. A. Baldock, Y. Gélinas, C. Lee, M. Peterson, and S. G. Wakeham (2001). Evidence for non-selective preservation of organic matter in sinking marine particles. In: *Nature* 409.6822, pp. 801–804 (cit. on p. 23).

Henson, S., F. Le Moigne, and S. Giering (2019). Drivers of carbon export efficiency in the global ocean. In: *Global biogeochemical cycles* 33.7, pp. 891–903 (cit. on p. 20).

Henson, S. A., C. Laufkötter, S. Leung, S. L. Giering, H. I. Palevsky, and E. L. Cavan (2022). Uncertain response of ocean biological carbon export in a changing world. In: *Nature Geoscience* 15.4, pp. 248–254 (cit. on pp. 90, 101, 124, 133).

Henson, S. A., R. Sanders, and E. Madsen (2012). Global patterns in efficiency of particulate organic carbon export and transfer to the deep ocean. In: *Global Biogeochemical Cycles* 26.1, n/a–n/a. DOI: 10.1029/2011gb004099 (cit. on pp. 20, 132, 158).

Henson, S. A., R. Sanders, E. Madsen, P. J. Morris, F. L. Moigne, and G. D. Quartly (2011). A reduced estimate of the strength of the ocean's biological carbon pump. In: *Geophysical Research Letters* 38.4, n/a–n/a. DOI: 10.1029/2011gl046735 (cit. on pp. 19, 131).

Herndl, G. J. and T. Reinthaler (2013). Microbial control of the dark end of the biological pump. In: *Nature Geoscience* 6.9, pp. 718–724. DOI: 10.1038/ngeo1921 (cit. on pp. 21–23).

Hijmans, R. J. (2012). Cross-validation of species distribution models: removing spatial sorting bias and calibration with a null model. In: *Ecology* 93.3, pp. 679–688 (cit. on p. 106).

Hollande, A, J Cachon, and M Cachon-Enjumet (1965). Les modalités de l'enkystement présporogénétique chez les acanthaires. In: *Protistologica* 1.2, pp. 91–104 (cit. on p. 119).

Holm, S. (1979). A simple sequentially rejective multiple test procedure. In: *Scandinavian journal of statistics*, pp. 65–70 (cit. on p. 143).

Honjo, S., D. W. Spencer, and W. D. Gardner (1992). A sediment trap intercomparison experiment in the Panama Basin, 1979. In: *Deep Sea Research Part A. Oceanographic Research Papers* 39.2, pp. 333–358 (cit. on p. 181).

Houpert, L., X Durrieu de Madron, P. Testor, A. Bosse, F. d'Ortenzio, M.-N. Bouin, D. Dausse, H. Le Goff, S. Kunesch, M. Labaste, et al. (2016). Observations of open-ocean deep convection in the northwestern M editerranean S ea: Seasonal and interannual variability of mixing and deep water masses for the 2007-2013 Period. In: *Journal of Geophysical Research: Oceans* 121.11, pp. 8139–8171 (cit. on p. 144).

Hoving, H.-J. T., P. Neitzel, H. Hauss, S. Christiansen, R. Kiko, B. H. Robison, P. Silva, and A. Körtzinger (2020). In situ observations show vertical community structure of pelagic fauna in the eastern tropical North Atlantic off Cape Verde. In: *Scientific Reports* 10.1, p. 21798 (cit. on p. 121).

Howe, A. T., D. Bass, J. M. Scoble, R. Lewis, K. Vickerman, H. Arndt, and T. Cavalier-Smith (2011). Novel Cultured Protists Identify Deep-branching Environmental DNA Clades of Cercozoa: New Genera Tremula, Micrometopion, Minimassisteria, Nudifila, Peregrinia. In: *Protist* 162.2, pp. 332–372. DOI: 10.1016/j.protis.2010.10.002 (cit. on p. 26).

Hurd, D. C. and K. Takahashi (1983). On the estimation of minimum mechanical loss during an in situ biogenic silica dissolution experiment. In: *Marine Micropaleontology* 7.5, pp. 441–447. DOI: 10.1016/0377-8398(83)90019-1 (cit. on p. 33).

Ikenoue, T., K. R. Bjørklund, S. B. Kruglikova, J. Onodera, K. Kimoto, and N. Harada (2015). Flux variations and vertical distributions of siliceous Rhizaria (Radiolaria and Phaeodaria) in the western Arctic Ocean: indices of environmental changes. In: *Biogeosciences* 12.6, pp. 2019–2046. DOI: 10.5194/bg-12-2019-2015 (cit. on p. 33).

Ikenoue, T., K. Kimoto, Y. Okazaki, M. Sato, M. C. Honda, K. Takahashi, N. Harada, and T. Fujiki (2019). Phaeodaria: An Important Carrier of Particulate Organic Carbon in the Mesopelagic Twilight Zone of the North Pacific Ocean. In: *Global Biogeochemical Cycles* 33.8, pp. 1146–1160. DOI: 10.1029/2019gb006258 (cit. on pp. 25, 31, 33, 47, 48, 63, 97, 98, 122, 126, 195).

Ikenoue, T., K. Takahashi, and S. Tanaka (2012). Fifteen year time-series of radiolarian fluxes and environmental conditions in the Bering Sea and the central subarctic Pacific, 1990–2005. In: *Deep Sea Research Part II: Topical Studies in Oceanography* 61-64, pp. 17–49. DOI: 10.1016/j.dsr2.2011.12.003 (cit. on p. 125).

Irigoien, X., T. A. Klevjer, A. Røstad, U. Martinez, G. Boyra, J. L. Acuña, A. Bode, F. Echevarria, J. I. Gonzalez-Gordillo, S. Hernandez-Leon, et al. (2014). Large mesopelagic fishes biomass and trophic efficiency in the open ocean. In: *Nature communications* 5.1, p. 3271 (cit. on pp. 90, 97).

Irisson, J.-O., S.-D. Ayata, D. J. Lindsay, L. Karp-Boss, and L. Stemmann (2022). Machine learning for the study of plankton and marine snow from images. In: *Annual review of marine science* 14, pp. 277–301 (cit. on pp. 36, 149).

Iversen, M. H. and H. Ploug (2010). Ballast minerals and the sinking carbon flux in the ocean: carbon-specific respiration rates and sinking velocity of marine snow aggregates. In: *Biogeosciences* 7.9, pp. 2613–2624. DOI: 10.5194/bg-7-2613-2010 (cit. on pp. 21, 22, 132, 174).

— (2013). Temperature effects on carbon-specific respiration rate and sinking velocity of diatom aggregates – potential implications for deep ocean export processes. In: *Biogeosciences* 10.6, pp. 4073–4085. DOI: 10.5194/bg-10-4073-2013 (cit. on p. 21).

Iversen, M. H. and R. S. Lampitt (2020). Size does not matter after all: No evidence for a size-sinking relationship for marine snow. In: *Progress in Oceanography* 189, p. 102445. DOI: 10.1016/j.pocean.2020.102445 (cit. on pp. 133, 134, 149, 159, 172, 173, 176).

Iversen, M. H. and L. K. Poulsen (2007). Coprorhexy, coprophagy, and coprochaly in the copepods Calanus helgolandicus, Pseudocalanus elongatus, and Oithona similis. In: *Marine Ecology Progress Series* 350, pp. 79–89 (cit. on p. 133).

Iversen, M. H., N. Nowald, H. Ploug, G. A. Jackson, and G. Fischer (2010). High resolution profiles of vertical particulate organic matter export off Cape Blanc, Mauritania: Degradation processes and ballasting effects. In: *Deep Sea Research Part I: Oceanographic Research Papers* 57.6, pp. 771–784 (cit. on p. 176).

Jackson, G. A. (1993). Flux feeding as a mechanism for zooplankton grazing and its implications for vertical particulate flux. In: *Limnology and Oceanography* 38.6, pp. 1328–1331. DOI: 10.4319/lo.1993.38.6.1328 (cit. on p. 69).

Jonkers, L., H. Hillebrand, and M. Kucera (2019). Global change drives modern plankton communities away from the pre-industrial state. In: *Nature* 570.7761, pp. 372–375 (cit. on p. 124).

Kaempf, J. and P. Chapman (Aug. 2016). The Functioning of Coastal Upwelling Systems. In: pp. 31–65. ISBN: 978-3-319-42522-1. DOI: 10.1007/978-3-319-42524-5_2 (cit. on p. 16).

Keeling, P. J. and F. Burki (2019). Progress towards the Tree of Eukaryotes. In: *Current Biology* 29.16, R808–R817. DOI: 10.1016/j.cub.2019.07.031 (cit. on pp. 24, 25, 194).

Kelley, D. and C. Richards (2023). oce: Analysis of Oceanographic Data. R package version 1.8-1. URL: https://CRAN.R-project.org/package=oce (cit. on p. 162).

Kerkhoff, A. J. and B. J. Enquist (2009). Multiplicative by nature: Why logarithmic transformation is necessary in allometry. In: *Journal of Theoretical Biology* 257.3, pp. 519–521. DOI: 10.1016/j.jtbi.2008.12.026 (cit. on p. 52).

Kharbush, J. J., H. G. Close, B. A. Van Mooy, C. Arnosti, R. H. Smittenberg, F. A. Le Moigne, G. Mollenhauer, B. Scholz-Böttcher, I. Obreht, B. P. Koch, et al. (2020). Particulate organic carbon deconstructed: molecular and chemical composition of particulate organic carbon in the ocean. In: *Frontiers in Marine Science* 7, p. 518 (cit. on p. 21).

Kiko, R., M. Picheral, D. Antoine, M. Babin, L. Berline, T. Biard, E. Boss, P. Brandt, F. Carlotti, S. Christiansen, et al. (2022). A global marine particle size distribution dataset obtained with the Underwater Vision Profiler 5. In: *Earth System Science Data* 14.9, pp. 4315–4337 (cit. on p. 41).

Kilmer, J. T. and R. L. Rodríguez (2017). Ordinary least squares regression is indicated for studies of allometry. In: *Journal of evolutionary biology* 30.1, pp. 4–12 (cit. on p. 52).

Kiørboe, T. (2013). Zooplankton body composition. In: *Limnology and Oceanography* 58.5, pp. 1843–1850. DOI: 10.4319/lo.2013.58.5.1843 (cit. on pp. 63, 69, 198).

Kiørboe, T., K. Andersen, and H. Dam (1990). Coagulation efficiency and aggregate formation in marine phytoplankton. In: *Marine Biology* 107, pp. 235–245 (cit. on p. 174).

Klaas, C. and D. E. Archer (2002). Association of sinking organic matter with various types of mineral ballast in the deep sea: Implications for the rain ratio. In: *Global Biogeochemical Cycles* 16.4, pp. 63–1–63–14. DOI: 10.1029/2001gb001765 (cit. on pp. 23, 133).

Knauer, G. A., J. H. Martin, and K. W. Bruland (1979). Fluxes of particulate carbon, nitrogen, and phosphorus in the upper water column of the northeast Pacific. In: *Deep Sea Research Part A. Oceanographic Research Papers* 26.1, pp. 97–108 (cit. on p. 138).

Knecht, N. S., F. Benedetti, U. Hofmann Elizondo, N. Bednaršek, S. Chaabane, C. de Weerd, K. T. Peijnenburg, R. Schiebel, and M. Vogt (2023). The impact of zooplankton calcifiers on the marine carbon cycle. In: *Global Biogeochemical Cycles* 37.6, e2022GB007685 (cit. on p. 126).

Krause, J. W., M. W. Lomas, and D. M. Nelson (2009). Biogenic silica at the Bermuda Atlantic Time-series Study site in the Sargasso Sea: Temporal changes and their inferred controls based on a 15-year record. In: *Global Biogeochemical Cycles* 23.3 (cit. on p. 99).

Kubryakov, A. and S. Stanichny (2022). Sinking velocity of small particles in the Black Sea: Vertical distribution and seasonal variability from continuous Bio-Argo measurements of backscattering. In: *Journal of Marine Systems* 227, p. 103695 (cit. on p. 134).

Kuhn, M., J. Wing, S. Weston, A. Williams, C. Keefer, A. Engelhardt, T. Cooper, Z. Mayer, B. Kenkel, R. C. Team, et al. (2020). Package 'caret'. In: *The R Journal* 223, p. 7 (cit. on p. 52).

Kwiatkowski, L., O. Torres, L. Bopp, O. Aumont, M. Chamberlain, J. R. Christian, J. P. Dunne, M. Gehlen, T. Ilyina, J. G. John, et al. (2020). Twenty-first century ocean warming, acidification, deoxygenation, and upper-ocean nutrient and primary production decline from CMIP6 model projections. In: *Biogeosciences* 17.13, pp. 3439–3470 (cit. on pp. 101, 200).

Kwon, E. Y., F. Primeau, and J. L. Sarmiento (2009). The impact of remineralization depth on the air–sea carbon balance. In: *Nature Geoscience* 2.9, pp. 630–635. DOI: 10.1038/ngeo612 (cit. on pp. 19, 90, 132, 158, 194).

Laget, M., N. Llopis-Monferrer, J.-F. Maguer, A. Leynaert, and T. Biard (2023). Elemental content allometries and silicon uptake rates of planktonic Rhizaria: Insights into their ecology and

role in biogeochemical cycles. In: *Limnology and Oceanography* 68.2, pp. 439–454 (cit. on pp. 45, 91, 92, 97, 104, 200).

Lam, P. J. and J. K. Bishop (2007). High biomass, low export regimes in the Southern Ocean. In: *Deep Sea Research Part II: Topical Studies in Oceanography* 54.5-7, pp. 601–638. DOI: 10.1016/j.dsr2.2007.01.013 (cit. on p. 23).

Lampitt, R. S., I. Salter, and D. Johns (2009). Radiolaria: Major exporters of organic carbon to the deep ocean. In: *Global Biogeochemical Cycles* 23.1, n/a–n/a. DOI: 10.1029/2008gb003221 (cit. on pp. 33, 47, 122, 185).

Lampitt, R. S., E. P. Achterberg, T. R. Anderson, J. Hughes, M. Iglesias-Rodriguez, B. A. Kelly-Gerreyn, M. Lucas, E. Popova, R. Sanders, J. Shepherd, et al. (2008a). Ocean fertilization: a potential means of geoengineering? In: *Philosophical Transactions of the Royal Society A: Mathematical, Physical and Engineering Sciences* 366.1882, pp. 3919–3945 (cit. on p. 158).

Lampitt, R. S., B Boorman, L Brown, M. Lucas, I. Salter, R. Sanders, K Saw, S Seeyave, S. J. Thomalla, and R. Turnewitsch (2008b). Particle export from the euphotic zone: Estimates using a novel drifting sediment trap, 234Th and new production. In: *Deep Sea Research Part I: Oceanographic Research Papers* 55.11, pp. 1484–1502 (cit. on p. 173).

Lampitt, R. and A. Antia (1997). Particle flux in deep seas: regional characteristics and temporal variability. In: *Deep Sea Research Part I: Oceanographic Research Papers* 44.8, pp. 1377–1403 (cit. on p. 121).

Lampitt, R., I Salter, B. de Cuevas, S Hartman, K. Larkin, and C. Pebody (2010). Long-term variability of downward particle flux in the deep northeast Atlantic: Causes and trends. In: *Deep Sea Research Part II: Topical Studies in Oceanography* 57.15, pp. 1346–1361 (cit. on pp. 19, 158).

Langer, M. R., A. E. Weinmann, S. Lötters, J. M. Bernhard, and D. Rödder (2013). Climate-driven range extension of Amphistegina (Protista, Foraminiferida): models of current and predicted future ranges. In: *PloS one* 8.2, e54443 (cit. on p. 123).

Laufkötter, C., J. G. John, C. A. Stock, and J. P. Dunne (2017). Temperature and oxygen dependence of the remineralization of organic matter. In: *Global Biogeochemical Cycles* 31.7, pp. 1038–1050. DOI: 10.1002/2017gb005643 (cit. on p. 21).

Laurenceau-Cornec, E. C., F. A. C. L. Moigne, M. Gallinari, B. Moriceau, J. Toullec, M. H. Iversen, A. Engel, and C. L. De La Rocha (2020). New guidelines for the application of Stokes' models to the sinking velocity of marine aggregates. In: *Limnology and Oceanography* 65.6, pp. 1264–1285. DOI: 10.1002/lno.11388 (cit. on p. 133).

Laurenceau-Cornec, E. C., T. W. Trull, D. M. Davies, C. L. De La Rocha, and S. Blain (2015). Phytoplankton morphology controls on marine snow sinking velocity. In: *Marine Ecology Progress Series* 520, pp. 35–56. DOI: 10.3354/meps11116 (cit. on pp. 173, 174, 176).

Laws, E. A., P. G. Falkowski, W. O. Smith Jr, H. Ducklow, and J. J. McCarthy (2000). Temperature effects on export production in the open ocean. In: *Global biogeochemical cycles* 14.4, pp. 1231–1246 (cit. on pp. 95, 97, 106, 131, 200).

Lazarus, D. B., B. Kotrc, G. Wulf, and D. N. Schmidt (2009). Radiolarians decreased silicification as an evolutionary response to reduced Cenozoic ocean silica availability. In: *Proceedings of the National Academy of Sciences* 106.23, pp. 9333–9338. DOI: 10.1073/pnas.0812979106 (cit. on pp. 123, 125).

Lê, S., J. Josse, and F. Husson (2008). FactoMineR: an R package for multivariate analysis. In: *Journal of statistical software* 25, pp. 1–18 (cit. on pp. 143, 163).

Le Moigne, F. A., S. A. Henson, E. Cavan, C. Georges, K. Pabortsava, E. P. Achterberg, E. Ceballos-Romero, M. Zubkov, and R. J. Sanders (2016). What causes the inverse relationship between primary production and export efficiency in the Southern Ocean? In: *Geophysical Research Letters* 43.9, pp. 4457–4466 (cit. on p. 20).

Leblanc, K., A. Lafond, V. Cornet, J. Legras, B. Marie, and B. Quéguiner (2021). Deep particle stocks following the summer bloom around the Kerguelen islands: Insights into diatoms physiological state, community structure and mortality modes. In: *Journal of Marine Systems* 222, p. 103609 (cit. on p. 122).

Legendre, L and J Le Fèvre (1992). Interactions between hydrodynamics and pelagic ecosystems: relevance to resource exploitation and climate change. In: *South African journal of marine science* 12.1, pp. 477–486 (cit. on p. 158).

Legendre, L. and R. B. Rivkin (2008). Planktonic food webs: microbial hub approach. In: *Marine Ecology Progress Series* 365, pp. 289–309 (cit. on p. 122).

Leles, S. G. et al. (2017). Oceanic protists with different forms of acquired phototrophy display contrasting biogeographies and abundance. In: *Proceedings of the Royal Society B: Biological Sciences* 284.1860, p. 20170664. DOI: 10.1098/rspb.2017.0664 (cit. on pp. 118, 119).

Leynaert, A. (1993). La production de silice biogenique dans l'ocean: de la mer de weddell a l'ocean antarctique. PhD thesis. Paris 6 (cit. on p. 51).

Leynaert, A., P. Tréguer, C. Lancelot, and M. Rodier (2001). Silicon limitation of biogenic silica production in the Equatorial Pacific. In: *Deep Sea Research Part I: Oceanographic Research Papers* 48.3, pp. 639–660 (cit. on p. 99).

Leynaert, A., P. Tréguer, D. M. Nelson, and Y Del Amo (1996). ^{32}Si as a tracer of biogenic silica production: methodological improvements. In: *Integrated Marine System Analysis* (cit. on p. 51).

Lindemann, C., Ø. Fiksen, K. H. Andersen, and D. L. Aksnes (2016). Scaling laws in phytoplankton nutrient uptake affinity. In: *Frontiers in Marine Science* 3, p. 26 (cit. on p. 67).

Llopis Monferrer, N., T. Biard, M. M. Sandin, F. Lombard, M. Picheral, A. Elineau, L. Guidi, A. Leynaert, P. J. Treguer, and F. Not (2022). Siliceous Rhizaria abundances and diversity in the Mediterranean Sea assessed by combined imaging and metabarcoding approaches. In: *Frontiers in Marine Science* 9, p. 895995 (cit. on p. 127).

Llopis-Monferrer, N., D. Boltovskoy, P. Tréguer, M. M. Sandin, F. Not, and A. Leynaert (2020). Estimating Biogenic Silica Production of Rhizaria in the Global Ocean. In: *Global Biogeochemical Cycles* 34.3. DOI: 10.1029/2019gb006286 (cit. on pp. 23, 32, 37, 41, 47, 48, 51, 53, 57, 59–61, 64, 67, 68, 74, 75, 80–82, 91, 92, 99, 104, 105, 122, 197, 198, 200).

Llopis Monferrer, N., A. Leynaert, P. Tréguer, A. Gutiérrez-Rodríguez, B. Moriceau, M. Gallinari, M. Latasa, S. l'Helguen, J.-F. Maguer, K. Safi, et al. (2021). Role of small Rhizaria and diatoms in the pelagic silica production of the Southern Ocean. In: *Limnology and Oceanography* 66.6, pp. 2187–2202 (cit. on pp. 48, 96, 99).

Locarnini, M., A. Mishonov, O. Baranova, T. Boyer, M. Zweng, H. Garcia, D Seidov, K. Weathers, C. Paver, I Smolyar, et al. (2018). World ocean atlas 2018, volume 1: Temperature. In: (cit. on pp. 104, 105).

Lombard, F. et al. (2019). Globally Consistent Quantitative Observations of Planktonic Ecosystems. In: *Frontiers in Marine Science* 6. DOI: 10.3389/fmars.2019.00196 (cit. on pp. 35, 36, 132, 159, 175).

Longhurst, A. R. (2010). Ecological geography of the sea. Elsevier (cit. on p. 106).

López-Urrutia, Á., E. San Martin, R. P. Harris, and X. Irigoien (2006). Scaling the metabolic balance of the oceans. In: *Proceedings of the National Academy of Sciences* 103.23, pp. 8739–8744 (cit. on p. 21).

Lutz, M., R. Dunbar, and K. Caldeira (2002). Regional variability in the vertical flux of particulate organic carbon in the ocean interior. In: *Global biogeochemical cycles* 16.3, pp. 11–1 (cit. on p. 19).

Mackas, D., W. Greve, M. Edwards, S. Chiba, K Tadokoro, D Eloire, M. Mazzocchi, S Batten, A. Richardson, C. Johnson, et al. (2012). Changing zooplankton seasonality in a changing ocean: Comparing time series of zooplankton phenology. In: *Progress in Oceanography* 97, pp. 31–62 (cit. on p. 123).

Maggi, F and J. Winterwerp (2004). Method for computing the three-dimensional capacity dimension from two-dimensional projections of fractal aggregates. In: *Physical Review E* 69.1, p. 011405 (cit. on pp. 157, 177).

Maldonado, M., M. López-Acosta, C. Sitjà, M. García-Puig, C. Galobart, G. Ercilla, and A. Leynaert (2019). Sponge skeletons as an important sink of silicon in the global oceans. In: *Nature Geoscience* 12.10, pp. 815–822. DOI: 10.1038/s41561-019-0430-7 (cit. on p. 123).

Mansour, J. S., A. Norlin, N. L. Monferrer, S. L'Helguen, and F. Not (2021). Carbon and nitrogen content to biovolume relationships for marine protist of the Rhizaria lineage (Radiolaria and

Phaeodaria). In: *Limnology and Oceanography*. DOI: 10.1002/lno.11714 (cit. on pp. 37, 48, 52, 54–60, 79, 80, 82, 197).

Many, G, X. D. de Madron, R. Verney, F. Bourrin, P. Renosh, F Jourdin, and A Gangloff (2019). Geometry, fractal dimension and settling velocity of flocs during flooding conditions in the Rhône ROFI. In: *Estuarine, Coastal and Shelf Science* 219, pp. 1–13 (cit. on pp. 157, 177).

Marron, A. O., S. Ratcliffe, G. L. Wheeler, R. E. Goldstein, N. King, F. Not, C. de Vargas, and D. J. Richter (2016). The Evolution of Silicon Transport in Eukaryotes. In: *Molecular Biology and Evolution* 33.12, pp. 3226–3248. DOI: 10.1093/molbev/msw209 (cit. on pp. 67, 199).

Mars Brisbin, M., O. D. Brunner, M. M. Grossmann, and S. Mitarai (2020). Paired high-throughput, in-situ imaging and high-throughput sequencing illuminate acantharian abundance and vertical distribution. In: DOI: 10.1101/2020.02.27.967349 (cit. on pp. 119, 127).

Marsay, C. M., R. J. Sanders, S. A. Henson, K. Pabortsava, E. P. Achterberg, and R. S. Lampitt (2015). Attenuation of sinking particulate organic carbon flux through the mesopelagic ocean. In: *Proceedings of the National Academy of Sciences* 112.4, pp. 1089–1094. DOI: 10.1073/pnas.1415311112 (cit. on p. 21).

Martin, A. et al. (2020). The oceans' twilight zone must be studied now, before it is too late. In: *Nature* 580.7801, pp. 26–28. DOI: 10.1038/d41586-020-00915-7 (cit. on pp. 18, 90).

Martin, J. H., G. A. Knauer, D. M. Karl, and W. W. Broenkow (1987). VERTEX [Vertical Transport and Exchange]: carbon cycling in the northeast Pacific. In: *Deep Sea Research Part B. Oceanographic Literature Review* 34.9, p. 753. DOI: 10.1016/0198-0254(87)90148-8 (cit. on pp. 19, 20, 158).

Martin, P., J. T. Allen, M. J. Cooper, D. G. Johns, R. S. Lampitt, R. Sanders, and D. A. H. Teagle (2010). Sedimentation of acantharian cysts in the Iceland Basin: Strontium as a ballast for deep ocean particle flux, and implications for acantharian reproductive strategies. In: *Limnology and Oceanography* 55.2, pp. 604–614. DOI: 10.4319/lo.2010.55.2.0604 (cit. on p. 119).

Martin-Jézéquel, V., M. Hildebrand, and M. A. Brzezinski (2000). Silicon metabolism in diatoms: implications for growth. In: *Journal of phycology* 36.5, pp. 821–840 (cit. on p. 23).

Martini, S. and S. H. Haddock (2017). Quantification of bioluminescence from the surface to the deep sea demonstrates its predominance as an ecological trait. In: *Scientific reports* 7.1, pp. 1–11 (cit. on p. 17).

McClain, C. R., A. G. Boyer, and G. Rosenberg (2006). The island rule and the evolution of body size in the deep sea. In: *Journal of Biogeography* 33.9, pp. 1578–1584 (cit. on p. 125).

McDonnell, A. M. P. and K. O. Buesseler (2010). Variability in the average sinking velocity of marine particles. In: *Limnology and Oceanography* 55.5, pp. 2085–2096. DOI: 10.4319/lo.2010.55.5.2085 (cit. on pp. 38, 133, 134, 150).

McNown, J. S. and J. Malaika (1950). Effects of particle shape on settling velocity at low Reynolds numbers. In: *Transactions, American Geophysical Union* 31.1, p. 74. DOI: 10.1029/tr031i001p00074 (cit. on pp. 21, 132).

Meijering, E., O. Dzyubachyk, and I. Smal (2012). Methods for cell and particle tracking. In: *Methods in enzymology* 504, pp. 183–200 (cit. on p. 139).

Menden-Deuer, S. and E. J. Lessard (2000). Carbon to volume relationships for dinoflagellates, diatoms, and other protist plankton. In: *Limnology and Oceanography* 45.3, pp. 569–579. DOI: 10.4319/lo.2000.45.3.0569 (cit. on pp. 46, 48, 53, 56, 62, 63, 68, 69, 117, 196, 197).

Michaels, A. (1988). Vertical distribution and abundance of Acantharia and their symbionts. In: *Marine Biology* 97, pp. 559–569 (cit. on p. 31).

Michaels, A. F., D. A. Caron, N. R. Swanberg, F. A. Howse, and C. M. Michaels (1995). Planktonic sarcodines (Acantharia, Radiolaria, Foraminifera) in surface waters near Bermuda: abundance, biomass and vertical flux. In: *Journal of Plankton Research* 17.1, pp. 131–163. DOI: 10.1093/plankt/17.1.131 (cit. on pp. 48, 63).

Miklasz, K. A. and M. W. Denny (2010). Diatom sinkings speeds: Improved predictions and insight from a modified Stokes' law. In: *Limnology and Oceanography* 55.6, pp. 2513–2525. DOI: 10.4319/lo.2010.55.6.2513 (cit. on p. 66).

Mitra, A., K. J. Flynn, J. M. Burkholder, T. Berge, A. Calbet, J. A. Raven, E. Granéli, P. M. Glibert, P. J. Hansen, D. K. Stoecker, et al. (2014). The role of mixotrophic protists in the biological carbon pump. In: *Biogeosciences* 11.4, pp. 995–1005 (cit. on p. 24).

Mitra, A., K. J. Flynn, U. Tillmann, J. A. Raven, D. Caron, D. K. Stoecker, F. Not, P. J. Hansen, G. Hallegraeff, R. Sanders, et al. (2016). Defining planktonic protist functional groups on mechanisms for energy and nutrient acquisition: incorporation of diverse mixotrophic strategies. In: *Protist* 167.2, pp. 106–120 (cit. on pp. 118, 119).

Monroy, P., E. Hernández-García, V. Rossi, and C. López (2017). Modeling the dynamical sinking of biogenic particles in oceanic flow. In: *Nonlinear Processes in Geophysics* 24.2, pp. 293–305. DOI: 10.5194/npg-24-293-2017 (cit. on p. 16).

Moore, J. K., W. Fu, F. Primeau, G. L. Britten, K. Lindsay, M. Long, S. C. Doney, N. Mahowald, F. Hoffman, and J. T. Randerson (2018). Sustained climate warming drives declining marine biological productivity. In: *Science* 359.6380, pp. 1139–1143. DOI: 10.1126/science.aao6379 (cit. on p. 124).

Moreira, D., S. von der Heyden, D. Bass, P. López-García, E. Chao, and T. Cavalier-Smith (2007). Global eukaryote phylogeny: combined small-and large-subunit ribosomal DNA trees support monophyly of Rhizaria, Retaria and Excavata. In: *Molecular phylogenetics and evolution* 44.1, pp. 255–266 (cit. on p. 25).

Morley, J. J. and J. C. Stepien (1984). Siliceous microfauna in waters beneath Antarctic sea ice. In: *Marine ecology progress series*, pp. 207–210 (cit. on p. 96).

Mortlock, R. A. and P. N. Froelich (1989). A simple method for the rapid determination of biogenic opal in pelagic marine sediments. In: *Deep Sea Research Part A. Oceanographic Research Papers* 36.9, pp. 1415–1426 (cit. on p. 57).

Nakamura, Y., I. Imai, A. Yamaguchi, A. Tuji, F. Not, and N. Suzuki (2015). Molecular Phylogeny of the Widely Distributed Marine Protists, Phaeodaria (Rhizaria, Cercozoa). In: *Protist* 166.3, pp. 363–373. DOI: 10.1016/j.protis.2015.05.004 (cit. on pp. 28, 49).

Nakamura, Y., I. Imai, A. Yamaguchi, A. Tuji, and N. Suzuki (2013). Aulographis japonica sp. nov. (Phaeodaria, Aulacanthida, Aulacanthidae), an abundant zooplankton in the deep sea of the Sea of Japan. en. In: *Plankton and Benthos Research* 8.3, pp. 107–115. ISSN: 1880-8247, 1882-627X. DOI: 10.3800/pbr.8.107 (cit. on pp. 28–31, 96, 97).

Nakamura, Y., I. Iwata, R. S. Hori, N. Uchiyama, A. Tuji, M. J. Fujita, D. Honda, and H. Ohfuji (2018a). Elemental composition and ultrafine structure of the skeleton in shell-bearing protists —A case study of phaeodarians and radiolarians. In: *Journal of Structural Biology* 204.1, pp. 45–51. DOI: 10.1016/j.jsb.2018.06.008 (cit. on pp. 27, 33, 46, 65).

Nakamura, Y., M. M. Sandin, N. Suzuki, A. Tuji, and F. Not (2020). Phylogenetic revision of the order entactinaria—Paleozoic relict radiolaria (Rhizaria, SAR). In: *Protist* 171.1, p. 125712 (cit. on p. 27).

Nakamura, Y., R. Somiya, M. Kanda, A. Yamaguchi, A. Tuji, and R. S. Hori (2018b). Gazelletta kashiwaensis sp. nov.(Medusettidae, Phaeodaria, Cercozoa), its morphology, phylogeny, distribution, and feeding behavior. In: *Journal of Eukaryotic Microbiology* 65.6, pp. 923–927 (cit. on p. 121).

Nakamura, Y., R. Somiya, N. Suzuki, M. Hidaka-Umetsu, A. Yamaguchi, and D. J. Lindsay (2017). Optics-based surveys of large unicellular zooplankton: a case study on radiolarians and phaeodarians. In: *Plankton and Benthos Research* 12.2, pp. 95–103. DOI: 10.3800/pbr.12.95 (cit. on p. 64).

Nakamura, Y. and N. Suzuki (2015). Phaeodaria: Diverse Marine Cercozoans of World-Wide Distribution. In: *Marine Protists*. Springer Japan, pp. 223–249. DOI: 10.1007/978-4-431-55130-0_9 (cit. on pp. 28, 46, 47, 68, 90, 91, 96, 99, 121, 194, 197).

Nakamura, Y., A. Tuji, K. Kimoto, A. Yamaguchi, R. S. Hori, and N. Suzuki (2021). Ecology, Morphology, Phylogeny and Taxonomic Revision of Giant Radiolarians, Orodaria ord. nov.(Radiolaria; Rhizaria; SAR). In: *Protist* 172.3, p. 125808 (cit. on pp. 26, 27).

Nikolaev, S. I., C. Berney, J. F. Fahrni, I. Bolivar, S. Polet, A. P. Mylnikov, V. V. Aleshin, N. B. Petrov, and J. Pawlowski (2004). The twilight of Heliozoa and rise of Rhizaria, an emerging

supergroup of amoeboid eukaryotes. In: *Proceedings of the National Academy of Sciences* 101.21, pp. 8066–8071. DOI: 10.1073/pnas.0308602101 (cit. on pp. 25, 26).

Not, F., R. Gausling, F. Azam, J. F. Heidelberg, and A. Z. Worden (2007). Vertical distribution of picoeukaryotic diversity in the Sargasso Sea. In: *Environmental Microbiology* 9.5, pp. 1233–1252. DOI: 10.1111/j.1462-2920.2007.01247.x (cit. on p. 120).

Nowald, N., G. Fischer, V. Ratmeyer, M. Iversen, C Reuter, and G. Wefer (2009). In-situ sinking speed measurements of marine snow aggregates acquired with a settling chamber mounted to the Cherokee ROV. In: *Oceans 2009-Europe*. IEEE, pp. 1–6 (cit. on pp. 134, 173, 174).

Nowicki, M., T. DeVries, and D. A. Siegel (2022). Quantifying the carbon export and sequestration pathways of the ocean's biological carbon pump. In: *Global Biogeochemical Cycles* 36.3, e2021GB007083 (cit. on pp. 19, 95, 97, 106, 132, 200).

Ogane, K., A. Tuji, N. Suzuki, A. Matsuoka, T. Kurihara, and R. S. Hori (2010). Direct observation of the skeletal growth patterns of polycystine radiolarians using a fluorescent marker. In: *Marine Micropaleontology* 77.3-4, pp. 137–144 (cit. on p. 28).

Okubo, A. (1987). Fantastic Voyage into the Deep: Marine Biofluid Mechanics. In: *Lecture Notes in Biomathematics*. Springer Berlin Heidelberg, pp. 32–47. DOI: 10.1007/978-3-642-93360-8_3 (cit. on p. 38).

Omand, M. M., E. A. D'Asaro, C. M. Lee, M. J. Perry, N. Briggs, I. Cetini, and A. Mahadevan (2015). Eddy-driven subduction exports particulate organic carbon from the spring bloom. In: *Science* 348.6231, pp. 222–225. DOI: 10.1126/science.1260062 (cit. on p. 132).

Omand, M. M., R. Govindarajan, J. He, and A. Mahadevan (2020). Sinking flux of particulate organic matter in the oceans: Sensitivity to particle characteristics. In: *Scientific Reports* 10.1. DOI: 10.1038/s41598-020-60424-5 (cit. on pp. 38, 133).

Paffenhöfer, G.-A. (1998). Heterotrophic protozoa and small metazoa: feeding rates and prey-consumer interactions. In: *Journal of Plankton Research* 20.1, pp. 121–133 (cit. on p. 24).

Panaïotis, T., M. Babin, T. Biard, F. Carlotti, L. Coppola, L. Guidi, H. Hauss, L. Karp-Boss, R. Kiko, F. Lombard, et al. (2023). Three major mesoplanktonic communities resolved by in situ imaging in the upper 500 m of the global ocean. In: *Global Ecology and Biogeography* (cit. on p. 41).

Pante, E. and B. Simon-Bouhet (2013). marmap: a package for importing, plotting and analyzing bathymetric and topographic data in R. In: *PLoS One* 8.9, e73051 (cit. on pp. 154, 161).

Passow, U. (2004). Switching perspectives: Do mineral fluxes determine particulate organic carbon fluxes or vice versa? In: *Geochemistry, Geophysics, Geosystems* 5.4 (cit. on p. 23).

Passow, U. and C. A. Carlson (2012). The biological pump in a high CO2 world. In: *Marine Ecology Progress Series* 470, pp. 249–271. DOI: 10.3354/meps09985 (cit. on pp. 19, 158).

Passow, U. and C. L. De La Rocha (2006). Accumulation of mineral ballast on organic aggregates. In: *Global Biogeochemical Cycles* 20.1 (cit. on p. 23).

Pernice, M. C., C. R. Giner, R. Logares, J. Perera-Bel, S. G. Acinas, C. M. Duarte, J. M. Gasol, and R. Massana (2015). Large variability of bathypelagic microbial eukaryotic communities across the world's oceans. In: *The ISME Journal* 10.4, pp. 945–958. DOI: 10.1038/ismej.2015.170 (cit. on p. 120).

Peterson, M. L., S. G. Wakeham, C. Lee, M. A. Askea, and J. C. Miquel (2005). Novel techniques for collection of sinking particles in the ocean and determining their settling rates. In: *Limnology and Oceanography: Methods* 3.12, pp. 520–532 (cit. on pp. 134, 172).

Picheral, M., C. Catalano, D. Brousseau, H. Claustre, L. Coppola, E. Leymarie, J. Coindat, F. Dias, S. Fevre, L. Guidi, et al. (2022). The Underwater Vision Profiler 6: an imaging sensor of particle size spectra and plankton, for autonomous and cabled platforms. In: *Limnology and Oceanography: Methods* 20.2, pp. 115–129 (cit. on pp. 36, 37, 132, 135, 136, 139, 159–161, 181, 195, 201).

Picheral, M., S. Colin, and J.-O. Irisson (2017). EcoTaxa, a tool for the taxonomic classification of images (cit. on pp. 36, 103, 139, 161, 199).

Picheral, M., L. Guidi, L. Stemmann, D. M. Karl, G. Iddaoud, and G. Gorsky (2010). The Underwater Vision Profiler 5: An advanced instrument for high spatial resolution studies of particle size

spectra and zooplankton. In: *Limnology and Oceanography: Methods* 8.9, pp. 462–473. DOI: 10.4319/lom.2010.8.462 (cit. on pp. 36, 37, 92, 103, 132, 144, 159, 195, 199).

Pilskaln, C. H., C. Lehmann, J. B. Paduan, and M. W. Silver (1998). Spatial and temporal dynamics in marine aggregate abundance, sinking rate and flux: Monterey Bay, central California. In: *Deep Sea Research Part II: Topical Studies in Oceanography* 45.8-9, pp. 1803–1837 (cit. on pp. 134, 149, 174).

Piña-Ochoa, E., S. Høgslund, E. Geslin, T. Cedhagen, N. P. Revsbech, L. P. Nielsen, M. Schweizer, F. Jorissen, S. Rysgaard, and N. Risgaard-Petersen (2010). Widespread occurrence of nitrate storage and denitrification among Foraminifera and Gromiida. In: *Proceedings of the National Academy of Sciences* 107.3, pp. 1148–1153 (cit. on p. 121).

Platt, T and K Denman (1977). Organisation in the pelagic ecosystem. In: *Helgoländer Wissenschaftliche Meeresuntersuchungen* 30, pp. 575–581 (cit. on p. 143).

Platt, T., D. S. Rao, and B. Irwin (1983). Photosynthesis of picoplankton in the oligotrophic ocean. In: *Nature* 301.5902, pp. 702–704 (cit. on p. 119).

Ploug, H., M. H. Iversen, and G. Fischer (2008). Ballast, sinking velocity, and apparent diffusivity within marine snow and zooplankton fecal pellets: Implications for substrate turnover by attached bacteria. In: *Limnology and Oceanography* 53.5, pp. 1878–1886 (cit. on p. 174).

Ploug, H., A. Terbrüggen, A. Kaufmann, D. Wolf-Gladrow, and U. Passow (2010). A novel method to measure particle sinking velocity in vitro, and its comparison to three other in vitro methods. In: *Limnology and Oceanography: Methods* 8.8, pp. 386–393. DOI: 10.4319/lom.2010.8.386 (cit. on pp. 39, 133).

Polet, S (2004). Small-Subunit Ribosomal RNA Gene Sequences of Phaeodarea Challenge the Monophyly of Haeckel's Radiolaria. In: *Protist* 155.1, pp. 53–63. DOI: 10.1078/1434461000164 (cit. on p. 26).

Polovina, J. J., E. A. Howell, and M. Abecassis (2008). Ocean's least productive waters are expanding. In: *Geophysical Research Letters* 35.3. DOI: 10.1029/2007gl031745 (cit. on pp. 31, 96, 101).

Pondaven, P., M. Gallinari, S. Chollet, E. Bucciarelli, G. Sarthou, S. Schultes, and F. Jean (2007). Grazing-induced changes in cell wall silicification in a marine diatom. In: *Protist* 158.1, pp. 21–28 (cit. on p. 64).

Primeau, F. (2005). Characterizing transport between the surface mixed layer and the ocean interior with a forward and adjoint global ocean transport model. In: *Journal of Physical Oceanography* 35.4, pp. 545–564 (cit. on p. 158).

R Core Team (2020). R: A Language and Environment for Statistical Computing. R Foundation for Statistical Computing. Vienna, Austria. URL: https://www.R-project.org/ (cit. on p. 52).

— (2022). R: A Language and Environment for Statistical Computing. R Foundation for Statistical Computing. Vienna, Austria. URL: https://www.R-project.org/ (cit. on pp. 143, 162).

Ramondenc, S., M. Goutx, F. Lombard, C. Santinelli, L. Stemmann, G. Gorsky, and L. Guidi (2016). An initial carbon export assessment in the Mediterranean Sea based on drifting sediment traps and the Underwater Vision Profiler data sets. In: *Deep Sea Research Part I: Oceanographic Research Papers* 117, pp. 107–119 (cit. on pp. 22, 36, 132, 148).

Ratnarajah, L., R. Abu-Alhaija, A. Atkinson, S. Batten, N. J. Bax, K. S. Bernard, G. Canonico, A. Cornils, J. D. Everett, M. Grigoratou, et al. (2023). Monitoring and modelling marine zooplankton in a changing climate. In: *Nature Communications* 14.1, p. 564 (cit. on pp. 123, 124).

Redfield, A. C. (1934). On the proportions of organic derivatives in sea water and their relation to the composition of plankton. Vol. 1. university press of liverpool Liverpool (cit. on p. 63).

Reshetnyak, V. V. (1966). Glubokovodnye radiolyarii Phaeodaria severo zapadnoi chasti Tikhogo okeana. (The deepwater radiolarians Phaeodaria from the northwestern Pacific Ocean). In: *Fauna SSSR. Radiolyarii* 94, pp. 1–208 (cit. on p. 29).

Reynolds, O. (1883). XXIX. An experimental investigation of the circumstances which determine whether the motion of water shall be direct or sinuous, and of the law of resistance in parallel channels. In: *Philosophical Transactions of the Royal Society of London* 174, pp. 935–982. DOI: 10.1098/rstl.1883.0029 (cit. on p. 38).

Richardson, A. J. (2008). In hot water: zooplankton and climate change. In: *ICES Journal of Marine Science* 65.3, pp. 279–295 (cit. on p. 123).

Richardson, T. L. and G. A. Jackson (2007). Small Phytoplankton and Carbon Export from the Surface Ocean. In: *Science* 315.5813, pp. 838–840. DOI: 10.1126/science.1133471 (cit. on p. 121).

Riemann, F. (1989). Gelatinous phytoplankton detritus aggregates on the Atlantic deep-sea bed: structure and mode of formation. In: *Marine Biology* 100, pp. 533–539 (cit. on p. 122).

Riley, J. S., R. Sanders, C. Marsay, F. A. C. L. Moigne, E. P. Achterberg, and A. J. Poulton (2012). The relative contribution of fast and slow sinking particles to ocean carbon export. In: *Global Biogeochemical Cycles* 26.1, n/a–n/a. DOI: 10.1029/2011gb004085 (cit. on pp. 33, 34, 173).

Robinson, C. et al. (2010). Mesopelagic zone ecology and biogeochemistry –a synthesis. In: *Deep Sea Research Part II: Topical Studies in Oceanography* 57.16, pp. 1504–1518. DOI: 10.1016/j.dsr2.2010.02.018 (cit. on pp. 17, 21, 90, 97, 158, 199).

Sarmiento, J. L. and J. Toggweiler (1984). A new model for the role of the oceans in determining atmospheric P CO2. In: *Nature* 308.5960, pp. 621–624 (cit. on p. 158).

Sieburth, J. M. (1979). Sea microbes: a survey of the habitats, field and laboratory methods, morphology, nutrition, taxonomy, and ecology of marine bacteria, fungi, microalgae, and protozoa. (Cit. on p. 16).

Sierra, R., M. V. Matz, G. Aglyamova, L. Pillet, J. Decelle, F. Not, C. de Vargas, and J. Pawlowski (2013). Deep relationships of Rhizaria revealed by phylogenomics: a farewell to Haeckel's Radiolaria. In: *Molecular phylogenetics and evolution* 67.1, pp. 53–59 (cit. on pp. 26, 46).

Siever, R, S. Schneider, and P. Boston (1991). Silica in the oceans: Biological-geochemical interplay. In: *Scientists on gaia*, pp. 287–295 (cit. on p. 46).

Silver, M. W. and M. M. Gowing (1991). The "particle" flux: Origins and biological components. In: *Progress in Oceanography* 26.1, pp. 75–113. DOI: 10.1016/0079-6611(91)90007-9 (cit. on p. 19).

Spindler, M. and K. Beyer (1990). Distribution, abundance and diversity of Antarctic acantharian cysts. In: *Marine Micropaleontology* 15.3-4, pp. 209–218 (cit. on p. 119).

Steinberg, D. K., C. A. Carlson, N. R. Bates, S. A. Goldthwait, L. P. Madin, and A. F. Michaels (2000). Zooplankton vertical migration and the active transport of dissolved organic and inorganic carbon in the Sargasso Sea. In: *Deep Sea Research Part I: Oceanographic Research Papers* 47.1, pp. 137–158 (cit. on p. 132).

Steinberg, D. K., J. S. Cope, S. E. Wilson, and T Kobari (2008a). A comparison of mesopelagic mesozooplankton community structure in the subtropical and subarctic North Pacific Ocean. In: *Deep Sea Research Part II: Topical Studies in Oceanography* 55.14-15, pp. 1615–1635 (cit. on pp. 96, 97).

Steinberg, D. K. and M. R. Landry (2017). Zooplankton and the Ocean Carbon Cycle. In: *Annual Review of Marine Science* 9.1, pp. 413–444. DOI: 10.1146/annurev-marine-010814-015924 (cit. on pp. 23, 24).

Steinberg, D. K., B. A. S. V. Mooy, K. O. Buesseler, P. W. Boyd, T. Kobari, and D. M. Karl (2008b). Bacterial vs. zooplankton control of sinking particle flux in the ocean's twilight zone. In: *Limnology and Oceanography* 53.4, pp. 1327–1338. DOI: 10.4319/lo.2008.53.4.1327 (cit. on pp. 20, 21, 90, 97, 98, 194).

Stemmann, L and E Boss (2012). Plankton and particle size and packaging: from determining optical properties to driving the biological pump. In: *Annual Review of Marine Science* 4, pp. 263–290 (cit. on pp. 33, 34, 98, 102, 159).

Stemmann, L., M. Youngbluth, K. Robert, A. Hosia, M. Picheral, H. Paterson, F. Ibanez, L. Guidi, F. Lombard, and G. Gorsky (2008). Global zoogeography of fragile macrozooplankton in the upper 100–1000 m inferred from the underwater video profiler. In: *ICES Journal of Marine Science* 65.3, pp. 433–442. DOI: 10.1093/icesjms/fsn010 (cit. on pp. 31, 36, 90, 93, 132).

Sterner, R. W. and J. J. Elser (2017). Ecological Stoichiometry. Princeton university press (cit. on p. 63).

Stoderegger, K. E. and G. J. Herndl (1999). Production of exopolymer particles by marine bacterioplankton under contrasting turbulence conditions. In: *Marine Ecology Progress Series* 189, pp. 9–16 (cit. on p. 21).

Stoecker, D. K., P. J. Hansen, D. A. Caron, and A. Mitra (2017). Mixotrophy in the Marine Plankton. In: *Annual Review of Marine Science* 9.1, pp. 311–335. DOI: 10.1146/annurev-marine-010816-060617 (cit. on pp. 118, 119, 124).

Stokes, G. G. (1851). On the effect of the internal friction of fluids on the motion of pendulums. Vol. 9. Trans. Cambridge Philos. Soc. (cit. on pp. 22, 38, 76, 133, 198).

Strelkov, A. and V. Reshetnyak (1959). Novaya zhiznennaya forma u radiolyariy. In: *Zool. Zhur* 38, pp. 355–361 (cit. on p. 49).

Stukel, M. R., T. Biard, J. Krause, and M. D. Ohman (2018). Large Phaeodaria in the twilight zone: Their role in the carbon cycle. In: *Limnology and Oceanography* 63.6, pp. 2579–2594. DOI: 10.1002/lno.10961 (cit. on pp. 30, 32, 47, 48, 53, 62, 65, 68, 69, 75, 91, 92, 97, 104, 105, 117, 126, 198–200).

Stukel, M. R., J. P. Irving, T. B. Kelly, M. D. Ohman, C. K. Fender, and N. Yingling (2023). Carbon sequestration by multiple biological pump pathways in a coastal upwelling biome. In: *Nature communications* 14.1, p. 2024 (cit. on pp. 19, 20, 132, 158).

Stukel, M. R., M. D. Ohman, T. B. Kelly, and T. Biard (2019). The Roles of Suspension-Feeding and Flux-Feeding Zooplankton as Gatekeepers of Particle Flux Into the Mesopelagic Ocean in the Northeast Pacific. In: *Frontiers in Marine Science* 6. DOI: 10.3389/fmars.2019.00397 (cit. on pp. 25, 34, 37, 41, 91, 98, 120, 195).

Stukel, M. R., H. Song, R. Goericke, and A. J. Miller (2017). The role of subduction and gravitational sinking in particle export, carbon sequestration, and the remineralization length scale in the California Current Ecosystem. In: *Limnology and Oceanography* 63.1, pp. 363–383. DOI: 10.1002/lno.10636 (cit. on pp. 20, 132, 158).

Sugiyama, K. and O. R. Anderson (1997). Experimental and observational studies of radiolarian physiological ecology, 6. Effects of silicate-supplemented seawater on the longevity and weight gain of spongiose radiolarians Spongaster tetras and Dictyocoryne truncatum. In: *Marine Micropaleontology* 29.2, pp. 159–172 (cit. on p. 67).

Suzuki, N. and Y. Aita (2011). Radiolaria: achievements and unresolved issues: taxonomy and cytology. In: *Plankton and Benthos Research* 6.2, pp. 69–91. DOI: 10.3800/pbr.6.69 (cit. on p. 26).

Suzuki, N. and F. Not (2015). Biology and Ecology of Radiolaria. In: *Marine Protists*. Springer Japan, pp. 179–222. DOI: 10.1007/978-4-431-55130-0_8 (cit. on pp. 26, 28, 46, 47, 49, 90, 91, 118, 120, 125, 194, 197).

Suzuki, N. and M. Oba (2015). Oldest Fossil Records of Marine Protists and the Geologic History Toward the Establishment of the Modern-Type Marine Protist World. In: *Marine Protists*. Springer Japan, pp. 359–394. DOI: 10.1007/978-4-431-55130-0_15 (cit. on pp. 90, 101).

Takahashi, K., D. C. Hurd, and S. Honjo (1983). Phaeodarian Skeletons: Their Role in Silica Transport to the Deep Sea. In: *Science* 222.4624, pp. 616–618. DOI: 10.1126/science.222.4624.616 (cit. on pp. 32, 39, 123).

Takahashi, K. (1982). Vertical flux, ecology and dissolution of Radiolaria in tropical oceans: implications for the silica cycle. PhD thesis. Massachusetts Institute of Technology (cit. on p. 32).

— (1987). Radiolarian flux and seasonality: Climatic and El Nino response in the subarctic Pacific, 1982-1984. In: *Global Biogeochemical Cycles* 1.3, pp. 213–231. DOI: 10.1029/gb001i003p00213 (cit. on p. 125).

— (1997). Time-series fluxes of Radiolaria in the eastern subarctic Pacific Ocean. In: *News of Osaka Micropaleonotlogists, Special Volume* 10, pp. 299–309 (cit. on pp. 124, 125).

Takahashi, K. and O. R. Anderson (2000). Class Phaeodaria. In: *The second illustrated guide to the protozoa*. Lee JJ, Leedale GF, Brandbury P. Society of Protozoologists, pp. 981–994 (cit. on pp. 27, 28).

Takahashi, K. and S. Honjo (1981). Vertical Flux of Radiolaria: A Taxon-Quantitative Sediment Trap Study from the Western Tropical Atlantic. In: *Micropaleontology* 27.2, p. 140. DOI: 10.2307/1485284 (cit. on p. 32).

— (1983). Radiolarian skeletons: size, weight, sinking speed, and residence time in tropical pelagic oceans. In: *Deep Sea Research Part A. Oceanographic Research Papers* 30.5, pp. 543–568. DOI: 10.1016/0198-0149(83)90088-2 (cit. on pp. 33, 66).

Takahashi, K. and D. C. Hurd (2007). Micro- and ultra-structures of phaeodarian Radiolaria. In: (cit. on p. 27).

Takahashi, K. T. and G. W. Hosie (2020). Report on the status and trends of Southern Ocean zooplankton based on the SCAR Southern Ocean continuous plankton recorder (SO-CPR) survey. In: (cit. on p. 125).

Taucher, J., L. T. Bach, A. F. Prowe, T. Boxhammer, K. Kvale, and U. Riebesell (2022). Enhanced silica export in a future ocean triggers global diatom decline. In: *Nature* 605.7911, pp. 696–700 (cit. on p. 101).

Taucher, J., L. T. Bach, U. Riebesell, and A. Oschlies (2014). The viscosity effect on marine particle flux: A climate relevant feedback mechanism. In: *Global Biogeochemical Cycles* 28.4, pp. 415–422 (cit. on pp. 22, 133).

Team, R. C. (2020). R Core Team R: a language and environment for statistical computing. In: *Foundation for Statistical Computing* (cit. on p. 106).

Testor, P., L. Coppola, and A. Bosse (2022). MOOSE-GE 2022 cruise, Pourquoi pas ? R/V. DOI: 10.17600/18001854. URL: https://campagnes.flotteoceanographique.fr/campagnes/18001854/ (cit. on p. 144).

Thomalla, S. J., A. J. Poulton, R. Sanders, R. Turnewitsch, P. M. Holligan, and M. I. Lucas (2008). Variable export fluxes and efficiencies for calcite, opal, and organic carbon in the Atlantic Ocean: A ballast effect in action? In: *Global Biogeochemical Cycles* 22.1 (cit. on p. 173).

Trégouboff, G (1956). Prospection biologique sous-marine dans la région de Villefranche-sur-Mer en juin 1956. In: *Bulletin de l'Institut Océanographique* 1085, pp. 1–24 (cit. on p. 120).

Tréguer, P., L. Lindner, A. J. van Bennekom, A. Leynaert, M. Panouse, and G. Jacques (1991). Production of biogenic silica in the Weddell-Scotia Seas measured with 32Si. In: *Limnology and Oceanography* 36.6, pp. 1217–1227 (cit. on p. 51).

Tréguer, P. J. and C. L. De La Rocha (2013). The World Ocean Silica Cycle. In: *Annual Review of Marine Science* 5.1, pp. 477–501. DOI: 10.1146/annurev-marine-121211-172346 (cit. on p. 99).

Trubovitz, S., D. Lazarus, J. Renaudie, and P. J. Noble (2020). Marine plankton show threshold extinction response to Neogene climate change. In: *Nature Communications* 11.1. DOI: 10.1038/s41467-020-18879-7 (cit. on p. 124).

Trudnowska, E., L. Lacour, M. Ardyna, A. Rogge, J. O. Irisson, A. M. Waite, M. Babin, and L. Stemmann (2021). Marine snow morphology illuminates the evolution of phytoplankton blooms and determines their subsequent vertical export. In: *Nature communications* 12.1, p. 2816 (cit. on pp. 134, 143, 150, 159, 162, 165, 167, 172, 173, 176).

Trull, T., S. Bray, K. Buesseler, C. Lamborg, S. Manganini, C. Moy, and J. Valdes (2008). In situ measurement of mesopelagic particle sinking rates and the control of carbon transfer to the ocean interior during the Vertical Flux in the Global Ocean (VERTIGO) voyages in the North Pacific. In: *Deep Sea Research Part II: Topical Studies in Oceanography* 55.14-15, pp. 1684–1695. DOI: 10.1016/j.dsr2.2008.04.021 (cit. on pp. 133, 134, 172, 201).

Tréguer, P. J. et al. (2021). Reviews and syntheses: The biogeochemical cycle of silicon in the modern ocean. In: *Biogeosciences* 18.4, pp. 1269–1289. DOI: 10.5194/bg-18-1269-2021 (cit. on pp. 23, 47, 99, 102, 122).

Turner, J. T. (2002). Zooplankton fecal pellets, marine snow and sinking phytoplankton blooms. In: *Aquatic microbial ecology* 27.1, pp. 57–102 (cit. on pp. 22, 133, 159, 201).

Turner, J. T. (2015). Zooplankton fecal pellets, marine snow, phytodetritus and the ocean's biological pump. In: *Progress in Oceanography* 130, pp. 205–248. DOI: 10.1016/j.pocean.2014.08.005 (cit. on pp. 17, 22, 194).

Urrere, M. A. and G. A. Knauer (1981). Zooplankton fecal pellet fluxes and vertical transport of particulate organic material in the pelagic environment. In: *Journal of Plankton Research* 3.3, pp. 369–387 (cit. on p. 22).

Valavi, R., J. Elith, J. J. Lahoz-Monfort, and G. Guillera-Arroita (2018). blockCV: An r package for generating spatially or environmentally separated folds for k-fold cross-validation of species distribution models. In: *Biorxiv*, p. 357798 (cit. on p. 106).

Vargas, C. de et al. (2015). Eukaryotic plankton diversity in the sunlit ocean. In: *Science* 348.6237, pp. 1261605–1261605. DOI: 10.1126/science.1261605 (cit. on p. 118).

Vilgrain, L., F. Maps, M. Picheral, M. Babin, C. Aubry, J.-O. Irisson, and S.-D. Ayata (2021). Trait-based approach using in situ copepod images reveals contrasting ecological patterns across an Arctic ice melt zone. In: *Limnology and Oceanography* 66.4, pp. 1155–1167 (cit. on pp. 134, 150).

Villa-Alfageme, M., F. C. de Soto, E. Ceballos, S. L. C. Giering, F. A. C. L. Moigne, S. Henson, J. L. Mas, and R. J. Sanders (2016). Geographical, seasonal, and depth variation in sinking particle speeds in the North Atlantic. In: *Geophysical Research Letters* 43.16, pp. 8609–8616. DOI: 10.1002/2016gl069233 (cit. on pp. 134, 172, 174, 175).

Villa-Alfageme, M., F De Soto, F. A. Le Moigne, S. Giering, R. Sanders, and R García-Tenorio (2014). Observations and modeling of slow-sinking particles in the twilight zone. In: *Global Biogeochemical Cycles* 28.11, pp. 1327–1342 (cit. on pp. 133, 134, 172, 201).

Villar, E., V. Dani, E. Bigeard, T. Linhart, M. Mendez-Sandin, C. Bachy, C. Six, F. Lombard, C. Sabourault, and F. Not (2018). Symbiont chloroplasts remain active during bleaching-like response induced by thermal stress in Collozoum pelagicum (Collodaria, Retaria). In: *Frontiers in Marine Science* 5, p. 387 (cit. on p. 123).

Volk, T. and M. I. Hoffert (1985). Ocean carbon pumps: Analysis of relative strengths and efficiencies in ocean-driven atmospheric CO2 changes. In: *The carbon cycle and atmospheric CO2: natural variations Archean to present* 32, pp. 99–110 (cit. on pp. 131, 158, 194).

Walt, S. Van der, J. L. Schönberger, J. Nunez-Iglesias, F. Boulogne, J. D. Warner, N. Yager, E. Gouillart, and T. Yu (2014). scikit-image: image processing in Python. In: *PeerJ* 2, e453 (cit. on p. 139).

Wickham, H. (2011). The split-apply-combine strategy for data analysis. In: *Journal of statistical software* 40, pp. 1–29 (cit. on p. 162).

Wickham, H., M. Averick, J. Bryan, W. Chang, L. D. McGowan, R. François, G. Grolemund, A. Hayes, L. Henry, J. Hester, et al. (2019). Welcome to the Tidyverse. In: *Journal of open source software* 4.43, p. 1686 (cit. on pp. 143, 162).

Williams, J. and S. Giering (2022). In situ particle measurements deemphasize the role of size in governing the sinking velocity of marine particles. In: *Geophysical Research Letters* 49.21, e2022GL099563 (cit. on pp. 22, 39, 133).

Wilson, S. E., H. A. Ruhl, and K. L. Smith (2013). Zooplankton fecal pellet flux in the abyssal northeast Pacific: A 15 year time-series study. In: *Limnology and Oceanography* 58.3, pp. 881–892. DOI: 10.4319/lo.2013.58.3.0881 (cit. on p. 19).

Worden, A. Z., M. J. Follows, S. J. Giovannoni, S. Wilken, A. E. Zimmerman, and P. J. Keeling (2015). Rethinking the marine carbon cycle: Factoring in the multifarious lifestyles of microbes. In: *Science* 347.6223, pp. 1257594–1257594. DOI: 10.1126/science.1257594 (cit. on p. 24).

Yeo, I.-K. and R. A. Johnson (2000). A new family of power transformations to improve normality or symmetry. In: *Biometrika* 87.4, pp. 954–959 (cit. on pp. 143, 162).

Yuasa, T. and O. Takahashi (2016). Light and electron microscopic observations of the reproductive swarmer cells of nassellarian and spumellarian polycystines (Radiolaria). In: *European Journal of Protistology* 54, pp. 19–32. DOI: 10.1016/j.ejop.2016.02.007 (cit. on p. 68).

Zasko, D. N. and I. I. Rusanov (2005). Vertical distribution of radiolarians and their role in epipelagic communities of the East Pacific Rise and the Gulf of California. In: *Biology Bulletin* 32.3, pp. 279–287 (cit. on p. 120).

Zweng, M., D Seidov, T. Boyer, M. Locarnini, H. Garcia, A. Mishonov, O. Baranova, K. Weathers, C. Paver, I Smolyar, et al. (2019). World ocean atlas 2018, volume 2: Salinity. In: (cit. on p. 105).

Scientific activities carried out during the thesis

Scientific publications

1. **Laget, M.**, Llopis-Monferrer, N., Maguer, J. F., Leynaert, A., Biard, T. (2023). Elemental content allometries and silicon uptake rates of planktonic Rhizaria: Insights into their ecology and role in biogeochemical cycles. *Limnology and Oceanography, 68*(2), 439-454.

Oral and poster presentations

5. **Laget, M.**, Picheral, M., Catalano, C., Guidi, L., Biard, T. 2023. In situ imaging sheds light on particle sinking velocities in the North Atlantic. Ocean Twilight Zone Symposium (Woods Hole, USA). Poster presentation.

4. **Laget, M.**, Picheral, M., Catalano, C., Guidi, L., Biard, T. 2023. High-throughput imaging sheds light on marine particle in situ sinking behavior in the Mediterranean Sea. Aquatic Science Meeting (Palma de Mallorca, Spain). Oral presentation.

3. **Laget, M.**, Picheral, M., Catalano, C., Guidi, L., Biard, T. 2023. High-throughput imaging to observe in situ sinking behavior of marine particles: artificial intelligence for carbon fluxes assessment?. Workshop Artificial Intelligence for Ocean, Atmosphere and Climate (Brest, France). Poster presentation.

2. **Laget, M.**, Llopis-Monferrer, N., Maguer, J.F., Leynaert, A., Biard, T. 2022. Elemental mass of modern Rhizaria: from cellular scale to global biogeochemical cycles. InterRad XVI (Ljubljana, Slovenia). Oral presentation. Best presentation award for young scientist.

1. **Laget, M.**, Picheral, M., Catalano, C., Biard, T. 2022. Direct in situ observations of particle flux in the California Current Ecosystem: new perspectives from coupled sediment traps and in situ imaging data. Ocean Science Meeting (virtual meeting). Oral presentation.

Teaching and supervision

Teaching

2021-2023: Biostatistics (undergraduate, 59 h), Oceanographic techniques (undergraduate, 8 h), Marine Ecosystem Structure and Functioning (master, 11 h), Coastal flora and fauna (undergraduate, 9 h)

Internship supervision

Apr-Jun 2023, Julia Butel (1st year Master student at Université du Littoral Côte d'Opale) - *Contribution of Phaeodaria to carbon fluxes in the California Current*

Apr-Jun 2022, Zoé Garmirian (1st year Master student at Sorbonne Université) - *Spatial variability of particulate organic carbon vertical fluxes in the California Current using gel trap imaging*

Apr-Jun 2021, Martin Bourges (1st year Master student at Université du Littoral Côte d'Opale) - *Measuring carbon content of Rhizaria*

Oceanographic cruises

16th Jan.– 14th Mar. 2022. BLOOFINZ cruise, onboard R/V Roger Revelle. Chief scientist: Mike Landry.

13th Jul.– 13th Aug. 2021. Process cruise P2107 (CCE-LTER), onboard R/V Roger Revelle. Chief scientists: Mike Stukel and Katherine Barbeau.

Science communication and outreach

2022 - Fêtes de la Science (Science Festival), Laboratoire d'Océanologie et de Géosciences, 6 days dedicated to activities for school students and the general public

2022 - The Micropalaeontological Society, Image competition award
2022 - Pint of Science presentation, *Plankton and the ocean carbon sink*, Amiens, France
2021-2022 - *What's in a drop of seawater?*, Plankton observation with elementary and middle school students organized by CNRS, 5 days in total

Additional training

2021 - Underwater Vision Profiler 5 and 6 user training, Institut de la Mer de Villefranche, France

Miscellaneous

2021-2023 - Newsletter facilitation, Laboratoire d'Océanologie et de Géosciences

Résumé

Les océans épipélagique et mésopélagique jouent un rôle clé dans la production, le recyclage et le transfert de la matière organique et minérale vers l'océan profond. Les Rhizaria (comprenant les Radiolaria et les Phaeodaria) sont des protistes planctoniques qu'on retrouve dans ces couches de l'océan mondial. Ils peuvent être mixotrophes ou hétérotrophes, et certains d'entre eux forment des squelettes de silice. De plus, ces organismes peuvent agréger du matériel détritiques autour d'eux, formant ainsi des particules sédimentant rapidement. L'échantillonnage de ces organismes fragiles est difficile par le biais de méthodes traditionnelles comme les filets à plancton, mais les avancées en imagerie in situ ont amélioré les estimations de leur abondance et de leur rôle dans les flux élémentaires. Cependant, en raison du manque de mesures au niveau cellulaire, notre compréhension de leur biomasse mondiale en carbone et de leur rôle dans les processus biogéochimiques reste limitée. Pour combler ces lacunes, le contenu en carbone de divers taxons de Rhizaria a été mesuré, couvrant un large spectre de tailles, et une relation allométrique a été établie, révélant une densité de carbone globalement faible par rapport aux protistes plus petits. À l'aide de *boosted regression trees* et d'un ensemble de données global collecté à l'aide de l'Underwater Vision Profiler (UVP) 5, comprenant plus de 167 000 images de Rhizaria enregistrées dans le monde entier, la biomasse mondiale en carbone des Rhizaria >600 μm a été ré-estimée à 1,7 % de la biomasse totale du mésozooplancton dans les 500 premiers m de la colonne d'eau. Cette biomasse s'est révélée être dix fois plus élevée dans la zone mésopélagique que dans la zone épipélagique. Ensuite, il a été estimé que les Phaeodaria mésopélagiques, se nourrissant du flux de particules, peuvent intercepter de 3,8 à 9,2 % du flux de carbone particulaire exporté de la zone euphotique. Dans l'océan Austral, où leur abondance était précédemment considérée faible, ce taux d'interception est de 11,2-23,4 %. De plus, les taux de production de silice biogénique (bSi) des Phaeodaria ont été estimés, constituant la première quantification de la production de bSi dans la zone mésopélagique. En tant que seuls producteurs de bSi dans cette zone, ils jouent un rôle significatif dans son recyclage, co-dominant le cycle du silicium aux côtés des diatomées et des éponges. Enfin, une nouvelle méthodologie pour mesurer la vitesse de sédimentation des particules marines à l'aide de l'UVP6 monté sur un piège à sédiments a été introduite. Après la collecte d'environ 9 000 valeurs de vitesse de sédimentation dans l'Atlantique Nord, aucune relation forte n'a été trouvée entre les mesures morphologiques fournies par l'UVP6 et celles-ci. Au lieu de cela, il a été observé que les vitesses de sédimentation augmentent avec la profondeur et sont influencées par les conditions environnementales. Ces résultats mettent en évidence l'importance de prendre en compte la composition des communautés phytoplanctoniques et zooplanctoniques, pour estimer la vitesse et affiner les estimations de flux qui utilisent l'imagerie in situ.

Mots-clés Rhizaria, cycle du carbone, cycle du silicium, imagerie in situ, biomasse, vitesse de sédimentation

Abstract

The epipelagic and mesopelagic oceans play a key role in the production, recycling, and transfer of both organic and mineral matter to the deep ocean. Rhizaria (including Radiolaria and Phaeodaria) are planktonic protists thriving in these layers throughout the world ocean. They can display either mixotrophic or heterotrophic feeding behavior, and some of them form silica skeletons. Furthermore, these organisms can aggregate detrital material around them, forming fast-sinking particles. Sampling these fragile organisms is challenging, but advances in in situ imaging techniques have improved estimates of their abundance and roles in element fluxes. Still, due to a lack of measurements at the cellular level, our understanding of their global carbon biomass and their roles in biogeochemical processes remains limited. To fill this gap, the carbon content of diverse rhizarian taxa was measured, covering a broad size spectrum, and an allometric relationship was established, revealing an overall low carbon density compared to smaller protists. Using boosted regression trees and a global Underwater Vision Profiler (UVP) 5 dataset, including >167,000 rhizarian images recorded all over the world ocean, global carbon biomass of >600-μm Rhizaria was reestimated to be 1.7% of the total mesozooplankton biomass within the upper 500 m of the water column. This biomass was found to be 10-fold higher in the mesopelagic than in the epipelagic layer. Subsequently, mesopelagic flux-feeder Phaeodaria were estimated to intercept 3.8-9.2% of the gravitational POC flux exported out of the euphotic zone. In the Southern Ocean, where their abundance was previously shown to be low, this interception rate can reach as high as 11.2-23.4%. In addition, biogenic silica (bSi) production rates of Phaeodaria were estimated, being the first quantification of bSi production in the mesopelagic layer. As the sole bSi producers in this layer, they play a significant role in its recycling, co-dominating the silicon cycle along with diatoms and sponges. Lastly, a new methodology to measure the sinking speed of marine particles using the UVP6 mounted on a sediment trap was introduced. After collecting approx. 9,000 measurements of particle sinking speeds in the North Atlantic, no strong relationships were found between morphological measurements provided by the UVP6 and sinking speeds. Instead, it was observed that sinking speeds increased with depth and were influenced by environmental conditions. These results highlight the importance of considering community composition, including both phytoplankton and zooplankton, for speed estimation and to refine flux estimates using in situ imaging.

Keywords Rhizaria, carbon cycle, silicon cycle, in situ imaging, biomass, sinking speed